

UNIVERSITY OF OKLAHOMA

GRADUATE COLLEGE

**THERMAL STRATIFICATION IN LIQUID STORAGE TANK USING AN  
INLET POROUS MANIFOLD**

**A DISSERTATION**

**SUBMITTED TO THE GRADUATE FACULTY**

in partial fulfillment of the requirements for the

degree of

**DOCTOR OF PHILOSOPHY**

**By**

**NOEL M. BROWN**

Norman, Oklahoma  
2003

UMI Number: 3104295

**UMI**<sup>®</sup>

---

UMI Microform 3104295

Copyright 2003 by ProQuest Information and Learning Company.

All rights reserved. This microform edition is protected against  
unauthorized copying under Title 17, United States Code.

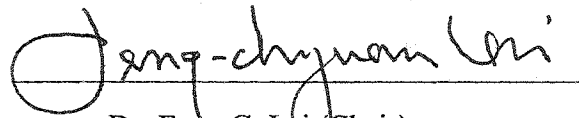
ProQuest Information and Learning Company  
300 North Zeeb Road  
P.O. Box 1346  
Ann Arbor, MI 48106-1346

**© Copyright by Noel M. Brown 2003  
All Rights Reserved**

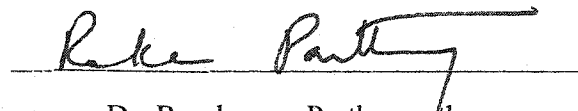
**THERMAL STRATIFICATION IN A LIQUID STORAGE TANK USING AN  
INLET POROUS MANIFOLD**

**A DISSERTATION APPROVED FOR THE SCHOOL OF AEROSPACE AND  
MECHANICAL ENGINEERING**

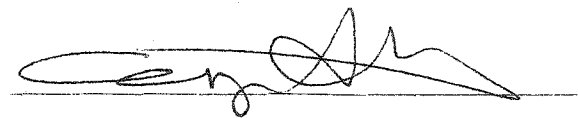
BY

  
Dr. Feng C. Lai (Chair)

  
Dr. Tom Love

  
Dr. Ramkumar Parthasarathy

  
Dr. Semion Gutman

  
Dr. Cengiz M. Altan

## ACKNOWLEDGEMENTS

The author would like to express his appreciation and gratitude to Professor Feng Chyuan Lai, for being an outstanding faculty advisor and the chairman of this Dissertation Committee. His suggestion of this topic is greatly appreciated. Over the last four years his guidance, inspiration, and patience were the most significant factors that led to the completion of this work.

The author also respectfully acknowledges the support of Dr. Tom Love, an emeritus professor, who returns from retirement to serve on this committee. The author would also like to thank Dr. Ramkumar Parthasarathy, Dr. Semion Gutman, Dr. Cengiz M. Altan, and Dr. William Sutton for their time, valuable advice and suggestions as members of this dissertation committee. In addition, their classes over the years have provided the foundation for this study.

The author thanks Fulbright LASPAU for awarding him a fellowship to pursue this degree. The author would also like to thank the directors of the School of Aerospace and Mechanical Engineering for providing me the graduate teaching assistantships over the past two years. The experience I gained will always be cherished.

Also, the research grants received from the Graduate College and the Graduate Student Senate to provide the initial funding for my research project is greatly appreciated. Sincere gratitude to Mr. Huan Do, a undergraduate research assistant, who helped me with the data collection. All beneficial suggestions and stimulating discussions from Mrs. Meirong Huang and Mr. Chea Chin Ngo are greatly respected. In addition, a special thank to the workshop team of Mr. Billy Mays, Mr. Greg Williams and

Mr. Rustin Heflin for their assistance in the design, fabrication and improvement of the experimental setup.

The author would also like to thank Dr. Henry Neeman, Mr. Brandon George and the Center for Analysis and Prediction of Storms (CAPS) for the use of a supercomputer, which was instrumental in the completion of this study on time.

The author thanks his wife Pauline and two beautiful daughters Noella and Danielle for all their understanding and endurance during some difficult times, without which this work could not have been accomplished. To my mother, sisters and brothers who have supported me throughout the years. Also, to Emily Smith who was always there to provide me inner peace and strength through some difficult times.

Lastly, this work is dedicated in memory of my father who always taught me to strive for excellence.

## TABLE OF CONTENTS

ACKNOWLEDGEMENTS .....	iv
TABLE OF CONTENTS .....	vi
LIST OF TABLE .....	ix
LIST OF FIGURES .....	x
NOMENCLATURE .....	xiv
ABSTRACT .....	xviii
CHAPTER 1 INTRODUCTION AND LITERATURE REVIEW	
1.1 Introduction .....	1
1.2 Literature Review .....	3
1.2.1 Thermal Stratification in Thermal Storage Tank .....	3
1.2.2 Stratification Enhancement using Porous Manifold .....	9
1.2.3 Flow in Porous Media .....	12
1.2.4 Determination of Slip Coefficient at the Interface between a Liquid Layer and a Porous Medium .....	15
1.3 Scope of Present Study .....	17
CHAPTER 2 DETERMINATION OF SLIP COEFFICIENT AT THE INTERFACE BETWEEN A LIQUID LAYER AND A POROUS MEDIUM.	
2.1 Introduction .....	19
2.2 Theoretical Background .....	20
2.2.1 Flow in a Channel of Permeable Wall .....	20
2.2.2 Longitudinal Permeability .....	24
2.2.3 Radial Permeability .....	25
2.3 Experimental Setup .....	26
2.3.1 Test Section .....	26
2.3.2 Upstream Plenum .....	34
2.3.3 Downstream Plenum .....	35
2.3.4 Control Unit .....	35
2.3.5 Reservoir Unit .....	36
2.4 Experimental Procedure .....	37
2.4.1 Calibration of Pressure Transducers .....	37
2.4.2 Calibration of Experimental Setup .....	38
2.4.3 Measurement of Longitudinal Permeability .....	39
2.4.4 Measurement Radial Permeability .....	40
2.4.5 Determination of the Slip Coefficient at the Interface between	

	the Fluid Layer and the Porous Tube .....	41
2.5	Results and Discussion .....	42
2.6	Conclusion .....	54
CHAPTER 3	STRATIFICATION ENHANCEMENT AND FLOW VISUALIZATION IN A LIQUID STORAGE TANK	
3.1	Introduction .....	55
3.2	Experimental Setup .....	57
	3.2.1 Storage Tank .....	57
	3.2.2 Inlet Distributor .....	63
	3.2.3 Porous Manifold .....	66
	3.2.4 Charging Loop .....	66
	3.2.5 Data Acquisition System .....	68
3.3	Experimental Procedure .....	68
	3.3.1 Flow Visualization .....	72
3.4	Results and Discussion .....	73
	3.4.1 Effects of Inlet Temperature on Thermal Stratification .....	74
	3.4.2 Effects of Inlet Reynolds Number on Thermal Stratification ...	77
	3.4.3 Degree of Stratification .....	77
	3.4.4 Flow Visualization .....	81
3.5	Conclusion .....	88
CHAPTER 4	NUMERICAL STUDY OF THERMAL STRATIFICATION IN A LIQUID STORAGE TANK WITH A POROUS MANIFOLD	
4.1	Introduction .....	89
4.2	Governing Equations .....	91
	4.2.1 Fluid Region .....	91
	4.2.2 Porous Region .....	93
4.3	Boundary and Interface Conditions .....	95
4.4	Finite-Difference Equations and Numerical Methods .....	98
	4.4.1 Derivation of Finite Difference Equations .....	98
	4.4.2 Upwind Scheme .....	102
	4.4.3 Finite Difference Equations in the Fluid Region .....	105
	4.4.4 Finite Difference Equations in the Porous Region .....	108
4.5	Procedure for Numerical Solution .....	109
4.6	Validation of Numerical Code .....	111
4.7	Results and Discussion .....	112
	4.7.1 Numerical Simulation of Experimental Cases .....	120
	4.7.2 Thermal Stratification in a Liquid Storage Tank .....	124
	a. The Effects of Richardson Number .....	127
	b. Effects of Reynolds Number .....	137
	c. Effects of Rayleigh Number .....	142
	d. Degree of Stratification .....	145
4.8	Conclusion .....	148

CHAPTER 5	CONCLUSIONS	
5.1	Introductory Remarks	150
5.2	Determination of the Slip Coefficient	151
5.3	Stratification Enhancement in a Liquid Storage Tank	152
5.4	Numerical Study	153
5.5	Future Work	154
REFERENCES		156
APPENDIX A		160
APPENDIX B		172
APPENDIX C		189
APPENDIX D		213

## LIST OF TABLES

Table 2.1	List of components of the experimental apparatus and their specification. ....	31
Table 2.2	Validation of experimental setup. ....	46
Table 2.3	Measured longitudinal and radial permeability's of porous tubes. ....	48
Table 3.1	List of components of the experimental apparatus and their specifications. ....	60
Table 4.1	Description of OSCER cluster hardware ....	119
Table 4.2	Thermophysical properties of water and nylon ....	120

## LIST OF FIGURES

Figure 2.1	Schematic drawing of the experimental setup used to measure the longitudinal permeability of a porous tube.....	27
Figure 2.2	Photograph of the experimental setup used to measure the longitudinal permeability of a porous tube.....	28
Figure 2.3	Photograph of the test section without porous tube. ....	30
Figure 2.4	Photograph of the test section with porous tube in place.....	30
Figure 2.5	Schematic drawing of the experimental setup used to measure the radial permeability of a porous tube. ....	43
Figure 2.6	Photograph of the experimental setup used to measure the radial Permeability of a porous tube. ....	44
Figure 2.7	Theoretical flow rate vs. experimental flow rate. ....	46
Figure 2.8	Photograph of materials used to fabricate porous tubes, a) fiberglass mesh and b) nylon mesh ....	47
Figure 2.9	Longitudinal permeability of porous tubes with various wall thicknesses.....	48
Figure 2.10	Radial permeability of porous tubes with various wall thicknesses.....	51
Figure 2.11	Slip coefficient as a function of Reynolds number for a fiberglass tube with various wall thicknesses.....	53
Figure 3.1	Schematic drawing of the experimental setup. ....	58
Figure 3.2	Photograph of the experimental setup. ....	59
Figure 3.3	Photograph of the storage tank with porous manifold and inlet distributor. ....	64
Figure 3.4	Photograph of the inlet distributor. ....	65
Figure 3.5	Photograph of the constant temperature bath (Fisher Scientific	

	Isotemp Refrigerated Circulator 1013S) and micro-flow pump .....	67
Figure 3.6	Photograph of the labview software used in the data collection. ....	69
Figure 3.7	Photograph of the National Instrument SC-2345 signal conditioning chassis with analog and digital input. ....	70
Figure 3.8	Temperature profile for an inlet flow at $T_i = 27.9$ °C and $u_i = 0.0315$ m/s ( $Re = 10691.0$ , $Ra = 7.34 \times 10^9$ and $Ri = 1.0$ ) .....	75
Figure 3.9	Temperature profile for an inlet flow at $T_i = 28.2$ °C and $u_i = 0.0315$ m/s ( $Re = 10445.0$ , $Ra = 2.015 \times 10^9$ and $Ri = 3.04$ ) .....	75
Figure 3.10	Temperature profile for an inlet flow at $T_i = 32.0$ °C and $u_i = 1.25 \times 10^{-3}$ m/s ( $Re = 438.8$ , $Ra = 2.89 \times 10^9$ and $Ri = 2648.8$ ) ..	76
Figure 3.11	Temperature profile for an inlet flow at $T_i = 55.0$ °C and $u_i = 1.25 \times 10^{-3}$ m/s ( $Re = 559.0$ , $Ra = 2.79 \times 10^{10}$ and $Ri = 20691.2$ )	76
Figure 3.12	Temperature profile for an inlet flow at $T_i = 29.0$ °C and $u_i = 0.0138$ m/s ( $Re = 4782.2$ , $Ra = 2.25 \times 10^9$ and $Ri = 12.84$ ) .....	78
Figure 3.13	Temperature profile for an inlet flow at $T_i = 28.9$ °C and $u_i = 0.0315$ m/s ( $Re = 10948.9$ , $Ra = 1.25 \times 10^9$ and $Ri = 1.82$ ) .....	78
Figure 3.14	Degree of stratification as a function of Richardson and Peclet numbers .....	80
Figure 3.15	Mixing tank temperature for various Richardson numbers .....	82
Figure 3.16	Temperature profile for the first flow visualization experiment .....	84
Figure 3.17	Flow visualization for an inlet flow at $T_i = 49.0$ °C and $u_i = 1.25 \times 10^{-3}$ m/s ( $Re = 500$ , $Ra = 1.16 \times 10^{10}$ , and $Ri = 9087.3$ ) .....	85
Figure 3.18	Temperature profile for the second flow visualization experiment .....	86
Figure 3.19	Flow visualization for an inlet flow at $T_i = 26.0$ °C and $u_i = 4.34 \times 10^{-3}$ m/s ( $Re = 1650.1$ , $Ra = 7.43 \times 10^9$ , and $Ri = 527.24$ ) ..	87
Figure 4.1	Configuration and coordinate system of a cylindrical tank. ....	90
Figure 4.2	The control volume of nodal point P in a two-dimensional computational domain. ....	101

Figure 4.3	Flow fields in a storage tank with a porous manifold at $Ri = 0.01$ , a) Yee and Lai (2001), b) present study .....	113
Figure 4.4	Temperature fields in a storage tank with a porous manifold at $Ri = 0.01$ , a) Yee and Lai (2001), b) present study .....	114
Figure 4.5	Flow fields in a storage tank with a porous manifold at $Ri = 100$ , a) Yee and Lai (2001), b) present study .....	115
Figure 4.6	Temperature fields in a storage tank with a porous manifold at $Ri = 100$ , a) Yee and Lai (2001), b) present study.....	116
Figure 4.7	Mix tank temperature in a storage tank with a porous manifold $0.01 \leq Ri \leq 100$ , a) Yee and Lai (2001), b) present study .....	117
Figure 4.8	Temperature profile at $\tau \cong 142$ for an inlet flow at $T_i = 28.19^\circ\text{C}$ and $u_i = 0.0315$ m/s ( $Ri = 3.04$ , $Re = 10445$ and $Ra = 2.0 \times 10^9$ ) .....	122
Figure 4.9	Temperature profile at $\tau \cong 236.5$ for an inlet flow at $T_i = 28.19^\circ\text{C}$ and $u_i = 0.0315$ m/s ( $Ri = 3.04$ , $Re = 10445$ and $Ra = 2.0 \times 10^9$ ) .....	122
Figure 4.10	Comparison of mixing tank temperatures obtained from the numerical and experimental results for an inlet flow at $T_i = 28.19^\circ\text{C}$ and $u_i = 0.0315$ m/s ( $Ri = 3.04$ , $Re = 10445$ and $Ra = 2.0 \times 10^9$ ) .....	123
Figure 4.11	Temperature profile at $\tau \cong 142$ for an inlet flow at $T_i = 29.0^\circ\text{C}$ and $u_i = 0.0138$ m/s ( $Ri = 12.84$ , $Re = 4782.2$ and $Ra = 2.25 \times 10^9$ ) .....	125
Figure 4.12	Temperature profile at $\tau \cong 236.5$ for an inlet flow $T_i = 29.0^\circ\text{C}$ and $u_i = 0.0138$ m/s ( $Ri = 12.84$ , $Re = 4782.2$ and $Ra = 2.25 \times 10^9$ ) .....	125
Figure 4.13	Comparison of mixing tank temperatures obtained from the numerical and experimental results for an inlet flow at $T_i = 29.0^\circ\text{C}$ and $u_i = 0.0138$ m/s ( $Ri = 12.84$ , $Re = 4782.2$ and $Ra = 2.25 \times 10^9$ ) .....	126
Figure 4.14	Flow fields in a charging process at $Re = 10^4$ and $Ra = 10^7$ , ( $Ri = 0.0185$ $\Delta\psi = 0.001$ ) .....	128
Figure 4.15	Temperature fields in a charging process at $Re = 10^4$ and $Ra = 10^7$ , $Ri = 0.0185$ , $\Delta\theta = 0.1$ ) .....	129
Figure 4.16	Flow fields in a charging process at $Re = 10^4$ and $Ra = 10^8$	

	( $Ri = 0.185, \Delta\psi = 0.001$ ) .....	130
Figure 4.17	Temperature fields in a charging process at $Re = 10^4$ and $Ra = 10^8$ ( $Ri = 0.185, \Delta\theta = 0.1$ ) .....	131
Figure 4.18	Flow fields in a charging process at $Re = 10^4$ and $Ra = 10^9$ ( $Ri = 1.85, \Delta\psi = 0.001$ ) .....	133
Figure 4.19	Temperature fields in a charging process at $Re = 10^4$ and $Ra = 10^9$ ( $Ri = 1.85, \Delta\theta = 0.1$ ) .....	134
Figure 4.20	Mixing tank temperature as a function of time for various Richardson numbers, $0.0185 \leq Ri \leq 1.85$ ( $Re = 10^4$ and $10^7 \leq Ra \leq 10^9$ ) e .....	136
Figure 4.21	Flow fields in a charging process at $Re = 10^2$ and $Ra = 10^7$ ( $Ri = 185.2, \Delta\psi = 0.001$ ). .....	138
Figure 4.22	Temperature fields in a charging process at $Re = 10^2$ and $Ra = 10^7$ ( $Ri = 185.2, \Delta\theta = 0.1$ ) .....	139
Figure 4.23	Flow fields in a charging process at $Re = 10^3$ and $Ra = 10^7$ ( $Ri = 1.85, \Delta\psi = 0.001$ ) .....	140
Figure 4.24	Temperature fields in a charging process at $Re = 10^3$ and $Ra = 10^7$ ( $Ri = 1.85, \Delta\theta = 0.1$ ) .....	141
Figure 4.25	Flow fields in a charging process at $Re = 10^3$ and $Ra = 10^9$ ( $Ri = 185.2, \Delta\psi = 0.001$ ) .....	143
Figure 4.26	Temperature fields in a charging process at $Re = 10^3$ and $Ra = 10^9$ ( $Ri = 185.2, \Delta\theta = 0.1$ ) .....	144
Figure 4.27	Degree of stratification for various Richardson numbers .....	146
Figure 4.28	Comparison of the degree of stratification obtained from the numerical and experimental results .....	147

## NOMENCLATURE

Bi	Biot number, $Bi = hr_t/k_f$
$c_f$	specific heat of fluid, [kJ/kg·K]
$c_s$	specific heat of solid phase of porous medium, [kJ/kg·K]
d	thickness of porous tube, [m]
Da	Darcy number, $Da = K/r_t^2$
Fr	Froude number $u/(lg)^{1/2}$
g	gravitational acceleration, [m/s <sup>2</sup> ]
Gr	Grashof number, $Gr = g\beta(T_i - T_\infty) r_t^3/\nu^2$
h	heat transfer coefficient, [W/m <sup>2</sup> K]
$k_f$	thermal conductivity of fluid, [W/mK]
$k_m$	thermal conductivity of porous medium, [W/mK]
$k_s$	thermal conductivity of solid phase of porous medium, [W/mK]
K	permeability of porous medium, [m <sup>2</sup> ]
l	height of cylindrical tank, [m]
L	dimensionless height of cylindrical tank, $L = l/r_t$
P	pressure, [Pa]
Pe	Peclet number, $Pe = Re \cdot Pr (u_i r_t / \alpha_f)$
Pe'	modified Peclet number, $Pe' = Re \cdot Pr (u_i r_t / \alpha_m)$
Pr	Prandtl number, $Pr = \nu / \alpha_f$
r	radial coordinate, [m]

$r_i$	inner radius of porous tube, [m]
$r_{in}$	inlet radius of cylindrical tank, [m]
$r_o$	outer radius of porous tube, [m]
$r_t$	radius of cylindrical tank, [m]
$R$	dimensionless distance in r-direction, $R = r/r_t$
$Ra'$	modified Rayleigh number, $Ra = g\beta K(T_i - T_\infty) r_t / \nu \alpha_m$
$Ra$	Rayleigh number, $Ra = Gr \cdot Pr$
$Re$	Reynolds number, $Re = ur_t / \nu$
$Ri$	Richardson number, $Ri = Gr / Re^2$
$R_{in}$	dimensionless inlet radius of cylindrical tank, $R_{in} = r_{in} / r_t$
$s$	distance of baffle from the inlet, [m]
$S$	dimensionless distance of baffle from the inlet, $S = s / r_t$
$t$	time, [s]
$t_{fil}$	filling time, [s]
$T$	temperature, [K]
$T_c$	temperature of cold wall, [K]
$T_h$	temperature of hot wall, [K]
$T_i$	inlet temperature, [K]
$T_{initial}$	initial temperature, [K]
$T_{mix}$	mixing tank temperature, [K]
$T_\infty$	ambient temperature, [K]
$u, v_z$	velocity in the z-direction, [m/s]
$u_i$	inlet velocity in z-direction, [m/s]

$U$	dimensionless velocity in z-direction, $U = u/u_i$
$U_f$	dimensionless velocity of fluid region z-direction
$u_m$	velocity of porous region in z-direction, [m/s]
$U_m$	dimensionless velocity of porous region z-direction
$v, v_r$	velocity in r-direction, [m/s]
$v_B$	slip velocity
$v_\theta$	velocity in $\theta$ -direction, [m/s]
$V$	dimensionless velocity in r-direction, $V = v/u_i$
$z$	axial coordinates, [m]
$Z$	dimensionless distance in z-direction, $Z = z/r_t$

#### Greek symbols

$\alpha_f$	thermal diffusivity of fluid, [m <sup>2</sup> /s]
$\alpha_m$	thermal diffusivity of porous medium, [m <sup>2</sup> /s]
$\beta_T$	coefficient of volumetric expansion due to temperature change, [1/K]
$\phi$	porosity of the medium
$\gamma$	slip coefficient
$\mu$	dynamic viscosity of fluid, [kg/m·s]
$\nu$	kinematic viscosity of fluid, [m <sup>2</sup> /s]
$\theta$	dimensionless temperature, $\theta = (T - T_\infty)/(T_i - T_\infty)$
$\theta_{mix}$	dimensionless mixing tank temperature
$\theta_w$	dimensionless temperature at wall

$\rho_f$	fluid density, [kg/m <sup>3</sup> ]
$\rho_s$	density of solid phase of porous medium, [kg/m <sup>3</sup> ]
$\rho_\infty$	density of fluid at $T_\infty$ , [kg/m <sup>3</sup> ]
$\sigma$	ratio of heat capacities of porous medium to fluid as defined in Eq. (2.28)
$\tau$	dimensionless time, $\tau = u_i t / r_i$
$\omega$	vorticity as defined in Eq. (2.8)
$\Omega$	dimensionless vorticity as defined in Eq. (2.12)
$\psi$	stream function, [m <sup>2</sup> /s]
$\Psi$	dimensionless stream function as defined in Eq. (2.12)

## ABSTRACT

This work investigated the conditions necessary for thermal stratification in liquid storage tank. The investigation involved the fabrication and testing of a porous manifold to determine its permeability and the slip coefficient that can be used at the interface between the porous wall and the fluid layer. A full-scale model of a thermal storage tank with an aspect ratio of 4 ( $l/r_t = 4$ ) using an inlet porous manifold was constructed and tested. The results were compared to those obtained from a numerical model of the same tank. After validation, the numerical model was used to further investigate the conditions necessary for thermal stratification. In general, this work was carried out in three major parts.

In the first part, fiberglass and nylon nettings were used to fabricate seven porous tubes, with various dimensions. Six tubes had an outer diameter of 1.9 cm and wall thickness ranging from 0.158 cm to 0.635 cm, and the other tube had dimensions of 10 cm outer diameter and wall thickness of 0.635 cm. The larger tube was similar to the inlet manifold used in the storage tank. Theoretical analysis for flow in a porous tube was first conducted. The solution was obtained using the slip coefficient condition at the interface between the porous wall and the fluid layer. Experiments were conducted to determine the permeability of each tube in both longitudinal and radial directions, and the slip coefficient that can be used at the interface. Due to the limitations in the present setup, the longitudinal permeability of the large tube was not measured but was estimated from a smaller tube of the same material and a similar wall thickness.

In the second part, a storage tank was constructed. The dimensions were kept as close as possible to those used in the previous study. A number of experiments were conducted to investigate the conditions necessary for stratification. Flow visualization experiments were also conducted to evaluate the effectiveness of the inlet porous manifold in promoting and maintaining the thermal stratification.

Finally, a numerical simulation of the thermal storage tank was conducted. A comparison with the experimental results was performed to evaluate the accuracy of the permeability and the slip coefficient measured in the first part of the study. It was then used to evaluate stratification at lower Richardson numbers.

Based on the results obtained, it was concluded that slip coefficient depended not only on the material but also on the Reynolds number, the permeability and the porous wall thickness. The longitudinal permeability depended on the material while the radial permeability was found to depend on the wall thickness.

Stratification was observed at a Richardson number as low as  $Ri = 0.615$ . However, the temperature difference required for the lower Richardson number was not practical, therefore, no attempt was made to go below this value. From the flow visualization experiment, it can be concluded that the porous manifold was able to reduce the shear-induced mixing between fluids of different temperature, thus was able to promote and maintain a stable stratification.

From the comparison between the numerical and experimental results one can conclude that the values of the permeability and the slip coefficient used in the simulation were close to its actual value. It was shown that very stable stratification could be

maintained at a Richardson number as low as  $Ri = 0.185$  using a porous manifold, which is lower than the critical value reported earlier by Sliwinski et al. (1978).

# CHAPTER ONE

## INTRODUCTION AND LITERATURE REVIEW

### 1.1 Introduction

Energy storage schemes are necessary for all energy-related applications (particular for those using alternative energy) because of the possible mismatch in the schedule for supply and demand. The most common thermal energy storage devices utilizes phase change materials (commonly known as eutectic salt), rock beds and liquid water. However, most of the solar houses in the United States utilize water because it is non-toxic, abundant, and have a high thermal capacity. In addition, its vapor-liquid phase equilibrium is suitable for the temperature range required for space and water heating.

In solar energy applications, cooler water from the lower section of the storage tank is circulated through the collectors where it is heated by direct solar radiation or by the working fluid (water or water glycol mixture) in a heat exchanger. The hot water is then returned to the storage tank where it can be used on demand. If the hot water is allowed to mix with cooler water in the tank, the extraction temperature to the load is lowered and the quality (usefulness) of the stored energy is degraded. Furthermore, the amount of energy collected may be increased if the collector inlet fluid temperature is lower than the mixed storage temperature.

In the early 1970's some analytical simulations of thermal stratification in storage tank were conducted by a number of investigators, who showed that stratification improves the performance of solar systems. For this reason, mixing should be minimized and stable thermal stratification should be maintained. Stratification involves the

formation of a sharp temperature gradient region (thermocline), between warmer water at the top of the tank and cooler water in the bottom.

Separation of hot and cold fluids may be accomplished naturally or by the use of physical barriers. A natural stratification scheme employs carefully designed inlet and outlet diffusers, which yield evenly distributed two-dimensional flow with low velocity to promote the formation of thermocline. The thermocline, which is defined as a region where there is a stable vertical temperature or density gradient, acts as a physical barrier for a natural stratification system. In contrast, physical barriers can be used to separate the warm and cool fluids. However, these would require additional material for a given amount of storage; thus increases the cost and poses operational difficulties.

Destratification in thermal storage tank is mostly due to plume entrainment, inlet mixing, and conduction along tank walls (Hollands and Lightstone (1989)). Plume entrainment may cause mixing even if mixing due to an inlet jet and conduction along tank walls are negligible. Naturally if cold fluid with zero vertical momentum enters a tank filled with warmer water, a downward plume will develop due to the higher density. The inlet fluid will drop to a level where its density matches the density of the surrounding fluid. This downward cold water plume will entrain warmer fluid in the tank causing mixing and the destruction of thermocline. Usually, this effect is localized to a small horizontal region near the inlet port, but under favorable conditions it may extend to include most of the tank volume. Low-flow thin-wall tanks with momentum diffusers are employed to control inlet mixing, and conduction along tank walls.

The motion taking place in a thermal storage tank generally combines the effects of forced and natural convections. The fluid extracted from the bottom of the tank is

usually heated and returned to the top of the tank. Simultaneously, a second circuit may be operating which extract warmer water from the top of the tank to supply a load and inject cooler water at an equal flow rate to the bottom of the tank. As a result of the density changes, which is accompanied by the thermocline that tends to form in the vicinity of the hot inlet, buoyancy driven flow is also present.

## **1.2 Literature Review**

In this section, a brief review of previous studies on thermal storage tanks and flow in porous media is presented.

### **1.2.1 Thermal Stratification in Thermal Storage Tank**

The motions taking place in thermal storage tank are fairly complex and the mathematical relations that describe them are often difficult to solve without making considerable assumptions. Early investigators have overcome some of these difficulties by postulating that a one-dimensional model of a perfectly stratified tank can provide an adequate representation of the temperature field. Cabelli (1977) and Gou and Wu (1985) conducted numerical studies on the behavior of two-dimensional storage tanks. Cabelli (1977) used the two-dimensional model he developed to test the validity of the one-dimensional assumptions, which have been popular at the time. He discovered that the significant parameter in determining convection is not so much the Grashof number but the ratio of  $(Gr/Re^2)$ . This ratio (known as the Richardson number) was important in promoting stratification. It was also found that the temperature could be predicted with reasonable accuracy using the one-dimensional model he derived. Later, his model was

compared with other models and it was discovered that a factor of one-half was omitted in the solution (Zurigat et al. (1989)).

While the two and three-dimensional models are more capable in accounting for different factors that affect the thermal storage tank performance, they are not suitable for use in a large energy system simulation. On the other hand, the one-dimensional models, although less accurate, are computationally more efficient. Their accuracy, however, could be improved by introducing empirical functions that account for the departure from one-dimensional flow behavior or by using design measures that would make the flow predominantly one-dimensional (Zurigat et al. (1991)). Further support for the one-dimensional models was obtained when Jaluria and Gupta (1982) developed a model to examine the degradation of thermal stratification with time in the absence of any external convective flow. This model also produced fairly good agreement with experimental data.

Gou and Wu (1985) used the alternating direction implicit (ADI) scheme to extend the work of Cabelli (1977) to include higher Reynolds and Grashof numbers. They also pointed out the importance of the Richardson number for characterization of the physical condition of flow patterns and temperature stratification inside a storage tank. They showed that a high degree of stratification will develop when the Richardson number is greater than unity.

Lavan and Thompson (1977) conducted an experimental study on the effects of inlet port location, inlet geometry, mass flow rate, ratio of length to diameter ( $L/D$ ), and inlet and outlet water temperature difference on stratification. The experimental results were given in terms of the extraction efficiency. The results showed that the extraction

efficiency was enhanced if the inlet and outlet ports were located near the end walls (supported later by Sliwinski et al. (1978) and Chang et al. (1983)). While a large inlet Reynolds number promoted mixing, a large temperature difference between the inlet cold water and the stored hot water produced a stabilizing effect even at high flow rates. They reported a mixing zone existing in the tank that was proportional to the tank diameter.

Sliwinski et al. (1978) conducted an experiment to determine what inlet and outlet conditions were favorable to produce stratification during charging in thermal storage tank. They revealed the presence of a constant temperature gradient (thermocline), which moved downward as the tank was charged and upward as the tank was discharged. Thermocline formation was shown to be a function of the Richardson ( $Ri = Gr/Re^2$ ) and Peclet numbers. There existed a critical value of the Richardson number ( $Ri = 0.244$ ), below which stratification was not possible. Their findings support the fact that cylindrical storage tanks are better storage devices compared to rectangular tanks.

Yoo et al. (1986) experimentally investigated the initial formation of thermocline and the factors affecting their formation. A traveling density current was found to be the governing mechanism in the formation of the thermocline (supported later by Homan and Soo (1997)). Their results also suggested that the inlet Froude number is the governing parameter to insure stratification. A Froude number of 2 was identified as the upper limiting values for optimal diffuser design.

Matsudaira and Tanaka (1979) proposed a model that divided the tank into two regions; a complete mixing region and a piston flow region. In this model, the hot and cold fluids mixed at a certain point, beyond which the flow was uniform and moving

parallel to the vertical walls of the tank (piston flow). Their model concentrated on the output response of the storage tank without relating it to the input conditions.

Heat losses to the ambient surroundings, thermal diffusion, inlet mixing during charging and vertical conduction in tank walls are some of the factors that contribute to the loss of energy in thermal storage tanks. If insulated thin wall tanks are used in short experiments (1 to 2 hours), the only factor that needs to be quantified is the inlet mixing. Zurigat et al. (1991) tried to quantify turbulent mixing in thermal storage tanks by means of an effective diffusive factor introduced in a one-dimensional analytical model. This factor has the effect of magnifying the molecular thermal diffusivity to include turbulent mixing. They conducted experiments to correlate the effective diffusivity factor with the flow parameter and inlet configuration. The inlet configurations used are side inlet, side inlet with perforated baffles and impingement inlet. Based on the correlations obtained, they concluded that the influence of inlet geometry on stratification was negligible for Richardson number above 3.6 (supported later by Ghajar and Zurigat (1991)).

The benefits of stratified storage in typical residential solar heating and cooling applications were assessed and critical design variables were identified by Sharp and Loehrke (1979). The approach taken was to simulate the operation first with well mixed storage and then stratified storage, in order to compare the fraction of the total heating or cooling load provided by the solar system over the simulated period.

A major portion of this study was devoted to setting the system parameters and assessing their influences on the relative advantages of one system over another. The results of these simulations (solar water heating, space heating and air conditioning

applications), showed that improved performance can be realized if stratification is maintained in the storage tank. The magnitude of the improvement depended strongly on certain design parameter such as collector efficiency, collector coolant flow rate, and tank volume, etc. When these parameters were chosen based on current design practice, an improvement in solar load fraction of 5 to 15 % was predicted with stratified storage compared to the identical system using mixed storage. Lowering the flow rate on both collector and load side of the tank increases temperature difference and may improve the absolute as well as relative performance of a stratified system.

Jaluria and Gupta (1982) conducted an experimental study on the decay of thermal stratification in water body employed for thermal energy storage. The water was first thermally stratified to different levels and then allowed to cool in the absence of external flow. It was found that the buoyancy-induced mixing maintained the upper layer essentially isothermal and gave rise to horizontal temperature homogeneity in the water body. The decrease in surface temperature was accompanied by an increase in the temperature of the bottom layer, followed later by an overall decrease in temperature throughout the water body. The cooling process was found to be strongly dependent on the initial temperature level and distribution.

The cooling of an isothermal water body was also considered. It was found that it remained isothermal for the duration of the experiment as a result of the buoyancy induced mixing that arises while a stratified region would reduce the mixing currents and energy transfer inside the region was mainly by thermal diffusion. These characteristics confirmed that stratified media are better energy storage systems as compared to mixed storage media.

Two-dimensional transient, flow and heat transfer characteristics in a sensible heat storage tank have been examined numerically by Chan et al. (1983). The inflow and outflow positions of a given storage tank were varied and its thermal performance were compared both in terms of the average temperature and the thermal storage efficiency. However, they concluded that the inflow velocity had no significant effect on the thermal storage efficiency. The transient average tank temperature was found to be related to the dimensionless filling time, and was unaffected by inflow velocity for the range of Reynolds number considered in their work.

Cai et al. (1993) developed a two dimensional numerical model to simulate the turbulent mixing processes occurred when a cold fluid was introduced into a tank containing warmer fluid. The tank was modeled as an open ended rectangular tank with a side-slot inlet adjacent to the bottom. It was shown that the stratification in the tank was dependent upon the inlet Archimedean and Reynolds numbers. Values of Archimedean number greater than 5 and Reynolds number less than 1000 produced a vertical stratification between the warm and cold fluids with nearly zero gradient in the horizontal direction of the tank. The larger the temperature difference between the inlet fluid and the tank fluid, the easier the thermocline was formed. The larger the ratio of the size of the tank to that of the inlet, the larger was the increase in the thickness of the vertical temperature gradients. The depth of which was first determined by the initial mixing and subsequently increased by vertical conduction between the fluid layers. Contrary to these results, Spall (1998) revealed that over the range he investigated ( $500 \leq Re \leq 3000$ ,  $0.5 \leq Ar \leq 5$ ), inlet Reynolds number played little role in determining the stratification properties of the fluid when the Archimedes number was held constant.

The predictions of fluid flow using a finite difference method are seriously affected by numerical diffusion, instability and computational cost. Discretization schemes based on conventional “upwind” or “donor cell” differencing of convective terms give rise to discretization error (numerical diffusion) that limits the accuracy of the prediction. This has led Ghajar and Zurigat (1991) to use the second order upwind scheme (SOUND) to study mixed convection in a stratified thermal storage tank. First, the second order upwind scheme and weighted upwind difference scheme (WUDS) were tested by application to simple flow problems with known analytical solutions. The results indicated that the performance of SOUND was much better than WUDS.

Stratified storage tanks may operate under constant or variable inlet conditions. At fixed collector flow rates; the latter condition is most frequently encountered due to the intermittent nature of solar radiation. Under these conditions conventional inlets discussed so far are known to produce severe mixing which degrades the thermal performance of the storage tank, and eventually the entire system. This has led some investigators to search for inlet designs, which utilize the hydrodynamic and hydrostatic effects to guide the incoming flow to the proper temperature level in the storage tank (Abu-Hamdan et al. (1992)). However, in some applications, partial stratification (as may be achieved in a tank with fixed inlet location and variable inlet flow rate and temperature) provided as much improvement over mixed storage as does ideal stratification.

### **1.2.2 Stratification Enhancement using Porous Manifold**

Lavan and Thompson (1977) were among the first to report the existence of a mixing region in the storage tank. This region, which extends to the order of a tank

diameter, was able to suppress stratification in tanks that had a fixed inlet and variable inlet temperature. From their results, they noticed that the use of multiple inlets produced better results. In an attempt to improve performance, two distributive inlet devices, which use large number of small holes to distribute the flow, were constructed and tested.

Experiments conducted by Loehrke et al. (1979) indicated that an inlet which introduces fluid into a tank at a fixed location may be designed to provide good stratification during charging by minimizing the depth of the mixing layer. This approach, however, enhances mixing under variable inlet conditions (Sharpe and Loehrke, 1979). In order to achieve better stratification, an inlet distributor is required which allows the incoming water to pass through the warmer upper region of the tank without mixing. To this end a vertical porous manifold has been introduced. This manifold minimizes shear induced mixing between fluids of unlike temperature, yet allows for out flows into the tank at almost any level. Two types of vertical manifolds were constructed and tested, the rigid porous manifold (RPM) and the flexible porous manifold (FPM). Test results showed that both manifolds had profile that was similar to that predicted for ideal stratification and much of this stratification was preserved during the recycling (change in inlet condition). However, the FPM was somewhat superior to the RPM during this period because it was able to continually satisfy the pressure matching requirements by changing its area, which was only satisfied on the average with discrete resistance elements.

Gari and Loehrke (1982) reported that the performance of RPM and FPM in both design and off-design operations far exceeded that of convectional inlets. They also developed simple one-dimensional models of the operation of these manifolds. The

models were demonstrated to be quantitatively and qualitatively correct by comparison with experiment conducted over a wide range of conditions. The models were used to identify important parameters, which are valuable as design tools.

In RPM the most important parameters are the dimensionless friction parameter and the dimensionless wall permeability while in FPM the friction is small and assumed negligible but manifold area and the density in the tank are important. The FPM used was constructed of nylon fabric, which was able to change its area constantly in order to match the pressures. Inflow was also not possible because of its inability to support a positive tank differential pressure. The model they proposed can be used as guidelines for selecting the porosity of the wall based on through flow requirements but provides no limit to the porosity and does not specify the size of the pores.

Numerical models to study the effect of various parameters on the thermal stratification in liquid storage tank (with and without porous inlet manifold) were developed by Yee and Lai (2001). The parameters include Richardson number, Biot number, Darcy number, baffle location and tube wall thickness. Their results confirmed, that stratification can be achieved for  $Ri \geq 1$ . However, the effect of Richardson number decreases once stratification was established. In their study, convective heat loss from the tank was expressed in terms of the Biot number. The study confirmed that a large convective heat loss suppressed the formation of thermocline and reduced the thermal storage efficiency. No appreciable difference in thermal stratification was observed for the range of Darcy number considered in this study ( $1 \times 10^{-7} \leq Da \leq 8 \times 10^{-7}$ ). An increased spacing between the baffle and the inlet resulted in more flow penetration through the porous wall that also increased the mixing tank temperature. This increased flow through

the porous tube was reduced with an increase in the wall thickness. At the same time an increased wall thickness might enhance the mixing tank temperature due to the elevated temperature of the porous tube, which in turn might result in the degradation of thermal stratification.

### **1.2.3 Flow in Porous Media**

Interest in fluid flow and heat transfer in porous media have been motivated by a broad range of applications, including geothermal systems, crude oil production, underground disposal of nuclear wastes, migration of ground water pollution, etc. A porous medium is considered to be a material consisting of a solid matrix with an interconnected void. The interconnectedness allows the flow of one or more fluid through the material (Kaviany 1995). In the past three decades, numerous experimental and theoretical investigations have been devoted to the steady state natural convection in two-dimensional, rectangular enclosure filled with a homogeneous porous medium.

Although most of the analytical works on fluid flow and heat transfer through porous media have been based on Darcy's law, which neglect the boundary and inertial effects, it is recognized that non-Darcian effects are quite important in some applications. In these cases, the inclusion of inertial and viscous terms in the formulation is required. Inertial effects can be accounted for through the so-called Forchheimer's extension, where Darcy's law is modified through the addition of a quadratic term in velocity. The inclusion of an additional viscous term in the Darcy's equation (Brinkman's extension) would account for the boundary effects (Nield and Bejan (1992)).

Chan et al. (1970) showed that for the case of natural convection in enclosed porous media with rectangular boundaries of different temperatures, Darcy's law is valid

when the Darcy's number based on the width of the porous bed is less than  $10^{-4}$ . The relative increases in heat transfer rate, corresponding to natural convection, are obtained as functions of the Darcy number  $Da$ , the Rayleigh number  $Ra$ , and the geometric aspect ratio  $L/D$ .

Lai and Kulacki (1991) studied free and mixed convection in horizontal porous layers locally heated from below. They derived correlations for the Nusselt number against the Rayleigh and Peclet numbers. The experimental Nusselt number compared well with the numerically calculated values, but they reported that improved agreement can be obtained if an effective thermal conductivity was used instead of the stagnated value.

When a fluid flows through a channel bounded by a porous medium, or flows around a porous body, the no-slip boundary condition at the surface of the porous medium does not apply. Beavers and Joseph (1967) were the first to propose this condition owing to the difficulties experienced in simultaneously solving the coupled equations for both porous and fluid regions.

Vafai and Thiyagaraja (1987) performed an analysis using the Brinkman's extension of Darcy's law on flow and heat transfer at the interface region between a fluid layer and a porous medium. Their results were checked against the slip boundary condition and were found to be in excellent agreement.

By employing Brinkman's extension of Darcy's law, Neale and Nader (1974) recognized that the no-slip matching condition gave consistent results with the slip flow using the Beavers and Joseph (1967) condition for Poiseuille flow in a channel for which the slip coefficient is taken to be  $(\mu_{\text{eff}}/\mu_f)^{1/2}$ . However, there have been some

controversies about the value of the effective viscosity  $\mu_{\text{eff}}$  in Brinkman's formulation. In general, taking the ratio of  $(\mu_{\text{eff}} / \mu_f)^{1/2} = 1$ , provides fair agreement with experimental data. Recently, James and Davis (2001) did some calculation on flow at the interface of a fibrous porous medium and found that the slip velocity in a pressure driven flow was one quarter of the velocity predicted by the Brinkman's model.

Beckermann et al. (1987) performed numerical and experimental studies to analyze the steady natural convection in a vertical rectangular enclosure partially filled with a layer of a fluid saturated porous medium. The flow in the porous medium was analyzed using the Brinkman-Forchheimer extended Darcy (BFD) model. The numerical model and temperature measurements were in good agreement with the flow visualization experiment. They concluded that the amount of fluid penetrating the porous layer depends strongly on the Darcy and Rayleigh numbers. For a relatively low product of  $Ra \cdot Da$ , the flow takes place primarily in the fluid layer and heat transfer in the porous layer is by conduction only. This result was also supported by James and Davis (2001).

Recently, Kaviany (1995) extended the earlier works of Sahraoui and Kaviany (1992) and presented a thorough review of Beavers and Joseph (1967) interface condition. He showed that contrary to the findings of Beavers and Joseph (1967), the slip coefficient is not only a function of the structure of the porous medium but also depends on the flow direction, gap size, permeability and the particle Reynolds number. The difficulties involved in determining the slip coefficient have increased the popularity of the BFD model. The BFD flow model allows investigators to treat the entire fluid/porous system as one single domain. By considering the regular fluid as a porous medium with an infinitely large permeability, only one set of governing equation is required for the

entire domain. This approach has been used by many investigators; Beckermann et al. (1987), Kim and Choi (1996) to name a few. However, it should be pointed out that there are still some uncertainties in this area. Givler and Altobelli (1994) reported that for some specific cases (flow through a packed bed of fixed spheres), the effective viscosity  $\mu_{\text{eff}}$  depends upon the volume fraction of spheres, i.e.  $(1 - \phi)$ . This has greatly discredited the BFD model.

#### **1.2.4 Determination of Slip Coefficient at the Interface between a Liquid Layer and a Porous Medium**

When dealing with the interface between a fluid layer and a porous medium, it has been customarily assumed that the tangential velocity is zero at the surface of the porous medium. Beavers and Joseph (1967) were the first to propose an alternative boundary condition, which admitted a non-zero tangential velocity (i.e., a slip velocity) at the surface of the porous medium. They conducted experiments to test the validity of the proposed boundary condition. It was shown that the dimensionless slip coefficient  $\gamma$ , depended only on the structure of the porous material. Owing to the inadequacies in the apparatus and instrumentation, Beaver et al. (1970) continued their earlier work to verify the slip-velocity and examine the influence of a porous bounding wall on the transition of laminar flow to turbulent flow. The experiments were conducted in similar conditions with similar materials as their earlier work. The results were found to be in excellent agreement with the theoretical predictions based on their model, which admits a slip velocity at the surface of the porous material. Their results also indicated that the breakdown of the laminar flow regime occurs at a lower Reynolds number in the presence of a porous boundary than in the presence of a solid bounding wall. Further

support for the slip boundary condition was received from Taylor (1971) and Richardson (1971) in companion papers that experimentally and analytically investigated a Couette-type flow bounded by a permeable material. Excellent agreement was found between the results from the slip velocity model and those of experiment.

Earlier, when Beavers and Joseph (1967) proposed the slip boundary condition, they also argued that the slip coefficient depended on the structure of the porous material but independent of the fluid. Beavers et al. (1974) investigated the slip boundary condition in the presence of gas flow. Their results demonstrated that a slip velocity at a porous boundary can be detected when the flowing fluid along the boundary is a gas. Their results were also in excellent agreement with the prediction based on the slip boundary condition, providing further justification for the use of the boundary condition. However, these results were inconclusive when making comparison between the slip coefficient obtained using air and with water (Sparrow et al., 1973), and additional experiments were recommended.

Recently James and Davis (2001) calculated the slip velocity for both Couette flow and Poiseuille flow at the interfacial region of an open porous medium in a channel. This was done by finding solutions for Stokes flows in a channel partially filled with a square array of widely spaced circular cylinders beside one wall. For shear driven flow, the slip velocity was found to depend only weakly on the solid volume fraction. For pressure driven flow, the slip velocity is found to be less than that under comparable shear-flow conditions, and depend on cylinder size relative to the height of the channel

### 1.3 Scope of Present Study

In order to realize the performance gain in thermal storage tank under variable inlet conditions, Loehrke et al. (1979) proposed the use of porous manifold. This study, which compared the performance of conventional inlets with both rigid and porous manifolds, gave no specific guidelines for the design of manifold. In addition, the analysis although effective was based on a simple, one-dimensional model. Thus, the temperature distribution in the tank was not accurate.

The present study seeks to develop a two-dimensional numerical model for a storage tank using a porous manifold. Earlier studies have shown that a porous manifold is beneficial for the establishment and maintenance of thermal stratification in a storage tank, which in turn can significantly increase the efficiency of energy utilization. To better design a thermal storage system, the model should be able to predict the flow and temperature fields in a storage tank subject to variable inlet temperatures. Although the theory that underlies the numerical model has been refined over the years, the data (i.e., the slip coefficients between a fluid and a porous surface) to be used in the model are scarce in the literature. In addition, an earlier study by Yee and Lai (2001) has shown that the slip coefficients based on the experimental work of Beavers and Joseph (1967) are not applicable for the optimal design of thermal storage tanks. Therefore, it is the objective of this study to conduct experiments to determine the slip coefficients that can be used in a numerical model to help in the design of a thermally stratified storage tank.

To this end, an experimental apparatus similar to that used by Beavers and Joseph (1967) is constructed. However, the test is conducted using various porous tubes. The porous tubes are constructed from wire screens. It is aimed at obtaining a correlation

between the slip coefficient and the permeability of a porous tube. This correlation is then used in the numerical model to predict the flow and temperature fields in a storage tank subject to variable inlet temperatures. Finally, a full-scale storage tank is constructed. The measurements of the temperature distribution and flow velocities are used to validate the numerical model.

## CHAPTER TWO

### DETERMINATION OF SLIP COEFFICIENT AT THE INTERFACE BETWEEN A LIQUID LAYER AND A POROUS MEDIUM

#### 2.1 Introduction

In search of the optimal design conditions, Yee and Lai (2001) have performed a numerical study to examine the effects of each design parameter on the formation and maintenance of thermal stratification in liquid a storage tank. In their formulation, the flow in the porous tube was based on Darcy's law and a slip coefficient was used at the interface between the fluid layer and the porous wall. Although their study has covered a wide range of the parameters involved, the slip coefficients were limited to those reported by Beavers and Joseph (1967) for some selected foametals. Based on the available data, their results showed that the porous manifold actually had an adverse effect on the formation of thermal stratification at low Richardson numbers (i.e., at high flow rates). The contour plots presented in their study provide evidence that at a low Richardson number, very little fluid is able to penetrate the porous tube because of the low permeability of the wall. Intuitively, if the porous tube were more permeable, a more favorable condition for the formation of thermal stratification might be attainable. In other words, for thermal stratification to be effective, the permeability of the porous tube has to be greater than those examined by Yee and Lai (2001), or reported by Beavers and Joseph (1967). To further narrow down the optimal design conditions, one needs to perform simulations using a more permeable tube, which in turn requires new data for the slip coefficient.

This chapter is devoted to the testing of new materials, which includes the measurement of their permeability slip coefficient that can be used as the matching condition at the fluid/porous medium interface. A review of the theoretical background will be presented in the next section, and a description of the experimental setup and discussion of the results will be followed in subsequent sections.

## 2.2 Theoretical Background

In order to better understand the experimental setup, the theories involved will be first discussed here. Flow in a channel of permeable wall will be discussed using Darcy's formulation. The theory behind the determination of slip coefficient, longitudinal and radial permeabilities will also be discussed.

### 2.2.1 Flow in a Channel of Permeable Wall

In the formulation of the governing differential equations, several assumptions have been made. First, the flow is assumed to be laminar, axisymmetric, steady, fully developed and incompressible. The thermo-physical properties are assumed constant except for the density in the body force term, in which the Boussinesq approximation is invoked.

$$\rho = \rho_{\infty} [1 - \beta (T - T_{\infty})] \quad (2.1)$$

The governing equations are, continuity equation:

$$\frac{1}{r} \frac{\partial}{\partial r} (r v_r) + \frac{1}{r} \frac{\partial}{\partial \theta} v_{\theta} + \frac{\partial}{\partial z} v_z = 0,$$

r-momentum equation:

$$\rho \left[ \frac{\partial v_r}{\partial t} + v_r \frac{\partial v_r}{\partial r} + \frac{v_{\theta}}{r} \frac{\partial v_r}{\partial \theta} + v_z \frac{\partial v_r}{\partial z} - \frac{v_{\theta}^2}{r} \right] =$$

$$-\frac{\partial P}{\partial r} + \mu \left[ \frac{1}{r} \frac{\partial}{\partial r} \left( r \frac{\partial v_r}{\partial r} \right) + \frac{\partial^2 v_r}{\partial z^2} - \frac{v_r}{r^2} + \frac{1}{r} \frac{\partial^2 v_r}{\partial \theta^2} - \frac{2}{r^2} \frac{\partial v_\theta}{\partial \theta} \right], \quad (2.2)$$

z-momentum equation:

$$\rho \left[ \frac{\partial v_z}{\partial t} + v_r \frac{\partial v_z}{\partial r} + \frac{v_\theta}{r} \frac{\partial v_z}{\partial \theta} + v_z \frac{\partial v_z}{\partial z} \right] = -\frac{\partial P}{\partial z} + F_z + \mu \left[ \frac{1}{r} \frac{\partial}{\partial r} \left( r \frac{\partial v_z}{\partial r} \right) + \frac{1}{r^2} \frac{\partial^2 v_z}{\partial \theta^2} + \frac{\partial^2 v_z}{\partial z^2} \right], \quad (2.3)$$

$\theta$ -momentum equation:

$$\rho \left[ \frac{\partial v_\theta}{\partial t} + v_r \frac{\partial v_\theta}{\partial r} + \frac{v_\theta}{r} \frac{\partial v_\theta}{\partial \theta} + v_z \frac{\partial v_\theta}{\partial z} - \frac{v_r v_\theta}{r} \right] = -\frac{1}{r} \frac{\partial P}{\partial \theta} + \mu \left[ \frac{1}{r} \frac{\partial}{\partial r} \left( r \frac{\partial v_\theta}{\partial r} \right) + \frac{\partial^2 v_\theta}{\partial z^2} - \frac{v_\theta}{r^2} + \frac{1}{r^2} \frac{\partial^2 v_\theta}{\partial \theta^2} + \frac{2}{r^2} \frac{\partial v_r}{\partial \theta} \right]. \quad (2.4)$$

For an isothermal flow in the channel, the governing equations can be simplified to give;

continuity equation:

$$\frac{1}{r} \frac{\partial}{\partial r} (r v_r) = 0, \quad (2.5)$$

r-momentum equation:

$$v_r \frac{\partial v_r}{\partial r} = -\frac{1}{\rho} \frac{\partial P}{\partial r} + \nu \left[ \frac{1}{r} \frac{\partial}{\partial r} \left( r \frac{\partial v_r}{\partial r} \right) - \frac{v_r}{r^2} \right], \quad (2.6)$$

z-momentum equation:

$$v_r \frac{\partial v_z}{\partial r} = -\frac{1}{\rho} \frac{\partial P}{\partial z} + \nu \left[ \frac{1}{r} \frac{\partial}{\partial r} \left( r \frac{\partial v_z}{\partial r} \right) \right], \quad (2.7)$$

$\theta$ -momentum equation:

$$0 = -\frac{1}{r\rho} \frac{\partial P}{\partial \theta}. \quad (2.8)$$

The boundary conditions used to solve the governing equations are;

$$r = 0, \quad \frac{\partial v_z}{\partial r} = 0, \quad v_r = 0. \quad (2.9)$$

$$r = r_0 \quad \frac{\partial v_z}{\partial r} = \frac{\gamma}{\sqrt{K_z}} (v_B - u_m), \quad v_r = 0. \quad (2.10)$$

in which  $\gamma$  is the dimensionless slip coefficient which depends only on the porous material (Beavers and Joseph (1967)),  $K$ , the permeability is a property of the material and  $v_B$  is the longitudinal velocity at the fluid/porous medium interface. Solving the continuity equation (Eq. (2.5)) one obtains  $v_r = \text{constant}$ . When applying the boundary condition Eq. (2.9) to the solution just obtained one get  $v_r = 0$  everywhere. From Eqs. (2.6) and (2.8), one can deduce that  $P$  is just a function of  $z$ . Equation (2.7) can thus be reduced to

$$\frac{r}{\mu} \frac{dP}{dz} = \frac{d}{dr} \left( r \frac{dv_z}{dr} \right), \quad (2.11)$$

which permits a general solution in the following form,

$$v_z = \frac{r^2}{4\mu} \frac{dP}{dz} + c_1 \ln r + c_2, \quad (2.12)$$

Apply the boundary conditions, Eqs. (2.9) and (2.10), to solve for the integrating constants  $c_1$  and  $c_2$ , one obtains

$$\text{at } r = 0, \quad c_1 = 0. \quad (2.13)$$

$$\text{at } r = r_0, \quad \frac{r_0}{2\mu} \frac{dP}{dz} = \frac{\gamma}{\sqrt{K_z}} \left( \frac{r_0^2}{4\mu} \frac{dP}{dz} + c_2 + \frac{K_z}{\mu} \frac{dP}{dz} \right) \quad (2.14)$$

$$\Rightarrow c_2 = \left( -\frac{dP}{dz} \right) \left[ \frac{r_0^2}{4\mu} + \frac{K_z}{\mu} - \frac{\sqrt{K_z} r_0}{\gamma 2\mu} \right] \quad (2.15)$$

This yields the velocity profile in the channel as

$$v_z = \left( -\frac{dP}{dz} \right) \left[ \frac{r_0^2}{4\mu} + \frac{K_z}{\mu} - \frac{\sqrt{K_z} r_0}{\gamma 2\mu} - \frac{r^2}{4\mu} \right] \quad (2.16)$$

The slip velocity at the interface between the fluid and porous layer,  $v_B$ , is given by,

$$v_B = \frac{K_z}{2\mu} \left( -\frac{dP}{dz} \right) \left[ 2 - \frac{r_0}{\gamma \sqrt{K_z}} \right], \quad (2.17)$$

or

$$v_B = \frac{K_z}{2\mu} \left( -\frac{dP}{dz} \right) \left[ 2 - \frac{\sigma}{\gamma} \right], \quad (2.18)$$

where  $\sigma = \frac{r_0}{\sqrt{K_z}}.$  (2.19)

The volume flow rate can be found from the velocity profile in the channel as

$$Q = 2\pi \int_0^{r_0} v_z r dr = \frac{2\pi}{\mu} \left( -\frac{dP}{dz} \right) \int_0^{r_0} \left[ \frac{r_0^2 r}{4} - \frac{r r_0}{2} \frac{\sqrt{K_z}}{\gamma} - \frac{r^3}{4} + K_z r \right] dr. \quad (2.20)$$

The volume flow rate per unit length through the porous channel is then,

$$Q = \frac{\pi r_0^4}{8\mu} \left( -\frac{dP}{dz} \right) \left[ 1 - \frac{4}{r_0} \frac{\sqrt{K_z}}{\gamma} + \frac{8K_z}{r_0^2} \right]. \quad (2.21)$$

On the other hand, for a channel bounded by impermeable wall, the volume flow

rate is given by

$$Q^* = \frac{\pi r^4}{8\mu} \left( -\frac{dP}{dz} \right). \quad (2.22)$$

where the asterisk is used to identify that the case is for impermeable wall.

The volume flow through the porous-annulus and a solid wall tube can be compared. For the condition of equal pressure gradient and radius, the ratio of equations (2.21) and (2.22) yields,

$$\frac{Q}{Q^*} = \left[ 1 - \frac{4\sqrt{K_z}}{r_0\gamma} + \frac{8K_z}{r_0^2} \right] = \left[ 1 - \frac{4}{\gamma\sigma} + \frac{8}{\sigma^2} \right] \quad (2.23)$$

which shows that, the presence of a porous wall resulted in a reduced flow. Furthermore, according to equation (2.23),  $Q/Q^*$  is a constant (independent of Reynolds number) for a channel fixed diameter and a given porous material.

### 2.2.2 Longitudinal Permeability

To determine the longitudinal permeability, it is assumed that the flow in the porous tube is steady, incompressible, axisymmetric, fully developed and in the Darcy's regime (Eq. (2.24)),

$$Re = \frac{\rho v K_z^{\frac{1}{2}}}{\mu} \ll 1. \quad (2.24)$$

Therefore, the Darcy's law, equation (2.25), (Nield and Bejan (1992)), is applicable.

$$v = \frac{K_z}{\mu} \frac{dp}{dx} = \frac{K_z}{\mu} \frac{\Delta P}{L} \quad (2.25)$$

Thus the velocity is determined as soon as the volume flow rate is known for each pressure gradient at known fluid temperature. The longitudinal permeability is calculated directly by making  $k$  the subject of the formula in equation (2.25),

$$K_z = \frac{v\mu}{\frac{\Delta P}{L}} \quad (2.26)$$

### 2.2.3 Radial Permeability

Under the same assumptions of longitudinal flow, Darcy's law for a radial flow can be expressed as (Amyx et al. (1960) and Dake (1978)),

$$Q = \frac{K_r A}{\mu} \frac{dP}{dr} \quad (2.27)$$

Since the flow rate is constant, it is the same across any radial area. Then equation (2.27) can be rewritten as

$$Q = \pi \frac{(2rl)K_r}{\mu} \frac{dP}{dr} \quad (2.28)$$

Separating the variables and integrating over the annular thickness,

$$\int_{P_i}^{P_o} dP = \frac{1}{2\pi} \frac{Q\mu}{K_r l} \int_{r_i}^{r_o} \frac{dr}{r} \quad (2.29)$$

we get

$$\Delta P = \frac{1}{2\pi} \frac{Q\mu}{K_r l} \ln \frac{r_o}{r_i} \quad (2.30)$$

or in terms of the permeability,

$$K_r = \frac{1}{\pi} \frac{Q\mu}{2l} \frac{\ln \frac{r_o}{r_i}}{\Delta P} \quad (2.31)$$

## 2.3 Experimental Setup

The experimental apparatus shown in Fig. 2.1 consists of five major components; the upstream plenum, the test section, the downstream plenum, the control unit and the reservoir unit. Figure 2.2 is a picture of the experimental set up whereas Table 2.1 lists the components and their specifications. The components are described in the following sections.

### 2.3.1 Test Section

The test section has been designed to facilitate experiments involving cylindrical tubes with permeable wall. It has an outer diameter of 1.90 cm (3/4 in.) and varying inner diameters. Figure 2.3 is a close-up look of the test section with pressure sensors in place. The basic structure consists of a 68.58-cm-(27 in.)-long, 2.54-cm-(1 in.)-diameter plexiglas tube with a wall thickness of 0.32 cm (1/8 in.). To facilitate the acceleration which was anticipated at the inlet to the test section, the first set of pressure sensor ports was placed 21.6 cm (8 1/2 in.) downstream of the inlet and the other were placed at an interval of 20.32 cm (8 in.) along the length of the tube. The pressure ports were placed opposite to each other to guarantee that the pressure was measured at exactly the same location along the porous tube. Three pressure taps were used to measure pressure in the

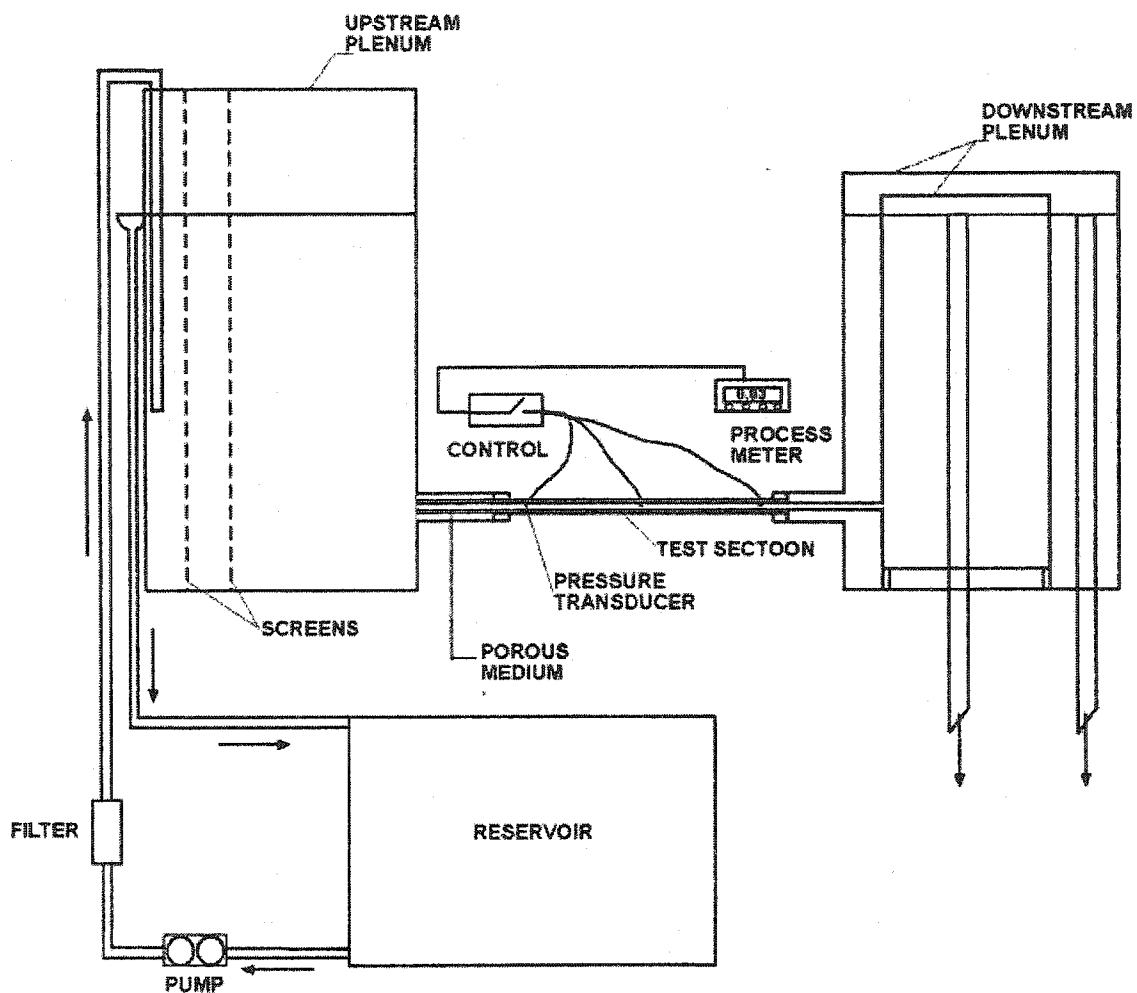


Figure 2.1 Schematic drawing of the experimental setup used to measure the longitudinal permeability of a porous tube.

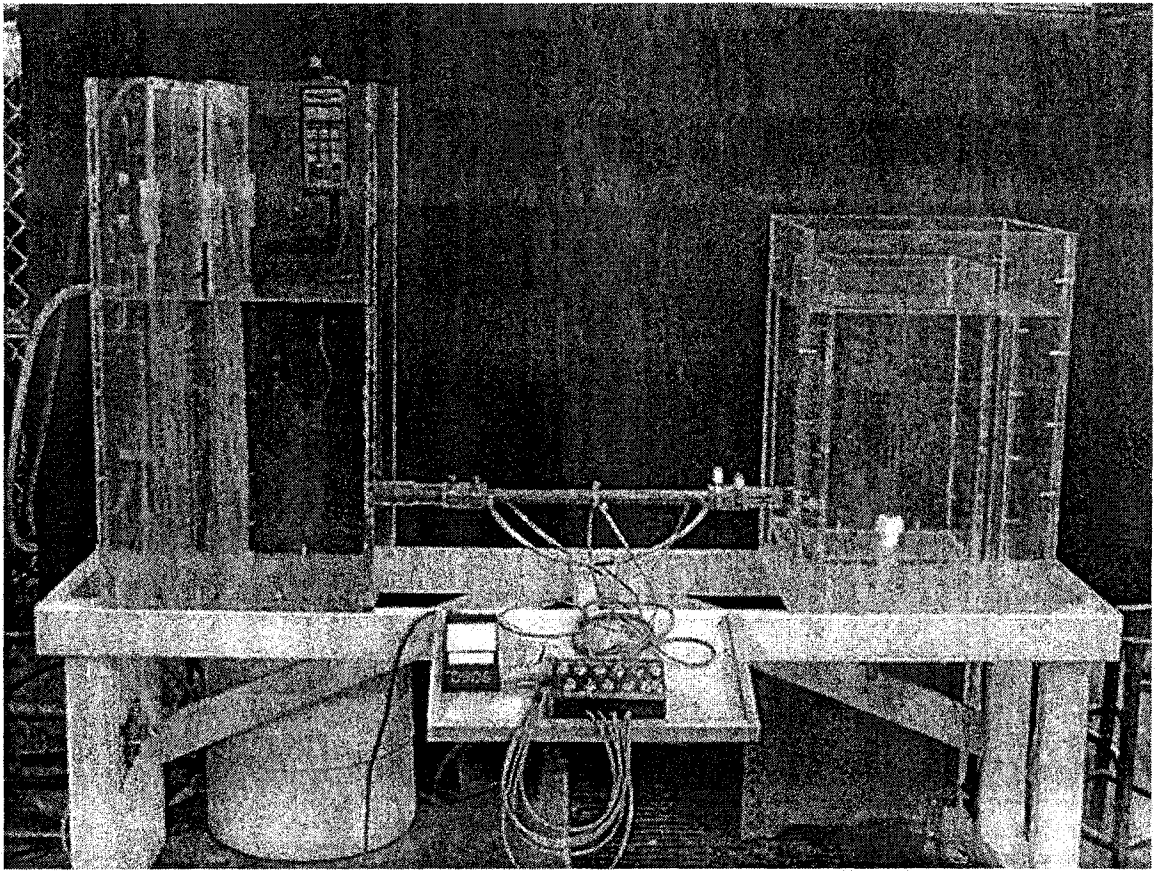


Figure 2.2 Photograph of the experimental setup used to measure the longitudinal permeability of a porous tube.

porous annulus while another three were used to record the pressure in the fluid region. The signals from the latter taps were brought out through a 1.59-mm-(1/16 in)-diameter stainless steel tubes inserted in the porous annulus. The stainless steel tube was held in place by a 0.64 cm (1/4 in.) Swagelok brass fitting screwed into the wall of the plexiglas tube. The pressure orifice associated with the other three pressure taps was 0.32 cm (1/8 in.). After the to installation of the taps, the wall of the tube was polished to a high degree of smoothness. Two flanges of 3.81-cm-(1 1/2 in.)-diameter were used to anchor the test section to the upstream and downstream plenums. These flanges ensured that the test section was leveled with the plenums. The distribution of the static pressure along the test section was obtained by Omega PX26 series differential and gage pressure transducers and read out by an Omega DP25B-S process meter. The pressure transducers are able to compensate for temperature fluctuation from 0 - 50 °C with a reading accuracy of 6.895 N/m<sup>2</sup> (0.001 Psi.).

The porous tubes were made from fiberglass mesh commonly used as mosquito nets for windows and doors and nylon mesh used in the building industry to hold insulation in sheet racks. The mesh with porosity ranging from 0.84 to 0.9 was carefully wrapped around rods with various sizes to achieve the desired dimensions. Once the desired outer diameter was reached (1.95 cm, 3/4 in.), the outer layer of the mesh was then sewed in place so that a uniform straight porous tube was obtained. Seven porous tubes were fabricated and used during the course of this experiment. Six tubes were 0.68

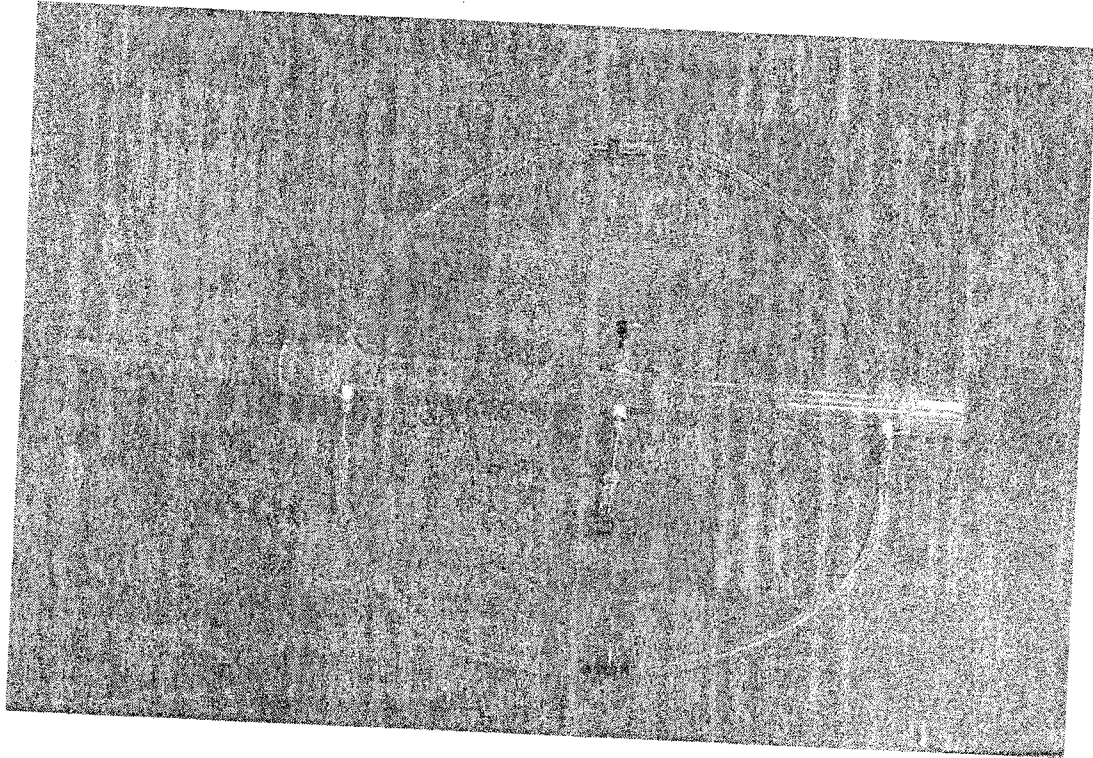


Figure 2.3 Photograph of the test section without porous tube.

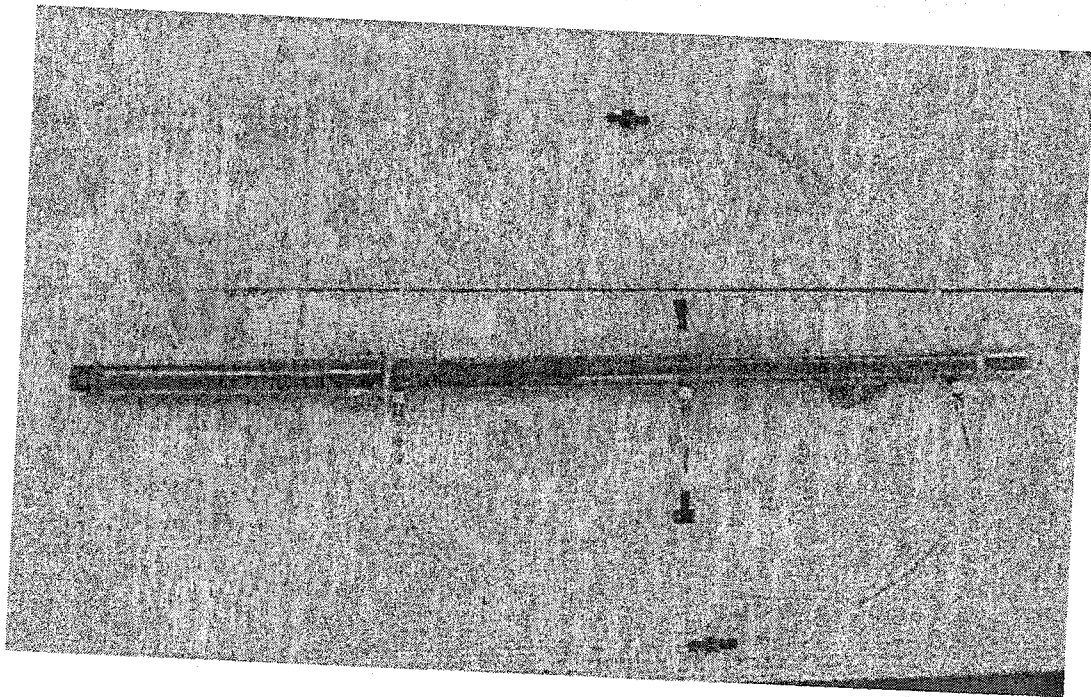


Figure 2.4 Photograph of the test section with porous tube in place.

Table 2.1 List of components of the experimental apparatus and their specification.

Items	Specification / Manufacturer	Unit
Test Section	A 2.54 cm diameter plexiglas tube with 0.3175 cm (1/8 in.) thick wall, 0.6858 m (27 in.) long. Three Swagelok 0.15875 cm (1/16 in.) brass male connectors, three pieces of stainless steel tubes 10.16 cm (4 in.) long, 0.15875 cm (1/16 in.) diameter, two plexiglas tubes 3.81 cm (1 1/2 in.) diameter with 0.635 cm (1/4 in.) thick wall and 3.81 cm long. Four Hose clamps 5.05 cm (2 in.) diameter, two 10.16 cm (4in.) x 3.81 cm (1 1/2 in.) diameter clear suction hoses.	Test Section
Radial Test Section	A 7.62 cm (3 in.) long section of 15.24 cm (6 in.) diameter clear acrylic tube, with 1.27cm (1/2 in.) thick wall. Both ends are sealed with a 15.24 cm (6 in.) diameter disc, fabricated from clear acrylic sheet, 1.27cm (1/2 in.) thick. One end is glued shut while the other end performed the function of a lid and is held in place by 8 size #8 machined screws. Two 0.25 x 0.375 ins. NPT brass barbed nipples and one 0.625 x 0.75 in. NPT PVC barbed nipple. Two Swagelok 0.15875 cm (1/16 in.) brass male connectors, two pieces of 15.24 cm (6 in.) long, 0.15875 cm (1/16 in.) steel tubes.	Test section
Upstream Plenum	Plexiglas Tank 0.9271 m x 0.4572 m x 0.4826m (36.5 in. x 18 in. x19 in.), made from 1.27 cm (0.5 in.) thick plexiglas sheet, glued and fastened together with IPS Weld-On #6 clear thickened acrylic cement and IPS Weld-On #3 water thin solvent cement, 100% clear silicone and 40 size #10 machined screws. Acrylic tube 15.24 cm (6 in.) long x 3.81 cm (1.5 in.) diameter and two fiberglass screens 0.915 m x 0.4572 m (36 in. x 18 in). Four overflow weirs located 0.5334 m,	Upstream Plenum

Table 2.1 continues

Items	Specification / Manufacturer	Unit
Upstream Plenum	0.66 m, 0.74 m and 0.84 m from the bottom of the tank. Three 1/2 in. NPT plugs and one 1/2 in x 5/8 in. NPT PVC barb nipple.	Upstream Plenum
Outer Downstream Plenum	Plexiglas tank, 0.686 m x 0.4572 m x 0.4826m (27 in. x 18 in. x 19 in.), made from 1.27 cm (0.5 in.) plexiglas sheet, glued and fastened together with IPS Weld-On #6 clear thickened acrylic cement and IPS Weld-On #3 water thin solvent cement, 100% clear silicone and 34 size #10 machined screws. Acrylic tube 10.16 cm (4 in.) long x 3.81cm (1 1/2 in.) diameter. Two 2.54 cm (1 in.) PVC compression fittings and one 0.686 m long 2.54 cm (1 in.) diameter acrylic tube.	Downstream Plenum
Inner Downstream Plenum	Plexiglas Tank 0.5461 m x 0.3048 m x 0.3048 m (21 1/2 in. x 12 in. x 12 in.), made from 1.27 cm (1/2 in.) plexiglas sheet, glued and fastened together with IPS Weld-On #6 clear thickened acrylic cement and IPS Weld-On #3 water thin solvent cement, 100% clear silicone and 30 size #10 machined screws. Acrylic tube 20.34 (8 in.) long by 1.27 cm (1/2 in.) diameter. A 2.54 cm (1 in.) PVC compression fittings and 0.686 m long 1 in. diameter acrylic tube.	Downstream Plenum
Pressure Transducers	Seven Omega PX26-005GV gauge pressure transducers. Three Omega PX26-001DV differential pressure transducers, excitation 10VDC, 16VDC max @ 2mA, output 100mV, 10m V/V, accuracy 1% FS	Control
Process meter and Controller	One Omega DP25B-S process meter. Input Range 0-100 mV, 0-10 V, +/- 5V, 0-20 mA, 4-20 mA. Max error +/- 0.03% of readings, +/- 1 count. Excitation Voltage Ac power 24 V @ 25	Control

Table 2.1 continues

Items	Specification / Manufacturer	Unit
Process meter and controller	mA, 12 V @ 50 mA, 10 V @ 120 mA. Input power 115/230 V ~-(Ac) +/- 10 %,50/60 Hz	Control
Thermocouple meter	One Omega Micro processor Thermometer Model HH23, resolution 0.1 °C, Temperature coefficient 0.02% rdg + 0.1 °C below 18 °C and over 28 °C. Input voltage 9V DC	Control
Thermocouple	One Omega J-Type precision fine wire thermocouple, 5Sc-TT-J-3036. Range to 480 °C	Control
Wiring	Omega 4 Conductor Copper wire TX4-100	Control
Switch Box	Twelve on/off maintained position toggle switches, four twelve position connector bars and one switch box.	Control
Connectors	Seven Omega 4 pin connectors CX136-4	Control
Filter	Parker 8F-F8L-5-B Inline Brass Filter. Filtration level 5 µm, 250 psi max pressure.	Reservoir
Pump	Little Giant Centrifugal pump, input power 115 Vac, 50/60 Hz, 1.25 amps, 1 PH, output capacity of 50 mL/s.	Reservoir
Storage Tank	One 55 gallon plastic storage container	Reservoir
Tubing	30 cm suction hose 5 cm (2 in.) by 3.81 cm (1.5 in.), 60 cm suction hose 2.54 cm (1 in.) by 1.9 cm (0.75 in.), 3 m clear plastic hose 1.27 cm (1/2 in.) by 0.95 cm (3/8 in.) and 60 cm clear plastic hose 0.95 cm (3/8 in.) by 0.635cm (1/4 in.).	Reservoir/Control
Hose Clamps	Eight 5/8 in. and four 2 in. hose clamps.	Reservoir
Surge Protector	Belkin Surge Suppressor, Suppressor voltage 330 V 15 A, 125 Vac, 60 Hz, 1875 W.	
Stop Watch	Sport Line stop watch, least count 0.01 sec.	
Measuring cylinders	Two 1000 mL Pyrex Beakers, least count 100 mL, one 250 mL measuring cylinder, least count 2 mL.	

m (27 in.) long with an outer diameter of 1.95 cm (0.75 in.). The inner diameters were 0.64 cm (1/4 in.), 0.95 cm (3/8 in.) and 1.27 cm (1/2 in.) respectively, which correspond to a wall thickness of 0.64 cm (1/4 in.), 0.48 cm (3/16 in.) and 0.32 cm (1/8 in.). One tube tested was 5 cm (2 in) long and 0.1016 m (4 in.) OD by 0.0889 m (3.5 in.) ID.

### **2.3.2 Upstream Plenum**

The upstream plenum was fabricated from a 1.27 cm-(1/2 in.)-thick plexiglas sheet. The upstream plenum itself serves a dual function of a flow control device and a calming chamber. The tank was designed with four overflow weirs so that the liquid level in the tank could be maintained at any desired height depending on which overflow weir was used. Thus, combined with any given weir, the tank would function as a constant head tank. Calming was achieved by two stiff fiberglass screens as well as by the substantial volume of liquid in the plenum chamber (see Table 2.1 for dimensions). The outlet of the plenum chamber was fitted with a 15.24 cm-(6 in.)-long, 3.81-cm-(1.5 in.) -diameter acrylic tube extension. This extension eliminated any vasoconstriction that might develop as the water exited the plenum it and also served as a mating surface for the test section. The upstream plenum was also fitted with one J-type thermocouple and a thermocouple meter and that could read within 0.01 °C.

### **2.3.3 Downstream Plenum**

Two plenum chambers were connected to at the downstream end of the test section. To allow for an independent collection, measurement, and control of co-axial flows through the channel and porous medium, the smaller tank was placed inside the larger tank. The height of liquid inside each of the downstream plenum chamber was set and maintained by adjustable weir through which the fluid exited the chamber. An independent adjustment of the two weirs facilitates the balance of the transverse pressure differences in the test section. Furthermore, the pressure gradient in the test section was mainly controlled by the adjustment of the weir in the downstream plenums.

Upon leaving the downstream plenum chamber, the fluid was directed to the drain except when it was used for calibration. When metering the flow rate, the fluid was collected in a beaker and its volume was measured. The time required to collect a given amount of fluid was recorded and the volumetric flow rate was determined.

### **2.3.4 Control Unit**

Measurement of the pressure distribution along the test section was achieved in two ways. One is to measure the gage pressures at three different locations along the test section and the other is to measure the differential pressure between the inlet and the outlet of the test section and the gage pressure at the center. The former would require switching between six pressure transducers and the latter would only require switching

between four transducers. Each pressure transducer functions on two independent circuits. First an excitation current was sent to the transducer by the DP25B-S process meter, the transducer in return would send a signal back to the meter in millivolts (mV) proportional to the pressure. The signal was converted and displayed directly in pounds per square inch (psi). The control was designed so that each circuit of the transducer was controlled by a separate switch. The corresponding signals from each transducer switch were sent to a separate connector bar, and one lead from each connector bar was connected to the meter. In order to read the signal of a particular transducer, the two switches controlling that transducer circuit must be placed in the “on” position. To read the pressure at other positions these switches were turned off and the desired switches were turned on.

### **2.3.5 Reservoir Unit**

The reservoir unit consists of a storage tank, a centrifugal pump and an inline filter. The storage tank also functions as a settling tank, where water was allowed to settle overnight in order to rid of entrained air and fine dust. A centrifugal pump was used to pump the water through the filter to the upstream plenum chamber (specifications of the pump and filter can be found in Table 2.1).

## **2.4 Experimental Procedure**

Prior to the experiment, it was necessary to assemble the components as shown in Fig. 2.1 and to calibrate the pressure transducers. The water stored in the tank was pumped to the upstream plenum at a constant rate of 50 ml/s through a 5  $\mu\text{m}$  filter. The overflow weir was set so that a constant level was maintained in the chamber and the excess liquid was returned to the storage tank. A carefully aligned inner tube, situated at the downstream end of the test section, directs the flow from the channel and the porous medium into separate plenum chambers.

In the downstream plenums the overflow weirs were adjusted to maintain similar pressure gradient in the porous medium and the core fluid region. The distribution of pressure in the test section was read from the Omega process meter. Upon leaving the downstream plenums, the flow was directed to a drain. During calibration, the quantity of fluid leaving each tank was separately collected and measured. The time and the amount of fluid collected were also recorded.

### **2.4.1 Calibration of Pressure Transducers**

To ensure the accuracy and consistency in the measurement of pressure distribution along the test section, it is necessary to calibrate the pressure transducers. Once the apparatus was assembled as shown in Fig. 2.1, water was pumped into the tank about 5 cm below the height of the overflow weir in the upstream chamber and was

allowed to settle. After the level in all three tanks was in equilibrium, the reading from each pressure transducer was recorded. More water was pumped into the tank to raise the level up by another centimeter or so. Once again time was given for water level in each tank to equalize and the reading from each pressure transducer was recorded. The overflow weir in the upstream plenum was closed and the process was repeated about ten times until the water level was about 5 cm above the level of the overflow weir. The data collected were used to generate a calibration curve for each of the pressure transducers to ensure that they were all reading the same value.

#### **2.4.2 Calibration of Experimental Setup**

To calibrate the experimental setup, the volume flow rate through a solid wall channel was compared to the theoretical results obtained using the Hagen-Poiseuille's equation, Eq. (2.22). A closer look at Eq. (2.22) reveals that for a given fluid temperature and tube diameter, the volume flow rate is a function of the pressure gradient. If the test section has been replaced by a 0.9525-m-(0.375 in.)-diameter tube, and the flow rate and pressure drop of water through a 0.4064-m-long section of the pipe are measured, Eq. (2.22) can be reduced to

$$Q = 4.9463 \times 10^{-7} \Delta P \quad (2.32)$$

The results obtained will be discussed in Section 2.5.

### 2.4.3 Measurement of Longitudinal Permeability

To measure the longitudinal permeability of the porous annulus, a rod with the inner diameter of each tube was used to block the flow in the core region of the channel. The test section with porous tube and rod in place was secured to the upstream and downstream plenums. The inner downstream plenum was removed because only flow in the porous annulus was to be measured. The pressure transducers were connected to measure the pressure gradient in the porous annulus. The water level in the upper and downstream plenums was adjusted to produce a steady flow through the porous annulus. The water flowing out of the downstream chamber was collected and its volume was recorded. The time required to collect the given amount of water was also noted. Measurements were taken over a 5 minute interval and a volume of approximately 57 ml was collected. By adjusting the overflow weir in the downstream plenum to increase the pressure gradient through the test section, and another set of data can be recorded. This procedure was repeated six times.

Once the measurements were taken for six different pressure settings, the sample tube was replaced by another tube and the procedure repeated. Often it is necessary to allow the porous tube to sit for a few hours to allow all the air to escape from the tube. The results obtained will be discussed in the results and discussion section.

#### 2.4.4 Measurement of Radial Permeability

A slightly different setup (Fig. 2.5) was required to measure the radial permeability. One plenum chamber is used to provide the hydrostatic head in the radial test section and the pressure gradient was measured across the wall of the test specimen. Figure 2.6 provides a photograph of the experimental setup.

A sample of the porous tube (7.6-cm-(3 in.)-long) was placed in the test section. One pressure probe was then inserted in the porous annulus to measure the pressure at the center of the tube, the other probe was placed a few millimeter from the outer surface of the tube to measure the outside pressure. Once the pressure probes were in place, the lid of the test section was replaced and tightened with 8 sizes #8 machined screws. To avoid leaking, the mating surface of the lid and test section was coated with a thin layer of silicone sealant and left for a few hours to cure. The radial test section was connected to the plenum chamber as seen in Fig. 2.5. The pressure transducer was connected to the pressure probe.

Water was pumped from the storage tank through a filter to the plenum chamber. Under a set hydrostatic head the water was allowed to flow around the porous annulus, the higher pressure on the outside forces the water to flow radially into the porous tube before it exits the test section. Upon leaving the test section the water was directed to the drain. Air trapped in the test section was removed through an air vent placed on the opposite side of the inlet. For the purpose of metering, the water exiting the test section

was collected and the volume and time were recorded. Air which might accumulate in the test section after prolong use, was removed through the air vent.

The overflow weir was adjusted to increase the pressure of water to flow across the porous wall. A typical measurement would use a sampling rate of 10 seconds due to the high rate of flow. Ten different pressure settings were used for each tube. Once the data were collected, the sample was replaced by another tube and the procedure was repeated. The results obtained will be discussed in the results and discussion section.

#### **2.4.5 Determination of the Slip Coefficient at the Interface between the Fluid**

##### **Layer and the Porous Tube**

To perform the present experiment, it requires a laminar, unidirectional, fully developed flow in a channel with a bounding porous annulus. Conditions necessary for the attainment of such a regime are the absence of transverse pressure gradient and the existence of identical, uniform axial pressure gradient in the channel and porous medium.

The porous tube to be tested was placed in the test section; the ends of the tube should be flush with both ends of the test section. Pressure probes were then inserted in the porous tube to measure the pressure at the inner section of the fluid/medium interface. The male connectors were tightened to ensure that the probes were stationary, and that no leak would occur. The apparatus was assembled as shown in Fig. 2.1.

A steady stream of water was allowed to flow through the test section as a result

of the hydraulic head which was maintained in the upstream plenum chamber. The water levels in downstream plenums were adjusted until the required pressure gradient was achieved in the test section. Downstream of the test section, the water was separated into two streams by a thin separator pipe, which conveyed the water from the inner core of the test section to the inner chamber, and the outer was allowed to flow in the outer chamber. The flows from both chambers were collected and measured.

## 2.5 Results and Discussion

Experiments were first performed to calibrate the experimental setup. The measured volume flow rates were compared to the predicted Poiseuille flow rates in Fig. 2.7. Table 2.2 shows that the results obtained from the experiments were in good agreement with those predicted by the theoretical solution over the range of Reynolds number considered. The maximum uncertainties of the measured and theoretical flow rates are  $\pm 2.3$  and  $\pm 3.0$  % respectively. The Reynolds number and relative error are defined in Eq. (2.33) and (2.34).

$$\text{Re} = \frac{DV\rho}{\mu} \quad (2.33)$$

$$\text{error} = \frac{Q_T - Q_{\text{Exp}}}{Q_T} \quad (2.34)$$

The results showed that in the laminar flow region ( $\text{Re} \leq 1500$ ), the experimental data were subject to errors of less than 1.5 %, while in the transition regime the errors were still less than 5%. These low experimental errors demonstrate that the experimental setup

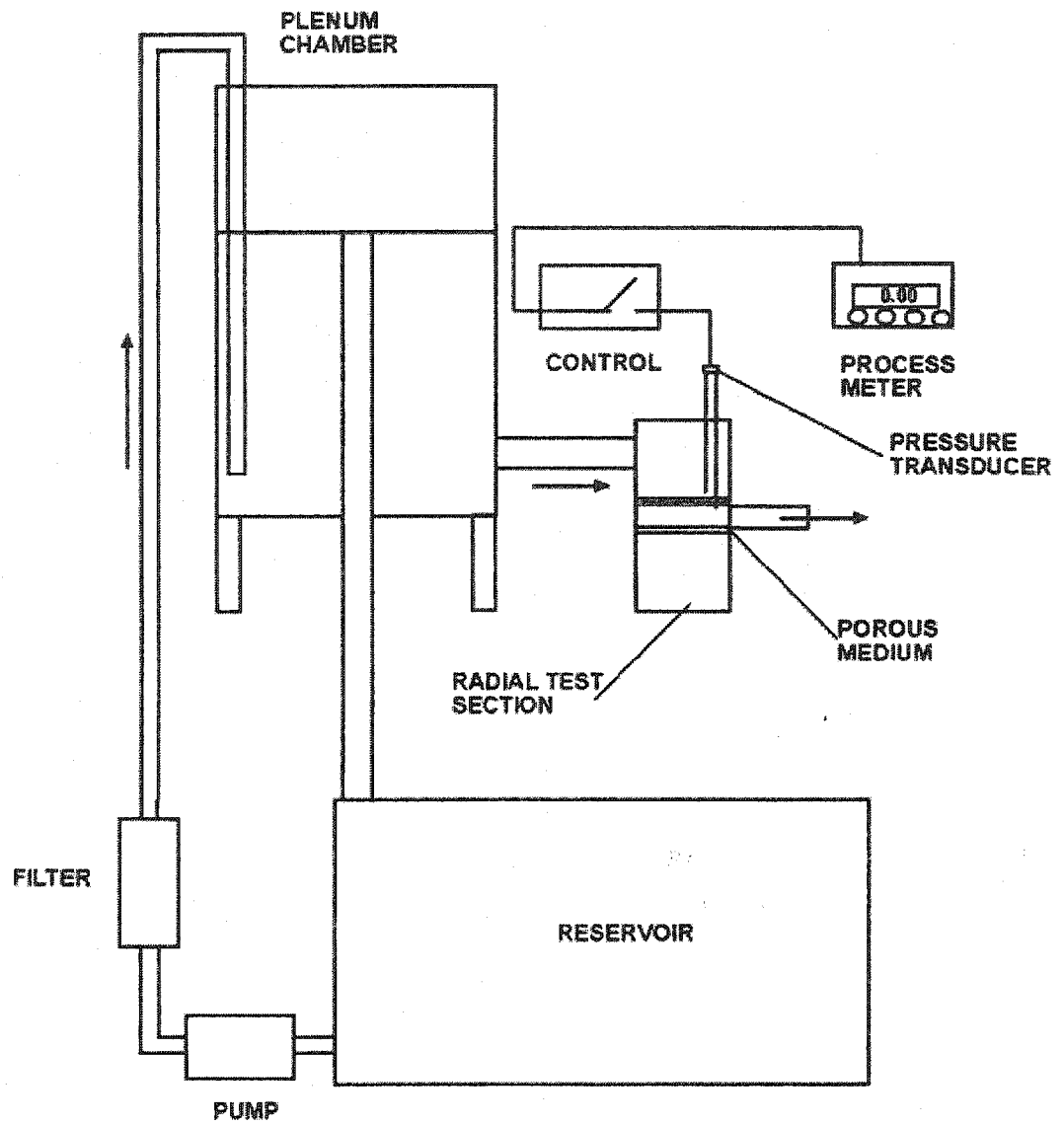


Figure 2.5 Schematic drawing of the experimental setup used to measure the radial permeability of a porous tube.



Figure 2.6 Photograph of the experimental setup used to measure the radial permeability of a porous tube.

and data collection were done correctly and thus should produce fairly decent results.

The problems of interest were characterized by a parallel, unidirectional, fully developed flow in the channel and the porous medium. The conditions necessary to establish such a flow field were the absence of transverse pressure gradient and the existence of identical, uniform axial pressure gradient in both the channel and the porous annulus. It was assumed that these conditions were fulfilled once the differential pressure across both the porous annulus and the channel were similar. This was readily achieved by adjusting the overflow weir in the downstream plenums.

To facilitate the correlation of the slip coefficient of the porous tubes under test ( Eq. 2.23), it was necessary to know their permeabilities. Preliminary experiments were performed to determine the permeability of the tubes in both longitudinal and radial directions. The porous tubes tested have a wall thickness of 0.0064 m, 0.0048 m, and 0.0032 m, (1/4 in. 3/16 in., and 1/8 in. respectively). In all, four tubes were tested; three of the tubes were made from a fiberglass mesh (Fig. 2.8(a)) and the other was made of a more permeable nylon mesh (Fig. 2.8 (b)) with a wall thickness of 0.0064 m. Two of the fiberglass tubes made were wrapped tight (0.0064 m and 0.0032 m) and the other was of a looser wrap (wall thickness of 0.00476 m), the nylon tubes had the same tightness as the loosely wrapped fiberglass tubes (a wall thickness of 0.0064 m and 0.0032 m).

The results of the longitudinal permeability measure are shown in Fig. 2.9, where  $Q\mu/A$  is plotted on the ordinate while the pressure gradient ( $dp/L$ ) in the porous annulus

Table 2.2 Validation of experimental setup

$\Delta p$ (psi)	$\Delta p$ (N/m <sup>2</sup> )	$Q_T$ (m <sup>3</sup> /s)	$Q_T$ (mL/s)	$Q_{Exp}$ (mL/s)	Re	Error %
0.0076	52.614	$2.60 \times 10^{-5}$	26.0	24.82	3294.12	4.64
0.006	41.25	$2.04 \times 10^{-5}$	20.4	19.49	2586.74	4.48
0.0041	28.27	$1.4 \times 10^{-5}$	13.98	13.54	1792.34	3.42
0.0033	22.62	$1.12 \times 10^{-5}$	11.18	11.3	1500.52	-1.11
0.0032	21.95	$1.1 \times 10^{-5}$	10.86	11.0	1461.5	-1.47

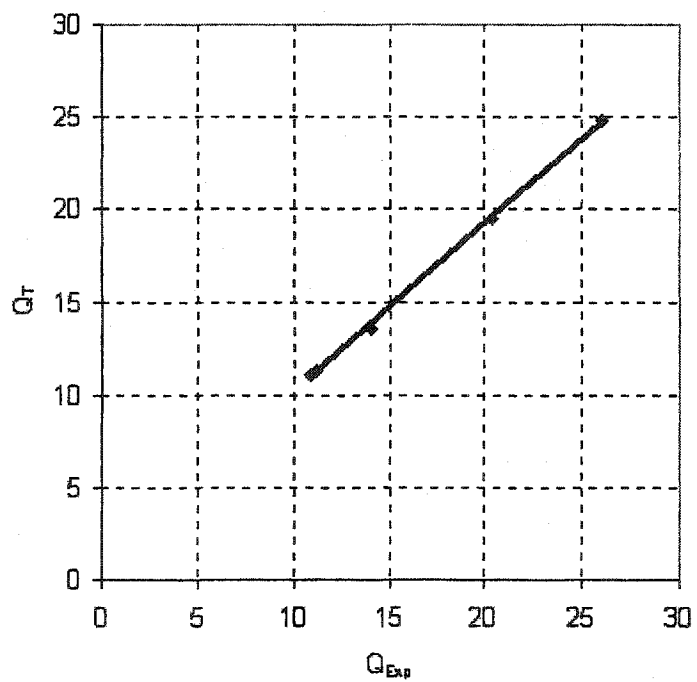


Figure 2.7 Theoretical flow rate vs. experimental flow rate

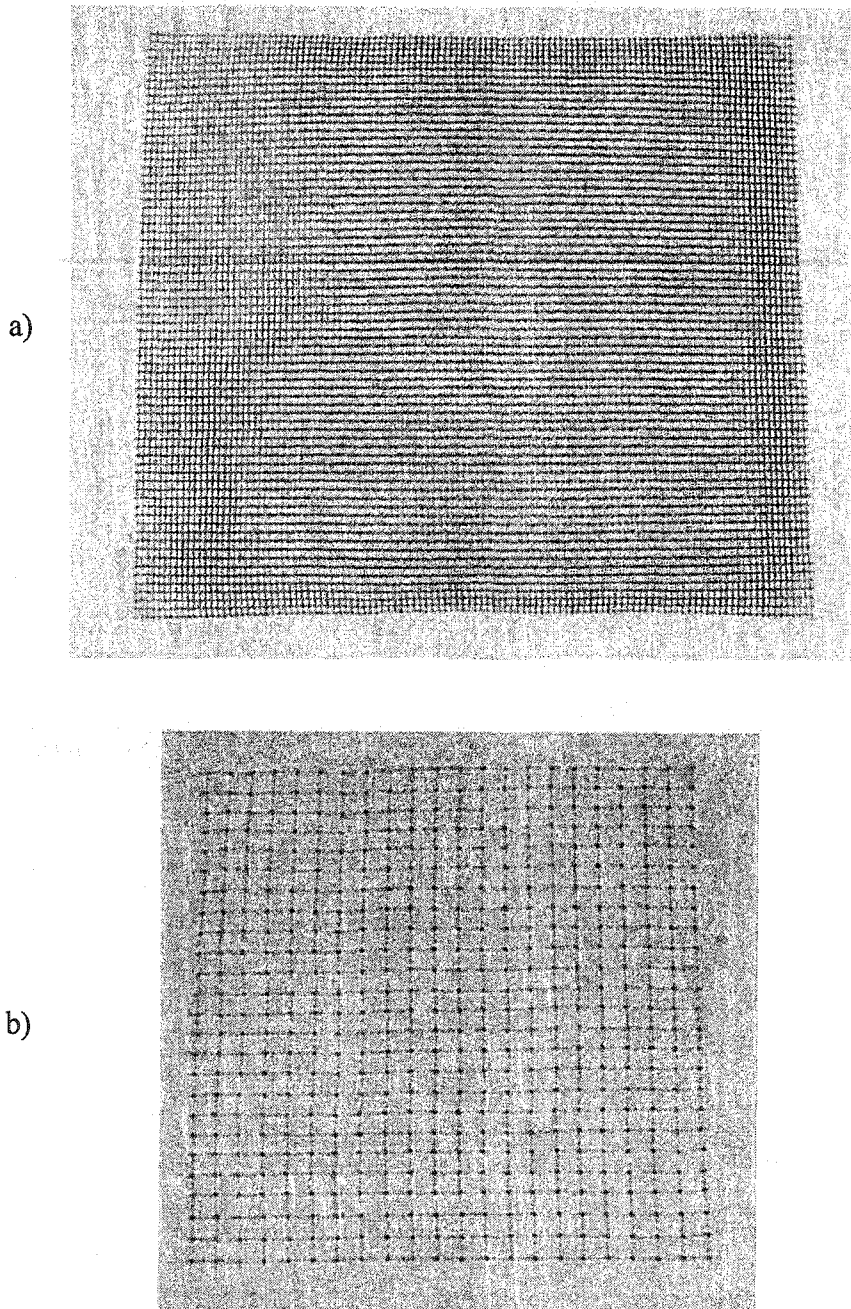


Figure 2.8 Photograph of materials used to fabricate porous tubes, a) fiberglass mesh and b) nylon mesh

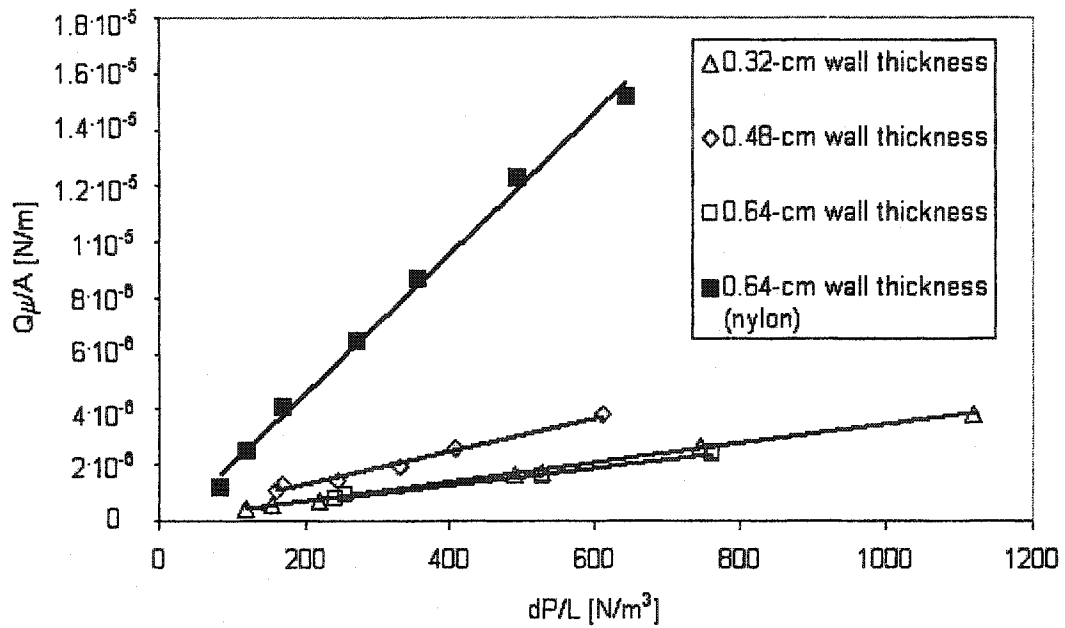


Figure 2.9 Longitudinal permeability of porous tubes with various wall thicknesses.

Table 2.3 Measured longitudinal and radial permeabilities of a porous tubes

Tube Wall Thickness (Material) m (in.)	Longitudinal Permeability m <sup>2</sup>	Radial Permeability m <sup>2</sup>
6.35 x 10 <sup>-3</sup> (1/4) (Fiberglass)	3 x 10 <sup>-9</sup>	6 x 10 <sup>-10</sup>
6.35 x 10 <sup>-3</sup> (1/4) (Nylon)	3 x 10 <sup>-8</sup>	1 x 10 <sup>-9</sup>
4.76 x 10 <sup>-3</sup> (3/16) (Fiberglass)	6 x 10 <sup>-9</sup>	7 x 10 <sup>-10</sup>
3.18 x 10 <sup>-3</sup> (1/8) (Fiberglass)	3 x 10 <sup>-9</sup>	4 x 10 <sup>-10</sup>
3.18 x 10 <sup>-3</sup> (1/8) (Nylon)		1 x 10 <sup>-9</sup>
1.59 x 10 <sup>-3</sup> (1/16) (Nylon)		7 x 10 <sup>-10</sup>
6.35 x 10 <sup>-3</sup> (1/4) (Nylon) 0.10 m OD x 0.09 m ID		1.05 x 10 <sup>-8</sup>

is the abscissa. A look at Eq. (2.26) indicates that the gradient of a line drawn through these points would yield the permeability. The curves are parameterized by the wall thickness, which are distinguished by separate symbols. The permeabilities calculated are summarized in Table 2.3. A complete set of the data can be found in Appendix A, and the maximum uncertainty associated with the measurements are shown in Appendix D.

The results show that the nylon tube has the highest permeability. This is due to the fact that the nylon mesh used to fabricate this tube has a higher surface porosity than the fiberglass mesh. As the fluid flow through the porous annulus, it encounters less resistance from the solid portion of the material, thus is able to flow faster. The fiberglass tubes on the other hand show that the tightly wrapped tubes have the same permeability while the looser tube has a permeability twice of the others. The finding of the experiment suggests that the longitudinal permeability is independent of the wall thickness but more dependent on the tightness of the wraps and the porosity of the mesh used to fabricate the tube. The looser the wrap and the higher the porosity of the wall, more fluid will be able to squeeze through the layers of each consecutive wraps, increasing the longitudinal permeability.

Figure 2.10 shows the increase in the volume flow rate across the porous tube wall in the radial direction as a function of the pressure gradient. The gradients of the curves represent the radial permeabilities of three fiberglass tubes (having a wall

thickness of 0.0064 m, 0.0048 m and 0.0032 m (1/4 in., 3/16 in., and 1/8 in., respectively)), and four nylon fiber tubes (having a wall thickness of 0.0064 m, 0.0032 m and 0.00156 m (1/4 in., 1/8 in., and 1/16 in., respectively)). The data are characterized by different symbols; a similar shape would represent the same wall thickness. Open symbols represent fiberglass while the solid symbols represent the nylon material. One of the tubes tested had a 0.10-m-OD and 0.09-m-ID.

As was expected, the looser wrapped tube (0.0048 m) had the highest permeability of the three fiberglass tubes. Intuitively, one would expect that as the tube wall thickness increases, the permeability would decrease. However, the results show that as the wall thickness was doubled, there was a fifty percent decrease in the flow rate which was not enough to offset the logarithmic ratio of the radii. The end results show that the thicker wall tube (0.0064 m) has a higher permeability than the thinner wall tube (0.0032 m). The values of the radial permeabilities are also summarized in Table 2.3. A complete set of the data can be found in Appendix A. The same trends were noticed with the nylon tubes. However, the nylon tubes were more permeable than the fiberglass tubes. For a similar wall thickness, the nylon tube had a permeability that was almost twice of the fiberglass tube. It can also be concluded that the radial permeability is also influenced by the diameter of the tube. It is observed that for a similar wall thickness, the tube with a larger diameter has a higher radial permeability.

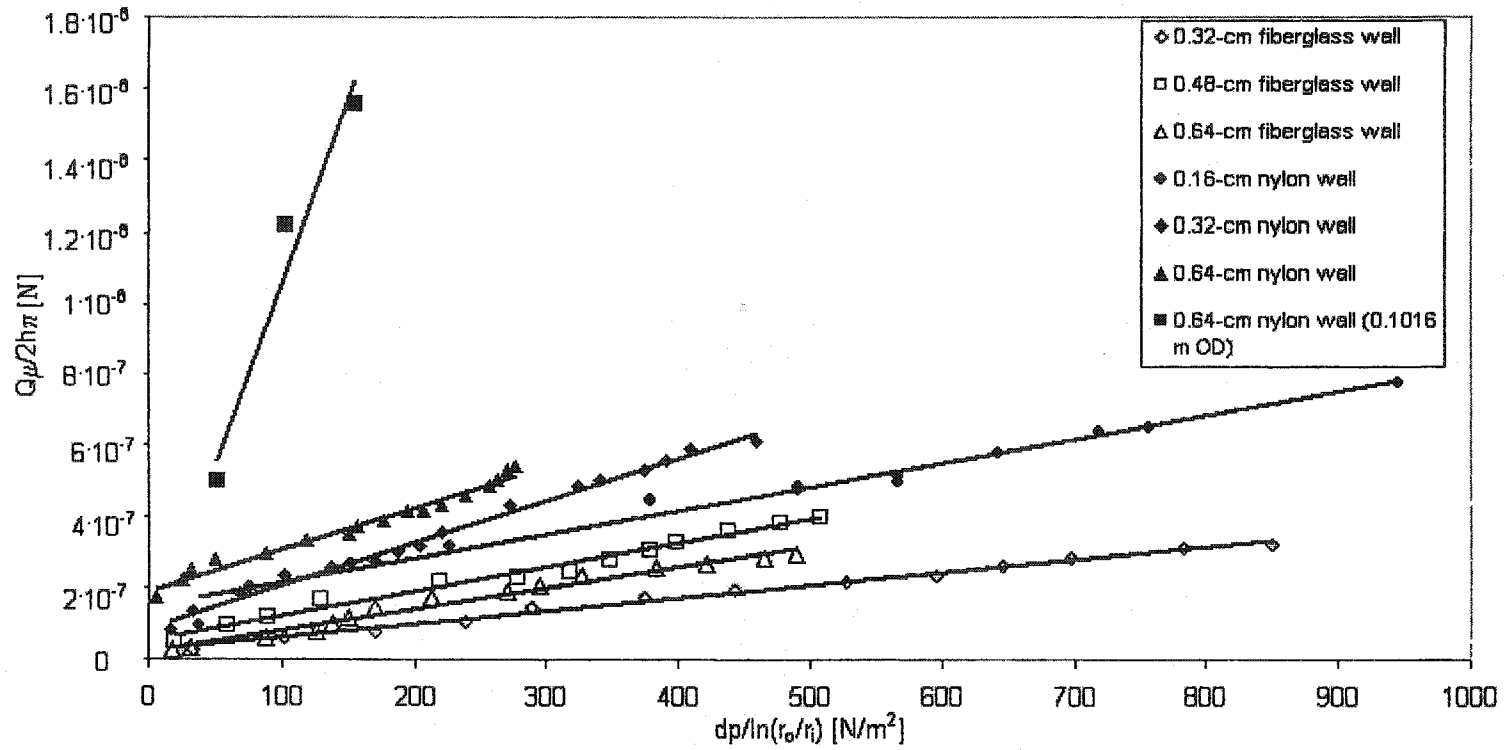


Figure 2.10 Radial permeability of porous tubes with various wall thicknesses.

The slip coefficients  $\gamma$  calculated from Eq. (2.23) are plotted as function of the Reynolds number within the porous medium ( $Re_m = vk^{1/2}/\nu$ ) in Fig. 2.11. The data from each tube are characterized by different symbols. The figure shows that the slip coefficients are found to correlate well with the Reynolds number in the following forms:

a) 0.0064-m-thick fiberglass tube;

$$\gamma = 0.2134Re_m^3 - 0.5624Re_m^2 + 0.3175Re_m + 0.1468 \quad (2.35)$$

with a correlation coefficient of 0.9191.

b) 0.0048-m-thick fiberglass tube;

$$\gamma = 0.0145Re_m^3 - 0.0764Re_m^2 + 0.0596Re_m + 0.2105, \quad (2.36)$$

with a correlation coefficient of 0.9231.

c) 0.0032-m-thick fiberglass tube;

$$\gamma = -0.0059Re_m^3 + 0.0317Re_m^2 - 0.0614Re_m + 0.0879, \quad (2.37)$$

with correlation coefficient of 0.8153.

d) 0.0064-m-thick nylon tube;

$$\gamma = 0.1227Re_m^3 - 0.3896Re_m^2 + 0.2688Re_m + 0.1494 \quad (2.38)$$

with correlation coefficient of 0.99.

The results obtained from the measurement of slip coefficient are listed in Appendix A and the maximum uncertainty associated with the measurements are shown in Appendix D. Figure 2.11 shows a constant value for the slip coefficient at low Reynolds numbers ( $Re_m \leq 0.5$ ) where Darcy's law was applicable. As the Reynolds

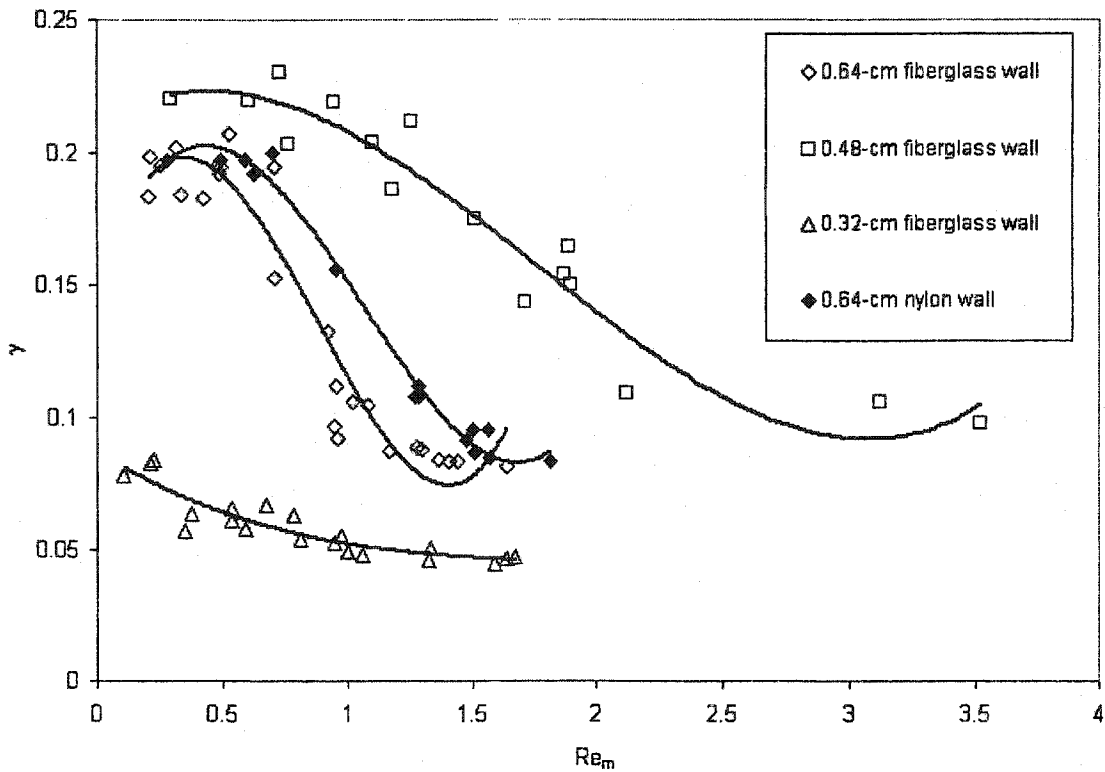


Figure 2.11 Slip coefficient as a function of the Reynolds number for fiberglass and nylon tubes with various wall thicknesses.

number increases, the value of the slip coefficient decreases sharply when the Reynolds number approaches unity. The data levels out at  $Re_m \geq 1.25$ . Although the longitudinal permeability for the fiberglass tube with a wall thickness of 0.0064 m and 0.0032 m are the same, yet they have very different values of the slip coefficient which indicates that there are other factors at work in determining the slip coefficient.

As expected, the high flow rate associated with the fiberglass tube with a thickness of 0.0048 m (resulting in a higher permeability) also results in a higher slip coefficient. Notice the similarities between the curves of the fiberglass and nylon tubes

with a thickness of 0.0064 m, the curves are quite similar except for the fact that the curve of the nylon tube is shifted to the right that indicates a higher permeability.

## **2.6 Conclusion**

The slip coefficients for several porous tubes are found to depend on factors other than the material. These results are good complement of the model proposed by Beavers and Joseph (1967). The slip coefficient has been found to depend on the Reynolds number, the permeability, and the thickness of the tube wall. The longitudinal permeability on the other hand is found to depend more on the gap between layers than on the actual thickness of the wall. The radial permeabilities obtained are less than expected.

## CHAPTER THREE

# STRATIFICATION ENHANCEMENT AND FLOW VISUALIZATION IN A LIQUID STORAGE TANK

### 3.1 Introduction

Separation of hot and cold fluids contained in a thermal storage tank may be desirable for many applications. This can be accomplished naturally or by the use of physical barriers. A natural stratification scheme employs carefully designed inlet and outlet diffusers, which yield evenly distributed two-dimensional flow with low velocity to promote the formation of thermocline. This thermocline, acts as a physical barrier for a natural stratification system. In contrast, physical barriers can be used to separate the warm and cool fluids. However, these would require additional material for a given amount of energy stored; thus increase the cost and pose operational complexities.

Destratification in thermal storage tank was due mainly to plume entrainment, and inlet mixing (Hollands and Lightstone (1989)). It was shown by Gari and Loehrke (1982) that a fixed inlet location was acceptable if the temperature of the water entering the tank was always beyond the temperature extremes of the stored water. Severe mixing can occur if the temperature of the inlet water fluctuates below the temperature extremes of the stored water. The latter case was more frequently encountered (in solar energy storage systems) due to the intermittent nature of solar radiation. If cooler water from the collector is returned to the top of the tank, a downward plume will develop as the cooler water flows through the warmer water stored in the tank, entraining warmer tank fluid until some equilibrium is established. Under such condition a fully mixed or a partially stratified tank would result.

In order to inhibit the inlet mixing and achieve a better stratification, it was proposed by Loehrke, et al. (1979) that the vertical inlet jet be enclosed in a porous shroud. Their porous shroud produced, in effect, a controlled buoyant jet which allowed the incoming water to pass through the warmer upper region of the tank without mixing. To this end, a vertical porous manifold was introduced, which would reduce shear-induced mixing between fluids of unlike temperatures. Two types of manifolds were constructed and tested, the Rigid Porous Manifold (RPM) and the Flexible Porous Manifold (FPM). Test results showed that both manifolds produced a temperature profile similar to that predicted for an ideal stratification. Much of this stratification was preserved during recycling (changes in the inlet condition). However, the FPM was somewhat superior to the RPM in the test because it was able to continually satisfy the pressure matching requirements by changing its area, which was only satisfied on the average with discrete resistance elements.

A numerical study conducted by Yee and Lai (2001) to predict the flow and temperature fields in a storage tank, indicated that a porous manifold with a low permeability had an adverse effect on the formation of thermal stratification at low Richardson numbers (i.e., at high flow rates). It was suggested that a more permeable tube would produce better results. Since very little data are available in the literature for the more permeable materials, experiment have to be conducted for new materials to determine their values of the slip coefficient and permeability. As a follow-up to the study discussed in chapter 2, one such new material is tested in real application to evaluate its effectiveness in the promotion of thermal stratification.

In this study a full-scale model of the storage tank that was used in the simulation

by Yee and Lai (2001) is actually constructed. The measurements of the temperature distribution and flow rates are used to evaluate the performance of a partially flexible porous manifold on the formation and maintenance of thermal stratification under various inlet conditions. The porous manifold was made from a nylon netting normally used in the building construction industry to hold insulation in sheet racks. Although the manifold is somewhat rigid, it is flexible enough to satisfy the pressure-matching requirement by changing its area slightly. The frictional properties are such that they prevent flow through the wall provided  $\rho > \rho_t$ . However, similar to FPM, this manifold will not support a large negative pressure.

An inlet distributor is employed to reduce the vertical momentum of the fluid entering the tank. Flow visualization experiment involving the use of color dye is also conducted. The ability of the inlet distributor to inhibit mixing under various inlet conditions and the ability of the porous manifold to suppress turbulent mixing will be visualized.

### **3.2 Experimental Setup**

A schematic drawing of the entire experimental setup is shown in Fig. 3.1 and a photograph is shown in Fig. 3.2. The setup consists of three main parts: the storage tank (with porous manifold and inlet distributor), a charging loop and the data acquisition system. Table 3.1 lists the components and their specifications. The components are described in the following sections.

#### **3.2.1 Storage Tank**

The storage tank was fabricated from a cast acrylic tube 1.22 m (48 in.) long and

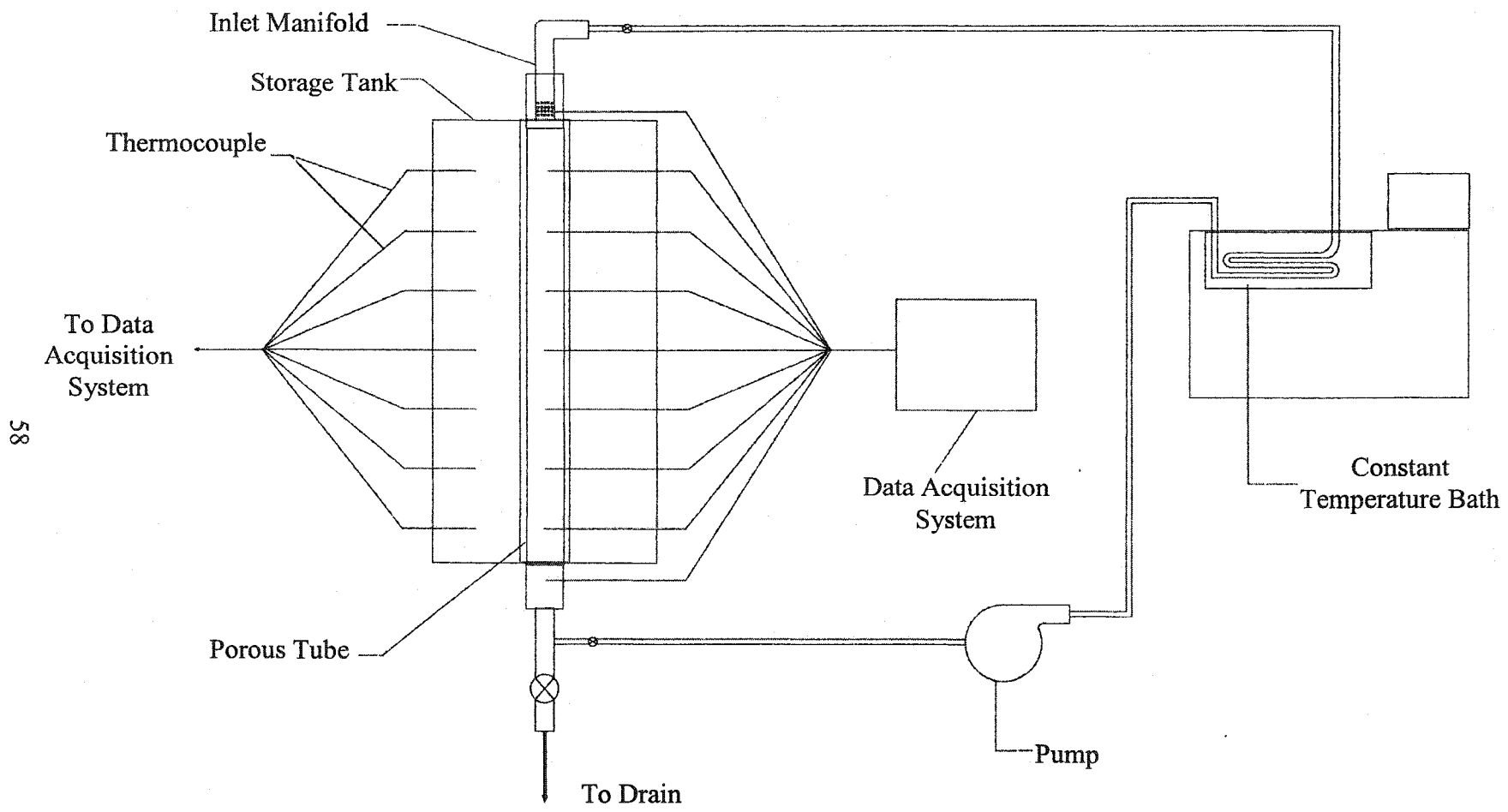


Figure 3.1 Schematic drawing of the experimental setup

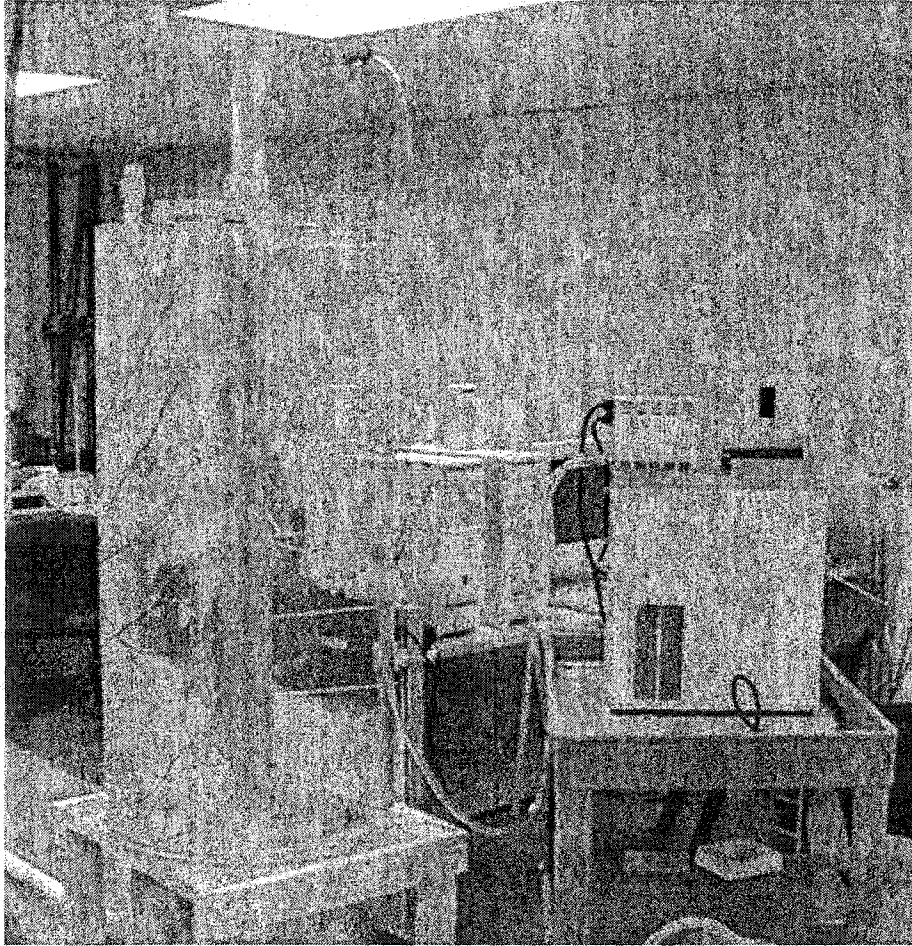


Figure 3.2 Photograph of the experimental setup

Table 3.1 List of the components of the experimental apparatus and their specifications.

Item	Specification / Manufacturer	Unit
Storage Tank	<p>Plexiglas tube: 0.61 m (24 in.) OD, 0.58 m (23 in.) ID, 1.22 m (48 in.) long. Two lids, 0.305 m (24 in.) diameter x 2.54 cm (1 in.) thick.</p> <p>Sixteen size #10 stainless steel machined screws.</p> <p>Seven stainless steel tubes 0.32 cm (1/8 in.) OD, 0.29 cm (1/9 in.) ID, 33 cm (13 in.) long.</p> <p>Fourteen stainless steel tubes 0.32 cm (1/8 in.) OD, 0.29 cm (1/9 in.) ID, 15 cm (6 in.) long.</p> <p>One 3 in. PVC pipe union, one 3 in. to 2 in. PVC reducer, one 2 in. PVC ball valve, one 3/4 in. PVC ball valve, one 2 in. 90° PVC elbow, one 3 in. ID PVC pipe, of 15.24 cm (6 in.) long, one 2 in. ID PVC pipe of 30.5 cm (12 in.) long, one 3/8 in. brass ball valve, one 3/8 in. brass barb nipple, one 3/8 in. brass male union.</p> <p>Twenty-two J-type thermocouples, manufactured from Omega thermocouple wire, # 24 gage, with a deviation of 1.5 °C at 205 °C. Operating range: -270 to 760 °C, sensitivity: 0.05 mV/ °C and a sensing uncertainty of ± 0.2 °C.</p> <p>Twenty feet, Manville's Gold Fiberglass, R-11 building insulation.</p>	Storage Tank
Inlet Distributor	<p>One 3/8 in. brass ball valve, one 5 cm (2 in.) ID acrylic pipe of 30 cm (12 in.) long, one 7.62 cm (3 in.) ID acrylic pipe of 15 cm (6 in.) long, one 2 in. 90° PVC elbow, one 2 in. PVC pipe of 15 cm (6 in.) long, one 2 in PVC union, one 2 in. x 3/4 in. PVC bushing, one 3/4 in. x 1/2 in. PVC bushing, one 3/8 in. x 2 in threaded galvanized pipe, 3/4 in. x 1/2 in. galvanized bushing, one 3/8 in. brass barb nipple, 5 ft. clear plastic hose with 3/8 in. ID and 1/2 in. OD.</p> <p>One J type thermocouple, manufactured from Omega thermocouple wire, # 24 gage, with a deviation of 1.5 °C at 205 °C.</p>	Storage Tank
Porous Manifold	8.9 cm (3.5 in.) ID, 10.2 cm (4 in.) OD, 1.21 m (47.5 in.) long nylon tube.	Storage Tank
Data Collection	Three Gateway computers with Intel Celeron processor, 127 MB RAM. LABVIEW Software version 6.8. Three National Instrument SC-2345 chassis each with eight SCC-TC01 thermocouple inputs. National Instrument 184749B-01 68-pin transfer cable of 1 m long.	Data Collection

Table 3.1 continue

Item	Specification / Manufacturer	Unit
Constant Temperature Bath	Fisher Instrument Isotemp Refrigerator Circulator 1013S Temperature Range: -30 - +150 °C Temperature Stability: ± 0.05 °C Pumping Capacity (60 Hz): 15 lpm at (0 M), 0 lpm at (3 M) Cooling Capacity (60 Hz): 660 watts @ +20 °C Circulator Work Area (L x W x D): 13.3 cm x 20.3 cm x 14.0 cm. Reservoir Volume: 13 liters Case Dimensions (L x W x D): 44.8 cm x 38.1 cm x 66.0 cm. Weight: 54 kg.	Charging Loop
Micro Pump	Cole-Parmer Masterflex Console Drive, 17 – 1700 ml/min reversible flow. Motor: 1/10 hp, 6 – 600 rpm continuous duty. Speed control accuracy ± 1%. Weight: 7 kg. 115 VAC, 50/60 Hz, 3 Amp.	Charging Loop
Centrifugal Pump	Little Giant centrifugal pump, 115 VAC, 50/60 Hz, 1.25 Amps, single phase, output capacity of 150 ml/s at 9000 RPM.	Charging Loop
Heat Exchanger	A 3/8 in. ID copper coil.	Charging Loop
Tubing	6 m (20 ft.) vinyl tubing, 3/8 in. ID and 5/8 in OD. Operating temperature -43 to 82 °C. Maximum pressure: 55 psi at 21 °C. Pipe insulation; 2 m, 5/8 in. ID and 1 1/2 in OD.	Charging Loop
Camera	Sony Digital Mavica Camera, 1.3 Mega Pixels, and a Samsonite tripod	Flow Visualization
Ink	Eberhard Faber water proof drawing ink, 29.6 ml	Flow Visualization

0.61 m (24 in.) in. outer diameter and 0.584 m (23 in.) in. inner diameter. Two circular discs were used as lids. Both discs were cut from a plexiglas sheet of 2.54 cm (1 in.) thick, with an outer diameter of 0.61 m (24 in.) and an inner diameter of 0.584 m (23 in.), each diameter was 1.27 cm (1/2 in.) deep to produce an outer shoulder.

The bottom lid was press fitted and glued to the tank wall to provide a tight seal. The joint was drilled and tapped for 16 size #10 stainless steel machined screws, which provided additional support. An 8.9 cm (3.5 in.) diameter through hole with a 10.16 cm (4 in.) diameter shoulder and a thickness of 1.27 cm (1/2 in.) was cut in the center of the bottom lid. A PVC pipe with an inner diameter of 3 in. and 15.24 cm (6 in.) long was glued to the through hole to form the outlet of the tank. The shoulder provided an anchoring surface for the porous manifold.

The outlet of the tank was connected with two ball valves. The 2 in. ball valve was used to discharge tank water to the drain while a 3/8 in. ball valve was used to circulate water in the charging loop. The inlet valve could be adjusted to maintain a constant inlet flow rate.

The top lid had a looser fit to provide an easy access to the tank. Two handles were mounted on the top lid for gripping. An 8.9 cm (3.5 in.) diameter through hole was cut in the center of the lid to facilitate the installation of the inlet distributor. A 1.9 cm (3/4 in) diameter through hole was drilled and tapped in the lid to accommodate a 3/4 in. ball valve. The ball valve functions as a pressure relief valve, which is necessary for high temperature operation.

The tank has an internal dimension of 0.58 m (23 in.) in diameter and 1.194 m (47 in.) in height, which provides an overall storage volume of 0.315 m<sup>3</sup> (315 liter). The

temperature distribution in the tank was measured using 21 temperature probes (in three groups of seven probes). One group of the probes was used to measure the temperatures of the water in the center of the porous manifold while the other two groups were used to measure the temperatures of the water in the tank. Each group of the temperature probe was spanned at  $120^{\circ}$  around the circumference of the tank. These probes were used to measure the water temperature at different height in the tank. The first was placed at 6.35 cm (2.5 in.) from the bottom lid of the tank, while the rest were placed at 17.8 cm (7 in.) intervals along the height of the tank. The storage tank with porous manifold and inlet distributor is shown in Fig. 3.3. During the experiment, the entire tank is insulated with 10 cm thick R11 fiberglass insulation.

### **3.2.2 Inlet Distributor**

In order to reduce the effects of mixing and entrainment, the inlet distributor took the form of a diffuser. The inlet pipe was increased from 3/8 in. to 2 in. to reduce the inlet velocity. The inlet distributor comprised of a 2-inch-diameter clear acrylic pipe with 40 1/4 inch diameter holes drilled at equidistance around the circumference of the pipe. The first set of holes were drilled 2.54 cm (1 in.) from the end of the pipe and the others were drilled at 1.27 cm (1/2 in.) intervals. The end of the pipe was closed so that the fluid would exit the pipe radially, thus reducing the axial momentum. As the fluid flowed out radially, it was allowed to trickle down the wall of a 3-inch-diameter acrylic pipe before it entered the tank. The inlet distributor was also fitted with a thermocouple to measure the temperature of the inlet flow. A picture of the inlet distributor is shown in Fig. 3.4.

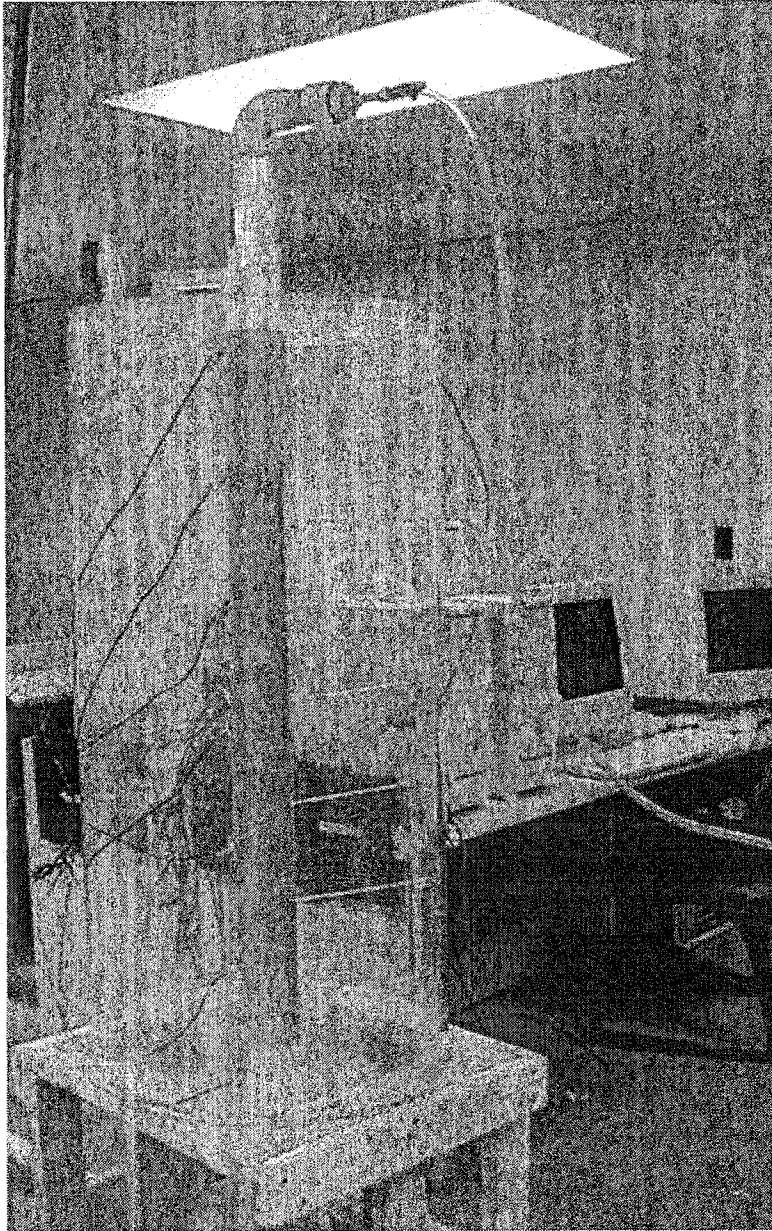


Figure 3.3 Photograph of the storage tank with porous manifold and inlet distributor

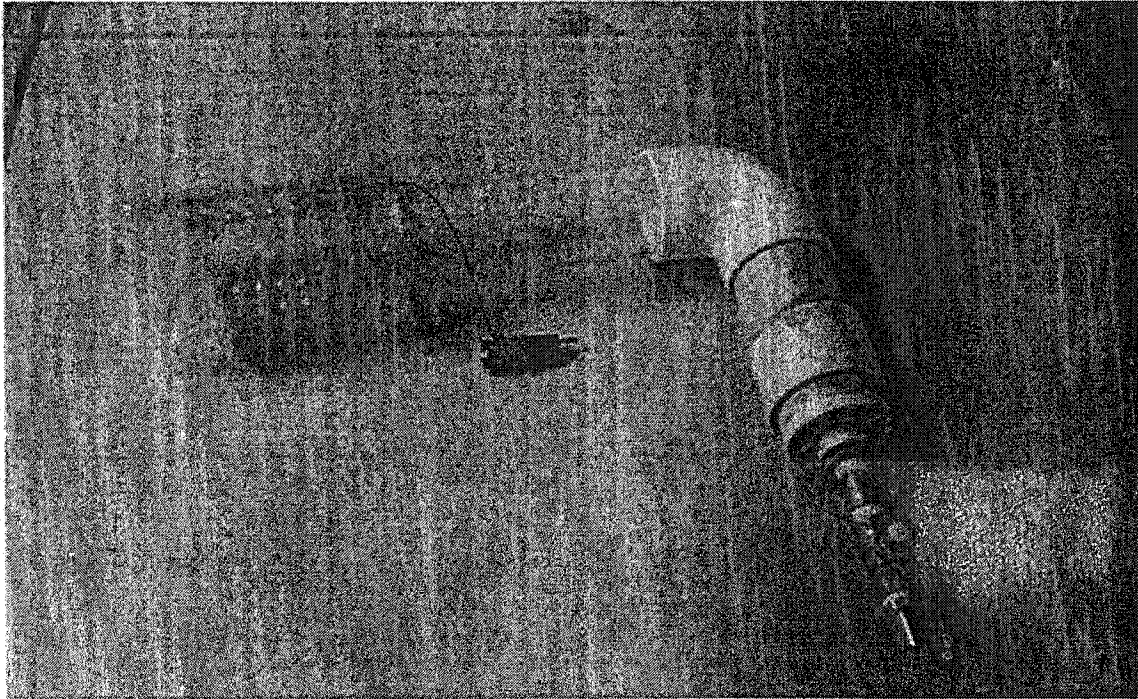


Figure 3.4 Photograph of the inlet distributor

### **3.2.3 Porous Manifold**

The porous manifold was made from blue nylon netting which is normally used in the building construction industry to hold insulation in sheet racks. The nylon net having a mesh size of 1/4 x 1/4 in. (surface porosity of 0.9), was first rolled on a 3.5-in.-diameter pipe until the desired outer diameter was obtained. Once the outer diameter was obtained, the nylon net was sewn in place to form the inlet manifold with an ID of 8.9 cm (3.5 in.) an OD of 10.2 cm (4 in.) and 120.6 cm (47.5 in.) long. The porous manifold sat in the shoulder that was cut off from the bottom lid and was held in place by a 3-in.-diameter acrylic tube from the inlet distributor. It should be noted that no additional support was needed since the manifold is strong enough to support its own weight and the hydrostatic pressure of the water in the tank.

### **3.2.4 Charging Loop**

The charging loop consisted of a micro pump, a constant temperature bath and a heat exchanger. It should be noted that the storage tank operated on a closed loop flow system. As shown in Fig. 3.1, water from the bottom (outlet) of the storage tank was pumped to the inlet of the tank through the heat exchanger immersed in the constant temperature bath. To reduce the heat loss to the ambient, the tube leading from the heat exchanger was insulated.

The constant temperature bath and the heat exchanger were used to insure a constant inlet temperature. The specifications of the Fisher Scientific Isotemp Refrigerated Circulator 1013S are presented in Table 3.1. The inlet and outlet of the constant temperature bath were capped off so that it was operated in the internal circulation mode. Its sole function was to maintain the water in the bath's reservoir at a

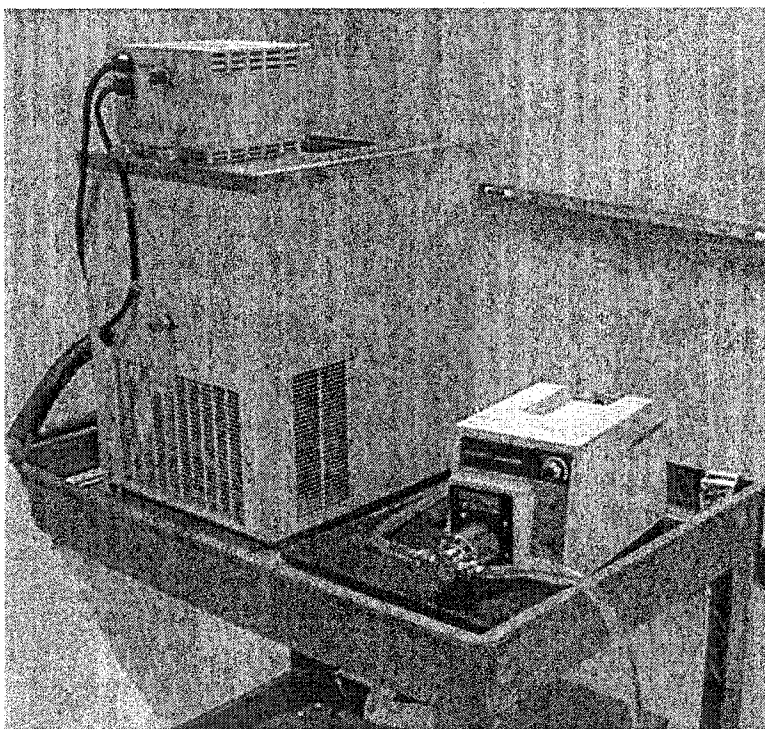


Figure 3.5 Photograph of the constant temperature bath (Fisher Scientific Isotemp Refrigerated Circulator 1013S) and micro-flow pump

constant temperature. Since the flow rate provided by the Isotemp Circulator (when operated in the external circulation mode) was beyond the desired range of the present study, a separate circulation loop was employed. The new flow circuit was driven by an external pump (a micropump or a small centrifugal pump, depending on the desired flow rate) through a heat exchanger that was immersed in the constant temperature bath. The temperature of the water in the bath's reservoir can be maintained at a desired set point with a stability of  $\pm 0.05$  °C. A picture of the constant temperature bath and micro pump is shown in Fig.3.5.

### **3.2.5 Data Acquisition System**

The specifications of the data acquisition system were presented in Table 3.1. Three Gateway computers with Intel Celeron processors were individually connected to a National Instrument SC-2345 chassis via a 68-pin E series cable. Each chassis had eight SCC-TC thermocouple inputs. The SCC-TC signal conditioning modules allowed direct connection to analog inputs and were able to output low-noise digital signals.

The collection of data was facilitated by the use of LABVIEW software (version 6.8). The sampling rate of temperatures can be set as desired. A personal computer used in the data acquisition and a National Instrument SC-2345 chassis are shown in Figs. 3.6 and 3.7 respectively.

### **3.3 Experimental Procedure**

Prior to the start of the experiment, the tank was assembled as shown in Fig.3.1. First, the temperature controller was set and sufficient time was allowed for the water in

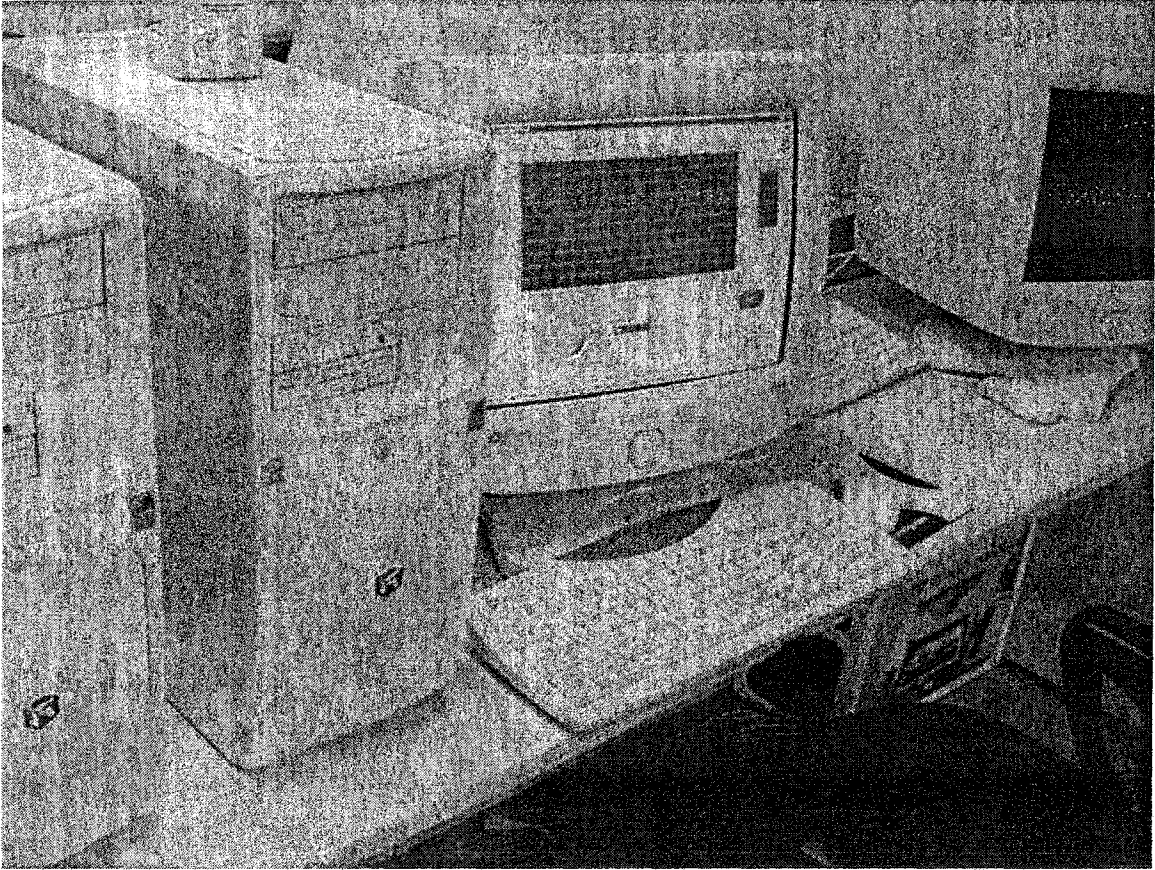


Figure 3.6 Photograph of the LabView software used in the data collection

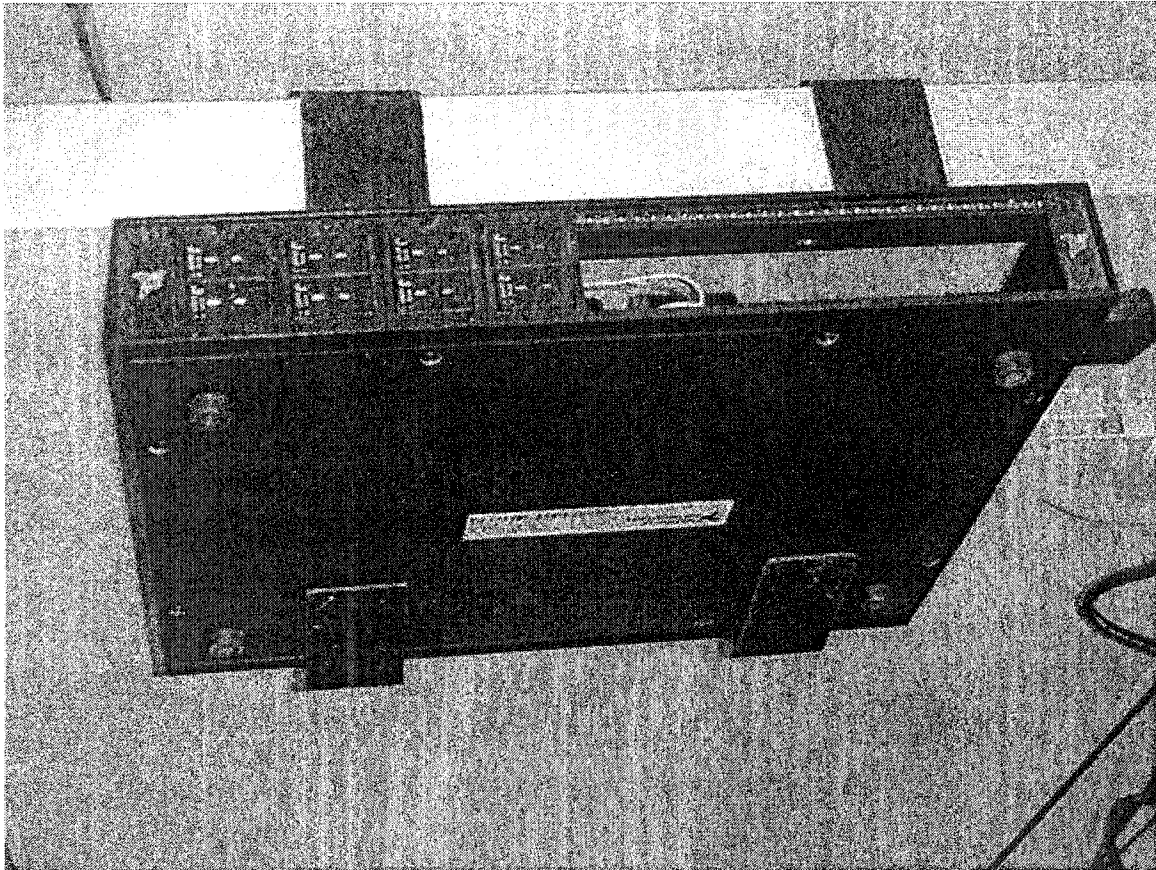


Figure 3.7 Photograph of the National Instrument SC-2345 signal conditioning chassis with analog and digital input.

the constant temperature bath to reach the set temperature. The range of the inlet temperature used in the experiment was between 30 °C to 61 °C and that of the flow rates was from 5.73 ml/s to 143.85 ml/s (with uncertainties of  $\pm 0.15$  ml/s and  $\pm 3.3$  ml/s, respectively). Normally, the temperature of the bath was set a few degrees above the desired inlet temperatures. However, for cases with a higher flow rate and a higher inlet temperature, a larger temperature setting was required. The liquid level in the bath was checked regularly to ensure that it was above the safety mark.

In the beginning of each experiment, the tank contained 315 liters of water at an uniform temperature of 26 °C. The thermocouples and the DAQ system were used to sample the tank water temperatures before the start of each experiment. The flow rate of the pump was adjusted either directly from the control panel of the pump or indirectly by using the valve assembly depending on which pump was used and the desired output. Finally, the flow rate was calibrated at the inlet of the tank to account for any losses, which might occur in the charging loop.

The experiment was initiated when the water temperature difference in the tank was less than 1.0 °C. The tank was charged with warm water at a constant temperature and a constant flow rate while cold water was discharged from the lower section of the tank. The temperatures in the tank, and the inlet and outlet temperatures were recorded at a sampling rate of one minute. The uncertainty associated with the temperature measurements was less than  $\pm 1$  °C. The duration of each experiment was dependent on the flow rate. At the lowest flow rate (5.7 ml/s), the filling time ( $t_{fil}$ ) was approximately 15 hours long. However, the experiment was continued for only twelve hours, which was 80% of the filling time. At a higher flow rate, the filling time was much shorter and the

duration of each experiment was never less than 80% of the filling time. At a higher flow rate and a lower inlet temperature, the duration of the experiment might exceed two filling time.

### **3.3.1 Flow Visualization**

Flow visualization experiments were conducted to confirm the operation of the porous manifold in the reduction of shear-induced mixing between the tank fluid and the fluid in the inlet manifold. Although shear-induced mixing between the tank and manifold fluids was reduced, mixing of the fluid inside the manifold might still occur. In any case, the inlet fluid should move downward in the porous manifold until the flow inertia was balanced by the thermal buoyancy before outflow occurred.

For the flow visualization experiments, the tank was first charged with warm water until a stable stratification was established. The charging time would depend on the flow rate and the inlet temperature. After the stratification was reached, the pump was switched off and the charging process was discontinued. The water in the constant temperature bath was replaced with cold water and the temperature controller was reset to a lower value. Time was allowed for the fluid temperature in the bath to stabilize.

Then the pump was switched on and the cold water was allowed to flow through the inlet for a few minutes to purge out any remaining hot water in the inlet tubes. Before the ink was injected to the inlet, the temperature of the inlet water was measured. Once the inlet temperature was confirmed, 5 ml of black ink was injected into the inlet tube. The insulation was removed from the tank to facilitate visualization. The flow pattern was video recorded and analyzed when the ink began to penetrate the manifold and flow into the tank. The height at which the ink flowed into the tank was noted.

### 3.4 Results and Discussion

Some of the tank temperature profiles measured during the experiments are shown in Figs. 3.8 and 3.9. The measured temperatures are shown on the ordinate, while the temperature probe locations with respect to the tank height are displayed on the abscissa. The first probe is located 6.35 cm (2.5 in.) from the bottom of the tank and the probe seven is located at the same distance below the top surface. The probes in between are evenly placed at 17.78 cm apart.

It is well known that the Richardson number (Eq. 3.1) and inversed Peclet numbers (Eq. 3.2) are important in the formation and maintenance of stratification in a thermal storage tank. As discussed earlier, the primary function of the inlet manifold is

$$Ri = \frac{Gr}{Re^2} \quad (3.1)$$

$$\frac{1}{Pe} = \frac{1}{PrRe} \quad (3.2)$$

to reduce the mixing between the inlet fluid and the fluid in the tank as well as the reduction of plume entrainment. Although some mixing may occur inside the manifold, the effects are not felt in the tank. As such, stable stratification can be maintained. It has been shown earlier that it is easy to maintain stratification at high Richardson number using a low-flow rate storage tank. A look at Eq. (3.1) reveals that the inlet temperature and the inlet flow rate can have influence over the Richardson number. For a given inlet temperature a higher inlet flow rate would result in a lower Richardson number, which in turn led to a stronger flow inertia and mixing by plume entrainment. The following discussion will examine the effects of the inlet flow rate (i.e., the inlet Reynolds number) and the inlet temperature (the Rayleigh number) on the condition of stratification.

Finally, a correlation between the Richardson number and temperature gradient will be developed.

### 3.4.1 Effects of Inlet Temperature on Thermal Stratification

Figures 3.8 and 3.9 show the tank temperature profile for a constant flow rate of 143.85 ml/s and inlet temperatures of 27.9 °C and 28.2 °C, which correspond separately to  $Ri = 1.0$  and 3.04 respectively. Although the inlet flow rates were the same the Reynolds number differed slightly due to the fact that the thermophysical properties of the fluid were evaluated at a mean temperature. The temperatures were sampled every minute at 21 locations. Seven thermocouples were used to measure the water temperature in the tank and another seven, which were in a plane spanning at  $120^\circ$  from that of the first seven probes, were used to check the assumption of axisymmetry.

The curves on each graph represented the tank water temperature distribution at different times. The filling time for these two experiments was calculated to be 36 minutes. The lines are plotted at every 3.6 minutes ( $0.1 t_{fill}$ ) till the end of the experiment. A complete set of the collected data can be found in Appendix C where the temperature profiles (both in the tank and inside the porous manifold) at the given time intervals are plotted separately.

An inspection of the figures revealed the presence of a region of nearly constant temperature gradient, which moved downward as the charging process continued. This is the thermocline region, which acts as barrier to separate the cold and warm fluids in naturally stratified systems (Sliwinski et al. (1978)). The depth at which this thermocline region first appeared in the tank increased as the Richardson number decreased. Fig. 3.8 shows that the thermocline region existed between the probes 5 and 6 while in Fig. 3.9

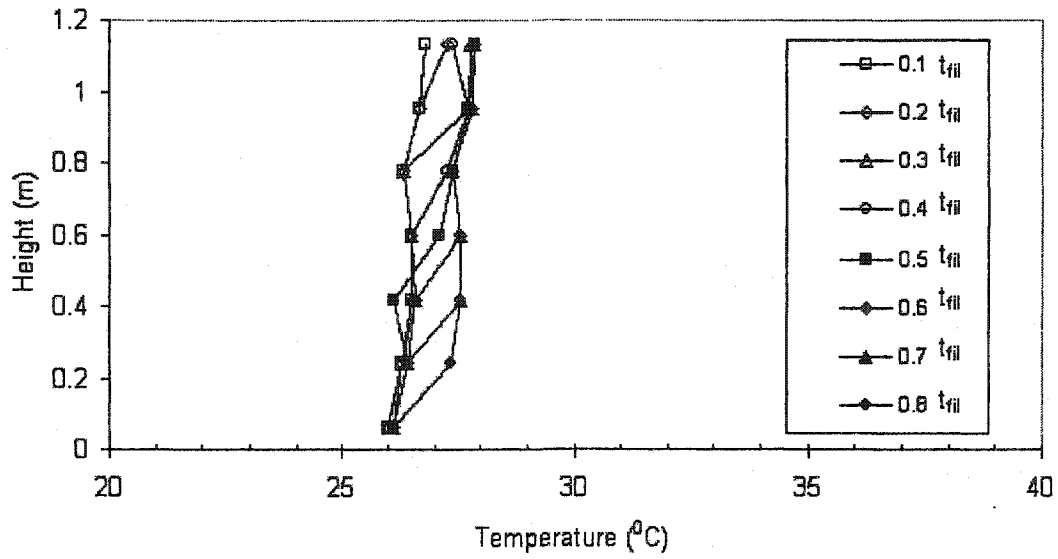


Figure 3.8 Temperature profile for an inlet flow at  $T_i = 27.9 \text{ }^\circ\text{C}$  and  $u_i = 0.0315 \text{ m/s}$  ( $Re = 10691.0$ ,  $Ra = 7.34 \times 10^8$  and  $Ri = 1.0$ )

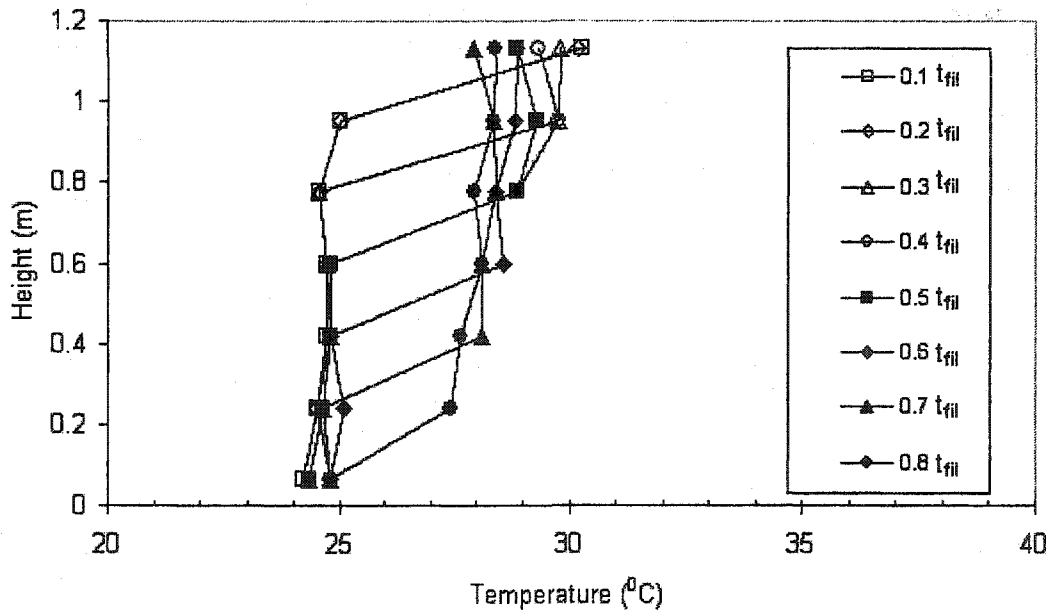


Figure 3.9 Temperature profile for an inlet flow at  $T_i = 28.2 \text{ }^\circ\text{C}$  and  $u_i = 0.0315 \text{ m/s}$  ( $Re = 10445.0$ ,  $Ra = 2.015 \times 10^9$  and  $Ri = 3.04$ )

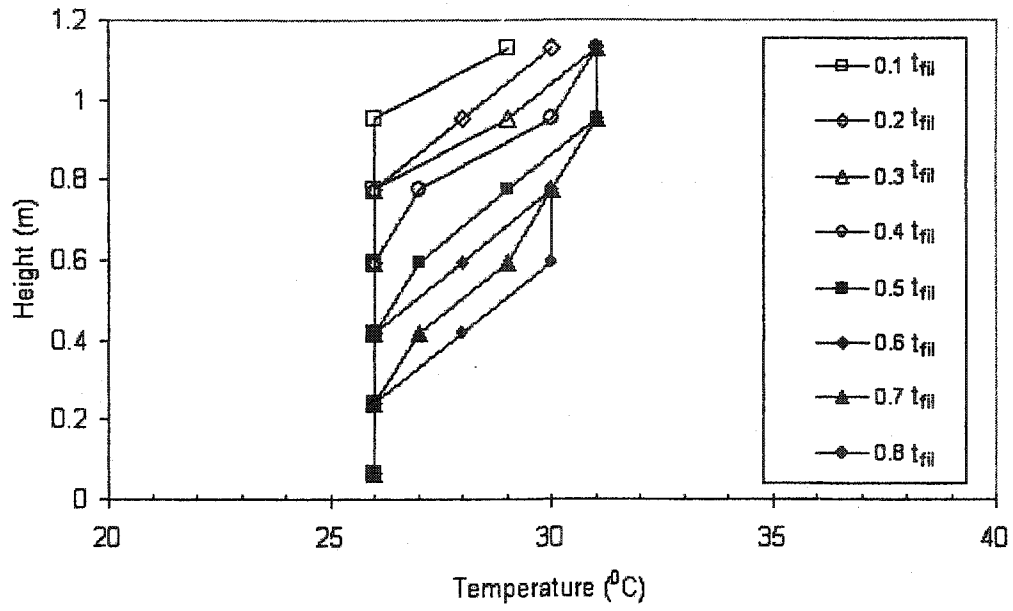


Figure 3.10 Temperature profile for an inlet flow at  $T_i = 32.0 \text{ }^\circ\text{C}$  and  $u_i = 1.25 \times 10^{-3} \text{ m/s}$  ( $Re = 438.8$ ,  $Ra = 2.89 \times 10^9$  and  $Ri = 2648.8$ )

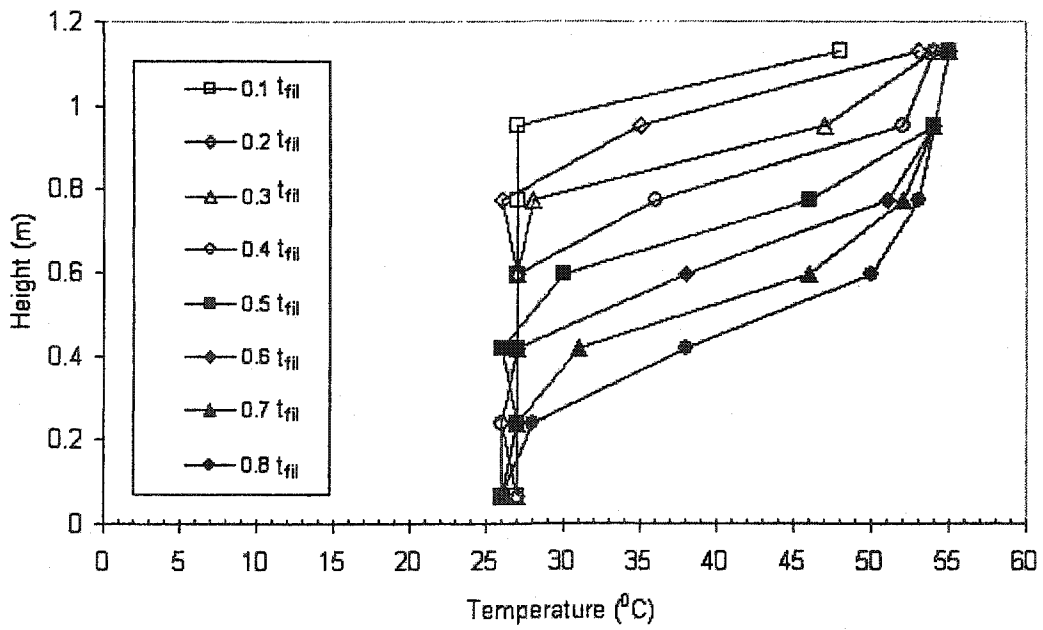


Figure 3.11 Temperature profile for an inlet flow at  $T_i = 55.0 \text{ }^\circ\text{C}$  and  $u_i = 1.25 \times 10^{-3} \text{ m/s}$  ( $Re = 559.0$ ,  $Ra = 2.79 \times 10^{10}$  and  $Ri = 20691.2$ )

the thermocline was between the probes 6 and 7. A similar trend was noted in Figs. 3.10 and 3.11 for a higher Richardson number. The almost parallel temperature profiles in Fig. 3.11, were a result of the high Richardson number.

### 3.4.2 Effects of Inlet Reynolds Number on Thermal Stratification

The Reynolds number used for the following discussion is defined as,

$$Re = \frac{u_i r_t}{\nu} \quad (3.3)$$

where  $r_t$  is the tank radius. Figures 3.12 and 3.13 show the effects of the inlet Reynolds number on the formation of thermocline. In these two experiments, the inlet temperatures are comparable within the uncertainties of the temperature measurement (i.e., 29.0 and 28.9 respectively). It was observed that at a lower inlet Reynolds number (Fig. 3.12), stratification developed before  $t = 0.2 t_{fill}$  and was maintained for the rest of the test duration. However, at a higher Reynolds number a stable stratification was delayed until  $t = 0.4 t_{fill}$ . Due to the negative effects of high inlet Reynolds number, low-flow rate storage tanks are recommended.

### 3.4.3 Degree of Stratification

The degree of stratification in a thermal storage tank can be characterized by the magnitude of the temperature gradient in the thermocline region and indirectly reflected by the mixing tank temperature. The magnitude of the temperature gradient was observed to be a function of both Richardson number (3.1) and inversed Peclet number (3.2). Once a stable stratification had established, the temperature gradients ( $\frac{dT}{dz}$ ) for the

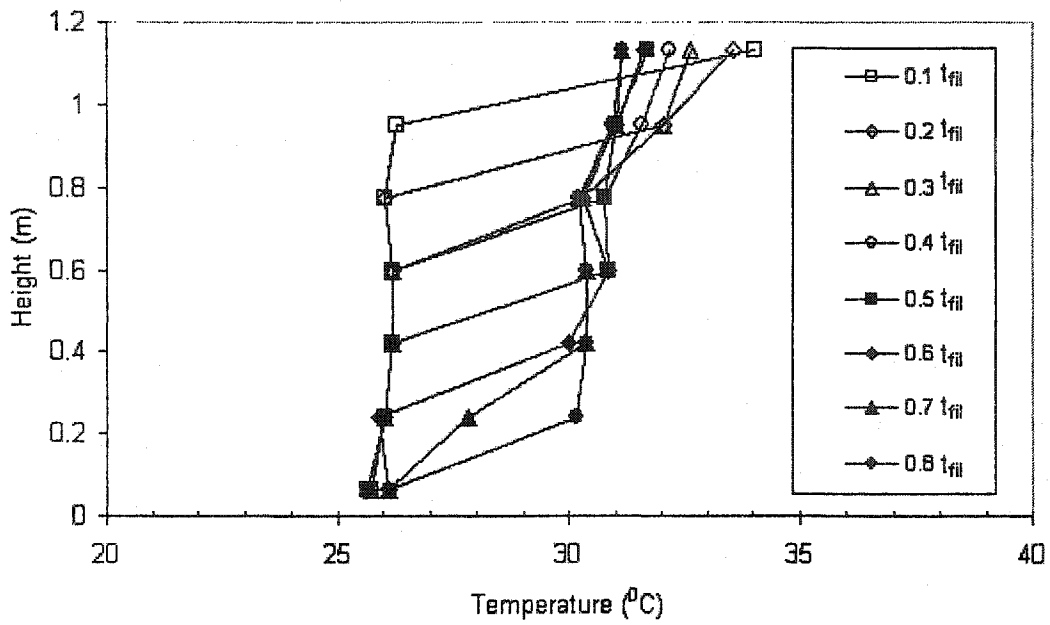


Figure 3.12 Temperature profile for an inlet flow at  $T_i = 29.0 \text{ }^\circ\text{C}$  and  $u_i = 0.0138 \text{ m/s}$  ( $Re = 4782.2$ ,  $Ra = 2.25 \times 10^9$  and  $Ri = 12.84$ )

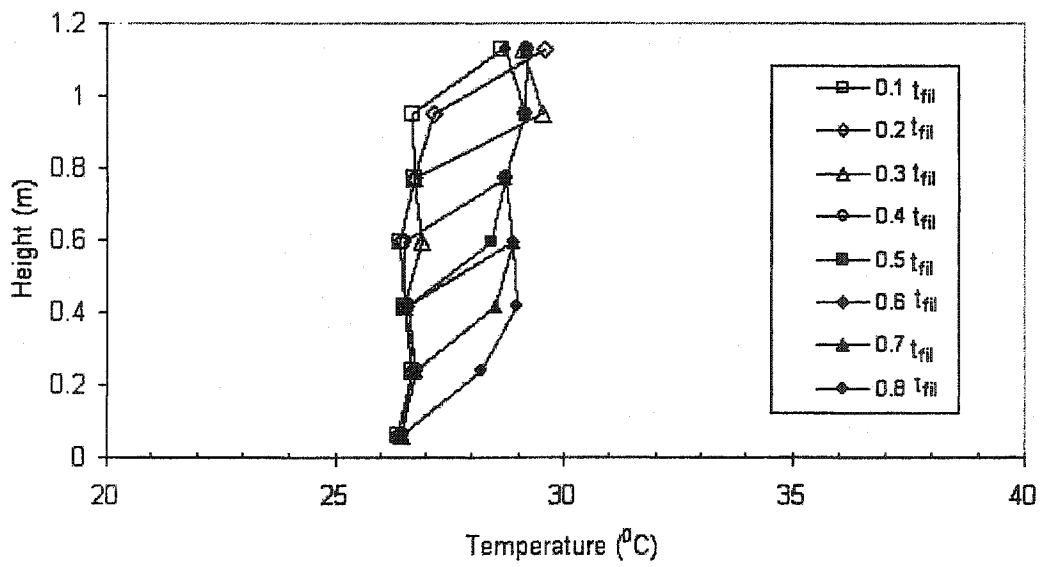


Figure 3.13 Temperature profile for an inlet flow at  $T_i = 28.9 \text{ }^\circ\text{C}$  and  $u_i = 0.0315 \text{ m/s}$  ( $Re = 10948.9$ ,  $Ra = 1.25 \times 10^9$  and  $Ri = 1.82$ )

remaining time intervals were measured. These values were averaged to determine the mean temperature gradient in the thermocline region for each experiment. The measured temperature gradient was then non-dimensionalized by dividing the initial temperature over the tank

$$\frac{T_i - T_{\text{initial}}}{l} \quad (3.4)$$

The degree of stratification can be shown to be a function of the Richardson number and the Peclet number (Fig.3.14). At low Richardson numbers, the relation can be correlated nicely using Eq. (3.5) with a correlation coefficient of 0.9421. At higher Richardson numbers, the degree of stratification becomes less dependant on the Richardson number and inversed Peclet number. The trend observed above agrees well with the results reported by Sliwinski et al. (1978).

$$\frac{dT/dz}{dT/L} = 5.3 + 2.235\text{Ri} - \frac{38422.42}{\text{Pe}} \quad (3.5)$$

The mixing tank temperature is also used to evaluate the thermal stratification.

The mixing tank temperature is defined as

$$T_{\text{mix}} = \frac{1}{\rho c_p \pi r_t^2 l} \int_0^{2\pi} \int_0^l \int_0^{r_t} \rho c_p (T - T_i) r dr dz + T_i \quad (3.6)$$

Since the flow is assumed to be axisymmetric, the above expression can be simplified to give

$$T_{\text{mix}} = \frac{2}{r_t^2 l} \int_0^l \int_0^{r_t} (T - T_i) r dr dz + T_i \quad (3.7)$$

Basically, it is a volume average tank water temperature. To facilitate the comparison with numerical results presented in the next chapter, the above equations can be cast into

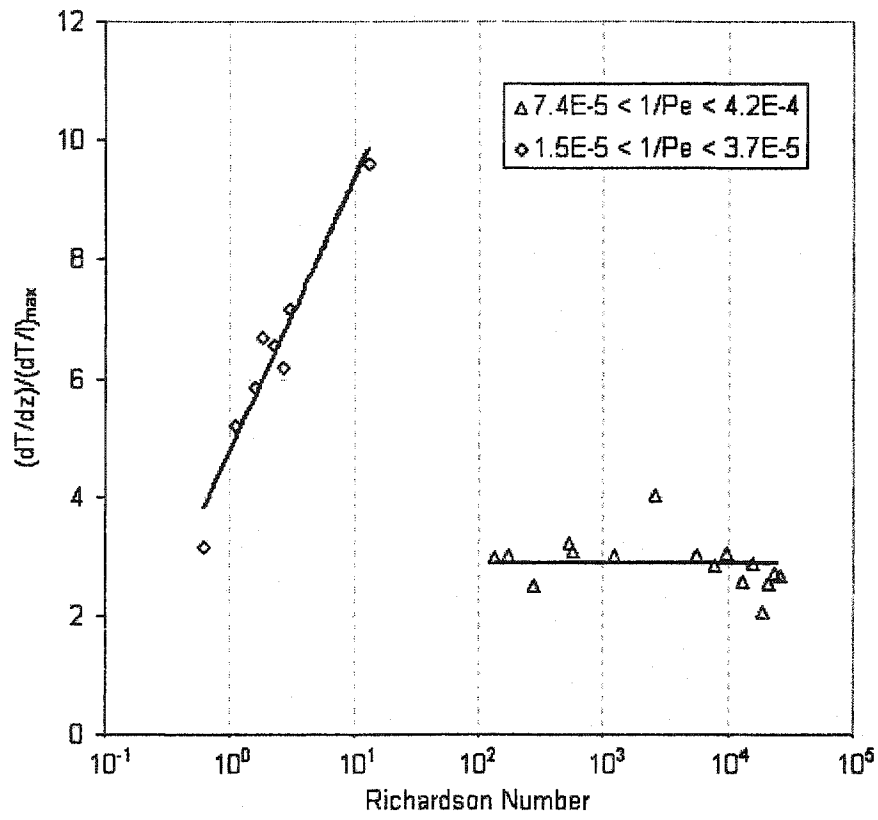


Figure 3.14 Degree of stratification as a function of Richardson and Peclet numbers

dimensionless form as

$$\theta_{\text{mix}} = \frac{2r_t}{1} \int_0^1 \int_0^1 \theta R dR dZ, \quad (3.8)$$

where the dimensionless variables are defined below,

$$R = \frac{r}{r_t}, \quad Z = \frac{z}{r_t}, \quad \theta = \frac{T - T_\infty}{T_i - T_\infty}, \quad (3.9)$$

The dimensionless mixing tank temperature as a function of the dimensionless time and Richardson number is shown in Fig. 3.15. A higher mixing tank temperature, which appears at a higher Richardson number, also indicates a higher degree of stratification.

#### 3.4.4 Flow Visualization

To perform the flow visualization experiment, the tank was first charged with water at an inlet temperature of 62 °C for five hours until the temperature profile in the tank became stratified as shown in Fig. 3.16. Once the thermal stratification established, the charging process inlet flow was stopped. The warm water in the constant temperature bath was replaced by cold water and reset to 49 °C. When the water temperature in the bath reached the setting temperature, the insulation was peeled back off the tank to facilitate visualization and picture-taking. The charging process was restarted with an inlet temperature of 49 °C and it was continued for a couple of minutes to purge any hot residual water that might remain in the inlet pipe before the injection of ink. A syringe was used to inject 5 ml of black ink to the inlet section of the tank. A picture (Fig. 3.17) was taken (a few minutes later). For the case shown, the inlet velocity was  $1.25 \times 10^{-3}$  m/s, which was corresponding to an inlet Reynolds number of 500.

From the temperature profile shown in Fig. 3.16, one would expect the ink

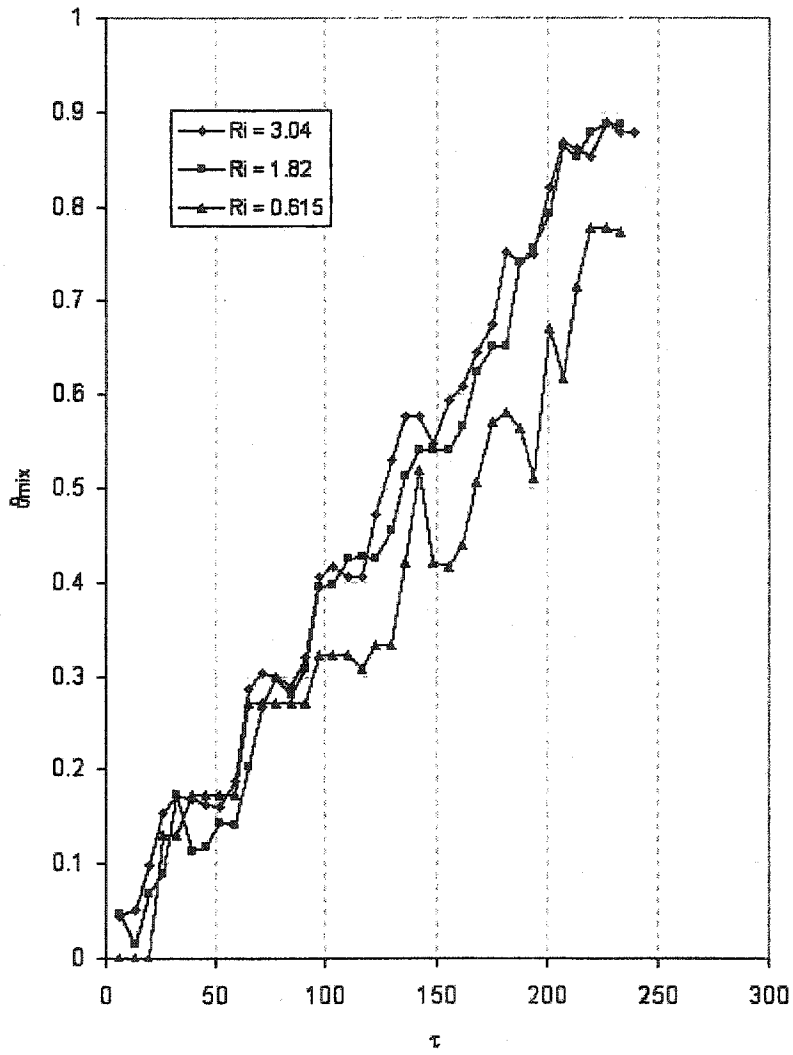


Figure 3.15 Mixing tank temperature for various Richardson numbers.

flowing out of the manifold at a height about the location of the fifth temperature probe. However, from Fig. 3.17, one observed that the ink actually exited the manifold just below the sixth probe. As stated earlier, the purpose of the manifold was to minimize the mixing between the inlet water and the water in the tank. In addition, it would direct the inlet water to a height where the neighboring tank water was approximately in the same temperature before the inlet water penetrated the porous wall. Apparently, the inlet water was heated up by the surrounding tank water in its descending along the manifold. It exited the manifold when the flow inertia was balanced by the thermal buoyancy.

As a result of heating by the surrounding tank water, the inlet water exited the manifold at a height slightly higher than expected. However, from the spreading of the black ink, which was mainly confined to a planar horizontal layer, one is certain that the porous manifold is effective in the establishing and maintaining a thermal stratification. The thickness of the layer was driven by the diffusion process of ink to the fresh water.

The flow visualization experiment was repeated at a higher Reynolds number ( $Re = 1650$ ). In this case the tank was first charged with an inlet water at  $37.5^{\circ}C$  for 150 minutes until a stratified temperature profile (Fig. 3.18) was established. The preparation for flow visualization was repeated for an inlet flow at  $26^{\circ}C$ . From the temperature profile (Fig. 3.18), one would expect outflow to take place around the third probe location. However, for the same reason discussed earlier, the actual outflow occurred the mid-height of the tank (Fig. 3.19).

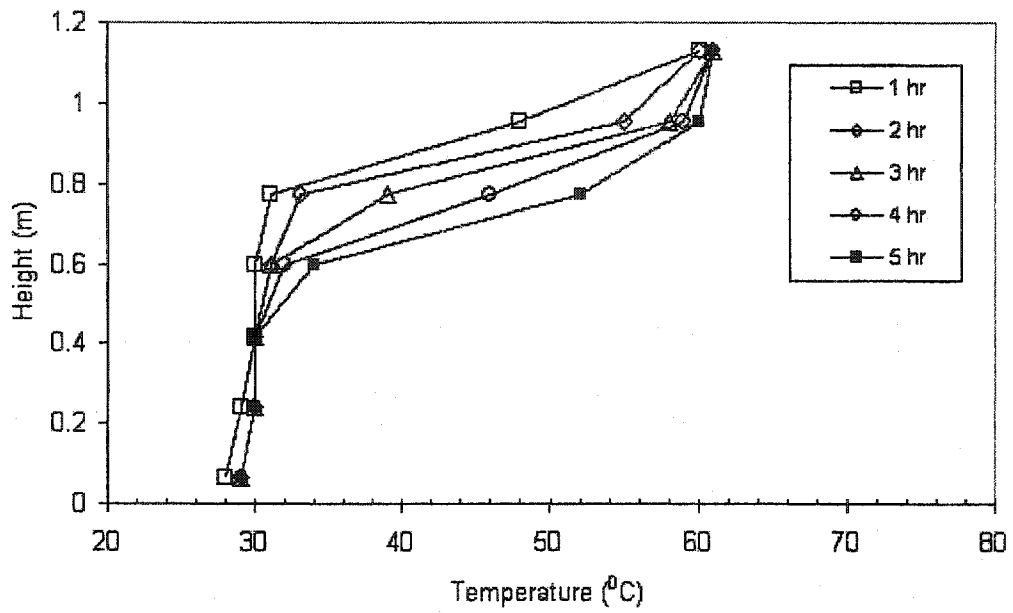


Figure 3.16 Temperature profile for the first flow visualization experiment.

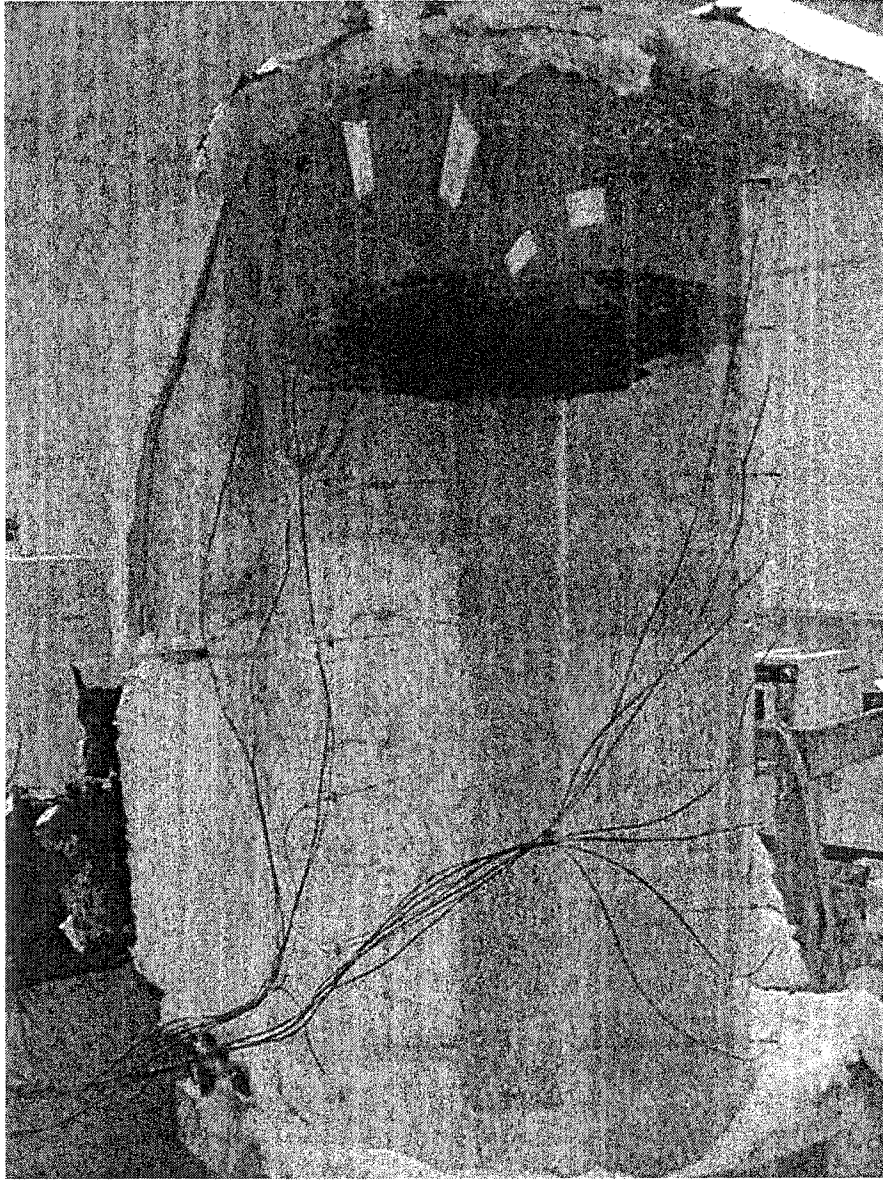


Figure 3.17 Flow visualization for an inlet flow at  $T_i = 49.0\text{ }^{\circ}\text{C}$  and  $u_i = 1.25 \times 10^{-3}\text{ m/s}$   
( $Re = 500$ ,  $Ra = 1.16 \times 10^{10}$ , and  $Ri = 9087.3$ )

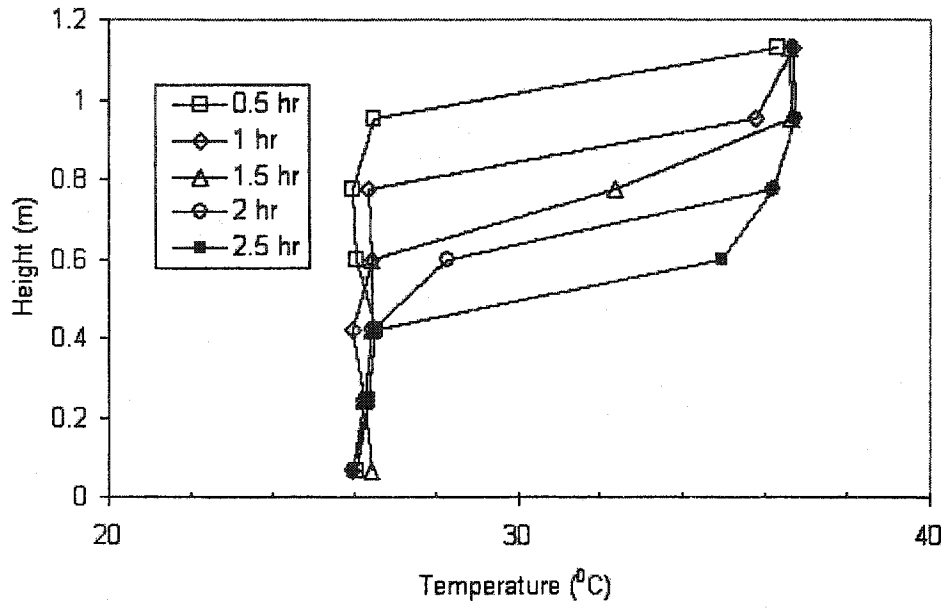


Figure 3.18 Temperature profile for the second flow visualization experiment.

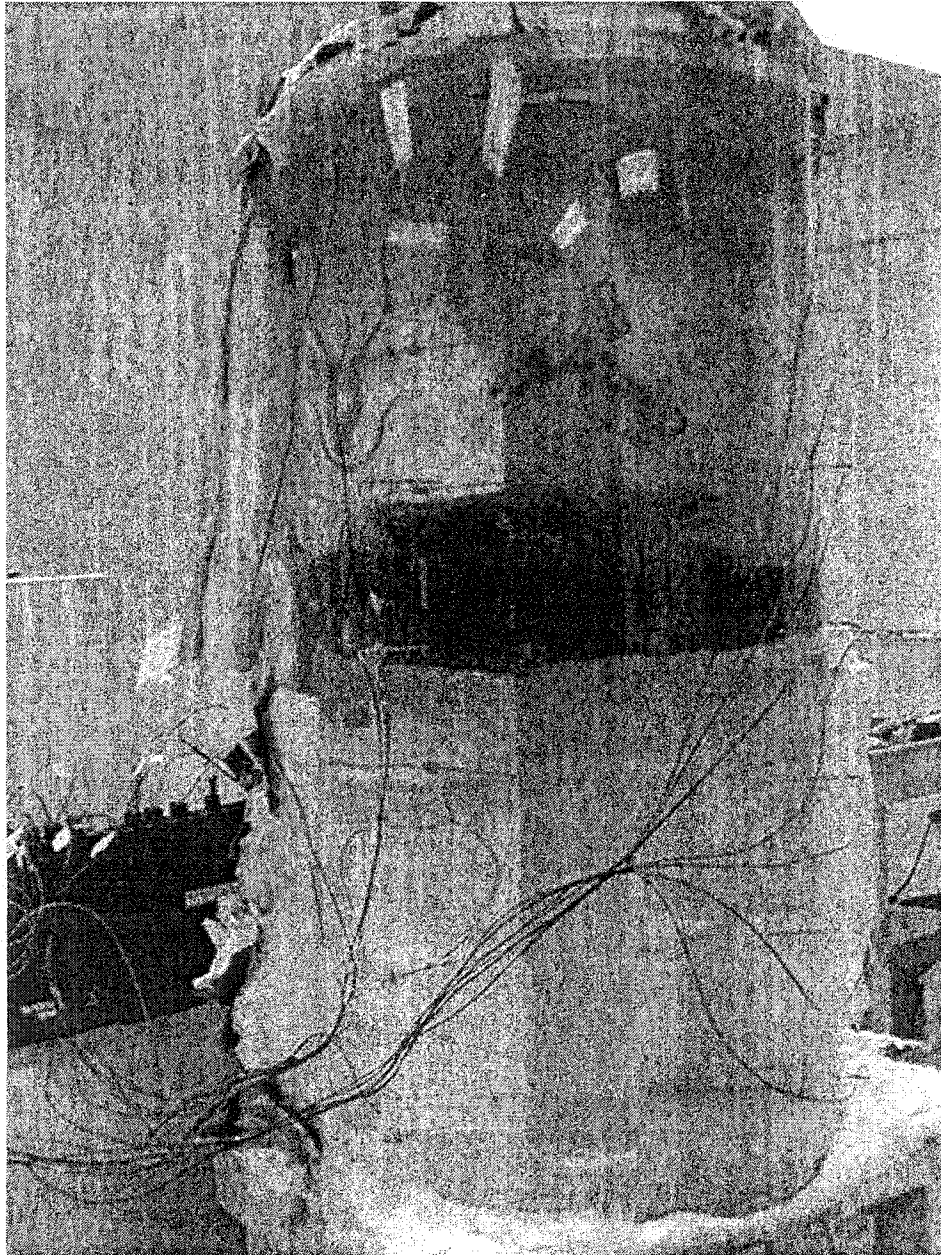


Figure 3.19 Flow visualization for an inlet flow at  $T_i = 26.0\text{ }^{\circ}\text{C}$  and  $u_i = 4.34 \times 10^{-3}\text{ m/s}$   
( $Re = 1650.1$ ,  $Ra = 7.43 \times 10^9$ , and  $Ri = 527.24$ )

### 3.5 Conclusion

A thermal storage tank was designed and constructed to investigate the effect of increase energy input rate due to stratification experimentally. A porous manifold was used to reduce the shear mixing between the inlet fluid and the fluid in the tank so as to enhance the degree of stratification in the tank. Stratification was shown to increase the effectiveness of thermal storage system. For the present study, stratification could be established at a Richardson number as low as 0.651. Due to the operational difficulties,  $Ri = 0.615$  was the limiting value for this experiment. A better equipment may be required for further investigation.

Thermocline acts as a barrier between the hot and cold fluids, and has been shown to move downward as the tank is charged. The depth at which a thermocline first formed in the tank is shown to be a function of the Richardson number.

The degree of stratification has been shown to be a function of the Richardson number and inversed Peclet number. It is observed from Fig. 3.14 that the degree of stratification is sensitive to the variation of Richardson number when the inversed Peclet number is small. However, the degree of stratification becomes insensitive to the Richardson number at a larger value of the inversed Peclet number. The mixing tank temperature is shown to be a good indicator of the thermal stratification.

The flow visualization experiment has been conducted. A numerical model of the storage tank has been developed and the results will be discussed in the following chapter.

## CHAPTER FOUR

# NUMERICAL STUDY OF THERMAL STRATIFICATION IN A LIQUID STORAGE TANK WITH A POROUS MANIFOLD

### 4.1 Introduction

In this chapter a numerical model of the thermal storage tank used in Chapter three will be developed. The results obtained from this numerical study will be compared with the results obtained from the experimental study in that chapter. Although the underlying theory of this numerical study is fairly well understood, the purpose of the comparison is to validate the numerical code developed. After a successful validation, the numerical model can be used to further study the performance of the storage tank at various Richardson numbers. The case for  $Ri = 0.615$  was the limiting case in the experimental study, however, the performance of the porous manifold and the tank as a whole at lower Richardson number is desired.

Governing equations for heat transfer in the fluid region and saturated porous medium are first presented and then transformed into dimensionless finite difference equations in terms of stream function, vorticity and temperature using the control volume approach. The influence of grid size over the numerical solution is discussed. In addition, the validation of numerical code is presented to ensure the accuracy of numerical solutions thus obtained.

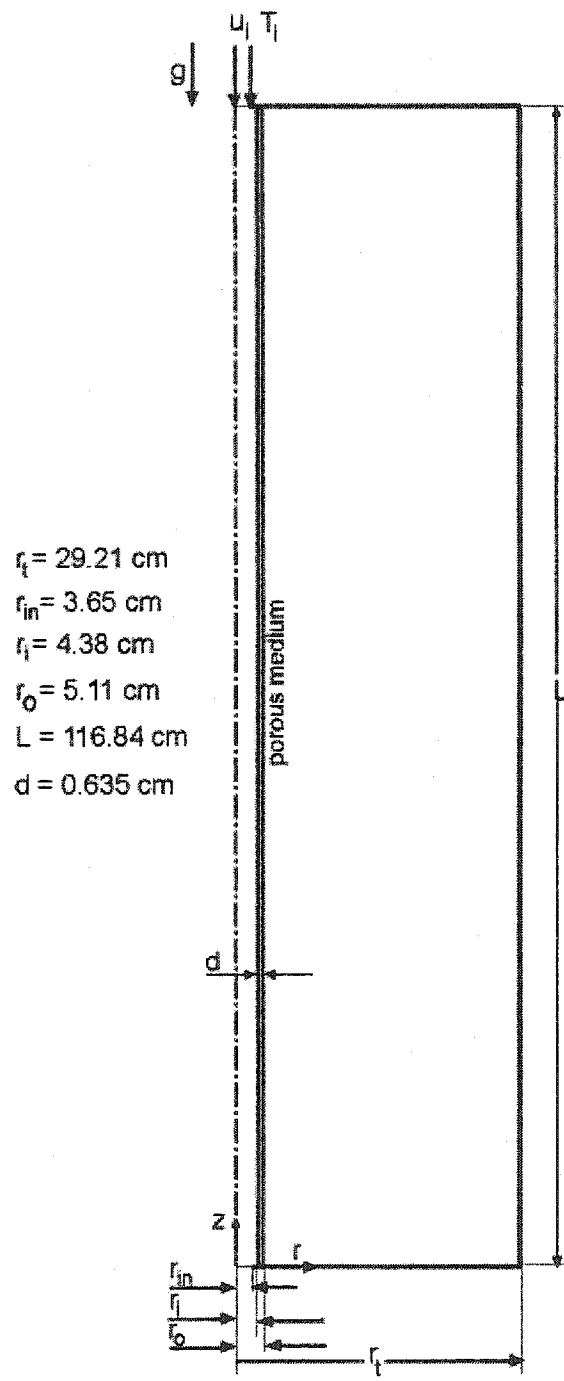


Figure 4.1 Configuration and coordinate system of a cylindrical tank

## 4.2 Governing Equations

### 4.2.1 Fluid Region

The physical configuration is shown in Figure 4.1. In the formulation of the governing differential equations, several assumptions were made. The flow was assumed to be laminar, axisymmetric and incompressible. The free stream velocity  $u_1$  is constant. The thermophysical properties are assumed constant, except for the density in the body force term, in which the Boussinesq approximation is invoked.

$$\rho = \rho_\infty [1 - \beta(T - T_\infty)] \quad (4.1)$$

Viscous dissipation is neglected in the energy equation. The governing equations are, continuity:

$$\frac{\partial}{\partial r}(rv) + \frac{\partial}{\partial z}(ru) = 0, \quad (4.2)$$

r-momentum equation:

$$\rho \left[ \frac{\partial v}{\partial t} + v \frac{\partial v}{\partial r} + u \frac{\partial v}{\partial z} \right] = -\frac{\partial P}{\partial r} + F_r + \mu \left[ \frac{1}{r} \frac{\partial}{\partial r} \left( r \frac{\partial v}{\partial r} \right) + \frac{\partial^2 v}{\partial z^2} - \frac{v}{r^2} \right] \quad (4.3)$$

z-momentum equation:

$$\rho \left[ \frac{\partial u}{\partial t} + v \frac{\partial u}{\partial r} + u \frac{\partial u}{\partial z} \right] = -\frac{\partial P}{\partial z} + F_z + \mu \left[ \frac{1}{r} \frac{\partial}{\partial r} \left( r \frac{\partial u}{\partial r} \right) + \frac{\partial^2 u}{\partial z^2} \right] + \rho_\infty g \beta (T - T_\infty) \quad (4.4)$$

energy equation:

$$\left[ \frac{\partial T}{\partial t} + v \frac{\partial T}{\partial r} + u \frac{\partial T}{\partial z} \right] = \alpha_r \left[ \frac{1}{r} \frac{\partial}{\partial r} \left( r \frac{\partial T}{\partial r} \right) + \frac{\partial^2 T}{\partial z^2} \right] \quad (4.5)$$

where  $u$  and  $v$  are the velocity component in the  $z$ - and  $r$ -direction, respectively.

To eliminate the pressure terms, Eqs. (4.3) and (4.4) are cross-differentiated and combined. With the introduction of vorticity,

$$\omega = \left( \frac{\partial v}{\partial z} - \frac{\partial u}{\partial r} \right), \quad (4.6)$$

the momentum and energy equations can be rewritten in the following conservation form;

$$\left[ \frac{\partial \omega}{\partial t} + \frac{\partial(v\omega)}{\partial r} + \frac{\partial(u\omega)}{\partial z} \right] = \nu \left[ \frac{\partial^2 \omega}{\partial z^2} + \frac{\partial}{\partial r} \left( \frac{1}{r} \frac{\partial(\omega r)}{\partial r} \right) \right] - \frac{\partial}{\partial r} [g\beta(T - T_\infty)], \quad (4.7)$$

$$\left[ \frac{\partial T}{\partial t} + \frac{1}{r} \frac{\partial(rvT)}{\partial r} + \frac{\partial(uT)}{\partial z} \right] = \alpha_r \left[ \frac{1}{r} \frac{\partial}{\partial r} \left( r \frac{\partial T}{\partial r} \right) + \frac{\partial^2 T}{\partial z^2} \right]. \quad (4.8)$$

The governing equations can be normalized using the following set of dimensionless variables;

$$\begin{aligned} R &= \frac{r}{r_i}, & Z &= \frac{z}{r_i}, & \tau &= \frac{t}{(r_i/u_i)}, & \theta &= \frac{T - T_\infty}{T_i - T_\infty}, \\ U &= \frac{u}{u_i}, & V &= \frac{v}{u_i}, & \Omega &= \frac{\omega}{u_i/r_i}, & \Psi &= \frac{\Psi}{u_i r_i^2}. \end{aligned} \quad (4.9)$$

The dimensionless governing equations are thus given by

$$\frac{\partial(RU)}{\partial Z} + \frac{\partial(RV)}{\partial R} = 0, \quad (4.10)$$

$$\left[ \frac{\partial \Omega}{\partial \tau} + \frac{\partial(V\Omega)}{\partial R} + \frac{\partial(U\Omega)}{\partial Z} \right] = \frac{1}{\text{Re}} \left[ \frac{\partial^2 \Omega}{\partial Z^2} + \frac{\partial}{\partial R} \left( \frac{1}{R} \frac{\partial(\Omega R)}{\partial R} \right) \right] - \frac{\text{Gr}}{\text{Re}^2} \frac{\partial \theta}{\partial R}, \quad (4.11)$$

$$\left[ \frac{\partial \theta}{\partial \tau} + \frac{1}{R} \frac{\partial(RV\theta)}{\partial R} + \frac{\partial(U\theta)}{\partial Z} \right] = \frac{1}{\text{Pe}} \left[ \frac{1}{R} \frac{\partial}{\partial R} \left( R \frac{\partial \theta}{\partial R} \right) + \frac{\partial^2 \theta}{\partial Z^2} \right], \quad (4.12)$$

where the Reynolds, Grashof, and Peclet numbers are defined as

$$\text{Re} = \frac{u_i r_i}{\nu}, \quad (4.13)$$

$$\text{Gr} = \frac{g\beta(T_i - T_\infty)r_i^3}{\nu^2}, \quad (4.14)$$

$$Pe = \frac{u_i r_i}{\alpha_f}. \quad (4.15)$$

The ratio  $Gr/Re^2$  in Eq. (4.11) is usually referred to as the Richardson number, which is a measure of the relative importance of the buoyancy force and flow inertia.

Clearly from the continuity equation, the dimensionless velocity components can be expressed in terms of the dimensionless stream function,

$$U = \frac{1}{R} \frac{\partial \Psi}{\partial R}, \quad \text{and} \quad V = -\frac{1}{R} \frac{\partial \Psi}{\partial Z}. \quad (4.16)$$

In terms of stream function, the dimensionless vorticity can be defined as;

$$\frac{1}{R} \frac{\partial^2 \Psi}{\partial Z^2} + \frac{\partial}{\partial R} \left( \frac{1}{R} \frac{\partial \Psi}{\partial R} \right) = -\Omega. \quad (4.17)$$

As suggested by Torrance (1968), a modified vorticity  $\Omega'$  is introduced to the equations to facilitate the numerical solution of Eqs. (4.11) and (4.12). In term of the modified vorticity, Eqs. (4.11), (4.12) and (4.17) becomes

$$\frac{1}{R} \frac{\partial^2 \Psi}{\partial Z^2} + \frac{\partial}{\partial R} \left( \frac{1}{R} \frac{\partial \Psi}{\partial R} \right) = -R\Omega', \quad (4.18)$$

$$\left[ \frac{\partial \Omega'}{\partial \tau} + V \frac{\partial \Omega'}{\partial R} + U \frac{\partial \Omega'}{\partial Z} \right] = \frac{1}{Re} \left[ \frac{\partial^2 \Omega'}{\partial Z^2} + \frac{1}{R} \frac{\partial}{\partial R} \left( \frac{1}{R} \frac{\partial (\Omega' R^2)}{\partial R} \right) \right] - \frac{Gr}{Re^2} \frac{\partial \theta}{\partial R}, \quad (4.19)$$

$$\left[ \frac{\partial \theta}{\partial \tau} + V \frac{\partial \theta}{\partial R} + U \frac{\partial \theta}{\partial Z} \right] = \frac{1}{Pe} \left[ \frac{1}{R} \frac{\partial}{\partial R} \left( R \frac{\partial \theta}{\partial R} \right) + \frac{\partial^2 \theta}{\partial Z^2} \right]. \quad (4.20)$$

#### 4.2.2 Porous Region

The porous medium is considered homogeneous but not isotropic. It is saturated with fluid and is in local thermodynamic equilibrium. The governing equations for the porous media are based on the Darcy's law in which the viscous drag and inertial terms

are neglected (Nield and Bejan (1992)). Hence, the results are valid only in the limit where the Reynolds number based on the volume average velocity and the pore diameter of the porous medium is small (i.e., on the order of unity). The governing equations for mass, momentum and energy in the porous manifold are;

$$\frac{\partial}{\partial r}(rv) + \frac{\partial}{\partial z}(ru) = 0, \quad (4.21)$$

$$\frac{\partial P}{\partial z} + g\rho + \frac{\mu}{K_z}u = 0, \quad (4.22)$$

$$\frac{\partial P}{\partial r} + \frac{\mu}{K_r}v = 0, \quad (4.23)$$

$$\sigma \frac{\partial T}{\partial t} + u \frac{\partial T}{\partial z} + v \frac{\partial T}{\partial r} = \alpha_m \left[ \frac{\partial^2 T}{\partial z^2} + \frac{1}{r} \frac{\partial}{\partial r} \left( r \frac{\partial T}{\partial r} \right) \right], \quad (4.24)$$

where  $\sigma$  is the ratio of the heat capacity of the porous medium and that of the fluid. It is defined as

$$\sigma = \frac{\phi(\rho c)_f + (1 - \phi)(\rho c)_s}{(\rho c)_f}, \quad (4.25)$$

where  $\phi$  is the porosity of the porous medium. The thermal conductivity of the porous medium depends strongly on the complex structure of the medium as reported by Nield and Bejan (1992). For simplicity, it is usually assumed that heat transfer in the solid and fluid phases occurs in parallel so that the thermal conductivity of the porous medium can be approximated by a weighted arithmetic mean of the thermal conductivity of each individual phase. In terms of mathematical expression, it is given by

$$k_m = (1 - \phi)k_s + \phi k_f. \quad (4.26)$$

In terms of the dimensionless variables from Eq. (4.9), the governing equations are reduced to

$$\frac{K_z}{K_r} \frac{1}{R} \frac{\partial^2 \Psi}{\partial Z^2} + \frac{\partial}{\partial R} \left( \frac{1}{R} \frac{\partial \Psi}{\partial R} \right) = \frac{Ra'}{Pe'} \frac{\partial \theta}{\partial R}, \quad (4.27)$$

$$\sigma \frac{\partial \theta}{\partial \tau} + \frac{1}{R} \frac{\partial \Psi}{\partial R} \frac{\partial \theta}{\partial Z} - \frac{1}{R} \frac{\partial \Psi}{\partial Z} \frac{\partial \theta}{\partial R} = \frac{1}{Pe'} \left[ \frac{\partial^2 \theta}{\partial Z^2} + \frac{1}{R} \frac{\partial}{\partial R} \left( R \frac{\partial \theta}{\partial R} \right) \right], \quad (4.28)$$

where the modified Rayleigh and Peclet numbers, which are different from those in the fluid region, are defined as;

$$Ra' = \frac{K_z g \beta (T_i - T_\infty) r_t}{\alpha_m \nu}, \quad (4.29)$$

and

$$Pe' = \frac{u_i r_t}{\alpha_m}. \quad (4.30)$$

### 4.3 Boundary and Interface Conditions

The governing equations are subject to specific initial and boundary conditions.

Initially, the system is assumed to be motionless and to have an initial temperature same as the constant ambient temperature  $T_\infty$ . In term of mathematical expression, the conditions are :

$$\tau = 0, \quad 0 \leq Z \leq L \quad \text{and} \quad 0 \leq R \leq 1 \quad \theta = \Omega = \Psi = 0. \quad (4.31)$$

At time  $\tau > 0$ , warmer water ( $Pr = 5.4$ ) is charged into the system with a constant velocity  $u_i$ . In term of mathematical expression, the conditions are:

$$R = 0, \quad 0 < Z < L, \quad \Psi = 0, \quad \frac{\partial \theta}{\partial R} = 0, \quad (4.32a)$$

$$R = 1, \quad 0 < Z < L, \quad \Psi = -\frac{1}{2} R_{in}^2, \quad \frac{\partial \theta}{\partial R} = Bi \theta_w, \quad (4.32b)$$

$$Z = 0, \quad 0 < R < R_{in}, \quad \frac{\partial \Psi}{\partial Z} = 0, \quad \frac{\partial \theta}{\partial Z} = 0, \quad (4.32c)$$

$$R_{in} < R < 1, \quad \Psi = -\frac{1}{2}R_{in}^2, \quad \frac{\partial\theta_w}{\partial Z} = 0, \quad (4.32d)$$

$$Z = L, \quad 0 < R < R_{in}, \quad \Psi = -\frac{1}{2}R^2, \quad \theta = 1, \quad (4.32e)$$

$$R_{in} < R < 1, \quad \Psi = -\frac{1}{2}R_{in}^2, \quad \frac{\partial\theta_w}{\partial Z} = 0. \quad (4.32f)$$

It should be mentioned that convective heat loss is only imposed on the vertical boundary as indicated by Eq. (4.32b). The thermal boundary condition is obtained by performing an energy balance on the vertical wall in which the thermal conductivity of the wall is assumed equal to that of the fluid. In terms of mathematical expression,

$$k_f \frac{\partial T_w}{\partial r} = h(T_w - T_\infty). \quad (4.33)$$

In the dimensionless form, it gives

$$\frac{\partial\theta_w}{\partial R} = \frac{hr_t}{k_f} \theta_w \quad \text{or} \quad \frac{\partial\theta_w}{\partial R} = Bi\theta_w. \quad (4.34)$$

The heat loss at the top and bottom walls is assumed to be negligible.

The boundary condition for vorticity at the no-slip boundaries, as determined by computational experiments, depends on the Rayleigh and Peclet numbers, the differencing method for interior points, the boundary conditions for stream function and temperature, and sometime on the initial condition (Roache, (1998)). The vorticity on the solid boundaries can be obtained by first reducing Eq. (4.17) to  $\Omega' = -(1/R^2) \partial^2\Psi/\partial Z^2$  along the top and bottom walls, and  $\Omega' = -\partial^2\Psi/\partial R^2$  along the vertical wall. A combination of Taylor series expansion for  $\Psi$  to examine the nature of the flow in the boundary region of a permeable interface near the walls, together with the boundary

condition that  $\Psi$  and its normal derivative are zeros gives the following wall vorticity approximations:

Top and bottom walls (Roache, (1998)):

$$\Omega'_w = \frac{7\Psi_w - 8\Psi_{w-1} + \Psi_{w-2}}{2R^2(\Delta Z)^2} + O\{(\Delta Z)^2\} \quad (4.35)$$

Vertical wall:

$$\Omega'_w = \frac{7\Psi_w - 8\Psi_{w-1} + \Psi_{w-2}}{2(\Delta R)^2} + O\{(\Delta R)^2\} \quad (4.36)$$

At the inlet and the exit of the flow, the vorticity and its first derivative of vorticity are assumed to be zero, respectively (Roache, (1998)).

$$Z = L, \quad 0 < R < R_{in}, \quad \Omega' = 0. \quad (4.37)$$

$$Z = 0, \quad 0 < R < R_{in}, \quad \frac{\partial \Omega'}{\partial Z} = 0. \quad (4.38)$$

Physically, Eq. (4.37) represents no vortex motion at the inlet and Eq. (4.38) for negligible change in vorticity in the axial direction at the exit.

To determine  $\Omega'$  along the centerline, a special form of the conservation equation is needed to avoid an indeterminate value as  $R \rightarrow 0$ . By applying the boundary condition at  $R = 0$  and using L'Hospital's rule, Eq. (4.19) is reduced to

$$\left[ \frac{\partial \Omega'}{\partial \tau} + U \frac{\partial \Omega'}{\partial Z} \right] = \frac{1}{\text{Re}} \left[ \frac{\partial^2 \Omega'}{\partial Z^2} + 4 \frac{\partial^2 \Omega'}{\partial R^2} \right] - \frac{\text{Gr}}{\text{Re}^2} \frac{\partial^2 \theta}{\partial R^2}. \quad (4.39)$$

The matching conditions at the fluid/porous interface are provided by empirical relationship as suggested by Beavers and Joseph (1967)

$$V_f \Big|_{R=R_i^-} = V_m \Big|_{R=R_i^+}, \quad (4.40)$$

$$\left. \frac{\partial U_f}{\partial R} \right|_{R=R_i^-} = \frac{\gamma r_i}{K_z^{1/2}} \left( U_f \Big|_{R=R_i^-} - U_m \Big|_{R=R_i^+} \right) \quad (4.41)$$

where  $U_f$  is the dimensionless axial velocity in the fluid and  $U_m$  is the dimensionless Darcian velocity in the porous medium. It is clear that  $U_f$  and  $\frac{\partial U_f}{\partial R}$  in Eq. (4.41) are evaluated at  $R = R_i^-$  and  $U_m$  is evaluated at interface  $R = R_i^+$ . The same relationship is applied at the interface  $R = R_0$ . The value of slip coefficient,  $\gamma$ , is independent of the viscosity of the fluid, but depends on the material properties that characterize the structure of the porous medium within the interface region. The values of slip coefficient for Nylon and Fiberglass tubes of different wall thickness are given in Eqs. (2.35) – (2.38) while their permeabilities are summarized in Table 2.3. In addition, the matching condition representing the continuity of temperature and heat flux across the fluid/porous interface are also employed and they are

$$\theta_f \Big|_{R=R_i^-} = \theta_m \Big|_{R=R_i^+}, \quad (4.42)$$

$$k_f \frac{\partial \theta_f}{\partial R} \Big|_{R=R_i^-} = k_m \frac{\partial \theta_m}{\partial R} \Big|_{R=R_i^+}. \quad (4.43)$$

## 4.4 Finite-Difference Equations and Numerical Methods

### 4.4.1 Derivation of Finite Difference Equations

The dimensionless governing equations for fluid and porous region are transformed into finite difference equations by using the control volume approach. In this approach, the finite difference equations are derived by integrating the governing equations over a finite control volume such that the specific physical quantities such as mass, momentum and energy are conserved. This approach ensures that the conservation

laws are satisfied over the control volume. Roache (1998) reported that this conservation system generally provides more accurate results.

A control volume for a two-dimensional domain is shown in Fig. 4.2. To derive the finite difference equations, the governing equations are formally integrated over this control volume. Proceeding with the formal integration of Eqs. (4.10), (4.11) and (4.12) for the fluid region one obtains:

$$\int_{Z,s}^{Z,n} \int_{R,w}^{R,e} \left\{ \frac{\partial}{\partial Z} \left( \frac{1}{R} \frac{\partial \Psi}{\partial Z} \right) + \frac{\partial}{\partial R} \left( \frac{1}{R} \frac{\partial \Psi}{\partial R} \right) + R\Omega' \right\} dRdZ = 0, \quad (4.44)$$

$$\int_{Z,s}^{Z,n} \int_{R,w}^{R,e} \left\{ R \frac{\partial \Omega'}{\partial \tau} + \left[ \frac{\partial \Psi}{\partial R} \frac{\partial \Omega'}{\partial Z} - \frac{\partial \Psi}{\partial Z} \frac{\partial \Omega'}{\partial R} \right] - \frac{1}{\text{Re}} \left[ \frac{\partial}{\partial Z} \left( R \frac{\partial \Omega'}{\partial Z} \right) + \frac{\partial}{\partial R} \left( \frac{1}{R} \frac{\partial}{\partial R} \left( R^2 \Omega' \right) \right) \right] + \frac{\text{Gr}}{\text{Re}^2} \frac{\partial \theta}{\partial R} \right\} dRdZ = 0, \quad (4.45)$$

$$\int_{Z,s}^{Z,n} \int_{R,w}^{R,e} \left\{ R \frac{\partial \theta}{\partial \tau} + \left[ \frac{\partial \Psi}{\partial R} \frac{\partial \theta}{\partial Z} - \frac{\partial \Psi}{\partial Z} \frac{\partial \theta}{\partial R} \right] - \frac{1}{\text{Pe}} \left[ \frac{\partial}{\partial Z} \left( R \frac{\partial \theta}{\partial Z} \right) + \frac{\partial}{\partial R} \left( R \frac{\partial \theta}{\partial R} \right) \right] \right\} dRdZ = 0. \quad (4.46)$$

By considering these equations one by one, Eq. (4.44) can be rewritten as

$$\int_{R,w}^{R,e} \left[ \left( \frac{1}{R} \frac{\partial \Psi}{\partial Z} \right)_n - \left( \frac{1}{R} \frac{\partial \Psi}{\partial Z} \right)_s \right] dR + \int_{Z,s}^{Z,n} \left[ \left( \frac{1}{R} \frac{\partial \Psi}{\partial R} \right)_e - \left( \frac{1}{R} \frac{\partial \Psi}{\partial R} \right)_w \right] dZ + \int_{Z,s}^{Z,n} \int_{R,w}^{R,e} R\Omega' dRdZ = 0, \quad (4.47)$$

where subscripts refer to node locations shown in Fig. 4.2.

If one assumes that

$$\left( \frac{1}{R} \frac{\partial \Psi}{\partial Z} \right)_n = \frac{1}{R_P} \left( \frac{\Psi_N - \Psi_P}{Z_N - Z_P} \right), \quad \left( \frac{1}{R} \frac{\partial \Psi}{\partial Z} \right)_s = \frac{1}{R_P} \left( \frac{\Psi_P - \Psi_S}{Z_P - Z_S} \right), \quad (4.48a,b)$$

$$\left( \frac{1}{R} \frac{\partial \Psi}{\partial R} \right)_e = \frac{1}{R_P + \Delta R/2} \left( \frac{\Psi_E - \Psi_P}{Z_E - Z_P} \right) \text{ and } \left( \frac{1}{R} \frac{\partial \Psi}{\partial R} \right)_w = \frac{1}{R_P - \Delta R/2} \left( \frac{\Psi_P - \Psi_W}{Z_P - Z_W} \right), \quad (4.49a,b)$$

Eq. (4.44) can be rewritten as,

$$\begin{aligned} & \frac{(\Psi_N - \Psi_P)(R_e - R_w)}{R_P} \left( \frac{R_e - R_w}{Z_N - Z_P} \right) - \frac{(\Psi_P - \Psi_S)(R_e - R_w)}{R_P} \left( \frac{R_e - R_w}{Z_P - Z_S} \right) + \frac{\Psi_E - \Psi_P}{R_P + \frac{\Delta R}{2}} \left( \frac{Z_n - Z_s}{R_E - R_P} \right) \\ & - \frac{\Psi_P - \Psi_W}{R_P - \frac{\Delta R}{2}} \left( \frac{Z_n - Z_s}{R_P - R_W} \right) + R_P \Omega' (R_e - R_w) (Z_n - Z_s) = 0, \end{aligned} \quad (4.50)$$

which lead to a successive substitution formula

$$\Psi_P = C_E \Psi_E + C_W \Psi_W + C_N \Psi_N + C_S \Psi_S + S_P, \quad (4.51)$$

where

$$C_E = \frac{C'_E}{\Sigma C}, \quad C_W = \frac{C'_W}{\Sigma C}, \quad C_N = \frac{C'_N}{\Sigma C}, \quad C_S = \frac{C'_S}{\Sigma C}, \quad S_P = \frac{S'_P}{\Sigma C}, \quad (4.52a)$$

$$C'_E = \frac{1}{2(R_P + \Delta R/2)} \left( \frac{Z_N - Z_S}{R_E - R_P} \right), \quad (4.52b)$$

$$C'_W = \frac{1}{2(R_P - \Delta R/2)} \left( \frac{Z_N - Z_S}{R_P - R_W} \right), \quad (4.52c)$$

$$C'_N = \frac{1}{2R_P} \left( \frac{R_E - R_W}{Z_N - Z_P} \right), \quad (4.52d)$$

$$C'_S = \frac{1}{2R_P} \left( \frac{R_E - R_W}{Z_P - Z_S} \right), \quad (4.52e)$$

$$S'_P = \frac{1}{4} R_P \Omega_P'' (Z_N - Z_S) (R_E - R_W), \quad (4.52f)$$

$$\Sigma C = C'_E + C'_W + C'_N + C'_S. \quad (4.52g)$$

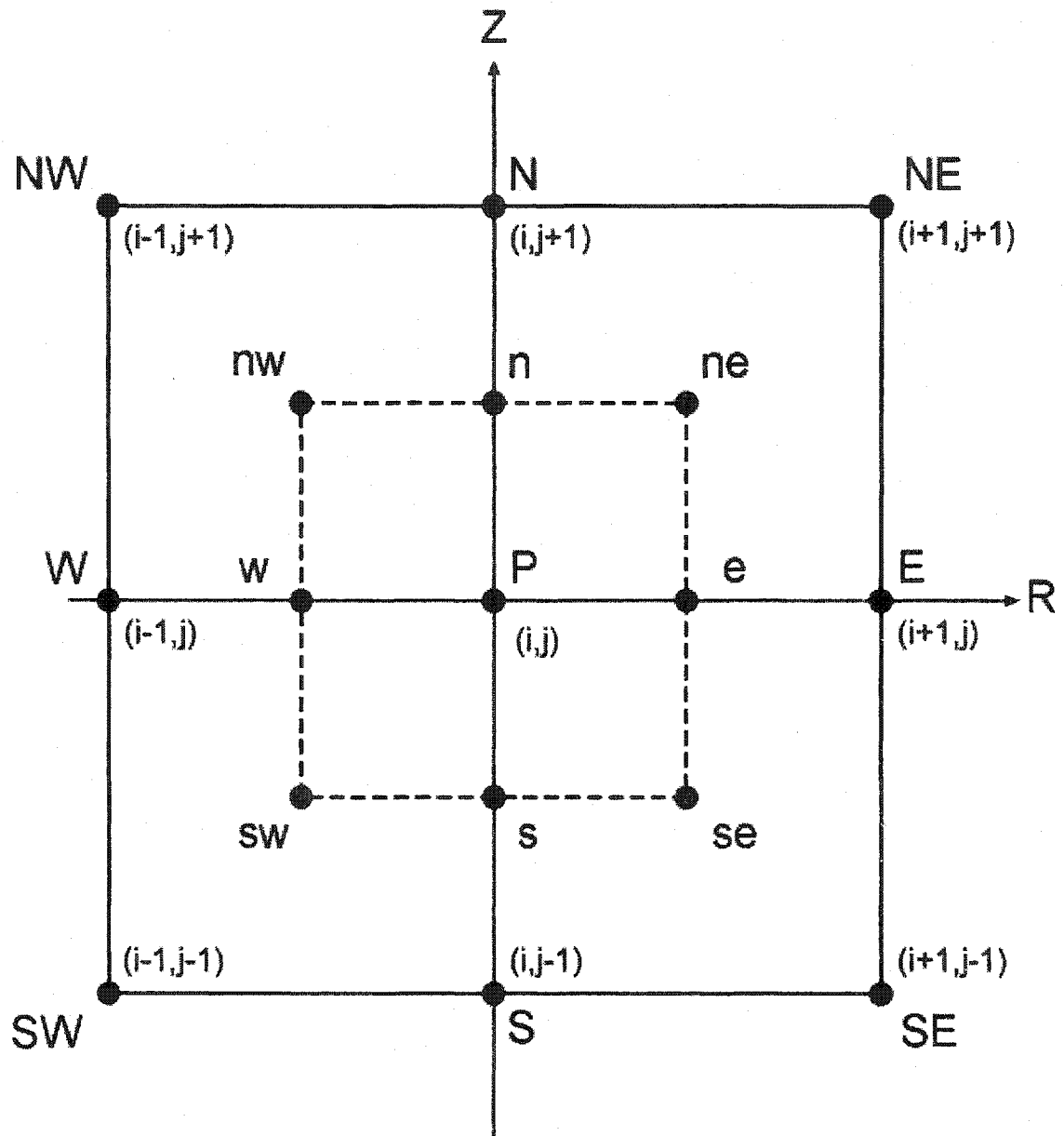


Figure 4.2 The control volume of nodal point  $P$  in a two-dimensional computational domain.

#### 4.4.2 Upwind Scheme

There are many ways to discretize the nonlinear convective term in Eqs.(4.45) and (4.46) (Torrance (1968)). The approximation of convection term by central differences has been shown to be unstable and may lead to false oscillatory solution when the Reynolds number (or Peclet number) exceeds a critical value. In principle, grid refinement can alleviate this problem, but the degree of refinement required is often impractical for engineering purposes. Thus, there have been a crucial need for a convection-diffusion formulation that leads to stable and accurate results with a grid of modest fineness.

Many schemes have been proposed to overcome this difficulty, and one well known and popular remedy is the upwind scheme, also known as the upwind-difference scheme, is employed in the present study.

Consider the convection terms in Eqs. (4.45) and (4.46). A closer examination of each equation shows a similarity in the convection terms, the differences are only in the primary variables, for example:  $\Omega'$  in Eq. (4.45) and  $\theta$  in Eq. (4.46). If these variables were replaced by a dummy variable  $\Phi$ , the terms can then be expressed in one single form.

$$I_{\text{conv}} = \int_{Z,s}^{Z,n} \int_{R,w}^{R,e} \left[ \frac{\partial}{\partial Z} \left( \Phi \frac{\partial \Psi}{\partial R} \right) - \frac{\partial}{\partial R} \left( \Phi \frac{\partial \Psi}{\partial Z} \right) \right] dR dZ. \quad (4.53)$$

Integration of Eq. (4.53) gives

$$I_{\text{conv}} = \int_{R,w}^{R,e} \left[ \left( \Phi \frac{\partial \Psi}{\partial R} \right)_n - \left( \Phi \frac{\partial \Psi}{\partial R} \right)_s \right] dR - \int_{Z,s}^{Z,n} \left[ \left( \Phi \frac{\partial \Psi}{\partial Z} \right)_e - \left( \Phi \frac{\partial \Psi}{\partial Z} \right)_w \right] dZ,$$

$$= \int_{R,w}^{R,e} \Phi_n \left( \frac{\partial \Psi}{\partial R} \right)_n dR - \int_{R,w}^{R,e} \Phi_s \left( \frac{\partial \Psi}{\partial R} \right)_s dR - \int_{Z,s}^{Z,n} \Phi_e \left( \frac{\partial \Psi}{\partial Z} \right)_e dZ + \int_{Z,s}^{Z,n} \Phi_w \left( \frac{\partial \Psi}{\partial Z} \right)_w dZ. \quad (4.54)$$

Take the first integration  $I_1$  of Eq. (4.54) as an example. If there exist an average value of  $\Phi_n$ ,  $\bar{\Phi}_n$ , lying between the maximum and minimum values of  $\Phi_n$  on the integration interval such that

$$\bar{\Phi}_n = \frac{\int_{R,w}^{R,e} \Phi_n \left( \frac{\partial \Psi}{\partial R} \right)_n dR}{\int_{R,w}^{R,e} \left( \frac{\partial \Psi}{\partial R} \right)_n dR} \cong \frac{\int_{R,w}^{R,e} \Phi_n \left( \frac{\partial \Psi}{\partial R} \right)_n dR}{(\Psi_{ne} - \Psi_{nw})}, \quad (4.55)$$

then

$$\int_{R,w}^{R,e} \Phi_n \left( \frac{\partial \Psi}{\partial R} \right)_n dR = \bar{\Phi}_n (\Psi_{ne} - \Psi_{nw}), \quad \int_{R,w}^{R,e} \Phi_s \left( \frac{\partial \Psi}{\partial R} \right)_s dR = \bar{\Phi}_s (\Psi_{se} - \Psi_{sw}), \quad (4.56a \text{ and } b)$$

$$\int_{Z,s}^{Z,n} \Phi_e \left( \frac{\partial \Psi}{\partial Z} \right)_e dZ = \bar{\Phi}_e (\Psi_{ne} - \Psi_{se}) \text{ and } \int_{Z,s}^{Z,n} \Phi_w \left( \frac{\partial \Psi}{\partial Z} \right)_w dZ = \bar{\Phi}_w (\Psi_{nw} - \Psi_{sw}). \quad (4.56c \text{ and } d)$$

The next task is to express  $\bar{\Phi}$  and  $\Psi$  in term of values at the nodes of the grid. To do this, three assumptions are made. First, it is assumed that  $\Phi$  is uniform within each control volume, and has the value which prevails at the particular node which the control volume encloses. The second assumption is that  $\bar{\Phi}_n$  (for example) takes on the  $\Phi$  value possessed by the fluid upstream of the n-face of the control volume in Fig. 4.2, which implies

$$\bar{\Phi}_n = \Phi_P, \quad \text{if } \Psi_{ne} - \Psi_{nw} > 0 \quad (4.57a)$$

$$\bar{\Phi}_n = \Phi_N, \quad \text{if } \Psi_{ne} - \Psi_{nw} < 0 \quad (4.57b)$$

In other words, if the direction of flow is from P to N (i.e.,  $\Psi_{ne} - \Psi_{nw}$  is positive),  $\bar{\Phi}_n$

must be equal to  $\Phi_P$ . If the direction of flow is from N to P (i.e.,  $\Psi_{ne} - \Psi_{nw}$  is negative),  $\bar{\Phi}_n$  must be equal to  $\Phi_N$ .

In terms of mathematical expression, the above argument can be written as

$$I_1 = \Phi_N \left[ \frac{(\Psi_{ne} - \Psi_{nw}) - |\Psi_{ne} - \Psi_{nw}|}{2} \right] + \Phi_P \left[ \frac{(\Psi_{ne} - \Psi_{nw}) + |\Psi_{ne} - \Psi_{nw}|}{2} \right]. \quad (4.58)$$

The third assumption is that the value of the stream function at a particular corner of the control volume is equal to the average value of the four neighboring nodes, then

$$\Psi_{ne} \approx \frac{\Psi_{NE} + \Psi_E + \Psi_P + \Psi_N}{4} \quad \text{and} \quad \Psi_{nw} \approx \frac{\Psi_{NW} + \Psi_W + \Psi_P + \Psi_N}{4}. \quad (4.59)$$

Similar expression can be obtained for all the other terms in Eq. (4.54). Adding them together, the sum of the integrals for all the convective terms gives

$$I_{\text{conv}} = A_E(\Phi_P - \Phi_E) + A_W(\Phi_P - \Phi_W) + A_N(\Phi_P - \Phi_N) + A_S(\Phi_P - \Phi_S) \quad (4.60)$$

where

$$A_E = \frac{1}{8} \left[ (\Psi_N + \Psi_{NE} - \Psi_{SE} - \Psi_S) + |\Psi_N + \Psi_{NE} - \Psi_{SE} - \Psi_S| \right] \quad (4.61a)$$

$$A_W = \frac{1}{8} \left[ (\Psi_S + \Psi_{SW} - \Psi_{NW} - \Psi_N) + |\Psi_S + \Psi_{SW} - \Psi_{NW} - \Psi_N| \right] \quad (4.61b)$$

$$A_N = \frac{1}{8} \left[ (\Psi_W + \Psi_{NW} - \Psi_{NE} - \Psi_E) + |\Psi_W + \Psi_{NW} - \Psi_{NE} - \Psi_E| \right] \quad (4.61c)$$

$$A_S = \frac{1}{8} \left[ (\Psi_E + \Psi_{SE} - \Psi_{SW} - \Psi_W) + |\Psi_E + \Psi_{SE} - \Psi_{SW} - \Psi_W| \right]. \quad (4.61d)$$

It is observed that the A's can never be negative, although they may be equal to zero. In fact, this is one of the features, which enables a converged solution to be obtained.

### 4.4.3 Finite Difference Equations in the Fluid Region

The integration of diffusion term in Eqs. (4.45) and (4.46) over the control volume is performed in the same way. All these lead to a successive substitution formula for the momentum equation as

$$\Omega'_P{}^{n+1} = \frac{4\Delta\tau}{R_P(R_E - R_W)(Z_N - Z_S)} \left[ C_E \Omega'_E{}^n + C_W \Omega'_W{}^n + C_N \Omega'_N{}^n + C_S \Omega'_S{}^n - C_P \Omega'_P{}^n + S_P \right] + \Omega'_P{}^n, \quad (4.62)$$

where

$$C_E = A_E + \frac{1}{Re} R_E^2 B_E, \quad (4.63a)$$

$$C_W = A_W + \frac{1}{Re} R_W^2 B_W, \quad (4.63b)$$

$$C_N = A_N + \frac{1}{Re} B_N, \quad (4.63c)$$

$$C_S = A_S + \frac{1}{Re} B_S, \quad (4.63d)$$

$$C_P = (A_E + A_W + A_N + A_S) + \frac{1}{Re} (R_P^2 B_E + R_P^2 B_W + B_N + B_S), \quad (4.63e)$$

$$B_E = \frac{1}{2(R_P + \Delta R/2)} \left( \frac{Z_N - Z_S}{R_E - R_P} \right), \quad (4.63f)$$

$$B_W = \frac{1}{2(R_P - \Delta R/2)} \left( \frac{Z_N - Z_S}{R_P - R_W} \right), \quad (4.63g)$$

$$B_N = \frac{R_P}{2} \left( \frac{R_E - R_W}{Z_N - Z_P} \right), \quad (4.63h)$$

$$B_S = \frac{R_P}{2} \left( \frac{R_E - R_W}{Z_P - Z_S} \right), \quad (4.63i)$$

$$S_P = -\frac{1}{4} \frac{Gr}{Re^2} \left( \frac{\partial \theta}{\partial R} \right)_P (R_E - R_W)(Z_N - Z_S), \quad (4.63j)$$

$$\left( \frac{\partial \theta}{\partial R} \right)_P = \frac{(\theta_E - \theta_P) \left( \frac{R_P - R_W}{R_E - R_P} \right) + (\theta_P - \theta_W) \left( \frac{R_E - R_P}{R_P - R_W} \right)}{R_E - R_W} \quad (4.63k)$$

and the energy equation as

$$\theta_P^{n+1} = \frac{4\Delta\tau}{R_P(R_E - R_W)(Z_N - Z_S)} \left[ C_E \theta_E^n + C_W \theta_W^n + C_N \theta_N^n + C_S \theta_S^n - \Sigma C \theta_P^n \right] + \theta_P^n, \quad (4.64)$$

where

$$C_E = A_E + \frac{1}{Pe} B_E, \quad (4.65a)$$

$$C_W = A_W + \frac{1}{Pe} B_W, \quad (4.65b)$$

$$C_N = A_N + \frac{1}{Pe} B_N, \quad (4.65c)$$

$$C_S = A_S + \frac{1}{Pe} B_S, \quad (4.65d)$$

$$B_E = \frac{R_E + R_P}{4} \left( \frac{Z_N - Z_S}{R_E - R_P} \right), \quad (4.65e)$$

$$B_W = \frac{R_W + R_P}{4} \left( \frac{Z_N - Z_S}{R_P - R_W} \right), \quad (4.65f)$$

$$B_N = \frac{R_P}{2} \left( \frac{R_E - R_W}{Z_N - Z_P} \right), \quad (4.65g)$$

$$B_s = \frac{R_p}{2} \left( \frac{R_E - R_W}{Z_p - Z_s} \right), \quad (4.65h)$$

$$\Sigma C = C_E + C_W + C_N + C_S. \quad (4.65i)$$

The governing equation for vorticity at the center line is derived using the same procedure as before. The dimensionless velocity  $U$  in Eq. (4.39) can be written in terms of the dimensionless stream function and by taking the limit  $\Delta R \rightarrow 0$  to avoid singularity at the centerline, which gives

$$U_c = \lim_{R \rightarrow 0} \frac{1}{R} \frac{\partial \Psi}{\partial R} = \lim_{R \rightarrow 0} \frac{\frac{\partial \Psi}{\partial R}}{R} = \frac{\frac{\partial^2 \Psi}{\partial R^2}}{\frac{\partial R}{\partial R}} = \frac{\partial^2 \Psi}{\partial R^2} = \frac{\partial}{\partial R} (\partial \Psi) = 2 \left( \frac{\partial \Psi}{R^2} \right)_c = \frac{2\Psi_E}{R_E^2}. \quad (4.66)$$

By doing so, the successive substitution formula for  $\Omega'$  is obtained as follows

$$\Omega_P'^{n+1} = \frac{4\Delta\tau}{(R_E - R_W)(Z_N - Z_S)} [C_E \Omega_E'^n + C_N \Omega_N'^n + C_S \Omega_S'^n - \Sigma C \Omega_P'^n + S_{PC}] + \Omega_P'^n, \quad (4.67)$$

where

$$C_E = \frac{4}{\text{Re}} \left( \frac{Z_N - Z_S}{R_E - R_P} \right), \quad (4.68a)$$

$$C_N = \frac{1}{\text{Re}} \left( \frac{R_E}{Z_N - Z_P} \right) - \frac{2\Psi_E}{R_E}, \quad (4.68b)$$

$$C_S = \frac{1}{\text{Re}} \left( \frac{R_E}{Z_P - Z_S} \right) + \frac{2\Psi_E}{R_E}, \quad (4.67c)$$

$$\Sigma C = C_E + C_N + C_S, \quad (4.68d)$$

$$S_{PC} = -\frac{\text{Gr}}{\text{Re}^2} (\theta_E - \theta_P) \left( \frac{Z_N - Z_S}{R_E - R_P} \right). \quad (4.68e)$$

#### 4.4.4 Finite Difference Equations in the Porous Region

The governing equations for the porous region are transformed into finite difference equations using the same procedure outlined earlier. The momentum equation (Eq. (4.27)) and the energy equation Eq. (4.28) are integrated over a control volume and they are given respectively by,

$$\int_{Z_s}^{Z_n} \int_{R_w}^{R_e} \left\{ \frac{\partial}{\partial Z} \left( \frac{1}{R} \frac{\partial \Psi}{\partial Z} \right) + \frac{\partial}{\partial R} \left( \frac{1}{R} \frac{\partial \Psi}{\partial R} \right) - \frac{Ra'}{Pe'} \frac{\partial \theta}{\partial R} \right\} dR dZ = 0, \quad (4.69)$$

$$\int_{Z_s}^{Z_n} \int_{R_w}^{R_e} \left\{ \sigma R \frac{\partial \theta}{\partial \tau} + \left[ \frac{\partial}{\partial Z} \left( \theta \frac{\partial \Psi}{\partial R} \right) - \frac{\partial}{\partial R} \left( \theta \frac{\partial \Psi}{\partial Z} \right) \right] - \frac{1}{Pe} \left[ \frac{\partial}{\partial Z} \left( R \frac{\partial \theta}{\partial Z} \right) + \frac{\partial}{\partial R} \left( R \frac{\partial \theta}{\partial R} \right) \right] \right\} dR dZ = 0. \quad (4.70)$$

The successive substitution formula for Eq. (4.69) is given by:

$$\Psi_{PP} = C_{EP} \Psi_E + C_{WP} \Psi_W + C_{NP} \Psi_N + C_{SP} \Psi_S + S_{PP}, \quad (4.71)$$

where the coefficient of C's are redefined as;

$$C_{EP}' = \frac{C_{EP}'}{\Sigma C_P}, \quad C_{WP}' = \frac{C_{WP}'}{\Sigma C_P}, \quad C_{NP}' = \frac{C_{NP}'}{\Sigma C_P}, \quad C_{SP}' = \frac{C_{SP}'}{\Sigma C_P}, \quad S_{PP}' = \frac{S_{PP}'}{\Sigma C_P}, \quad (4.72a)$$

$$C_{EP}' = \frac{1}{2(R_p + \Delta R/2)} \left( \frac{Z_N - Z_S}{R_E - R_P} \right), \quad (4.72b)$$

$$C_{WP}' = \frac{1}{2(R_p - \Delta R/2)} \left( \frac{Z_N - Z_S}{R_P - R_W} \right), \quad (4.72c)$$

$$C_{NP}' = \frac{K_z}{K_r} \frac{1}{2R_p} \left( \frac{R_E - R_W}{Z_N - Z_P} \right), \quad (4.72d)$$

$$C_{SP}' = \frac{K_z}{K_r} \frac{1}{2R_p} \left( \frac{R_E - R_W}{Z_P - Z_S} \right), \quad (4.72e)$$

the source term in Eq. (4.76) is defined as

$$S_{PP} = -\frac{1}{4} \frac{Ra'}{Pe'} \left( \frac{\partial \theta}{\partial R} \right)_P^n (R_E - R_W)(Z_N - Z_S) \Sigma C_P, \quad (4.72f)$$

where

$$\Sigma C_P = C_{EP}' + C_{WP}' + C_{NP}' + C_{SP}'. \quad (4.72g)$$

The successive substitution formula for Eq. (4.70) is obtained as

$$\theta_P^{n+1} = \frac{4\Delta\tau}{\sigma R_p (R_E - R_W)(Z_N - Z_S)} \left[ C_E \theta_E^n + C_W \theta_W^n + C_N \theta_N^n + C_S \theta_S^n - \Sigma C_P \theta_P^n \right] + \theta_P^n, \quad (4.73)$$

where the coefficients of C's are the same as those in Eqs.(4.68a) through (4.68d) except that the modified Peclet number is defined differently for a porous medium.

#### 4.5 Procedure for Numerical Solution

Using finite difference method, approximate solutions of the governing equations subject to the boundary and interface conditions can be obtained at a finite number of grid points having coordinates  $R = i\Delta R$ ,  $Z = j\Delta Z$  (uniform grid size), and at discrete times  $\tau^n$ , where  $i, j$  and  $n$  are integers. The symbol  $\tau^n$  denote the time level after  $n^{\text{th}}$  time step  $\Delta\tau$ . The values of  $\Psi$ ,  $\theta$ , and  $\Omega'$  at each grid point should be considered as average values over a small volume of fluids surrounding the point. These quantities are assumed known at a time  $\tau^n$ .

The procedure for advancement from time  $\tau^n$  to the new level  $\tau^{n+1} = \tau^n + \Delta\tau$  is as follows:

1. Temperature at all interior points are advanced using Eq. (4.64) and Eq. (4.73) for fluid and porous regions, respectively.
2. Interface conditions are applied in the temperature iteration.
3. Vorticity at all interior points is similarly advance using Eq. (4.62).
4. Stream function at all interior points will be brought up to date with the new vorticity and temperature fields using Eqs. (4.59) and (4.71) for fluid and porous regions, respectively. A technique called Successive Over-Relaxation (SOR) is adopted to accelerate the convergence.
5. Beavers-Joseph interface condition are implemented in the stream function iteration.
6. The vorticity on the solid boundaries is determined from the stream function using Eq. (4.35) and Eq. (4.36).
7. Hydrodynamics and thermal boundary conditions are applied.
8. Update all new quantities of  $\Omega'$  and  $\theta$  in the entire domain before the next time iteration begins.
9. Computation will be terminated if the specific time is reached.

In the present study, the successive over-relaxation (SOR) technique has been employed to obtain the new stream function in step 4. With this technique, the values of  $\Psi$  are calculated in a sequential scanning process. As each grid point is scanned, the corresponding value of that variable is updated. Hence, it always uses the newest value of the variable as soon as they becomes available. This method is known to be the simplest iterative scheme, and it requires less computer storage (Roach(1998)). The stream function iteration is terminated whenever the following condition is satisfied.

$$\max_{i,j} \left| \Psi_P^{S+1} - \Psi_P^S \right| < 0.0001 \quad (4.73)$$

where S is the number of iteration

#### 4.6 Validation of Numerical Code

To validate the numerical code thus developed, it was tested against the results reported for thermal stratification in liquid storage tank with a porous manifold by Yee and Lai (2001). In their study they considered the porous media to be isotropic, however, the present study considered the permeability to be a function of the direction. If the ratio of the permeability in Eq. (4.27) was set to unity (condition of isotropic porous medium), the set of equations derived in Eq. (4.73) for the stream function in the porous region would be similar to those derived in Eq. (4.57) for the fluid region. On that basis, comparison could be made. The fluid was considered initially motionless at a uniform temperature  $T_\infty$ . The tank was charged with hot water until the volume of fluid in the tank is replaced, corresponding to a dimensionless time  $\tau = 90$ . Computations were performed for two cases, with  $Ri = 0.01$  and  $100$  which correspond to  $Ra = 2160$ , and  $2.1 \times 10^{-7}$ , respectively. Due to symmetry, only half of the tank was considered. An excellent agreement was observed when comparing streamline and isotherms obtained from the present study with those given by Yee and Lai (2001) as shown in Figs. 4.3 – 4.6.

The codes were further validated using the mixing tank temperature which is defined as,

$$T_{\text{mix}} = \frac{2\pi(c\rho) \int_0^1 \int_0^r T r dr dz}{\pi r_i^2 (\rho c)}. \quad (4.74)$$

In dimensionless form, it gives

$$\theta_{\text{mix}} = \frac{2r_t \int_0^L \int_0^1 \theta R dR dZ}{1}. \quad (4.75)$$

Figure 4.7 shows the results obtained for the mixing tank temperature plotted against the dimensionless time. The plots were similar to those obtained by Yee and Lai (2001) for the cases with a porous tube ( $Ri = 0.01$ , and  $100$ ) and no heat loss at the wall ( $Bi = 0$ ).

#### 4.7 Results and Discussion

Numerical results for thermal stratification in a liquid storage tank is presented in this section. The aspect ratio ( $l/r_t$ ) of the storage tank considered is 4, which is typical for most HVAC applications. The flow and temperature fields are calculated using the procedures outlined in Section 4.5. First, two cases from the experiments conducted in Chapter 3 will be simulated and the results (temperature profile and the mixing tank temperature) are compared with those obtained in Chapter 3. Next, selected cases would be simulated to examine the degree of stratification produced as a function of the Richardson number.

The results are presented in terms of streamlines and isotherms contour plots. The dashed line in each plot represents the location of the porous tube. The effect of the buoyancy and inertial forces are measured using the dimensionless parameter, Richardson number ( $Ri$ ) defined as  $Gr/Re^2$  (Sliwinski et al. (1978)). Since the emphasis in this study is on the development of stratification, steady solution was not attempted. It is obvious that in the absence of heat loss the steady state solution would exhibit uniform temperature equal to the inlet temperature. Instead, computation was run for a

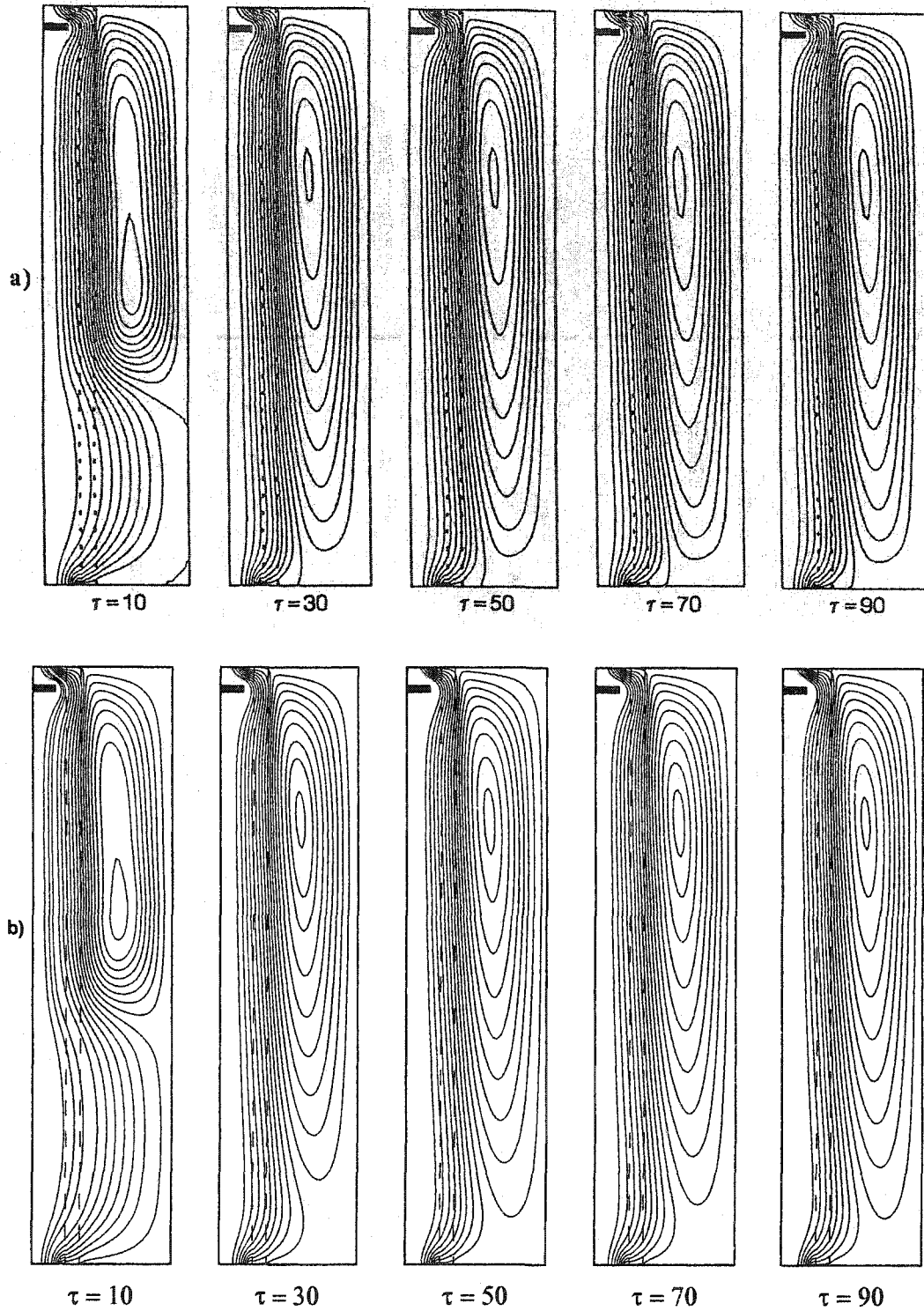


Figure 4.3 Flow fields in a storage tank with a porous manifold at  $Ri = 0.01$ , a) Yee and Lai (2001), b) present study.

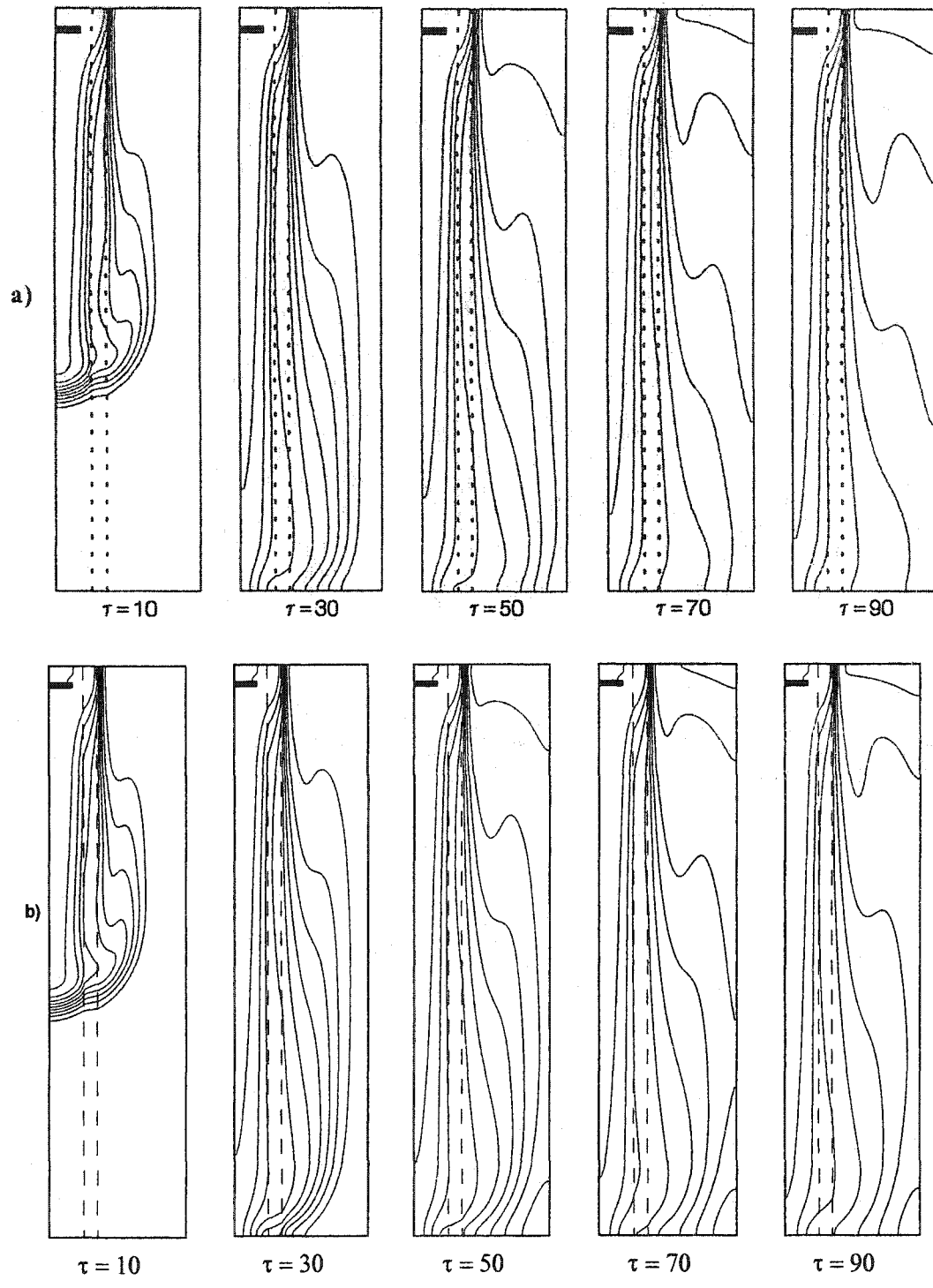


Figure 4.4 Temperature fields in a storage tank with a porous manifold at  $Ri = 0.01$ ,  
 a) Yee and Lai (2001) b) present study.

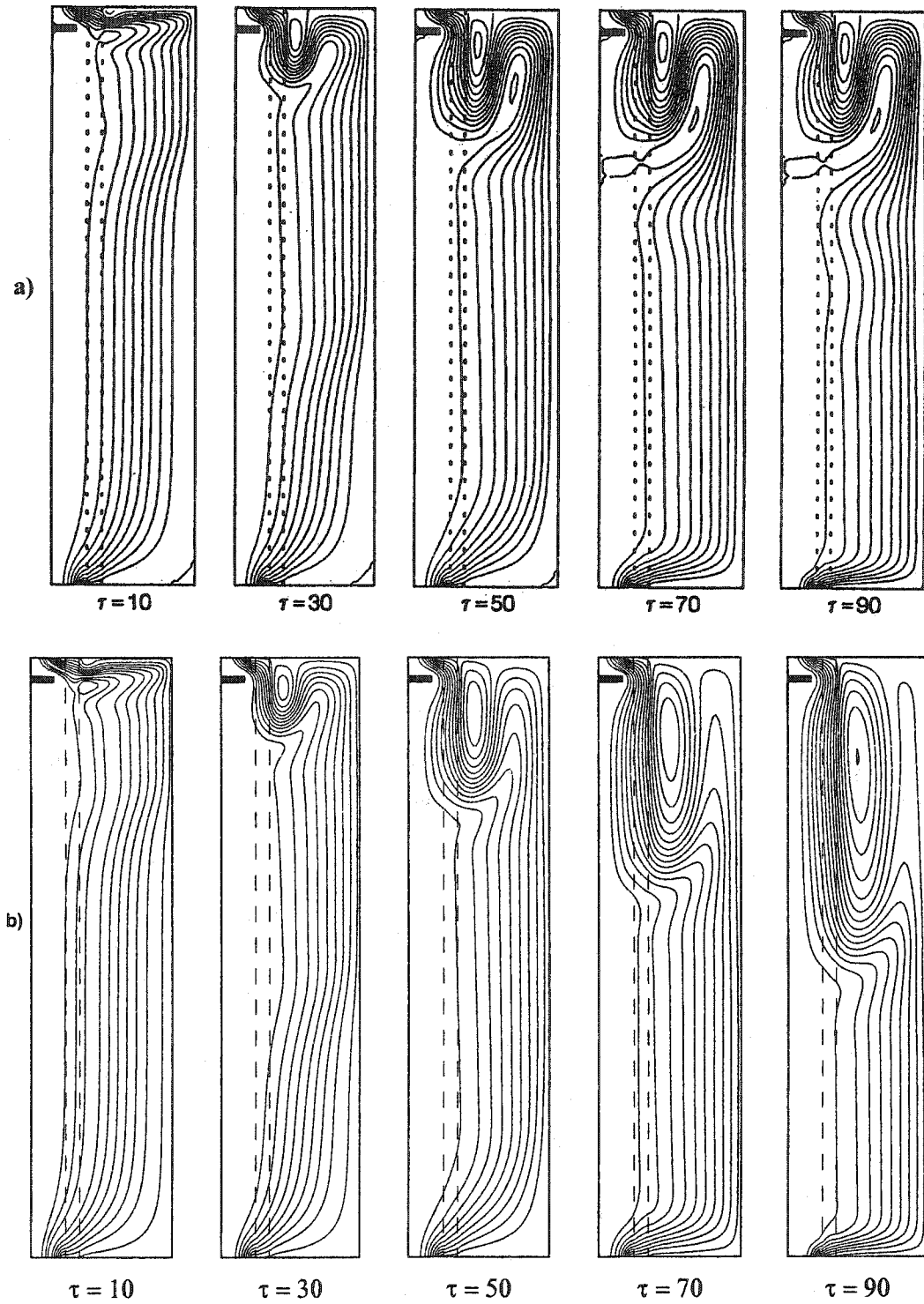


Figure 4.5 Flow fields in a storage tank with a porous manifold at  $Ri = 100$ , a) Yee and Lai (2001), b) present study.

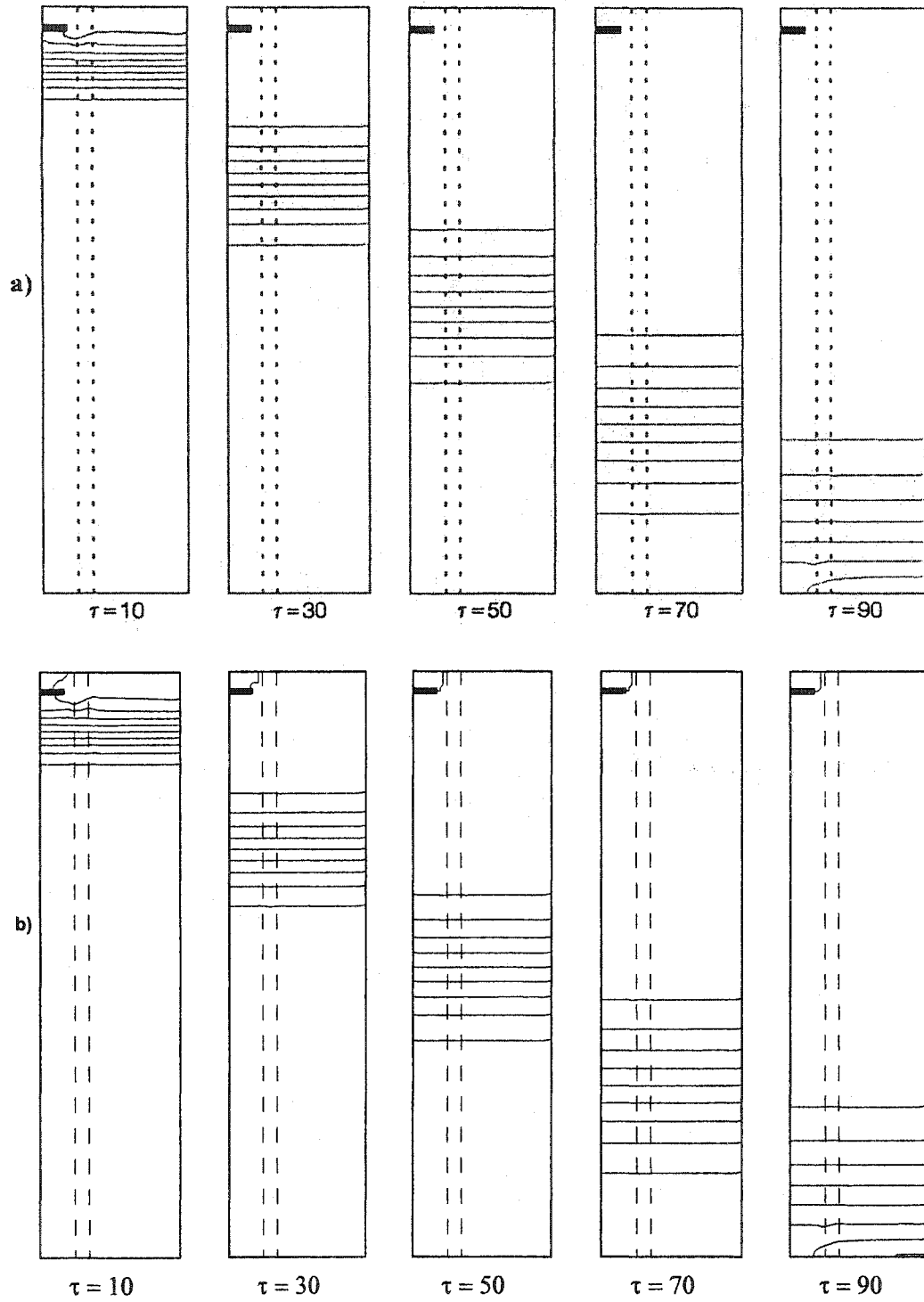


Figure 4.6 Temperature fields in a storage tank with a porous manifold at  $Ri = 100$ ,  
a) Yee and Lai (2001), b) present study.

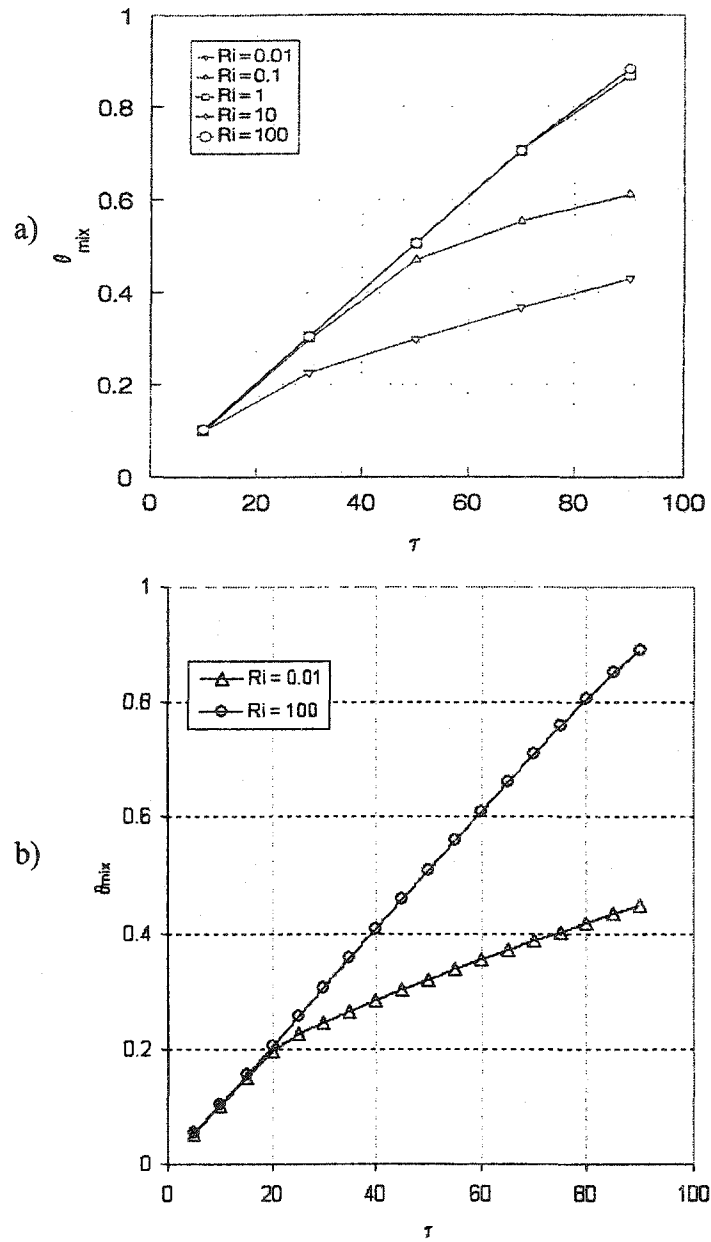


Figure 4.7 Mixing tank temperature in a storage tank with a porous manifold for  $0.01 \leq Ri \leq 100$ , a) Yee and Lai (2001), b) present study

dimensionless time period of 236.5, which was estimated to be the filling time required to replace the entire volume of water in the tank assuming no mixing was invoked.

In the simulation of the real cases, computations were performed for water properties being evaluated at an average temperature between the inlet fluid and the fluid initially in the tank. While in all other cases the fluid properties were calculated at an average water temperature of 30 °C. Solutions were sought for Richardson number varying from 0.018 to 18,518, by varying the Reynolds number and the Rayleigh number. In all calculations a uniform grid of 51 x 201 ( $\Delta R = 0.02$ ) was used. A constant time step of  $\Delta\tau = 1 \times 10^{-4}$  was used for cases of  $Ri \leq 100$ . However, at a higher Richardson number, a smaller time step was used to avoid numerical instability. In some cases the time step was reduced to as low as  $\Delta\tau = 1 \times 10^{-5}$ . For a low Richardson number ( $Ri = 0.018$ ), a typical run would take 14 hour of CPU time on a Dell Dimension Pentium4 (1.7 GHz and 216 MB RAM) personal computer, and up to 48 hour for a higher Richardson number ( $Ri = 18518.1$ ). However, CPU time was reduced to an average of 2 hours for a low Richardson number or a large time step ( $Ri < 100, \Delta\tau = 1 \times 10^{-4}$ ) and 6 hours for a higher Richardson number or smaller time step ( $Ri > 100, \Delta\tau = 1 \times 10^{-5}$ ). When using a supercomputer which consisted of a pool of 135 Pentium4 Xeon DP “Prestonia.” The specification and quantities are presented in Table 4.1.

Ideally, to utilize the capabilities of a supercomputer, the code has to be written in MPI (message passing interface) format. By doing this, one CPU can do instructional level parallelism, where a single processor can do multiple operation at the same time or multiple processing, where multiple CPUs work on different parts of the problem at the same time, resulting in a reduction of computation time. Even though this code was

Table 4.1 Description of OSCER cluster hardware

Item	Description	Quantities
Nodes	Compute	135
	Head	2
	Storage	6
	Fiber Channel connected to FAStT500 disk server	2
	Management (run PBS)	1
CPU's	Pentium4 Xeon DP "Prestonia" 2.0GHz 512 KB L2 cache	
Motherboard/Chipset	Supermicro/Intel 860 Compute nodes w/o SCSI controller Non-Compute nodes w/SCSI controller	1 per node
Main Memory	RDRAM	2 GB per nodes

developed from a serial algorithm, some parts of the numerical solution can be computed simultaneously and independent of each other. The supercomputer cluster was able to exploit these loop holes and provide a reduction in computational time. Each job is submitted to the head computer that passes it on to the management computer that is responsible for distributing the job to free or idle CPU in the pool to help in the computation. It is the management computer's job to watch each job and report when the job is completed.

In all the numerical solutions, the flow in the porous tube was modeled by Darcy's law. As such the inflow velocity or the inlet Reynolds number was set such that the value of  $u_m K_z^{1/2} / \nu$  is less than the order of unity to ensure the validity of Darcy's law. The slip coefficient used in the interface condition, Eq. (4.41), and the permeabilities used in Eq. (4.27) are taken from the experiments conducted in Chapter 2. For the present computations, Darcy number  $Da = (K/r_l)$  is taken to be  $3.516 \times 10^{-7}$  and slip

Table 4.2 Thermophysical properties of water and nylon

Material	Density, $\rho$ (kg/m <sup>3</sup> )	Specific Heat , $c_p$ (J/kg K)	Thermal Conductivity, k (W/m K)
Water	996	4179	0.615
Nylon 6	1140	1700	0.25

coefficient  $\gamma = 0.2$ , which are reasonable values within the Darcy's law range. Since the tank has been insulated with 3-in-thick of R-11 fiberglass insulation, the heat loss from the tank is negligible such that the Biot number in Eq. (4.34) can be assumed zero. The nylon fiber from which the porous tubes was fabricated had a surface porosity of 0.9. As far as the heat capacity and the thermal conductivity of the porous medium is concerned, the porosity is used as a weighting factor Eqs. (4.25) and (4.26). The thermophysical properties of water and nylon calculated at a mean water temperature of 30 °C are given in Table 4.2 (Kakac and Yener (1995)).

A well insulated condition ( $Bi = 0$ ) is considered for all the simulated cases. The incoming flow is delivered through an inlet diffuser, which consists of a 2-in-diameter acrylic pipe with holes drilled in it. These holes are of the same size and are equally spaced around the circumference of the pipe. The water is then allowed to trickle down the wall of a 3-in-diameter acrylic tube before it enters the tank.

#### 4.7.1 Numerical Simulation of Experimental Cases

For comparison, the numerical simulation was conducted using the physical properties of the porous tube that were measured in Chapter 2. The results will serve two purposes. First, the results will indicate if the physical properties of the porous tube are

reasonably close. Secondly, it will show how closely the simulation is able to represent the real case. The comparison will be made using the mixing tank temperature and the temperature profile in the tank.

Figure 4.8 shows the temperature profile in the tank during the numerical simulation and the experiment at two locations; the center of the porous tube (referred to as porous tube) and 12.7 cm from the tank wall (referred to as tank) at the time  $\tau = 142$  for the numerical simulation and  $\tau = 142.5$  for the experiment. A good agreement is found between the temperature profiles obtained from the experiment and the numerical simulation in the porous tube. While the agreement between these two results is not as good in the tank, the largest variation occurs at the location of probe 4. The error at this location was calculated to be 8.29 %, which would be about 2.3 °C, which is larger than our temperature uncertainty. Even though the discrepancy in time is small, the high inlet flow rate over that small time difference may cause an increase in temperature. The trend towards a higher temperature in the porous tube is encouraging because it indicates that the charging process is continuing.

Figure 4.9 shows similar temperature profiles at a later time  $\tau = 236.5$ . The temperature profiles indicate that a better agreement is obtained between the numerical and experiment results. In this case, the maximum error is found at the temperature probe 1.

Figure 4.10 shows the mixing tank temperature as predicted by the numerical simulation and that calculated from the experimental results. Here one observes a good agreement between the two results.

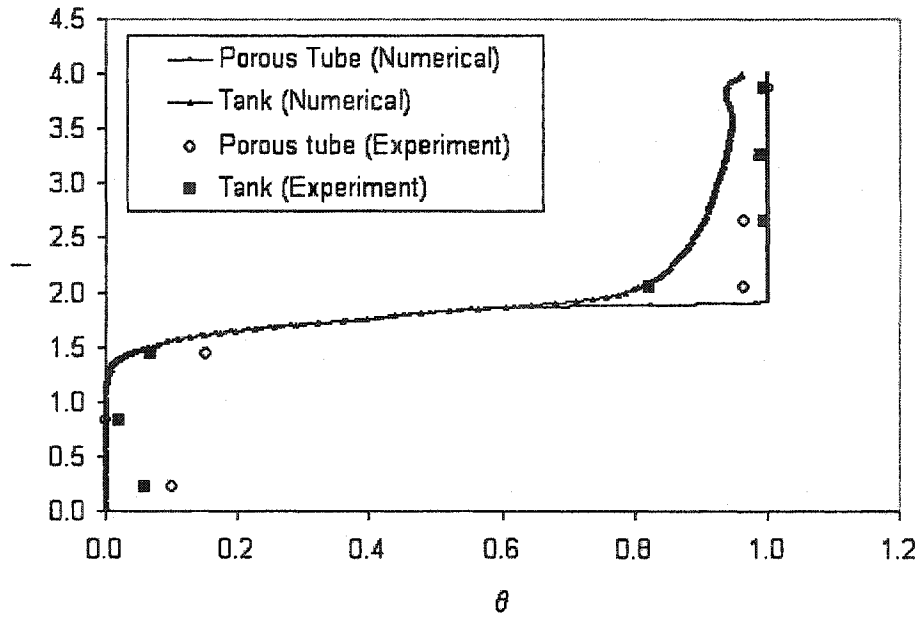


Figure 4.8 Temperature profiles at  $\tau \cong 142$  for an inlet flow at  $T_i = 28.19^\circ\text{C}$  and  $u_i = 0.0315 \text{ m/s}$  ( $Ri = 3.04$ ,  $Re = 10445$  and  $Ra = 2.0 \times 10^9$ )

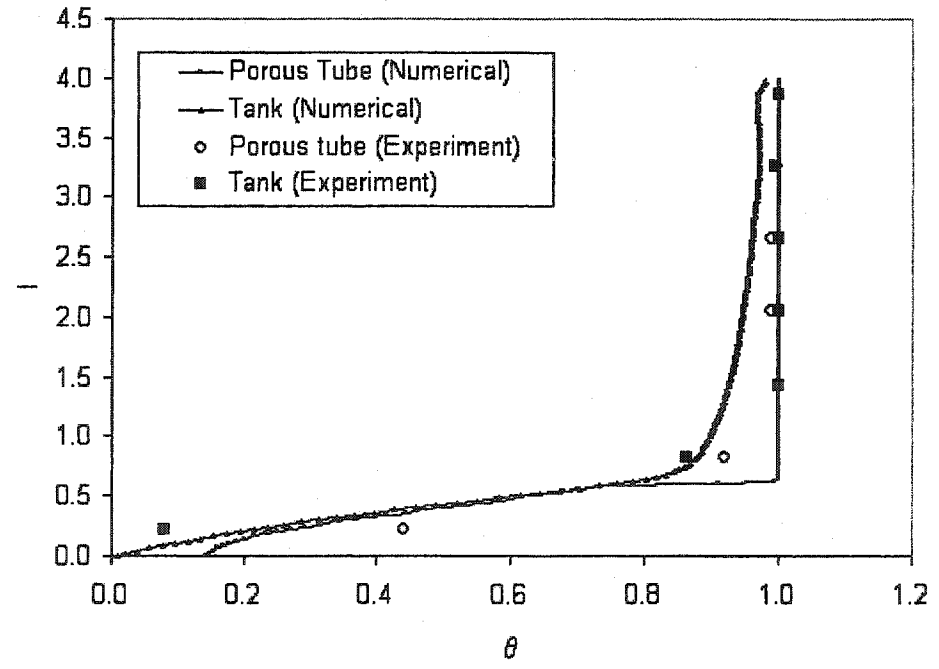


Figure 4.9 Temperature profiles at  $\tau \cong 236.5$  for an inlet flow at  $T_i = 28.19^\circ\text{C}$  and  $u_i = 0.0315 \text{ m/s}$  ( $Ri = 3.04$ ,  $Re = 10445$  and  $Ra = 2.0 \times 10^9$ )

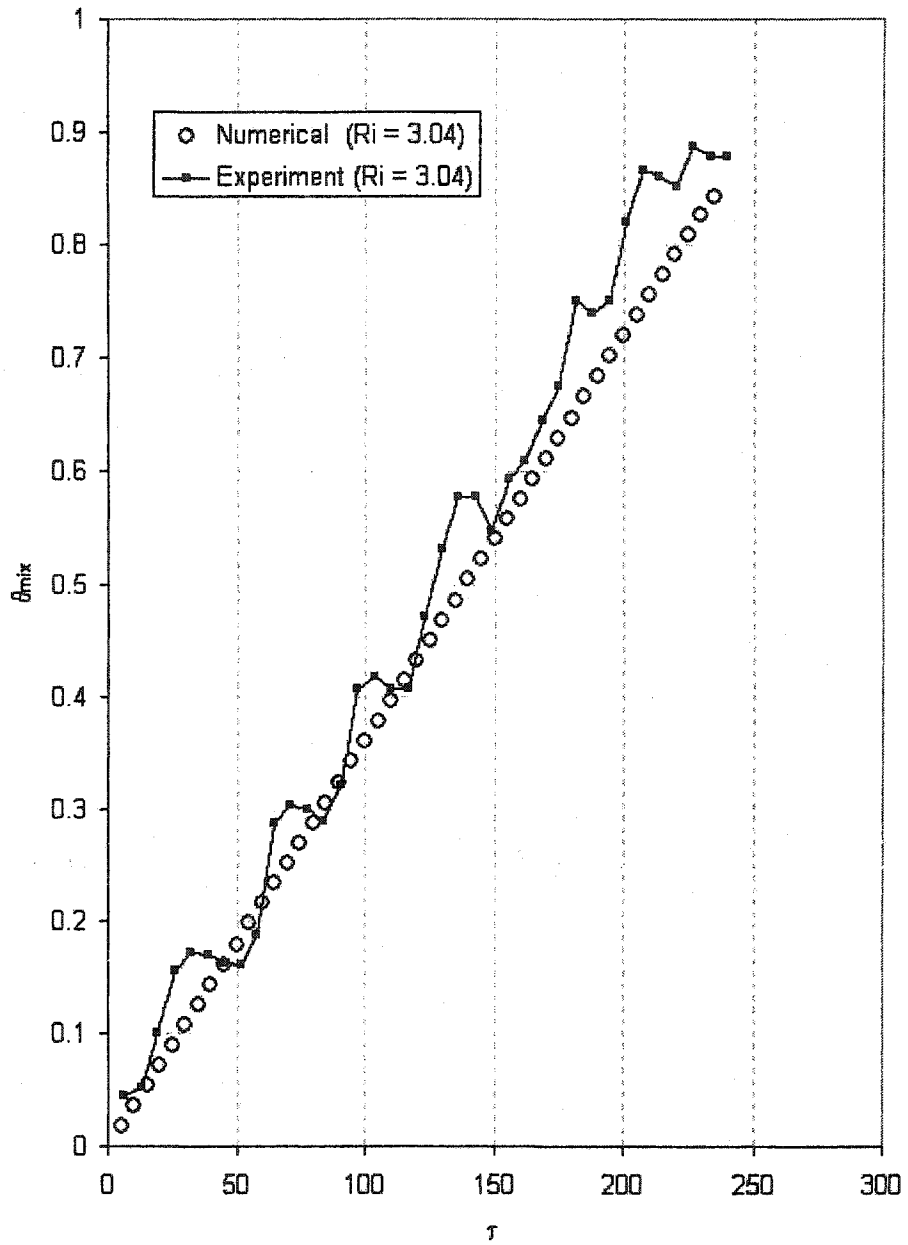


Figure 4.10 Comparison of mixing tank temperatures obtained from the numerical and experimental results for an inlet flow at  $T_i = 28.19^\circ\text{C}$  and  $u_i = 0.0315\text{ m/s}$  ( $Ri = 3.04$ ,  $Re = 10445$  and  $Ra = 2.012 \times 10^9$ )

Similar comparison of the tank temperature profiles and the mixing tank temperature is made for the case of an inlet flow at  $T_i = 29.0\text{ }^{\circ}\text{C}$  and  $u_i = 0.0138\text{ m/s}$  ( $Ri = 12.84$ ,  $Re = 4782.2$  and  $Ra = 2.25 \times 10^9$ ). The tank temperature profiles at  $\tau \cong 142$  and  $\tau \cong 236.5$  are presented in Figs. 4.11 and 4.12, respectively, and the mixing tank temperature is presented in Fig. 4.13. An excellent agreement can be found in the tank temperature between the numerical and the experiment results at  $\tau \cong 142$  (Fig. 4.11). However, the comparison is not so good at  $\tau \cong 236.5$ . Towards the end of the experiment, the tank fluid was heated up rapidly, this increase in the temperature was not detected in the numerical simulation. The warming trend is also observed in the mixing tank temperature. However, an excellent agreement is found between the mixing tank temperatures in Fig. 4.13. Over the charging process, the strength of the buoyancy force is compromised and heat is transferred mainly by diffusion. In general, the comparison between the numerical and experimental results is quite good. The numerical simulation can predict the temperature field in the tank with a reasonable accuracy.

#### **4.7.2 Thermal Stratification in a Liquid Storage Tank**

In order to investigate the effects of various governing parameters on the degree of stratification produced by the new porous manifold that was designed and tested in Chapters two and three, simulations have been conducted for a wide range of governing parameters,  $10^2 \leq Re \leq 10^4$  and  $10^7 \leq Ra \leq 10^9$  ( $0.0185 \leq Ri \leq 18,518$ ). The limiting case of  $Re = 10^4$  represents an operating condition in which the fluid enters the tank with a high flow velocity (i.e., a strong inertial force) as opposed to the case of  $Ra = 10^9$  in which the flow enters the tank at a high temperature with respect to the initial fluid temperature in the tank (i.e., a strong buoyancy force). It should be pointed out that the

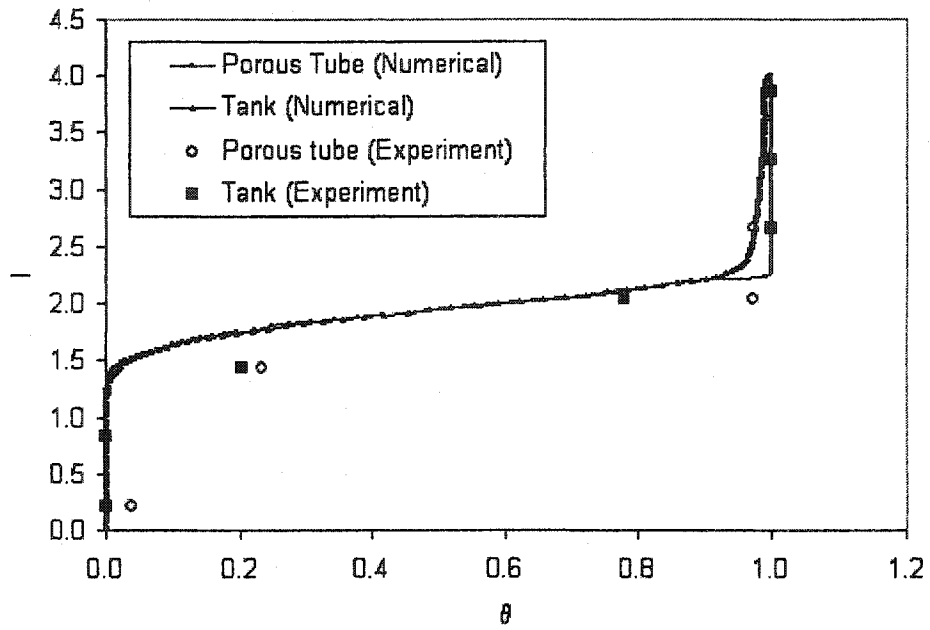


Figure 4.11 Temperature profiles at  $\tau \cong 142$  for an inlet flow at  $T_i = 29.0^\circ\text{C}$  and  $u_i = 0.0138\text{ m/s}$  ( $Ri = 12.84$ ,  $Re = 4782.2$  and  $Ra = 2.25 \times 10^9$ )

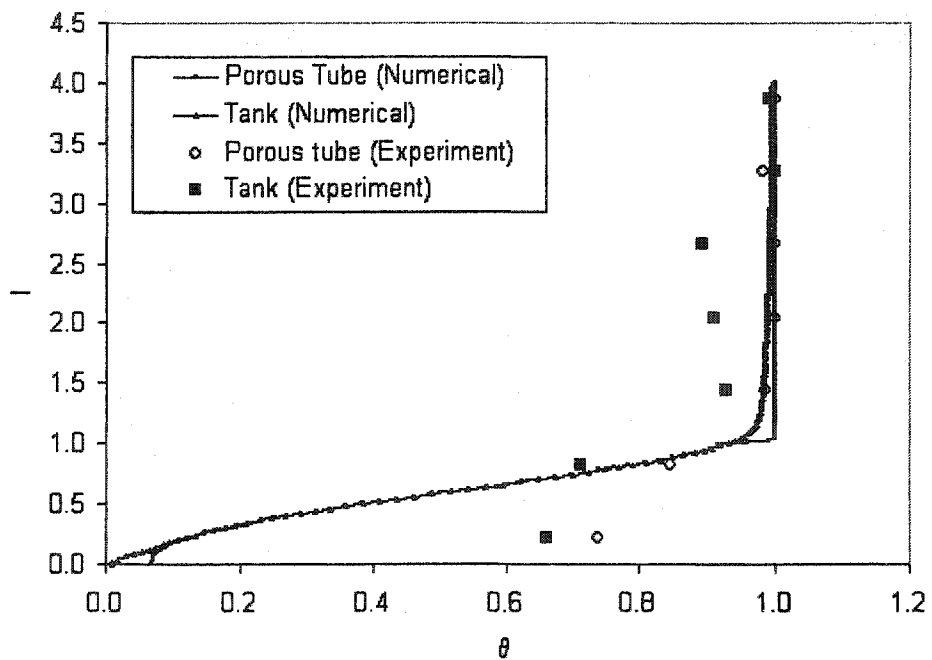


Figure 4.12 Temperature profiles at  $\tau \cong 236.5$  for an inlet flow at  $T_i = 29.0^\circ\text{C}$  and  $u_i = 0.0138\text{ m/s}$  ( $Ri = 12.84$ ,  $Re = 4782.2$  and  $Ra = 2.25 \times 10^9$ )

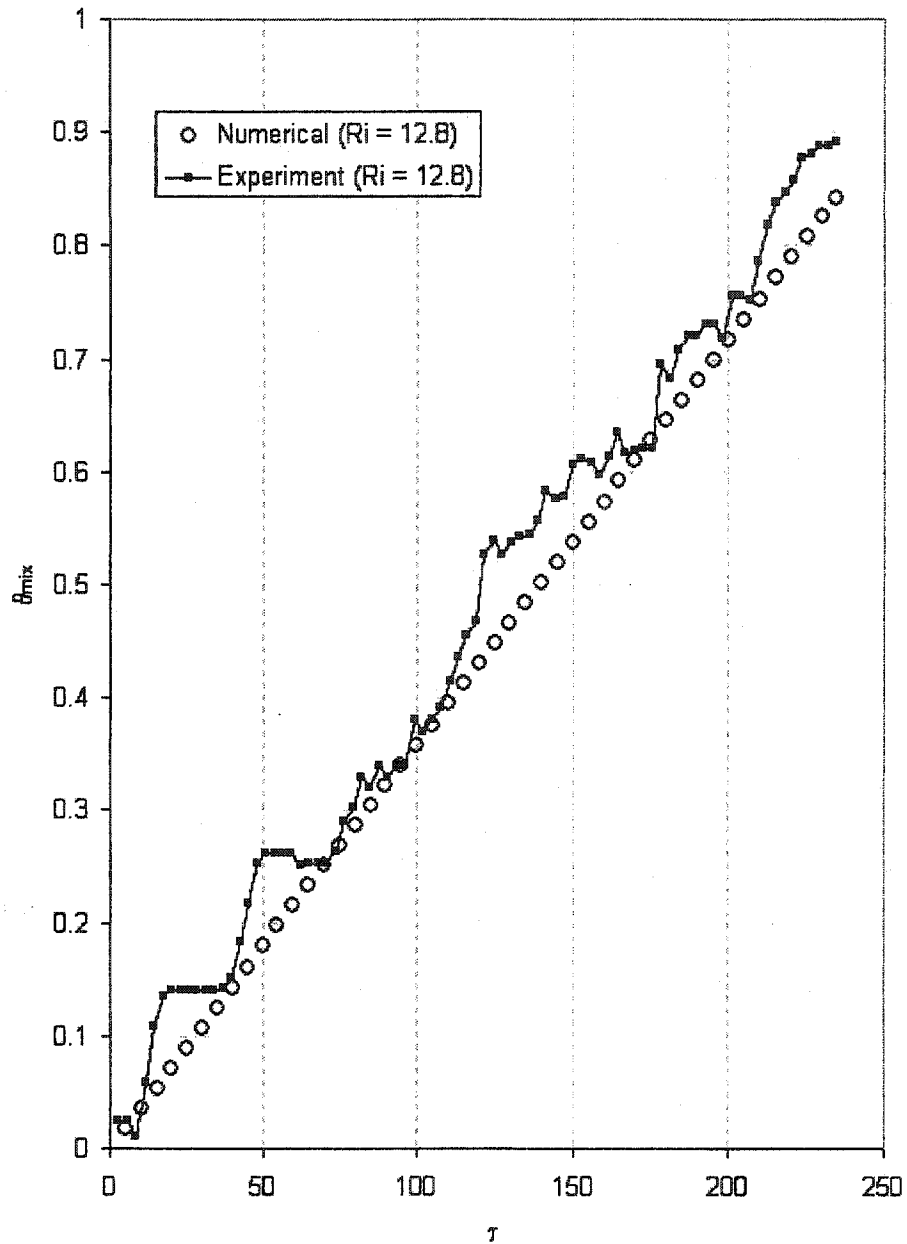


Figure 4.13 Comparison of mixing tank temperatures obtained from the numerical and experimental results for an inlet flow at  $T_i = 29.0\text{ }^{\circ}\text{C}$  and  $u_i = 0.0138\text{ m/s}$  ( $Ri = 12.84$ ,  $Re = 4782.2$  and  $Ra = 2.25 \times 10^9$ ).

Reynolds number used in this study is based entirely on the radius of the tank and not the radius of the inlet manifold. In other words, the flow relative to the inlet manifold is much smaller. Initially the fluid in the tank is at rest and considered to be at a uniform temperature. A well-insulated condition ( $Bi = 0$ ) is considered with flow coming in at the top of the tank and going out from the bottom. The tank is charged with hot water until the entire volume of water in the tank is replaced, assuming no mixing takes place.

**a. The Effects of Richardson Number**

The flow and temperature fields for the case of  $Ri = 0.0185$  ( $Re = 10^4$  and  $Ra = 10^7$ ) are presented in Figs 4.14 and 4.15, respectively. The plots are shown for every 20% of the filling time. Again the dotted line represents the location of the porous manifold. At  $\tau = 47.3$ , notice that the streamlines are parallel in the region of the porous tube between the entrance and exit. This indicates that inertial effects dominate the flow field and most of the hot water charged into the tank is forced out through the exit. Because of the flow entrainment and the constriction at the exit, two re-circulating cells develop in the lower section of the tank, which are responsible for severe mixing in the tank. As time progresses, the re-circulating cell that is close to the tank wall is elongated due to the buoyancy effects. This is a direct consequence of the reduction in buoyancy force resulting from the elevated water temperature in the tank. Notice that by  $\tau \cong 236.5$  the mixing cell has extended the entire length of the tank. From the isotherms (Fig. 4.15), it is observed that the hot water is channeled through the porous tube. Since only a small amount of hot water flows along the bottom of the tank. Notice that the entire upper half of the tank is still filled with cold water when 40% of the charging time has elapsed. Slowly buoyancy force lifts the warm water to the top of the tank, and by the end of the

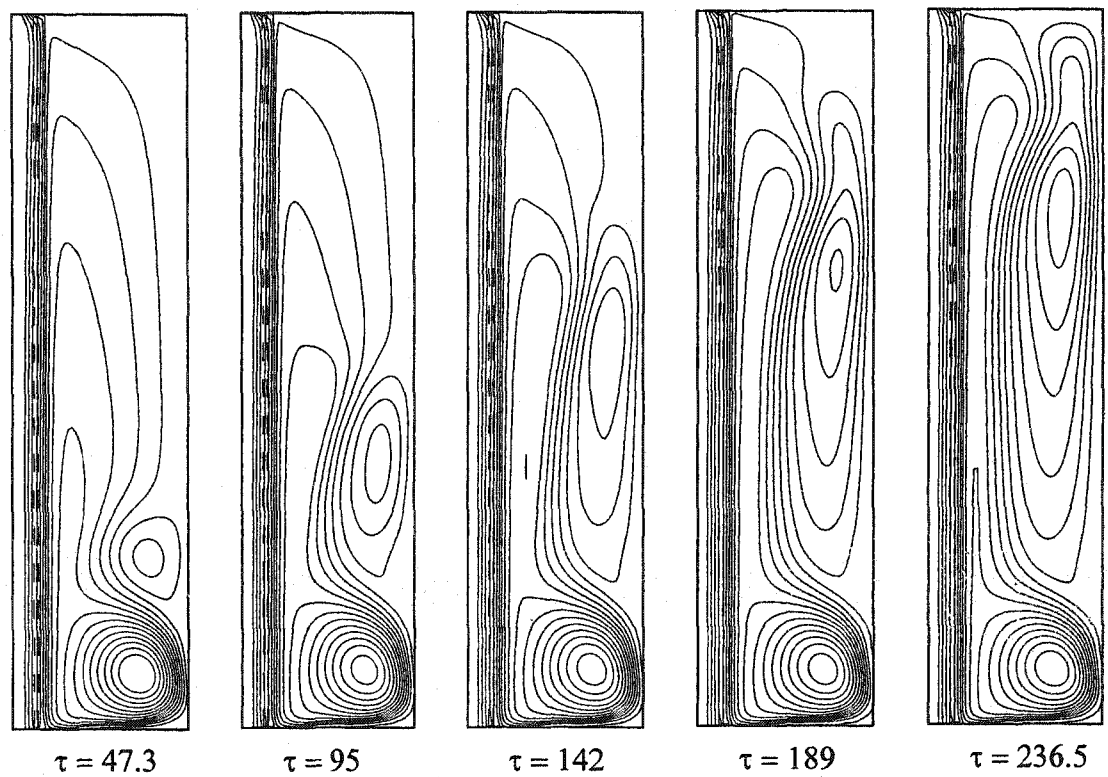


Figure 4.14 Flow fields in a charging process at  $Re = 10^4$  and  $Ra = 10^7$  ( $Ri = 0.0185$ ,  $\Delta\psi = 0.001$ ).

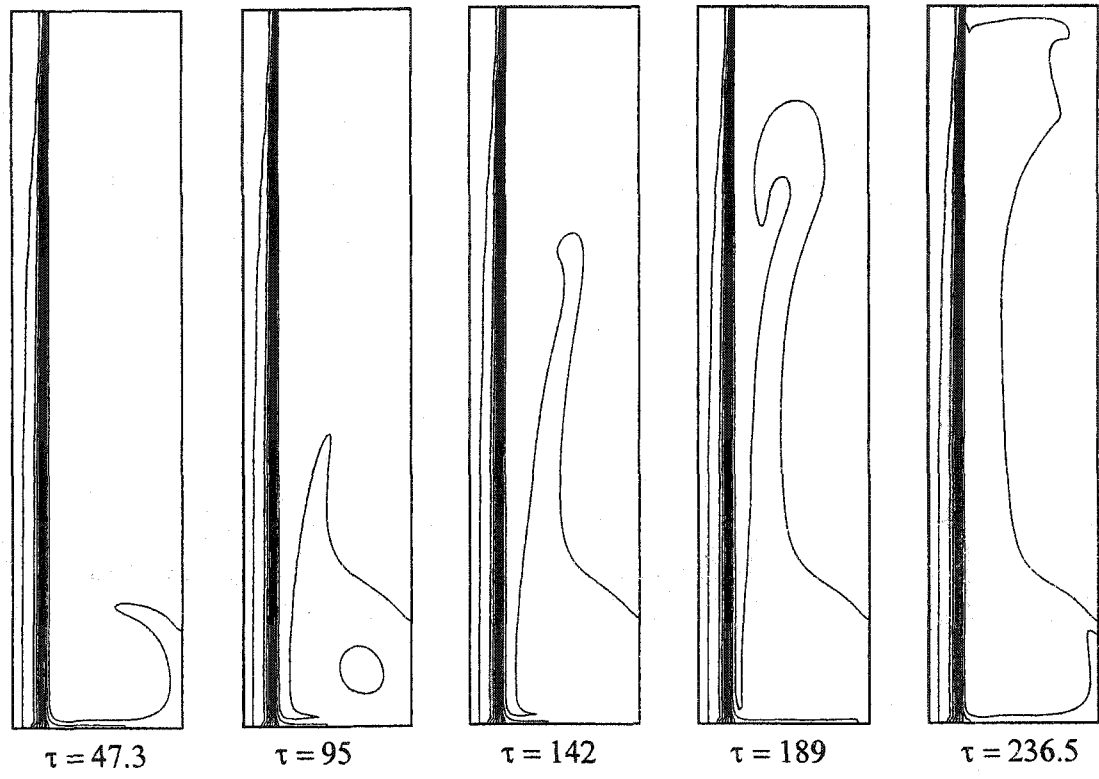


Figure 4.15 Temperature fields in a charging process at  $Re = 10^4$  and  $Ra = 10^7$   
 ( $Ri = 0.0185$ ,  $\Delta\theta = 0.1$ ).

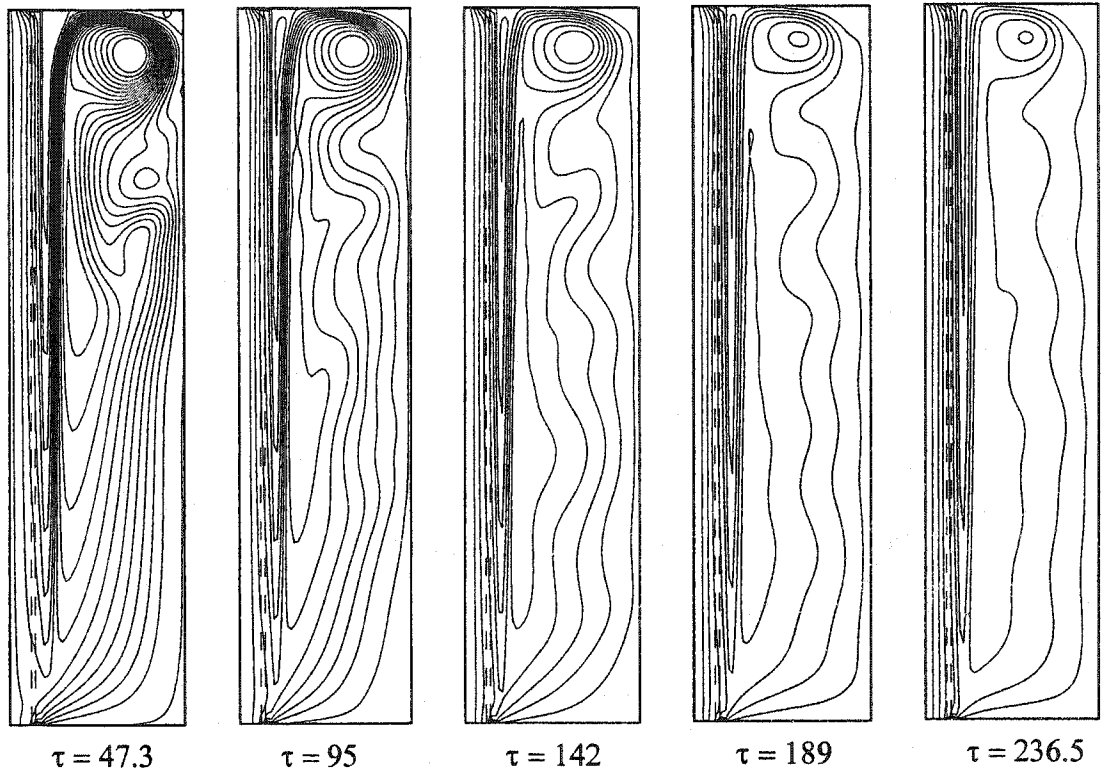


Figure 4.16 Flow fields in a charging process at  $Re = 10^4$  and  $Ra = 10^8$  ( $Ri = 0.185$ ,  $\Delta\psi = 0.001$ ).

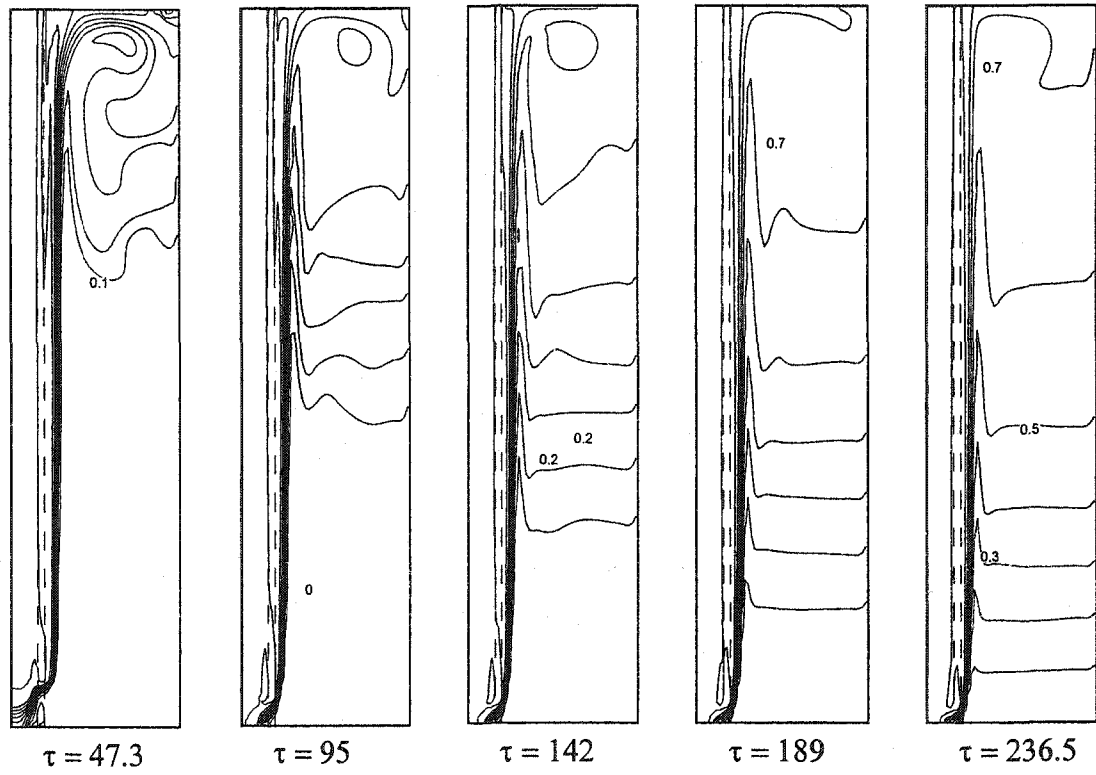


Figure 4.17 Temperature fields in a charging process at  $Re = 10^4$  and  $Ra = 10^8$  ( $Ri = 0.185$ ,  $\Delta\theta = 0.1$ ).

charging process, a large portion of the warm water is trapped between the manifold wall and a cold body of water in the center of the tank.

Flow and temperature fields in a charging process at  $Ri = 0.185$ ,  $Re = 10^4$  and  $Ra = 10^8$  are shown in Figs. 4.16 and 4.17, respectively. A similar trend is observed when the flow field is dominated by the inertial force. Notice that the water charged in the tank is forced all the way to the bottom of the tank before the buoyancy force is able to balance it. Penetration takes place close to the bottom of the tank, where the flow makes a u-turn and moves upward. The dominance of the inertial force can be observed by the concentration of streamlines at the top of the tank, where a strong re-circulating cell is induced adjacent to the top wall of the tank. The flow hits the wall and is forced to turn and flow downwards nearly parallel to the wall. The re-circulating cell first appeared in the tank as early as  $\tau = 47.3$  remains for the rest of the charging process. However, as the buoyancy force reduces over the time more and more of the hot water charged to the tank is allowed to exit the tank without mixing with the tank fluid. The isotherms (Fig. 4.17) show that at  $\tau = 47.3$  there is severe mixing in the upper region of the tank due to the presence of a strong re-circulating cell. However, the effect of the mixing is reduced as time advances. Stratification is seen forming in the mid-section of the tank (as early as  $\tau = 95$ ). The thermocline moves downward with time. Its thickness also increases with time due to the conduction taking place between water layers.

At  $Ri = 1.85$  ( $Re = 10^4$  and  $Ra = 10^9$ ), the buoyancy force is much stronger than the previous cases and the depth at which flow penetration through the porous tube is reduced. From the flow and temperature fields shown in Fig. 4.18 and 4.19, a re-circulating cell is still present in the top position of the tank. However, its effect is much

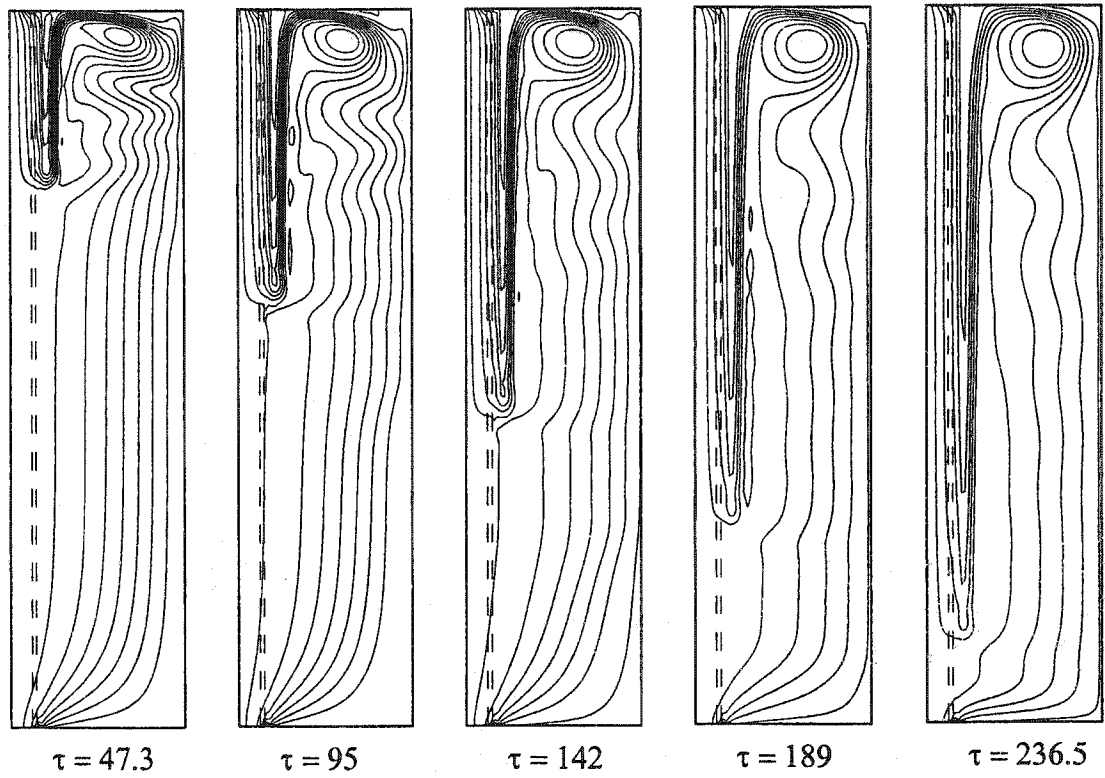


Figure 4.18 Flow fields in a charging process at  $Re = 10^4$  and  $Ra = 10^9$  ( $Ri = 1.85$ ,  $\Delta\psi = 0.001$ ).

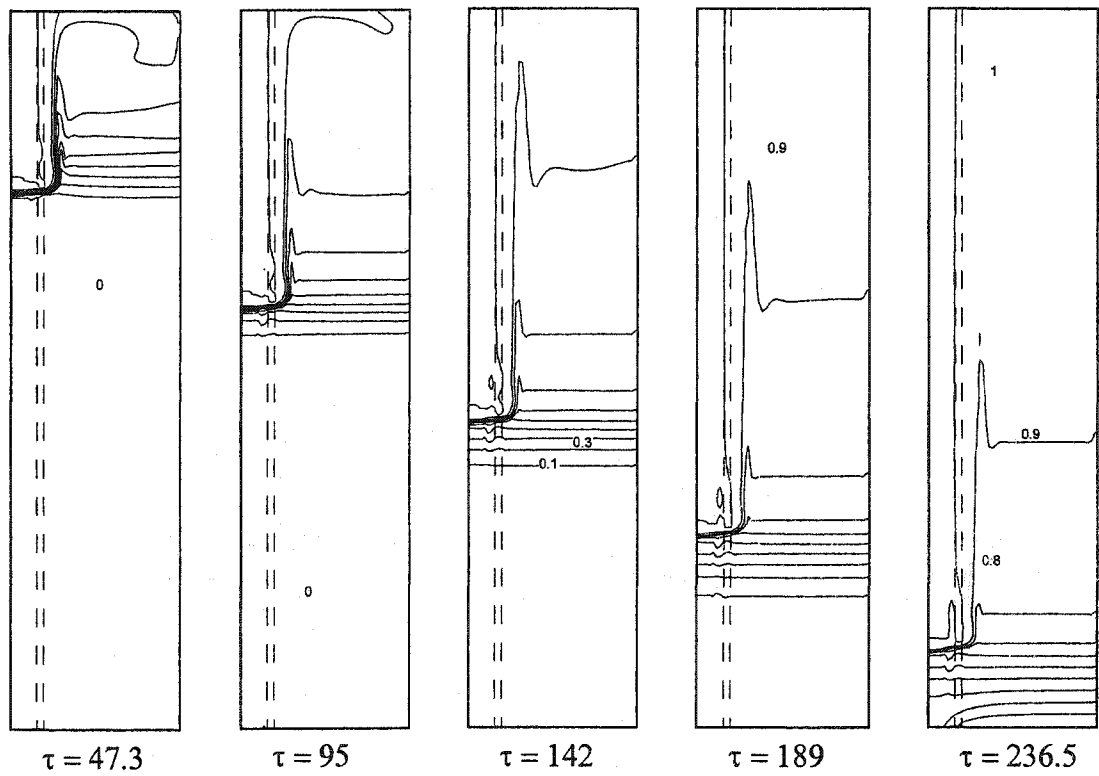


Figure 4.19 Temperature fields in a charging process at  $Re = 10^4$  and  $Ra = 10^9$   
 ( $Ri = 1.85$ ,  $\Delta\theta = 0.1$ ).

compromised due to the increased temperature of the tank water. With the advancement of time, the depth at which the inlet fluid penetrates the porous manifold is increased. The isotherms indicate that the effect of the re-circulating cell is not as destructive to the stratification as in the case of  $Ri = 0.185$ . The tank is stratified as early as  $\tau = 47.3$ . This stratification is maintained for the rest of the charging process.

The trend continues as the Richardson number is increased beyond 1.85. At  $Ri \geq 18.5$ , the flow is completely dominated by the effects of buoyancy. At  $Ri = 185.2$ , the flow is deflected to the top wall as soon as it enters the tank, as observed in the cases of  $Ri \geq 1.85$ . Excellent thermal stratification is maintained in the tank. The thermocline gets thicker over time due to an increase in the heat transfer by diffusion between the hot and cold water. The contour plots for these cases are not shown here but can be found in Appendix C.

The mixing tank temperature is a good indication of the level of stratification in a storage tank. Figure 4.24 shows the mixing tank temperature for various Richardson numbers,  $0.0185 \leq Ri \leq 1.85$  ( $Re = 10^4$  and  $10^7 \leq Ra \leq 10^9$ ) as a function of the filling time. The high inlet velocity associated with the case of  $Ri = 0.0185$  results in most of the inlet flow being discharged from the tank without interacting with the fluid in the tank. As a consequence, the mixing tank temperature is low. As the buoyancy force becomes stronger ( $Ri = 0.185$ ), it is able to balance out the inertial force before the inlet fluid is discharged from the tank. As the warmer fluid rises to the top of the tank, severe mixing occurs, which reduces the mixing tank temperature. With the advancement in time, the severity of the mixing is reduced due to a weaker buoyancy force. However, the mixing tank temperature is also reduced at this time due to the inability of the

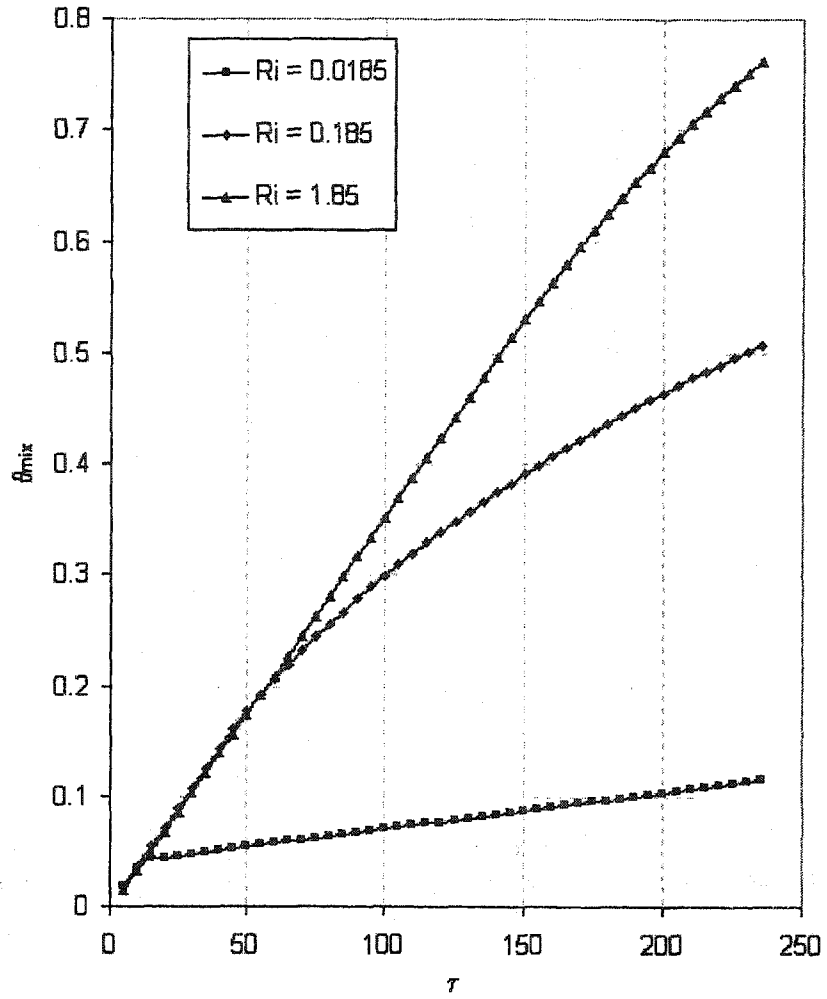


Figure 4.20 Mixing tank temperature as a function of time for various Richardson numbers,  $0.0185 \leq Ri \leq 1.85$ , ( $Re = 10^4$  and  $10^7 \leq Ra \leq 10^9$ ).

buoyancy force to balance the inertial force. As a consequence, more inlet fluid is discharged from the tank. This decrease in the mixing tank temperature is evident from Fig. 4.20, in the reduction of the gradient in a time interval  $50 \leq \tau \leq 100$  for the curve  $Ri = 1.85$ . The stratification which is seen at  $Ri \leq 1$  is confirmed by the high mixing tank temperature.

#### **b. Effects of Reynolds Number**

To evaluate the effects of the Reynolds number on the degree of stratification in the storage tank, one can compare the contour plots of flow and temperature fields at different Reynolds numbers. As the Reynolds number changes, the actual time scale changes in proportion to the ratio of the Reynolds number even though the dimensionless time may remain the same. In this section, a comparison is made for a fixed Rayleigh number at  $Ra = 10^7$  and a range of Reynolds number varying from  $10^2 \leq Re \leq 10^4$  ( $0.0185 \leq Ri \leq 185.2$ ). The flow and temperature fields at  $Re = 100$  ( $Ri = 185.2$ ) are shown in Figs. 4.21 and 4.22 respectively. Notice that the flow and temperature fields are completely dominated by the effects of buoyancy. The flow is deflected to the top wall as soon as it enters the tank. Moreover, the characteristic u-shape flow path associated with a strong buoyancy force becomes almost parallel to the top wall of the tank. As the flow approaches the vertical wall of the tank, it turns and flows downward, parallel to the wall before it exits the tank. As the buoyancy force decreases, the u-shape flow path becomes more visible. A small re-circulating cell is seen at the top of the tank. The linear distribution of the isotherms in Fig. 4.22 indicates that excellent thermal stratification is maintained inside the storage tank. The thermocline becomes thicker with time. As the Reynolds number is increased to  $10^3$  ( $Ri = 1.85$ ), the inertial force

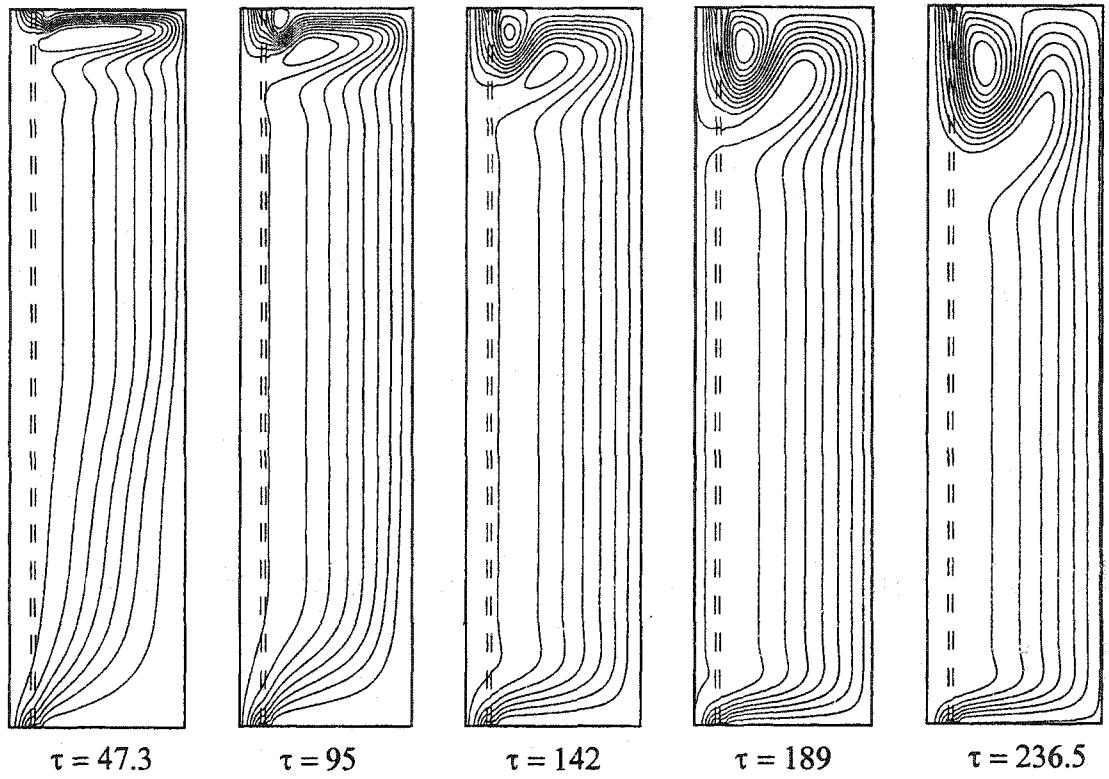


Figure 4.21 Flow fields in a charging process at  $Re = 10^2$  and  $Ra = 10^7$  ( $Ri = 185.2$ ,  $\Delta\psi = 0.001$ ).

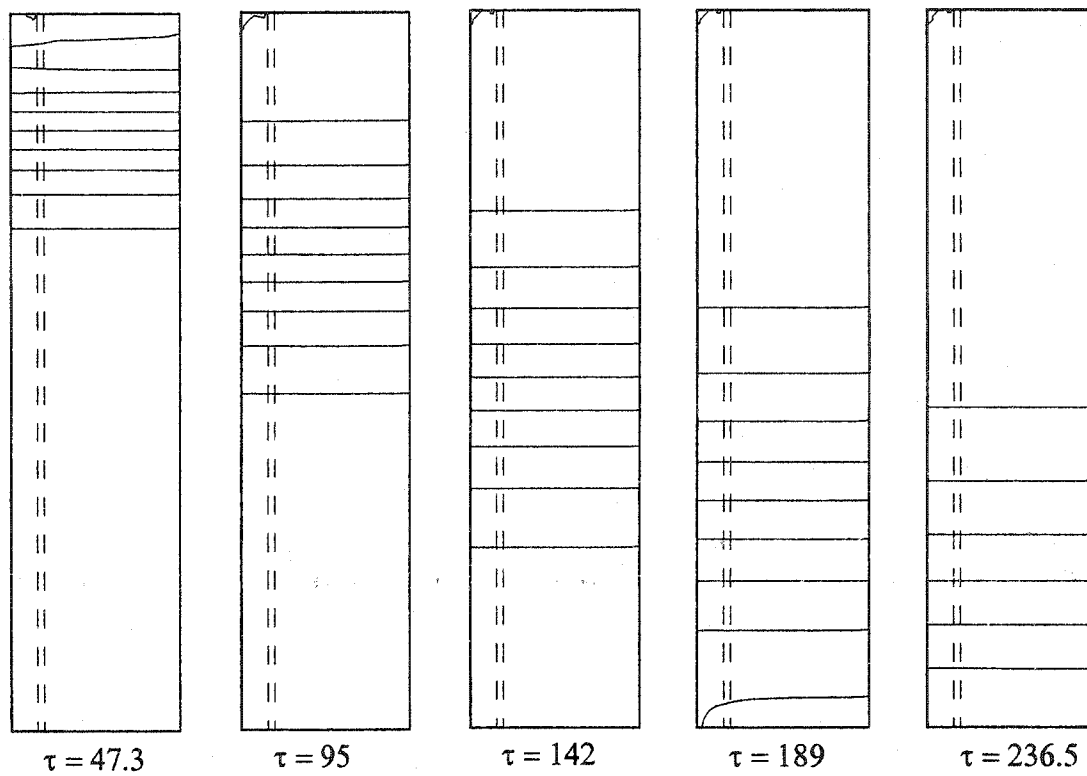


Figure 4.22 Temperature fields in a charging process at  $Re = 10^2$  and  $Ra = 10^7$  ( $Ri = 185.2, \Delta\theta = 0.1$ ).

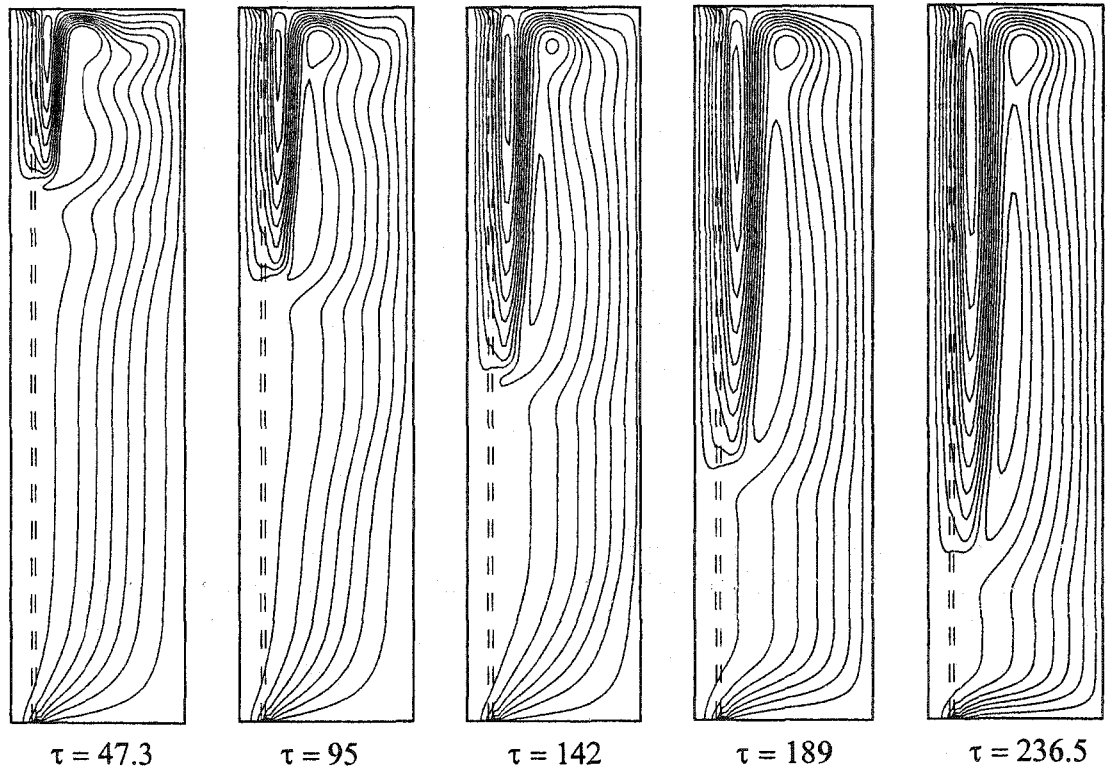


Figure 4.23 Flow fields in a charging process at  $Re = 10^3$  and  $Ra = 10^7$  ( $Ri = 1.85$ ,  $\Delta\psi = 0.001$ ).

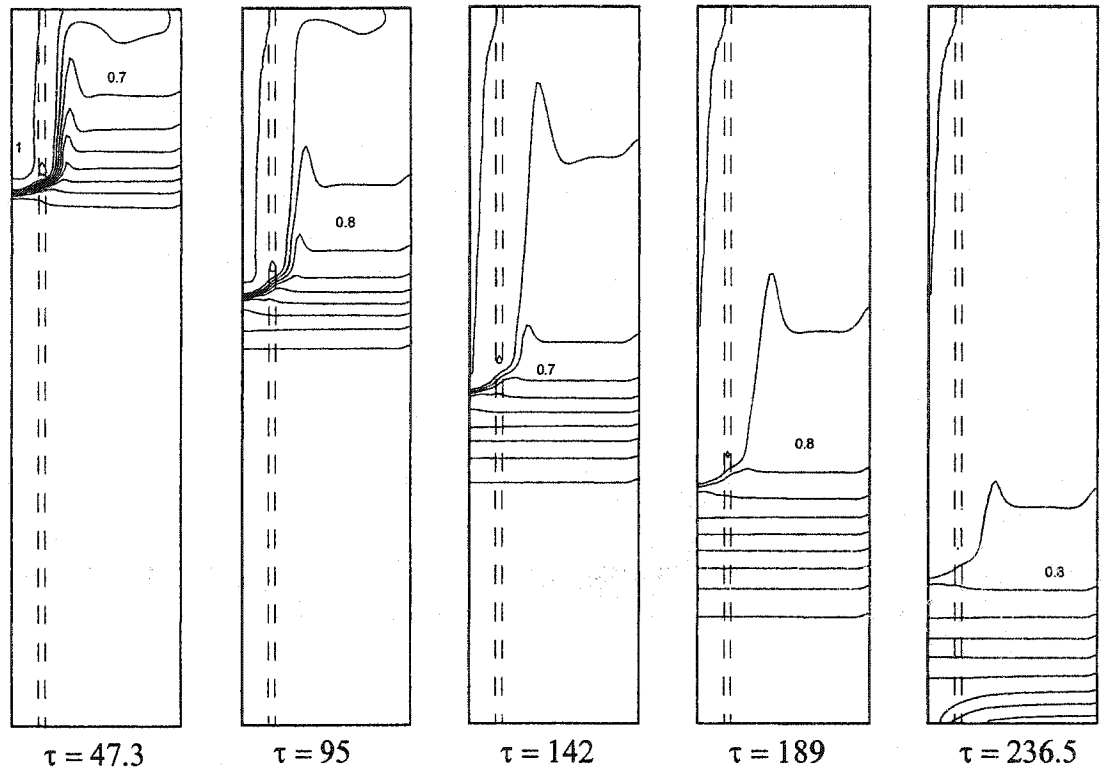


Figure 4.24 Temperature fields in a charging process at  $Re = 10^3$  and  $Ra = 10^7$  ( $Ri = 1.85, \Delta\theta = 0.1$ ).

becomes more important. This is visible from the larger u-shape flow path shown in Fig. 4.23, the depth at which flow penetration occurs also increases as the buoyancy force decreases. A re-circulating cell that is seen at the top of the tank which increases its strength as the time increases. The isotherms in Fig. 4.24 indicate that stratification is maintained in the tank as early as  $\tau = 47.3$ . At  $Re = 10^4$ , the flow field (Fig. 4.14) is totally dominated by inertial force and most of the fluid charged into the tank is forced out of the tank without mixing with the tank fluid. The isotherms (Fig. 4.15) shows that the stratification that was present at  $Re = 10^3$  is totally destroyed.

### c. Effects of Rayleigh Number

The effects of the Rayleigh number on the flow and temperature fields are examined in this section. An increase in the Rayleigh number can be interpreted physically as an increase in the inlet flow temperature. The discussion of the effects of Rayleigh number is focused on the case with a fixed Reynolds number  $Re = 10^3$  and  $10^7 \leq Ra \leq 10^9$  ( $1.85 \leq Ri \leq 185.2$ ). The flow and temperature fields for the  $Ra = 10^7$  are shown in Figs. 4.23 and 4.24, respectively. The streamlines indicate that both inertial and buoyancy forces are important at  $\tau = 47.3$ . The flow that is charged into the tank is able to penetrate the porous manifold at one fourth of the height and is deflected to the top of the tank. The depth at which flow penetration occurs increases as the buoyancy force decreases. From the isotherm, it is clear that thermal stratification is established at an early stage of the charging process. The dominance of the buoyancy force increases with the Rayleigh number and at  $Ra = 10^9$ , buoyancy effects totally dominate the flow and temperature fields as shown in Figs. 4.25 and 4.26, respectively. The flow is deflected to the top wall as soon as it enters the tank. The u-shape flow path stays at the top of the

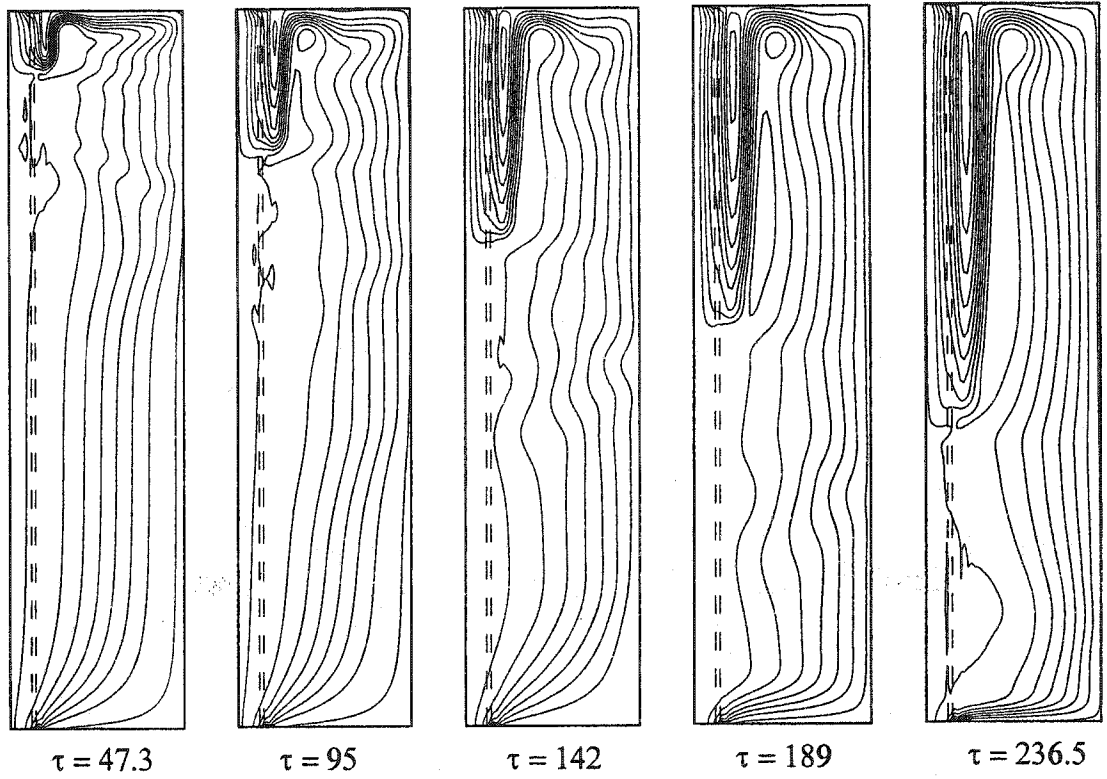


Figure 4.25 Flow fields in a charging process at  $Re = 10^3$  and  $Ra = 10^9$  ( $Ri = 185.2$ ,  $\Delta\psi = 0.001$ ).

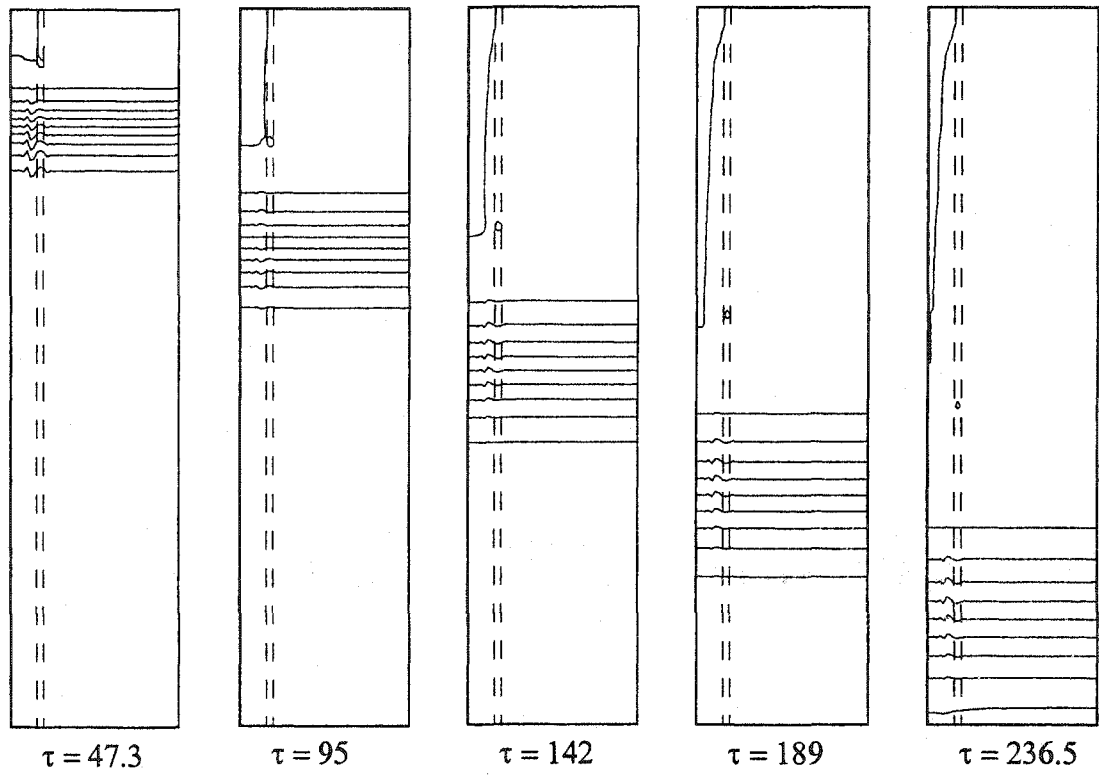


Figure 4.26 Temperature fields in a charging process at  $Re = 10^3$  and  $Ra = 10^9$   
 ( $Ri = 185.2$ ,  $\Delta\theta = 0.1$ ).

tank due to the strong buoyancy effects. The isotherms (Fig. 4.25) indicate an excellent thermal stratification is established in the tank early in the charging process.

#### d. Degree of Stratification

The degree of stratification was evaluated for the cases of  $0.185 \leq Ri \leq 185.2$ . For each case, the temperature profile in the tank (at the mid-section between the porous wall and tank wall) was used to calculate the dimensionless temperature gradient  $(d\theta/dZ)$ . The gradient was divided by the ratio of the maximum dimensionless temperature and the dimensionless height of the tank  $(d\theta_{\max}/L)$ . Figure 4.27 shows the ratio  $(d\theta/dZ)/(d\theta/L)_{\max}$  plotted as a function of the dimensionless filling time. Bear in mind that at a low Richardson number, a stable stratification is not developed until a later time in the charging process. The most interesting feature observed from the figure is the decay of the degree of stratification with time. The figure suggests that the degree of stratification approaches some asymptotic value over time. Notice that the asymptotic value increases with decrease in the inversed Peclet number, independent of the Richardson number. At  $1/Pe = 1.85 \times 10^{-3}$  the degree of stratification has the lowest value (with the exception of  $Ri = 0.185$ ). As the value of the inversed Peclet number decreases the degree of stratification increases. Another interesting feature of the graph is that the degree of stratification is almost the same for the cases of  $1/Pe = 1.85 \times 10^{-4}$ , except at the early time ( $\tau < 50$ ). Notice that the depth at which stratification first occurs decreases as the Richardson number decrease. The figure seems to suggest that at  $Ri = 18.5$  the degree of stratification is stronger than that at  $Ri = 185.2$ . However, a look at Figs. C.8 (Appendix C) and 4.26 reveals that the degrees of stratification are similar, but the thermoclines are much thicker in Fig. 4.26. As expected, at  $Ri = 0.185$ , the degree of stratification is much

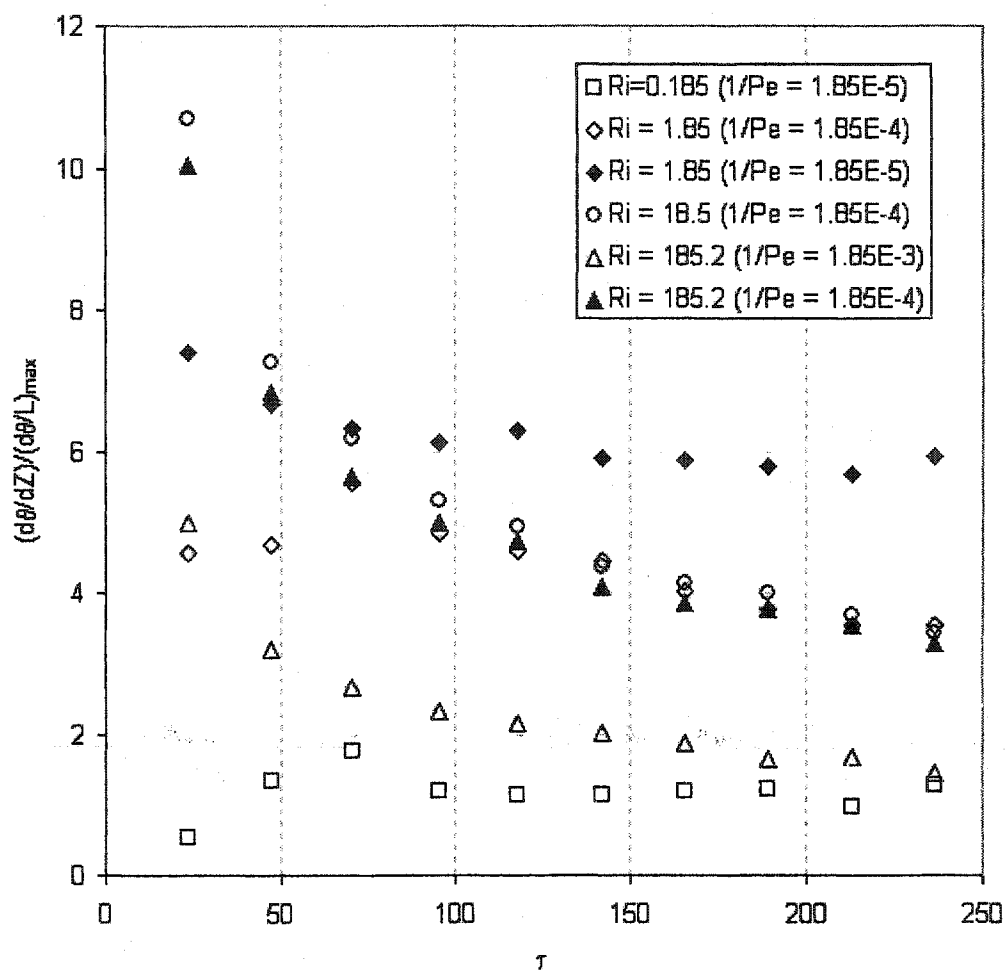


Figure 4.27 Degree of stratification for various Richardson numbers.

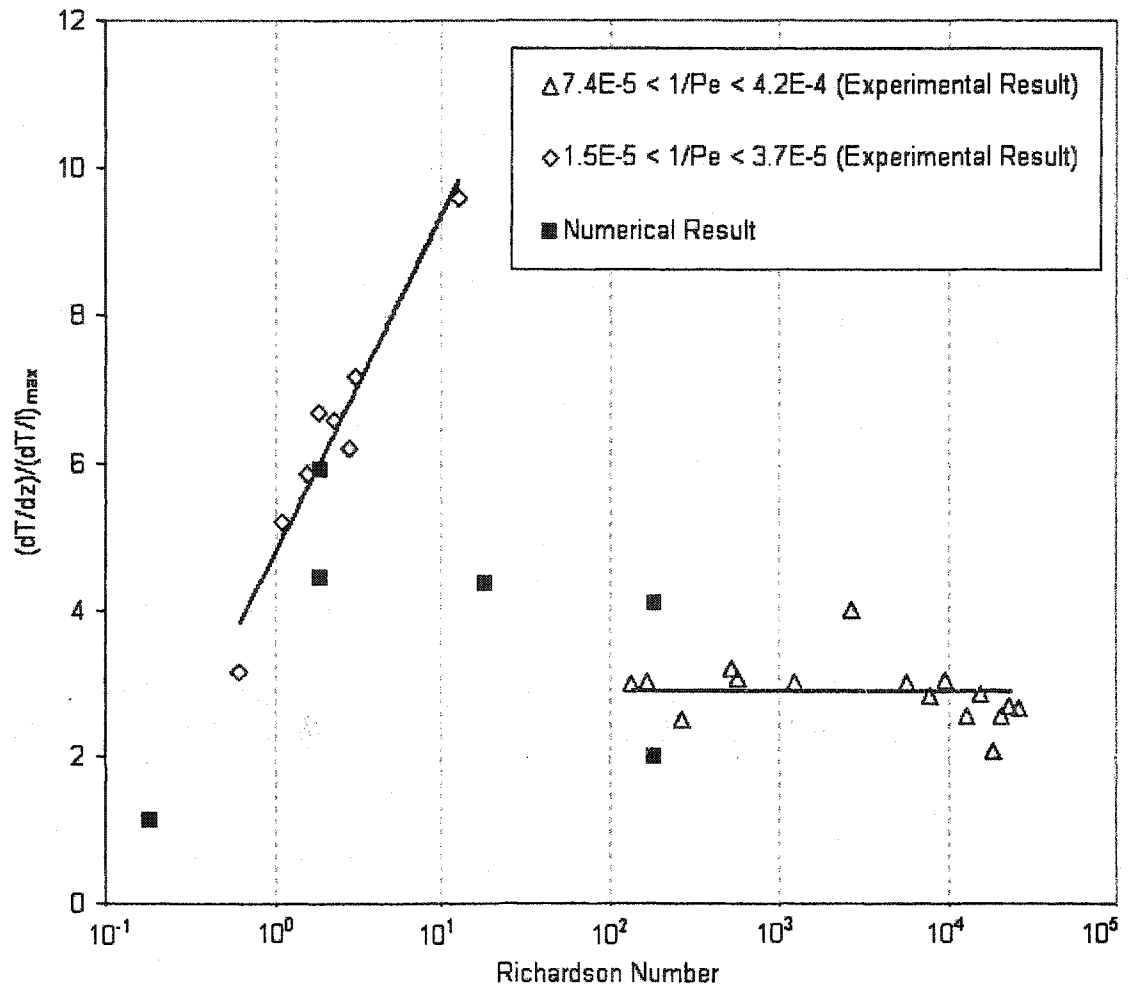


Figure 4.28 Comparison of the degree of stratification obtained from the numerical and experimental results.

smaller so that the resulting curve is flatter than those at a higher values of Richardson number. The degree of stratification from the numerical study was super-imposed on the plot obtained from the experiments (Fig. 4.28). The plot would indicate that a fairly good fit is obtained at  $Ri \leq 1.85$  ( $1/Pe \leq 1.85 \times 10^{-4}$ ).

#### 4.8 Conclusion

Although the numerical simulation did not perfectly reproduce the experiment results, the agreement between them was quite encouraging. The temperatures for the two cases examined showed a larger variation close to the end of the charging process, where the actual water body was heated up at a much faster rate than predicted. This can be due to the fact that in the simulated cases the thermophysical properties of the water was evaluated at an average temperature, which may introduce some errors in the numerical prediction. Similarly, the agreement of the mixing tank temperature was fairly good except towards the end of the charging process. The actual temperatures were much higher than those predicted by the numerical simulation.

The comparison between the numerical and experimental results seems to suggest that the physical properties of the porous tube (e.g., permeability and slip coefficient) used in the simulation were close to the actual values.

For most numerical studies, it is customary to assume that a porous medium in question is isotropic. As a result, the permeabilities are the same in both r and z-directions. However, in the present study, the porous manifold was considered to have a distinct permeability in the z-direction and in the r-direction. This was taken into account in the present formulation. With this provision, the case considered is more realistic. The new formulation seems to work well for most cases, but at a higher value of

Richardson number ( $Ri > 18.5$ ), some oscillation in the temperature was observed in the region of the porous tube. This tendency was more obvious at a higher Reynolds number. Physically the results exhibit a correct trend, however, more investigations are necessary to conclude if this is a physical or numerical instability.

The present investigation has covered a wide range of the Richardson number,  $0.0185 \leq Ri \leq 185.2$ . The present results show that a stable stratification can be achieved at a lower Richardson number than previously reported. A fairly stable stratification was observed in the tank at a Richardson number as low as 0.185. As reported by early researchers, a high inlet velocity (i.e., a high Reynolds number) was quite destructive to the formation of thermocline and a high inlet fluid temperature (i.e., a high Rayleigh number) on the other hand was very good at promoting stratification.

The degree of stratification was found to approach an asymptotic value over time. The degree of stratification obtained from this study appears to correlate well with those obtained in the experimental study (Chapter 3).

## CHAPTER FIVE

### CONCLUSIONS

#### 5.1 Introductory Remarks

Since the early 1970's it was shown that thermal stratification would improve the overall performance of a thermal storage system. In search of a viable source of renewable energy many researchers have conducted numerical, theoretical and experimental studies to investigate the conditions required for stratification in sensible heat storage. Although stratification could be maintained once the inlet water temperature was above the storage water temperature, severe mixing was observed once the temperature of the inlet water fluctuate below the temperature of the stored water.

Loehrke et al. (1979) introduced the use of vertical porous manifold that would reduce shear induced mixing between fluids of unlike temperature, thus enhancing stratification under variable inlet temperature. However, they gave little information on the physical properties of the porous manifold that could be used to promote stratification.

Driven by the scarcity of data on porous materials, a study of thermal stratification in sensible heat storage system was successfully completed. This study included theoretical, numerical and experimental investigations of new materials that can be used in the fabrication of a porous manifold to reduce mixing in storage systems.

Theoretical solution to determine the slip coefficient at the interface of a porous cylinder wall was conducted. The assumptions and solution procedures were

somewhat similar to those used earlier by Beavers and Joseph (1967), however, the present investigation used cylindrical coordinates. In the present investigation the permeability of the porous cylinder was considered to vary with direction.

The experimental study involving fabricating porous cylinders from fiberglass and nylon netting and conducting experiments to determine its permeability and the slip coefficient that can be used as matching conditions at the interface locations. The theoretical solutions were implemented in the calculations. A full-scale model of a thermal storage tank was constructed and tested. The inlet manifold used was made from similar material as those tested. Tests were conducted at varying Richardson number, which was shown to be very important in the formation of stratification.

Finally, a numerical study of the thermal storage tank was developed and tested. The permeability of the porous manifold and the matching conditions at the interface of the porous tube were taken from the experiments conducted earlier.

## **5.2 Determination of the Slip Coefficient**

The theoretical solution was obtained based on the assumption that a slip velocity existed at the permeable interface which was different from the mean filtration velocity that existed within the permeable material. The experimental data had suggested that a slip velocity was induced at the interface region between a moving fluid and a porous wall. The slip coefficient was found to depend on the factors other than the porous material. The slip coefficient was found to depend on the Reynolds number, the longitudinal permeability, and the thickness of the porous wall.

To facilitate the determination of the slip coefficient, experiments were first carried out to determine the permeability of the porous tubes under test. Seven tubes were fabricated and tested. The value of the longitudinal permeability was found to depend on the thickness of the porous wall and the gap size between consecutive layers. The radial permeability on the other hand depended more on the porosity of the material than the thickness of the wall, within the range of diameters and thickness considered in this experiment. The values of the radial permeability were much less than originally expected.

### **5.3 Stratification Enhancement in a Liquid Storage Tank**

A thermal storage tank was designed and constructed to experimentally investigate the effect of thermal stratification on the increase energy. A porous manifold was used to reduce the shear-induced mixing between the inlet fluid and the fluid in the tank, therefore enhancing the degree of stratification in the tank. Stratification was shown to increase the effectiveness of a thermal storage system. For the present study, stratification was observed at a Richardson number as low as 0.651. Due to the limitations of the experimental apparatus,  $Ri = 0.615$  was the lowest value that can be reached in this experimental study.

Twenty-three experimental runs at various Richardson numbers ( $0.651 \leq Ri \leq 26145.73$ ) were conducted to investigate the conditions necessary for stratification. Although it was known that stable stratification could be achieved at a Richardson number greater than 10, experiments at the higher Richardson number was conducted to investigate the degree of stratification and to see if a correlation could be developed between the degrees of stratification the Richardson and inverse Peclet

numbers. A very good correlation was developed at the lower Richardson numbers. However, the dependence of the degree of stratification on the Richardson number break down at higher values of Richardson and inverse Peclet numbers. The quality of the degree of stratification can also be judged from the mixing tank temperature. Although at values of  $Ri > 1$  very little distinction can be made between the values of the mixing tank temperature. It can be very useful at lower values of  $Ri$ , in distinguishing between the degrees of stratification.

Three flow visualization experiments were conducted using colored ink to evaluate how effective the porous manifold could reduce shear induced mixing. First, the tank was heated up until a stable stratification was established, then the temperature of the inlet water was reduced and colored with ink. The ink should flow down the manifold until its inlet momentum is balanced by buoyancy. The results were encouraging, although the out flows was above the expected levels in all cases, and more so in the case of lowest inlet velocity. It was apparent that the surrounding water in the tank was responsible for heating up the inlet water during its decent. However, the spreading of the ink was confined to a planar horizontal layer, from this one can be certain that the porous manifold is effective in the stabilizing and maintaining a thermal stratification.

#### **5.4 Numerical Study**

A numerical study was successfully performed to evaluate the flow and temperature fields in the storage tank. Although the comparisons were not exact in

all areas, it can be concluded that the numerical simulation provided a good representation of the flow and temperature fields in the storage tank.

From the numerical results, one could conclude that the stratification established at a low Richardson number ( $Ri = 0.185$ ) was fairly stable even though it was shown earlier by Sliwinski et al. (1978) that  $Ri = 0.244$  was the critical value below which a stratification was not possible. Since no stratification was detected at  $Ri = 0.0185$ , one could conclude that the critical value of the Richardson number would be in the region of  $0.0185 \leq Ri \leq 0.185$ . Encouraging, as it may seem the quality of the simulation break down at  $Ri > 185.2$ , and even at this level numerical instability is detected.

Unlike most numerical studies conducted in the past, the present study takes on the problem with an anisotropic porous manifold, which has different permeabilities in the  $z$  and  $r$ -directions. This challenge has posed some difficulties in the initial formulation but were easily overcome.

## **5.5 Future Work**

Although the present study has successfully investigated the enhancement of thermal stratification in a sensible heat storage tank using a porous manifold, there are still a few questions that remain to be answered. It is recommended that the present study be extended to address these questions both experimentally and numerically.

In the present study the numerical simulation was performed after the experiment. This is understandable as a start, however, in the future the numerical study should be used as a guide for experiment. Due to the limited funding for the present study, equipments with a high margin of errors was used. The numerical

simulation could solve this problem, and if experimental confirmation is required, it would provide a guideline of what to do and what not to do.

To improve the experimental study, more sensitive pressure transducers and a more sensitive pressure meter is required. For the present study, the lowest pressure that can be detected was  $6.895 \text{ N/m}^2$  (0.001 psi.). However, at the pressure the flow in a 3 cm diameter tube is already turbulent, as a result most of the investigation was conducted on smaller diameter tubes.

## REFERENCE

- Abu-Hamdan, M. G., Zurigat, Y. H., and Ghajar, A. J., "An Experimental Study of a Stratified Thermal Storage Under Variable Inlet Temperature for Different Inlet Designs," International Journal of Heat and Mass Transfer, Vol. 35, No. 8, pp. 1927-1934, 1992.
- Amyx, J. W., Bass, D. M., and Whiting, R. L., Petroleum Reservoir Engineering, Physical Properties, McGraw-Hill, New York, 1960.
- Beaver, G. S., and Joseph, D. D., "Boundary Condition at a Naturally Permeable Wall," Journal of Fluid Mechanics, Vol. 30, pp. 197-207, 1967.
- Beaver, G. S., Sparrow, E. M., and Magnuson, R. A., "Experiments on Coupled Parallel Flows in a Channel and a Bounding Porous Medium," Journal of Basic Engineering, Vol. 92, pp. 843-848, 1970.
- Beaver, G. S., Sparrow, E. M., and Masha, B. A., "Boundary Condition at a Porous Surface Which Bounds a Fluid Flow," AIChE Journal, Vol. 20, pp. 596-597, 1974.
- Beckermann, C., Ramadhyani, S., and Viskanta, R., "Natural Convection Flow and Heat Transfer between a Fluid Layer and a Porous Layer inside a Rectangular Enclosure," Journal of Heat Transfer, Vol. 109, pp. 363-370, 1987.
- Bouhdjar, A., Benkhelifa, A., and Harhad, A., "Numerical Study of Transient Mixed Convection in a Cylindrical Cavity," Numerical Heat Transfer, Part A, Vol. 31, pp. 305-324, 1997.
- Cabelli, A., "Storage Tanks - A Numerical Experiment," Solar Energy, Vol. 19, pp. 45-54, 1977.
- Cai, L., Stewart, Jr. W. E., and Sohn, C. W., "Turbulent Buoyant Flow into a Two Dimensional Storage Tank," International Journal of Heat and Mass Transfer, Vol. 36, No. 17, pp. 4247-4256, 1993.
- Chan, A. M. C., Smereka, P. S., and Giusti, D., "A Numerical Study of Transient Mixed Convection Flow in a Thermal Storage Tank," Journal of Solar Energy Engineering, Vol. 105, pp. 246-253, 1983.
- Chan, B. K. C., Ivey, C. M., and Barry, J. M., "Natural Convection in Enclosed Porous Media with Rectangular Boundaries," Journal of Heat Transfer, Vol. 92, pp. 21-27, 1970.
- Dake, L. P., Fundamentals of Reservoir Engineering, Elsevier Scientific Publishing Company, New York, 1978.

Fisher Scientific, Isotemp Refrigerated Circulators, Instruction and Operation Manual, 1996.

Gari, H. N., and Loehrke, R. I., "A Controlled Buoyant Jet for Enhancing Stratification in a Liquid Storage Tank," Journal of Fluid Engineering, Vol. 104, pp. 475-481, 1982.

Ghajar, A. J., and Zurigat, Y. H., "Numerical Study of the Effect of Inlet Geometry on Stratification in Thermal Energy Storage," Numerical Heat Transfer, Part A, Vol. 19, pp. 65-83, 1991.

Givler, R. C., and Altobelli, S. A., "A Determination of the Effective Viscosity for the Brinkman-Forchheimer Flow Model," Journal of Fluid Mechanics, Vol. 258, pp. 355-370, 1994

Guo, K. L., and Wu, S. T., "Numerical Study of Flow and Temperature Stratification in a Liquid Thermal Storage Tank," Journal of Solar Energy Engineering, Vol. 107, pp. 15-20, 1985.

Hollands, K. T. G., and Lightstone, M. F., "A Review of Low-Flow, Stratified-Tank Solar Water Heating System," Solar Energy, Vol. 43, No. 2, pp. 97-105, 1989.

Homan, K. O., and Soo, S. L., "Model of the Transient Stratified Flow into a Chilled-Water Storage Tank," International Journal of Heat and Mass Transfer, Vol. 40, pp. 4367-4377, 1997.

Jaluria, Y., and Gupta, S. K., "Decay of Thermal Stratification in a Water Body for Solar Energy Storage," Solar Energy, Vol. 28, No. 2, pp. 137-143, 1982.

James, D. F., and Davis, A. M. J., "Flow at the Interface of a Model Fibrous Porous Medium," Journal of Fluid Mechanics, Vol. 426, pp. 47-72, 2001.

Kakac, S., and Yener, Y., Convective Heat Transfer, Second Edition, CRC Press Inc. Boca Raton, Ann Arbor, 1995.

Kaviany, M., Principle of Heat Transfer in Porous Media, Second Edition, Springer-Verlag, New York, 1995.

Kim, S. J., and Choi, C. Y., "Convection Heat Transfer in Porous Fluid Layer Heated from Below," International Journal of Heat and Mass Transfer, Vol. 39, No. 2, pp. 319-329, 1996.

Lai, F. C., and Kulacki, F. A., "Experimental Study of Free and Mixed Convection in Horizontal Porous Layer Locally Heated from Below," International Journal of Heat and Mass Transfer, Vol. 34, No. 2, pp. 525-541, 1991.

- Lavan, Z., and Thompson, J., "Experimental Study of Thermally Stratified Hot Water Storage Tanks," Solar Energy, Vol. 19, pp. 519-524, 1977.
- Loehrke, R. I., Holzer, J. C., Gari, H. N., and Sharp, M. K., "Stratification Enhancement in Liquid Thermal Storage Tanks," Journal of Energy, Vol. 3, No. 3, pp.129 - 130, 1979.
- Matsudaira, H., and Tanaka, Y., "Dynamic Characteristic of a Heat Storage Water Tank – Part 1," ASHRAE Translations, Vol. 86, Part 1, pp. 110 – 124, 1979.
- Mohan, D. D., and Vaishnav, R. N., "Submerge Laminar Jet Impingement on a Plane," Journal of Fluid Mechanics, Vol. 114, pp. 213-236, 1982.
- National Instruments, Signal Conditioning SCC Series User Manual, Nation Instrument Corporate Headquarters, Austin, Texas, 2001.
- Neale, G., and Nader, W., "Practical Significant of Brinkman's Extension of Darcy's Law: Coupled Parallel Flows within a Channel and a Bounding Porous Medium," Canadian Journal of Chemical Engineering, Vol. 52, pp.475-478, 1974.
- Nield, D. A., and Bejan, A., Convection in Porous Media, Springer-Verlag, New York, 1992.
- Prasad, V., Kulacki, F. A., and Keyhani, M., "Natural Convection in Porous Media," Journal of Fluid Mechanics, Vol. 150, pp. 88-119, 1985.
- Richardson, S., "A Model for the Boundary Condition of a Porous Material, Part II," Journal of Fluid Mechanics, Vol. 49, pp. 327-336, 1971.
- Roache, P. J., Fundamentals of Computational Fluid Dynamics, Hermosa Publishers, Albuquerque, 1998.
- Sahraoui, M., and Kaviany, M., "Slip and No-slip Velocity Boundary Conditions at Interface of Porous, Plane Media," International Journal of Heat and Mass Transfer, Vol. 35, No. 4, pp. 927-943, 1992.
- Sharp, M. K., and Loehrke, R. I., "Stratified Thermal Storage in Residential Solar Energy Applications," Journal of Energy, Vol. 3, pp. 106-113, 1979.
- Sliwinski, B. J., Mech, A. R., and Shih T. S., "Stratification in Thermal Storage during Charging," 6<sup>th</sup> International Heat Transfer Conference, Toronto, Vol. 4, pp.149-154, 1978.
- Spall, R. E., "A Numerical Study of Transient Mixed Convection in Cylindrical Thermal Storage Tanks," International Journal of Heat and Mass Transfer, Vol. 41, No.13, pp. 2003-2011, 1998.

Sparrow, E. M., Beaver, G. S., Chen, T. S., and Lloyd, J. R., "Breakdown of Laminar Flow Regime in Permeable-Wall Ducts," Journal of Applied Mechanics, Vol. 40, pp. 337-342, 1973.

Taylor, G. I., "A Model for the Boundary Condition of a Porous Material, Part I," Journal of Fluid Mechanics, Vol. 49, pp. 319-326, 1971.

Torrance, K. E., "Comparison of Finite-Difference Computations of Natural Convection," Journal of Research of the National Bureau of Standards - B. Mathematical Science, Vol. 72B, No. 4, pp. 281-301, 1968.

Vafia, K., and Thiyagaraja, R., "Analysis of Flow and Heat Transfer at the Interface Region of a Porous Medium," International Journal of Heat and Mass Transfer, Vol. 30, pp. 1391-1405, 1987.

Yee, C. K., and Lai, F. C., "Effect of Porous Manifold on Thermal Stratification in Liquid Storage Tank," Solar Energy, Vol. 71, No. 4, pp. 241-254, 2001.

Yoo, J., Wildin, M. W., and Truman, C. R., "Initial Formation of a Thermocline in Stratified Thermal Storage Tanks," ASHRAE Transactions, Vol. 92, pp. 280-292, 1986.

Zurigat, Y. H., Maloney, K. J., and Ghajar, A. J., "A Comparison Study of One-Dimensional Models for Stratified Thermal Storage Tank," Journal of Solar Energy Engineering, Vol. 111, pp. 204-210, 1989.

Zurigat, Y. H., Liche, P. R., and Ghajar, A. J., "Influence of Inlet Geometry on Mixing in Thermocline Thermal Energy Storage," International Journal of Heat and Mass Transfer, Vol. 34, No.1, pp. 115-125, 1991.

## APPENDIX A

### Physical Properties of Porous Tubes

Table A.1	Longitudinal permeability of fiberglass porous tube with 0.00635-m-thick wall .....	162
Table A.2	Radial permeability of fiberglass porous tube with 0.00635-m-thick wall .....	162
Table A.3	Longitudinal permeability of fiberglass porous tube with 0.004762-m-thick wall .....	163
Table A. 4	Radial permeability of fiberglass porous tube with 0.004762 m-thick-wall .....	163
Table A.5	Longitudinal permeability of fiberglass porous tube with 0.003175-m-thick wall .....	164
Table A.6	Radial permeability of fiberglass porous tube with 0.003175 m-thick-wall .....	164
Table A.7	Longitudinal permeability of nylon fiber porous tube with 0.00635-m-thick wall .....	165
Table A.8	Radial permeability of nylon fiber porous tube with 0.00635-m-thick wall .....	165
Table A.9	Radial permeability of nylon fiber porous tube with 0.003175 m-thick-wall .....	166
Table A.10	Radial permeability of nylon fiber porous tube with 0.0015875-m-thick wall .....	167
Table A.11	Experimental results for the determination of slip coefficient on the fiberglass porous tube with 0.00635-m-thick wall .....	168
Table A.12	Experimental results for the determination of slip coefficient on the fiberglass porous tube with 0.0047625-m- thick wall .....	169
Table A.13	Experimental results for the determination of slip coefficient on the fiberglass porous tube with 0.003175-m-thick wall .....	170

Table A.14	Radial permeability of nylon fiber porous tube with 0.00635-m-thick wall .....	171
Table A.15	Results of experiments conducted to determine slip coefficient on nylon porous tube with 0.00635-m-thick wall .....	171

Table A.1 Longitudinal permeability of fiberglass porous tube with 0.00635-m-thick wall

$\Delta p$ (psi)	$\Delta p$ (N/m <sup>2</sup> )	$\Delta p/L$ (N/m <sup>3</sup> )	$Q$ $\times 10^{-6}$ (m <sup>3</sup> /s)	$v$ (m/s)	$K$ (m <sup>2</sup> )	Re
0.0142	97.67	240.34	0.19	$7.55 \times 10^{-4}$	$3.1 \times 10^{-9}$	0.042
0.015	103.42	254.5	0.24	$9.47 \times 10^{-4}$	$3.7 \times 10^{-9}$	0.057
0.031	213.74	525.94	0.41	$1.62 \times 10^{-3}$	$3.1 \times 10^{-9}$	0.089
0.0311	214.34	527.43	0.4	$1.58 \times 10^{-3}$	$3.0 \times 10^{-9}$	0.086
0.045	310.25	763.42	0.623	$2.46 \times 10^{-3}$	$3.2 \times 10^{-9}$	0.139
0.045	310.27	763.47	0.59	$2.34 \times 10^{-3}$	$3.1 \times 10^{-9}$	0.129

Table A.2 Radial permeability of fiberglass porous tube with 0.00635-m-thick wall

$\Delta p$ (psi)	$\Delta p$ (N/m <sup>2</sup> )	$\Delta p/(\ln(r_e/r_w))$ (N/m <sup>2</sup> )	$Q$ $\times 10^{-6}$ (m <sup>3</sup> /s)	$v$ (m/s)	$K$ (m <sup>2</sup> )	Re
0.003	20.68	18.83	3.05	$2.92 \times 10^{-3}$	$1.48 \times 10^{-9}$	0.112
0.005	34.47	31.38	3.84	$3.67 \times 10^{-3}$	$1.12 \times 10^{-9}$	0.122
0.014	96.53	87.86	6.84	$6.54 \times 10^{-3}$	$7.1 \times 10^{-10}$	0.174
0.02	137.9	125.52	8.34	$7.98 \times 10^{-3}$	$6.06 \times 10^{-10}$	0.196
0.022	151.69	138.1	11.0	$1.05 \times 10^{-2}$	$7.27 \times 10^{-10}$	0.283
0.024	165.48	150.63	12.9	$1.24 \times 10^{-2}$	$7.83 \times 10^{-10}$	0.344
0.027	186.17	169.45	15.7	$1.5 \times 10^{-2}$	$8.44 \times 10^{-10}$	0.434
0.034	234.43	213.39	18.5	$1.77 \times 10^{-2}$	$7.92 \times 10^{-10}$	0.496
0.043	296.48	269.87	20.6	$1.97 \times 10^{-2}$	$6.98 \times 10^{-10}$	0.52
0.047	324.1	294.98	22.6	$2.16 \times 10^{-2}$	$7.0 \times 10^{-10}$	0.569
0.052	358.54	326.36	25.1	$2.4 \times 10^{-2}$	$6.6 \times 10^{-10}$	0.635
0.061	420.6	382.84	27.7	$2.65 \times 10^{-2}$	$6.59 \times 10^{-10}$	0.677
0.067	461.96	420.50	29.3	$2.8 \times 10^{-2}$	$6.35 \times 10^{-10}$	0.703
0.074	510.2	464.43	30.1	$2.96 \times 10^{-2}$	$6.08 \times 10^{-10}$	0.727
0.078	573.81	489.54	32.3	$3.09 \times 10^{-2}$	$6.02 \times 10^{-10}$	0.755

Table A.3 Longitudinal permeability of fiberglass porous tube with 0.004762-m-thick wall

$\Delta p$ (psi)	$\Delta p$ (N/m <sup>2</sup> )	$\Delta p/L$ (N/m <sup>3</sup> )	$Q$ $\times 10^{-6}$ (m <sup>3</sup> /s)	$v$ (m/s)	$K$ (m <sup>2</sup> )	Re
0.0094	64.60	158.97	0.238	$1.11 \times 10^{-3}$	$7.02 \times 10^{-9}$	0.092
0.01	68.95	169.66	0.284	$1.33 \times 10^{-3}$	$7.85 \times 10^{-9}$	0.117
0.0144	99.29	244.31	0.31	$1.43 \times 10^{-3}$	$5.90 \times 10^{-9}$	0.110
0.0196	134.99	332.16	0.41	$1.91 \times 10^{-3}$	$5.76 \times 10^{-9}$	0.144
0.024	165.48	407.18	0.55	$2.56 \times 10^{-3}$	$6.3 \times 10^{-9}$	0.202
0.036	248.22	610.78	0.81	$3.77 \times 10^{-3}$	$6.2 \times 10^{-9}$	0.296

Table A.4 Radial permeability of fiberglass porous tube with 0.004762-m-thick wall

$\Delta p$ (psi)	$\Delta p$ (N/m <sup>2</sup> )	$\Delta p/(\ln(r_c/r_w))$ (N/m <sup>2</sup> )	$Q$ $\times 10^{-6}$ (m <sup>3</sup> /s)	$v$ (m/s)	$K$ (m <sup>2</sup> )	Re
0.002	13.79	19.89	5.52	$5.28 \times 10^{-3}$	$2.53 \times 10^{-9}$	0.265
0.006	41.37	59.68	10.2	$9.76 \times 10^{-3}$	$1.56 \times 10^{-9}$	0.384
0.009	62.05	89.53	12.8	$1.23 \times 10^{-2}$	$1.31 \times 10^{-9}$	0.442
0.013	89.63	129.31	17.8	$1.71 \times 10^{-2}$	$1.26 \times 10^{-9}$	0.603
0.022	151.69	218.84	23.7	$2.26 \times 10^{-2}$	$9.88 \times 10^{-10}$	0.709
0.028	193.06	278.53	24.9	$2.38 \times 10^{-2}$	$8.16 \times 10^{-10}$	0.678
0.032	220.64	318.32	26.6	$2.54 \times 10^{-2}$	$7.63 \times 10^{-10}$	0.7
0.035	241.32	348.16	30.0	$2.87 \times 10^{-2}$	$7.86 \times 10^{-10}$	0.801
0.038	262.01	378	33.5	$3.21 \times 10^{-2}$	$8.1 \times 10^{-10}$	0.91
0.04	275.8	397.89	35.4	$3.39 \times 10^{-2}$	$8.13 \times 10^{-10}$	0.963
0.044	303.38	437.68	39.5	$3.78 \times 10^{-2}$	$8.23 \times 10^{-10}$	1.08
0.048	330.96	477.47	4.17	$3.99 \times 10^{-2}$	$7.97 \times 10^{-10}$	1.12
0.051	351.64	507.31	4.33	$4.14 \times 10^{-2}$	$7.8 \times 10^{-10}$	1.15

Table A.5 Longitudinal permeability of fiberglass porous tube with 0.003175-m-thick wall

$\Delta p$ (psi)	$\Delta p$ (N/m <sup>2</sup> )	$\Delta p/L$ (N/m <sup>3</sup> )	$Q$ $\times 10^{-6}$ (m <sup>3</sup> /s)	$v$ (m/s)	$K$ (m <sup>2</sup> )	Re
0.007	48.26	118.76	0.0653	$4.13 \times 10^{-4}$	$3.48 \times 10^{-9}$	0.024
0.0092	63.4	156	0.0904	$5.71 \times 10^{-4}$	$3.67 \times 10^{-9}$	0.034
0.013	89.63	220.55	0.118	$7.5 \times 10^{-4}$	$3.39 \times 10^{-9}$	0.043
0.029	198.66	488.80	0.26	$1.65 \times 10^{-3}$	$3.36 \times 10^{-9}$	0.095
0.031	213.74	525.95	0.271	$1.71 \times 10^{-3}$	$3.26 \times 10^{-9}$	0.097
0.044	303.35	746.42	0.427	$2.70 \times 10^{-3}$	$3.61 \times 10^{-9}$	0.161
0.066	454.66	1118.74	0.606	$3.83 \times 10^{-3}$	$3.42 \times 10^{-9}$	0.223

Table A.6 Radial permeability of fiberglass porous tube with 0.003175-m-thick wall

$\Delta p$ (psi)	$\Delta p$ (N/m <sup>2</sup> )	$\Delta p/(\ln(r_e/r_w))$ (N/m <sup>2</sup> )	$Q$ $\times 10^{-6}$ (m <sup>3</sup> /s)	$v$ (m/s)	$K$ (m <sup>2</sup> )	Re
0.002	13.79	34.01	3.1	$2.97 \times 10^{-3}$	$8.32 \times 10^{-10}$	0.0852
0.006	41.37	102.03	6.5	$6.22 \times 10^{-3}$	$5.81 \times 10^{-10}$	0.149
0.01	68.95	170.05	8.46	$8.1 \times 10^{-3}$	$4.54 \times 10^{-10}$	0.172
0.014	96.53	238.07	11.4	$1.09 \times 10^{-2}$	$4.36 \times 10^{-10}$	0.226
0.017	117.21	289.09	15.8	$1.52 \times 10^{-2}$	$5.0 \times 10^{-10}$	0.338
0.022	151.69	374.11	18.7	$1.79 \times 10^{-2}$	$4.57 \times 10^{-10}$	0.382
0.026	179.27	442.13	21.1	$2.02 \times 10^{-2}$	$4.36 \times 10^{-10}$	0.42
0.031	213.74	527.16	23.4	$2.24 \times 10^{-2}$	$4.06 \times 10^{-10}$	0.45
0.035	241.32	595.2	25.7	$2.46 \times 10^{-2}$	$3.94 \times 10^{-10}$	0.485
0.038	262.0	646.2	28.6	$2.73 \times 10^{-2}$	$4.04 \times 10^{-10}$	0.547
0.041	282.7	697.21	30.9	$2.95 \times 10^{-2}$	$4.04 \times 10^{-10}$	0.592
0.046	317.17	782.23	33.7	$3.22 \times 10^{-2}$	$3.93 \times 10^{-10}$	0.637
0.05	344.75	850.26	35.3	$3.37 \times 10^{-2}$	$3.79 \times 10^{-10}$	0.654

Table A.7 Longitudinal permeability of nylon fiber porous tube with 0.00635-m-thick wall

$\Delta p$ (psi)	$\Delta p$ (N/m <sup>2</sup> )	$\Delta p/L$ (N/m <sup>3</sup> )	$Q$ $\times 10^{-6}$ (m <sup>3</sup> /s)	$v$ (m/s)	$K$ (m <sup>2</sup> )	Re
0.005	34.47	84.83	0.3	$1.18 \times 10^{-3}$	$1.4 \times 10^{-8}$	0.139
0.007	48.26	118.76	0.63	$2.49 \times 10^{-3}$	$2.1 \times 10^{-8}$	0.359
0.01	68.95	169.66	1.04	$4.1 \times 10^{-3}$	$2.42 \times 10^{-8}$	0.637
0.016	110.32	271.46	1.63	$6.43 \times 10^{-3}$	$2.37 \times 10^{-8}$	0.988
0.021	144.8	356.29	2.2	$8.68 \times 10^{-3}$	$2.44 \times 10^{-8}$	1.35
0.029	199.96	492.02	3.11	$1.23 \times 10^{-2}$	$2.5 \times 10^{-8}$	1.93
0.038	262.01	644.71	3.85	$1.52 \times 10^{-2}$	$2.36 \times 10^{-8}$	2.33

Table A.8 Radial permeability of nylon fiber porous tube with 0.00635-m-thick wall

$\Delta p$ (psi)	$\Delta p$ (N/m <sup>2</sup> )	$\Delta p/(\ln(r_e/r_w))$ (N/m <sup>2</sup> )	$Q$ $\times 10^{-6}$ (m <sup>3</sup> /s)	$v$ (m/s)	$K$ (m <sup>2</sup> )	Re
0.001	6.89	6.27	18.7	$1.79 \times 10^{-2}$	$2.72 \times 10^{-8}$	2.94
0.004	27.58	25.1	23.9	$2.29 \times 10^{-2}$	$8.7 \times 10^{-9}$	2.12
0.005	34.47	31.38	27.2	$2.60 \times 10^{-2}$	$7.9 \times 10^{-9}$	2.31
0.008	55.16	50.21	30.0	$2.87 \times 10^{-2}$	$5.45 \times 10^{-9}$	2.11
0.014	96.53	87.86	32.2	$3.08 \times 10^{-2}$	$3.35 \times 10^{-9}$	1.78
0.019	131	119.24	36.2	$3.46 \times 10^{-2}$	$2.77 \times 10^{-9}$	1.82
0.024	165.48	150.63	38.2	$3.66 \times 10^{-2}$	$2.32 \times 10^{-9}$	1.75
0.025	172.37	2156.9	40.3	$3.86 \times 10^{-2}$	$2.34 \times 10^{-9}$	1.86
0.028	193.06	175.73	42.2	$4.04 \times 10^{-2}$	$2.19 \times 10^{-9}$	1.88
0.031	213.74	194.56	45.1	$4.32 \times 10^{-2}$	$2.12 \times 10^{-9}$	1.98
0.033	227.53	207.11	45.5	$4.35 \times 10^{-2}$	$2.0 \times 10^{-9}$	1.94
0.035	241.32	219.66	47.2	$4.52 \times 10^{-2}$	$1.96 \times 10^{-9}$	1.99
0.038	262.01	238.49	50.2	$4.80 \times 10^{-2}$	$1.92 \times 10^{-9}$	2.1
0.041	282.69	257.32	53.2	$5.09 \times 10^{-2}$	$1.89 \times 10^{-9}$	2.2
0.042	289.6	263.6	55.2	$5.28 \times 10^{-2}$	$1.91 \times 10^{-9}$	2.3
0.043	296.48	269.87	58.0	$5.55 \times 10^{-2}$	$1.96 \times 10^{-9}$	2.45
0.044	303.38	276.15	59.0	$5.65 \times 10^{-2}$	$1.95 \times 10^{-9}$	2.48

Table A.9 Radial permeability of nylon fiber porous tube with 0.003175-m-thick wall

$\Delta p$ (psi)	$\Delta p$ (N/m <sup>2</sup> )	$\Delta p/(\ln(r_e/r_w))$ (N/m <sup>2</sup> )	Q x 10 <sup>-6</sup> (m <sup>3</sup> /s)	v (m/s)	K (m <sup>2</sup> )	Re
0.001	6.89	17.0	8.78	8.4 x 10 <sup>-3</sup>	4.72 x 10 <sup>-9</sup>	0.575
0.002	13.79	34.01	14.6	1.39 x 10 <sup>-2</sup>	3.91 x 10 <sup>-9</sup>	0.869
0.004	27.58	68.02	19.9	1.90 x 10 <sup>-2</sup>	2.67 x 10 <sup>-9</sup>	0.977
0.006	41.37	102.03	25.5	2.44 x 10 <sup>-2</sup>	2.28 x 10 <sup>-9</sup>	1.16
0.008	55.16	136.04	28.0	2.68 x 10 <sup>-2</sup>	1.88 x 10 <sup>-9</sup>	1.16
0.01	68.95	170.05	29.4	2.81 x 10 <sup>-2</sup>	1.58 x 10 <sup>-9</sup>	1.11
0.011	75.84	187.05	32.5	3.11 x 10 <sup>-2</sup>	1.59 x 10 <sup>-9</sup>	1.23
0.012	82.74	204.06	34.4	3.29 x 10 <sup>-2</sup>	1.54 x 10 <sup>-9</sup>	1.29
0.013	89.63	221.07	38.8	3.71 x 10 <sup>-2</sup>	1.6 x 10 <sup>-9</sup>	1.48
0.016	110.32	272.08	47.2	4.52 x 10 <sup>-2</sup>	1.58 x 10 <sup>-9</sup>	1.79
0.019	131	323.1	53.2	5.09 x 10 <sup>-2</sup>	1.5 x 10 <sup>-9</sup>	1.97
0.02	137.9	340.1	55.3	5.29 x 10 <sup>-2</sup>	1.48 x 10 <sup>-9</sup>	2.03
0.022	151.69	347.11	58.0	5.55 x 10 <sup>-2</sup>	1.41 x 10 <sup>-9</sup>	2.08
0.023	158.6	391.12	61.0	5.84 x 10 <sup>-2</sup>	1.42 x 10 <sup>-9</sup>	2.19
0.024	165.48	408.12	64.7	6.19 x 10 <sup>-2</sup>	1.45 x 10 <sup>-9</sup>	2.35
0.027	186.16	459.14	66.9	6.40 x 10 <sup>-2</sup>	1.33 x 10 <sup>-9</sup>	2.33

Table A.10 Radial permeability of nylon fiber porous tube with 0.0015875-m-thick wall

$\Delta p$ (psi)	$\Delta p$ (N/m <sup>2</sup> )	$\Delta p/(\ln(r_g/r_w))$ (N/m <sup>2</sup> )	Q $\times 10^{-6}$ (m <sup>3</sup> /s)	v (m/s)	K (m <sup>2</sup> )	Re
0.001	6.89	37.82	10.5	$1.00 \times 10^{-2}$	$2.53 \times 10^{-9}$	$4.8 \times 10^{-6}$
0.002	13.79	75.63	21.8	$2.08 \times 10^{-2}$	$2.63 \times 10^{-9}$	$1.01 \times 10^{-5}$
0.004	27.58	151.27	29.3	$2.80 \times 10^{-2}$	$1.77 \times 10^{-9}$	$1.12 \times 10^{-5}$
0.005	34.47	189.1	32.9	$3.14 \times 10^{-2}$	$1.59 \times 10^{-9}$	$1.19 \times 10^{-5}$
0.006	41.37	226.91	34.3	$3.28 \times 10^{-2}$	$1.38 \times 10^{-9}$	$1.16 \times 10^{-5}$
0.01	68.95	378.18	48.6	$4.65 \times 10^{-2}$	$1.17 \times 10^{-9}$	$1.51 \times 10^{-5}$
0.01	68.95	378.18	48.8	$4.67 \times 10^{-2}$	$1.18 \times 10^{-9}$	$1.52 \times 10^{-5}$
0.013	89.63	491.63	52.0	$4.98 \times 10^{-2}$	$9.66 \times 10^{-10}$	$1.47 \times 10^{-5}$
0.013	89.63	491.63	53.1	$5.08 \times 10^{-2}$	$9.87 \times 10^{-10}$	$1.52 \times 10^{-5}$
0.015	103.42	567.27	54.4	$5.21 \times 10^{-2}$	$8.76 \times 10^{-10}$	$1.46 \times 10^{-5}$
0.015	103.42	567.27	56.5	$5.41 \times 10^{-2}$	$9.1 \times 10^{-10}$	$1.55 \times 10^{-5}$
0.017	117.21	642.9	63.3	$6.06 \times 10^{-2}$	$8.99 \times 10^{-10}$	$1.73 \times 10^{-5}$
0.019	131.0	718.54	70.2	$6.71 \times 10^{-2}$	$8.92 \times 10^{-10}$	$1.91 \times 10^{-5}$
0.02	137.9	756.36	71.2	$6.81 \times 10^{-2}$	$8.6 \times 10^{-10}$	$1.9 \times 10^{-5}$
0.025	172.37	945.44	85.0	$8.13 \times 10^{-2}$	$8.21 \times 10^{-10}$	$2.22 \times 10^{-5}$

Table A.11 Experimental results for the determination of slip coefficient on fiberglass porous tube with 0.00635-m-thick wall

$\Delta p$ (N/m <sup>2</sup> )	$Q_m$ $\times 10^{-6}$ (mL/s)	$Q$ $\times 10^{-6}$ (mL/s)	$Q_T$ $\times 10^{-6}$ (mL/s)	$\Phi = \frac{Q}{Q_T}$	$\gamma$	$v$ $\times 10^{-3}$ (m/s)	$Re_m$
13.79	0.989	0.846	1.35	0.626	0.1836	3.9	0.2134
27.58	1.58	1.7	2.69	0.6274	0.1843	6.24	0.34142
32.75	1.01	2.15	3.2	0.655	0.199	3.99	0.2183
48.26	1.21	3.07	4.72	0.649	0.1956	4.78	0.26158
55.16	1.99	3.37	5.39	0.624	0.1826	7.85	0.428
55.16	2.28	3.47	5.39	0.642	0.1918	9.0	0.4918
62.05	2.22	3.94	6.07	0.6478	0.1949	8.76	0.4795
68.95	1.42	4.45	6.74	0.66	0.202	5.6	0.3206
82.74	2.3	5.19	8.09	0.641	0.195	9.08	0.4934
96.53	2.34	6.31	9.44	0.6684	0.207	9.24	0.53
117.21	3.12	7.42	11.46	0.647	0.1945	12.3	0.7046
117.21	3.12	6.26	11.46	0.55	0.1528	12.3	0.705
137.9	4.05	6.47	13.48	0.48	0.1323	16.0	0.915
186.16	4.22	6.97	18.2	0.3828	0.1115	16.7	0.953
193.06	4.53	6.63	18.9	0.3511	0.106	17.9	1.023
206.85	4.8	6.91	20.23	0.3415	0.1046	18.9	1.084
234.43	4.19	6.59	22.93	0.287	0.0966	16.5	0.9462
289.59	4.24	7.2	28.32	0.2543	0.0923	16.7	0.9578
351.64	5.65	7.77	34.39	0.2259	0.089	22.3	1.276
358.54	5.18	7.34	35.06	0.21	0.0872	20.4	1.17
379.22	5.74	8.04	37.09	0.21677	0.0879	22.7	1.296
475.75	6.05	8.47	46.53	0.182	0.08425	23.9	1.366
530.91	6.23	8.98	51.92	0.173	0.0833	24.6	1.406
572.28	6.38	9.66	55.97	0.1736	0.0834	25.2	1.44
648.13	7.26	9.72	63.39	0.154	0.0815	28.7	1.64

Table A.12 Experimental results for the determination of slip coefficient on fiberglass porous tube with 0.0047625-m-thick wall

$\Delta p$ (N/m <sup>2</sup> )	$Q_m$ $\times 10^{-6}$ (mL/s)	$Q$ $\times 10^{-6}$ (mL/s)	$Q_T$ $\times 10^{-6}$ (mL/s)	$\Phi = \frac{Q}{Q_T}$	$\gamma$	$v$ $\times 10^{-3}$ (m/s)	$Re_m$
6.895	0.807	2.403	3.42	0.702	0.22	3.78	0.2968
13.79	1.98	4.89	6.841	0.714	0.23	9.26	0.728
13.79	2.07	4.63	6.84	0.6763	0.203	9.7	0.763
20.68	2.58	7.19	10.26	0.7	0.219	12.1	0.948
20.68	3.42	7.08	10.26	0.6898	0.212	16.0	1.256
27.58	3.0	9.27	13.68	0.677	0.204	14.0	1.103
27.58	3.22	8.84	13.68	0.646	0.186	15.1	1.185
34.47	4.1	10.7	17.1	0.624	0.175	19.2	1.507
34.47	5.17	9.6	17.1	0.562	0.1503	24.2	1.901
41.37	5.14	12.3	20.52	0.6	0.1648	24.0	1.89
48.26	4.66	13.0	23.94	0.541	0.144	22.0	1.713
55.16	5.08	15.6	27.36	0.571	0.1537	23.8	1.87
68.95	5.77	13.6	34.2	0.397	0.11	27.0	2.12
68.95	8.5	12.9	34.2	0.377	0.106	39.7	3.124
82.74	9.59	13.5	41.04	0.329	0.098	44.9	3.53

Table A.13 Experimental results for the determination of slip coefficient on fiberglass porous tube with 0.003175-m-thick wall

$\Delta p$ (N/m <sup>2</sup> )	$Q_m$ $\times 10^{-6}$ (mL/s)	$Q$ $\times 10^{-6}$ (mL/s)	$Q_T$ $\times 10^{-6}$ (mL/s)	$\Phi = \frac{Q}{Q_T}$	$\gamma$	$v$ $\times 10^{-3}$ (m/s)	$Re_m$
6.895	0.3	5.76	10.81	0.5334	0.078	1.89	0.109
6.895	0.63	6.16	10.81	0.5694	0.084	4.02	0.231
13.79	0.6	12.1	21.62	0.56	0.0826	3.8	0.217
20.68	1.86	14.9	32.43	0.46	0.0672	11.7	0.674
20.68	1.05	14.0	32.43	0.431	0.0637	6.63	0.381
27.58	2.16	18.3	43.24	0.423	0.0629	13.6	0.783
27.58	1.48	19.5	43.24	0.451	0.066	9.32	0.535
34.47	1.48	22.1	54.05	0.408	0.0613	9.32	0.535
34.47	2.24	17.6	54.05	0.325	0.0537	14.1	0.8114
34.47	2.69	18.6	54.05	0.3448	0.0554	17.0	0.9752
41.37	2.6	20.1	64.87	0.31	0.0526	16.4	0.943
41.37	1.64	23.8	64.87	0.37	0.0576	10.3	0.60
55.16	3.68	24.6	86.49	0.285	0.0507	23.2	1.334
62.05	2.75	25.5	97.29	0.2615	0.04914	17.4	1.0
75.84	2.92	29.2	118.91	0.245	0.048	18.4	1.06
82.74	4.61	30.5	129.73	0.235	0.04744	29.1	1.672
89.63	4.52	31.2	140.54	0.2217	0.04663	28.5	1.64
110.325	3.65	37.2	172.98	0.215	0.04623	23.1	1.32
124.113	4.39	37.4	194.6	0.192	0.045	27.7	1.6

Table A.14 Radial permeability of nylon fiber porous tube with 0.00635-m-thick wall

$\Delta p$ (psi)	$\Delta p$ (N/m <sup>2</sup> )	$\Delta p/(\ln(r_e/r_w))$ (N/m <sup>2</sup> )	$Q \times 10^{-6}$ (m <sup>3</sup> /s)	$v$ (m/s)	$K$ (m <sup>2</sup> )	Re
0.001	6.89	51.636	54.3	0.00975	$9.6 \times 10^{-9}$	0.0488
0.002	13.79	103.27	133.4	0.0239	$1.179 \times 10^{-8}$	2.59
0.003	20.685	154.90	170.7	0.00306	$1.00 \times 10^{-8}$	3.06

Table A.15 Experimental results for the determination of slip coefficient on nylon porous tube with 0.00635 m thick wall

$\Delta p$ (N/m <sup>2</sup> )	$Q_m$ $\times 10^{-6}$ (mL/s)	$Q$ $\times 10^{-6}$ (mL/s)	$Q_T$ $\times 10^{-6}$ (mL/s)	$\Phi = \frac{Q}{Q_T}$	$\gamma$	$v$ $\times 10^{-3}$ (m/s)	$Re_m$
20.685	1.26	1.32	2.02	0.652	0.19754	4.97	0.28455
27.58	2.62	1.76	2.7	0.652	0.19754	10.3	0.5917
34.47	2.2	2.2	3.37	0.653	0.1976	8.68	0.4968
41.73	3.1	2.68	4.08	0.657	0.19992	12.2	0.7
41.73	4.23	2.26	4.05	0.559	0.1557	16.7	0.95532
62.05	2.78	3.9	6.07	0.643	0.19211	11.0	0.6278
68.95	5.68	2.43	6.74	0.36	0.10766	22.4	1.283
89.635	5.62	3.18	8.77	0.36	0.10805	22.2	1.27
96.53	5.68	3.63	9.44	0.385	0.112	22.4	1.283
124.11	6.93	3.35	12.1	0.276	0.09515	27.4	1.565
137.9	6.65	3.74	13.5	0.277	0.09533	26.2	1.502
158.58	6.54	3.79	15.5	0.244	0.0912	25.8	1.48
186.16	6.7	3.74	18.2	0.205	0.086728	26.4	1.513
206.85	6.96	3.86	20.2	0.191	0.085166	27.5	1.572
255.11	8.03	4.42	25.0	0.177	0.08376	31.7	1.8135

## APPENDIX B

### Tank Temperature Profile

Figure B.1	Temperature profile for an inlet flow at $T_i = 27.86$ °C and $u_i = 0.0315$ m/s ( $Re = 10691.0$ , $Ra = 7.34 \times 10^8$ and $Ri = 1.0$ ) .....	174
Figure B.2	Temperature profile for an inlet flow at $T_i = 28.3$ °C and $u_i = 0.0315$ m/s ( $Re = 10691.0$ , $Ra = 1.05 \times 10^9$ and $Ri = 1.56$ ) .....	174
Figure B.3	Temperature profile for an inlet flow at $T_i = 28.3$ °C and $u_i = 0.0315$ m/s ( $Re = 10948.9$ , $Ra = 1.25 \times 10^9$ and $Ri = 1.82$ ) .....	175
Figure B.4	Temperature profile for an inlet flow at $T_i = 29.45$ °C and $u_i = 0.0315$ m/s ( $Re = 10948.9$ , $Ra = 1.54 \times 10^9$ and $Ri = 2.24$ ) .....	175
Figure B.5	Temperature profile for an inlet flow at $T_i = 29.73$ °C and $u_i = 0.0315$ m/s ( $Re = 10948.9$ , $Ra = 1.89 \times 10^9$ and $Ri = 2.75$ ) .....	176
Figure B.6	Temperature profile for an inlet flow at $T_i = 28.2$ °C and $u_i = 0.0315$ m/s ( $Re = 10445$ , $Ra = 2.01 \times 10^9$ and $Ri = 3.04$ ) .....	176
Figure B.7	Temperature profile for an inlet flow at $T_i = 29.0$ °C and $u_i = 0.0137$ m/s ( $Re = 4782.2$ , $Ra = 2.25 \times 10^9$ and $Ri = 12.84$ ) .....	177
Figure B.8	Temperature profile for an inlet flow at $T_i = 33.35$ °C and $u_i = 6.74 \times 10^{-3}$ m/s ( $Re = 2457.14$ , $Ra = 4.45 \times 10^9$ and $Ri = 135.78$ ) .....	177
Figure B.9	Temperature profile for an inlet flow at $T_i = 35.87$ °C and $u_i = 6.74 \times 10^{-3}$ m/s ( $Re = 2501.8$ , $Ra = 5.66 \times 10^9$ and $Ri = 169.98$ ) ..	178
Figure B.10	Temperature profile for an inlet flow at $T_i = 33.1$ °C and $u_i = 4.33 \times 10^{-3}$ m/s ( $Re = 1581.0$ , $Ra = 3.7 \times 10^9$ and $Ri = 272.63$ ) ...	178
Figure B.11	Temperature profile for an inlet flow at $T_i = 37.53$ °C and $u_i = 4.33 \times 10^{-3}$ m/s ( $Re = 1650.1$ , $Ra = 7.43 \times 10^9$ and $Ri = 527.24$ )	179
Figure B.12	Temperature profile for an inlet flow at $T_i = 38.27$ °C and $u_i = 4.33 \times 10^{-3}$ m/s ( $Re = 1650.1$ , $Ra = 7.98 \times 10^9$ and $Ri = 566.4$ ) .	179
Figure B.13	Temperature profile for an inlet flow at $T_i = 40.8$ °C and $u_i = 3.31 \times 10^{-3}$ m/s ( $Re = 1292.1$ , $Ra = 1.04 \times 10^{10}$ and $Ri = 1244.49$ ) .....	180
Figure B.14	Temperature profile for an inlet flow at $T_i = 31.0$ °C and	

	$u_i = 1.25 \times 10^{-3}$ m/s (Re = 438.8 Ra = $2.89 \times 10^9$ and Ri = 2648.8) ..	180
Figure B.15	Temperature profile for an inlet flow at $T_i = 36.0$ °C and $u_i = 1.25 \times 10^{-3}$ m/s (Re = 463.7, Ra = $6.54 \times 10^9$ and Ri = 5717.56)	181
Figure B.16	Temperature profile for an inlet flow at $T_i = 39.0$ °C and $u_i = 1.25 \times 10^{-3}$ m/s (Re = 476.7, Ra = $9.06 \times 10^9$ and Ri = 7724.9) ..	181
Figure B.17	Temperature profile for an inlet flow at $T_i = 41.0$ °C and $u_i = 1.25 \times 10^{-3}$ m/s (Re = 418.25, Ra = $1.14 \times 10^{10}$ and Ri = 9627.9) .....	182
Figure B.18	Temperature profile for an inlet flow at $T_i = 46.0$ °C and $u_i = 1.25 \times 10^{-3}$ m/s (Re = 510.1, Ra = $1.61 \times 10^{10}$ and Ri = 12939.5) .....	182
Figure B.19	Temperature profile for an inlet flow at $T_i = 49.0$ °C and $u_i = 1.25 \times 10^{-3}$ m/s (Re = 525.9, Ra = $1.96 \times 10^{10}$ and Ri = 15398.4) .....	183
Figure B.20	Temperature profile for an inlet flow at $T_i = 52.0$ °C and $u_i = 1.25 \times 10^{-3}$ m/s (Re = 537.0, Ra = $2.4 \times 10^{10}$ and Ri = 18480.9) .	183
Figure B.21	Temperature profile for an inlet flow at $T_i = 55.0$ °C and $u_i = 1.25 \times 10^{-3}$ m/s (Re = 559.0, Ra = $2.79 \times 10^{10}$ and Ri = 20691.2) .....	184
Figure B.22	Temperature profile for an inlet flow at $T_i = 57.0$ °C and $u_i = 1.25 \times 10^{-3}$ m/s (Re = 563.4, Ra = $3.13 \times 10^{10}$ and Ri = 23093.7) .....	184
Figure B.23	Temperature profile for an inlet flow at $T_i = 61.0$ °C and $u_i = 1.25 \times 10^{-3}$ m/s (Re = 582.0, Ra = $3.64 \times 10^{10}$ and Ri = 26145.7) .....	185
Figure B.24	Mixing tank temperature for various Richardson numbers ( $1.82 \leq Ri \leq 0.651$ ) .....	186
Figure B.25	Mixing tank temperature for various Richardson numbers ( $3.04 \leq Ri \leq 2.24$ ) .....	187
Figure B.26	Mixing tank temperature for various Richardson numbers ( $170 \leq Ri \leq 1244.5$ ) .....	188

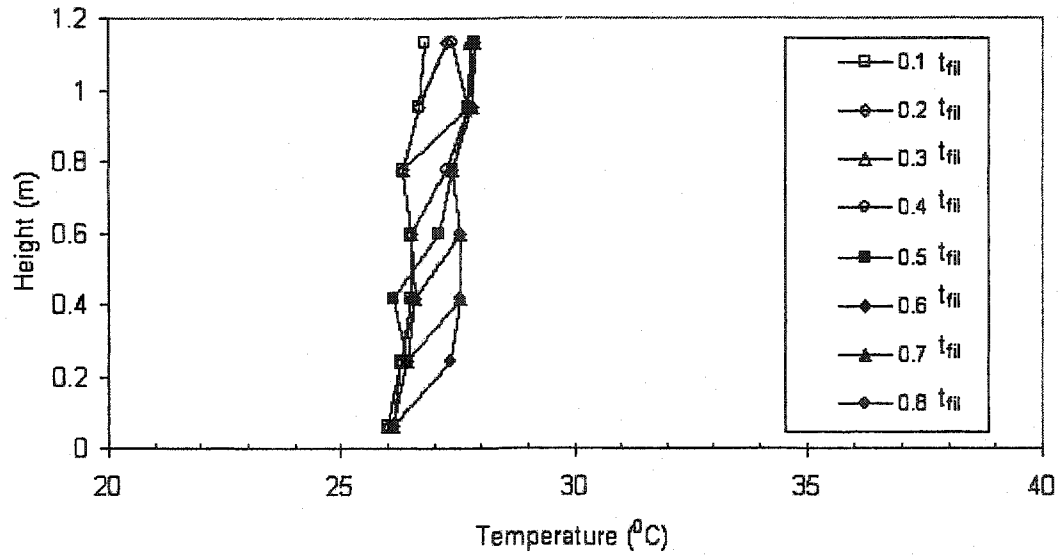


Figure B.1 Temperature profile for an inlet flow at  $T_i = 27.86 \text{ }^\circ\text{C}$  and  $u_i = 0.0315 \text{ m/s}$  ( $Re = 10691.0$ ,  $Ra = 7.34 \times 10^8$  and  $Ri = 1.0$ ).

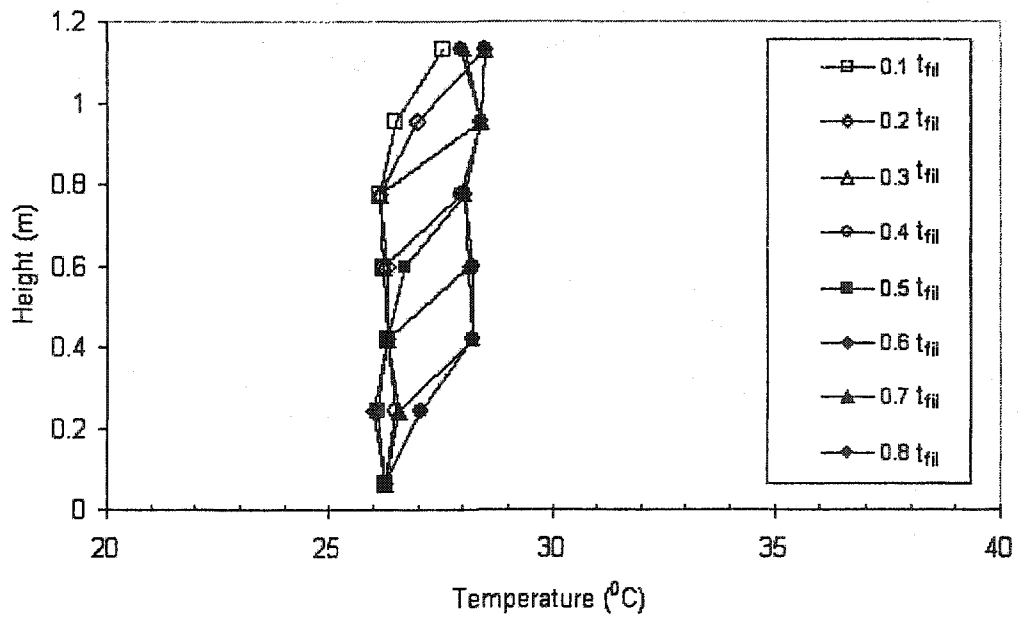


Figure B.2 Temperature profile for an inlet flow at  $T_i = 28.3 \text{ }^\circ\text{C}$  and  $u_i = 0.0315 \text{ m/s}$  ( $Re = 10691.0$ ,  $Ra = 1.05 \times 10^9$  and  $Ri = 1.56$ ).

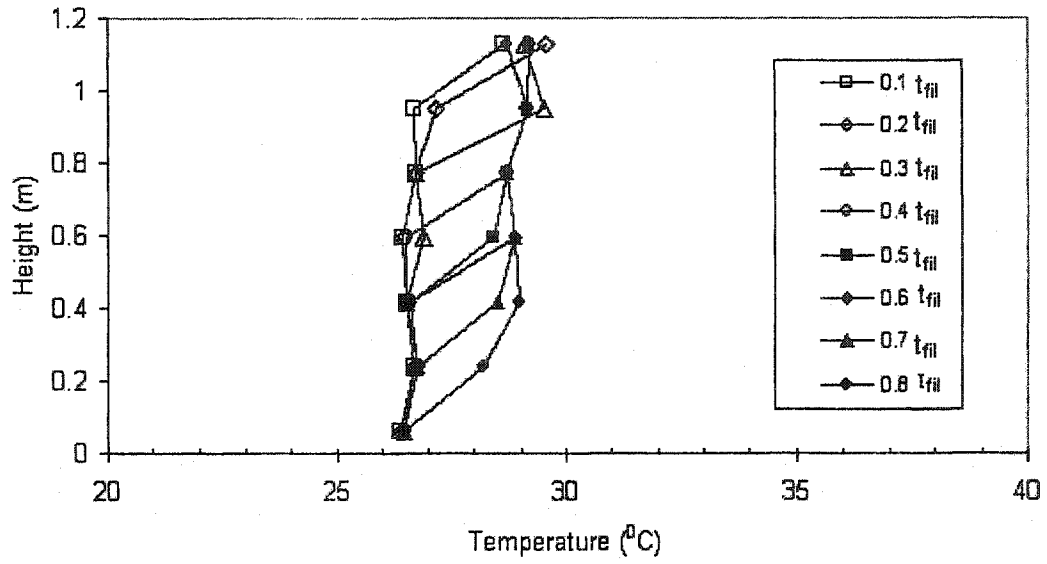


Figure B.3 Temperature profile for an inlet flow at  $T_i = 28.3 \text{ }^\circ\text{C}$  and  $u_i = 0.0315 \text{ m/s}$  ( $Re = 10948.9$ ,  $Ra = 1.25 \times 10^9$  and  $Ri = 1.82$ ).

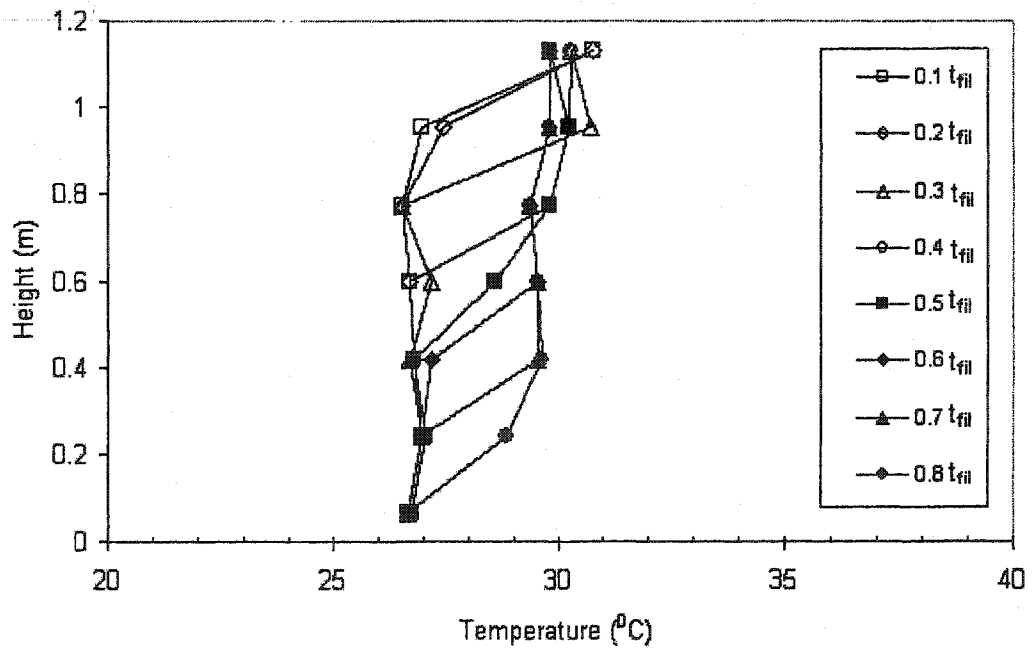


Figure B.4 Temperature profile for an inlet flow at  $T_i = 29.45 \text{ }^\circ\text{C}$  and  $u_i = 0.0315 \text{ m/s}$  ( $Re = 10948.9$ ,  $Ra = 1.54 \times 10^9$  and  $Ri = 2.24$ ).

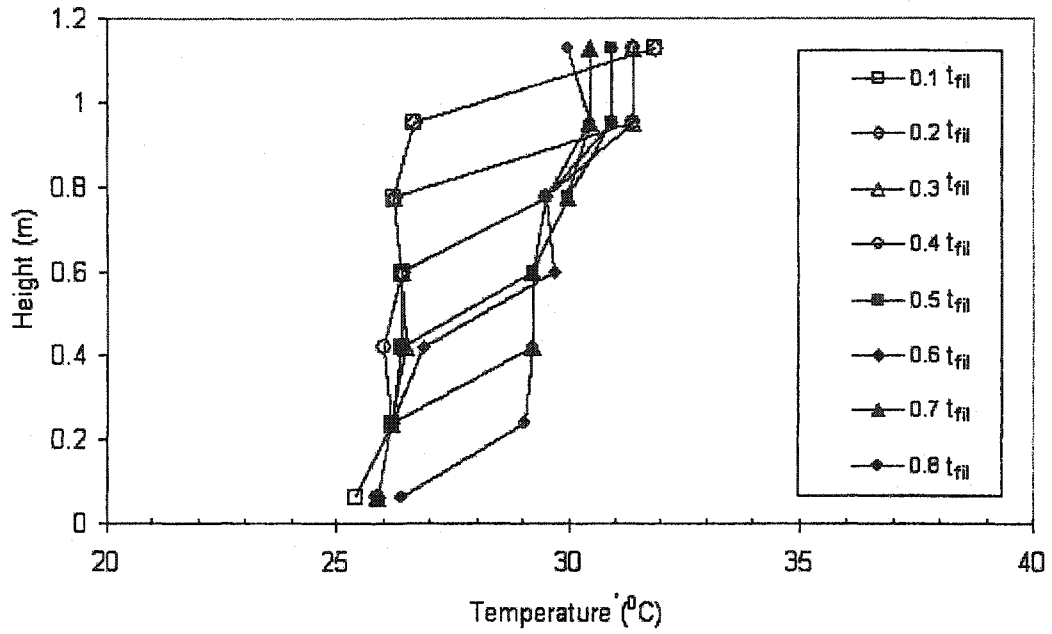


Figure B.5 Temperature profile for an inlet flow at  $T_i = 29.73 \text{ }^\circ\text{C}$  and  $u_i = 0.0315 \text{ m/s}$  ( $Re = 10948.9$ ,  $Ra = 1.89 \times 10^9$  and  $Ri = 2.75$ ).

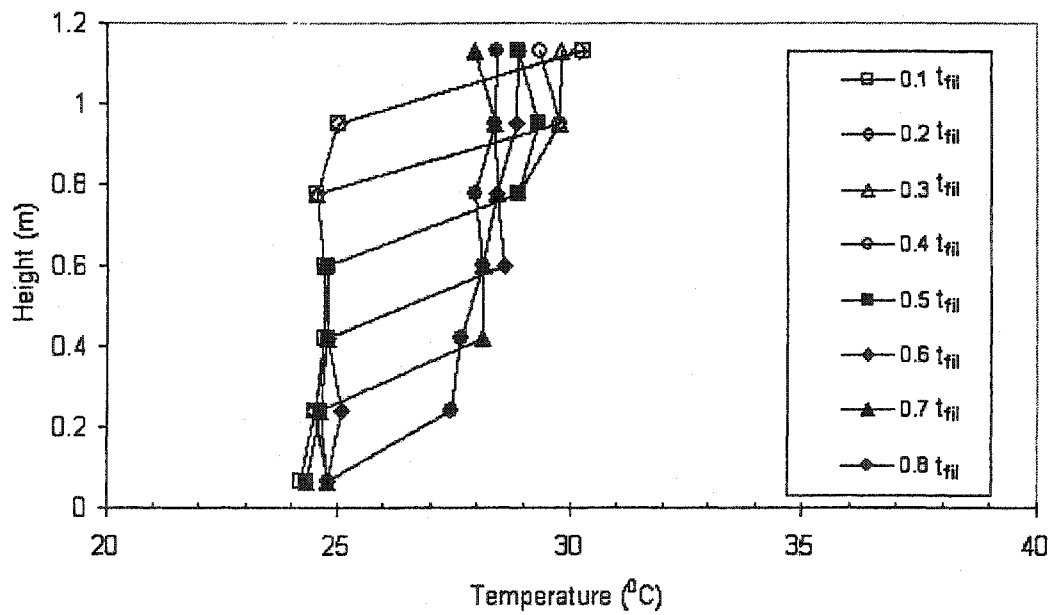


Figure B.6 Temperature profile for an inlet flow at  $T_i = 28.2 \text{ }^\circ\text{C}$  and  $u_i = 0.0315 \text{ m/s}$  ( $Re = 10445$ ,  $Ra = 2.01 \times 10^9$  and  $Ri = 3.04$ ).

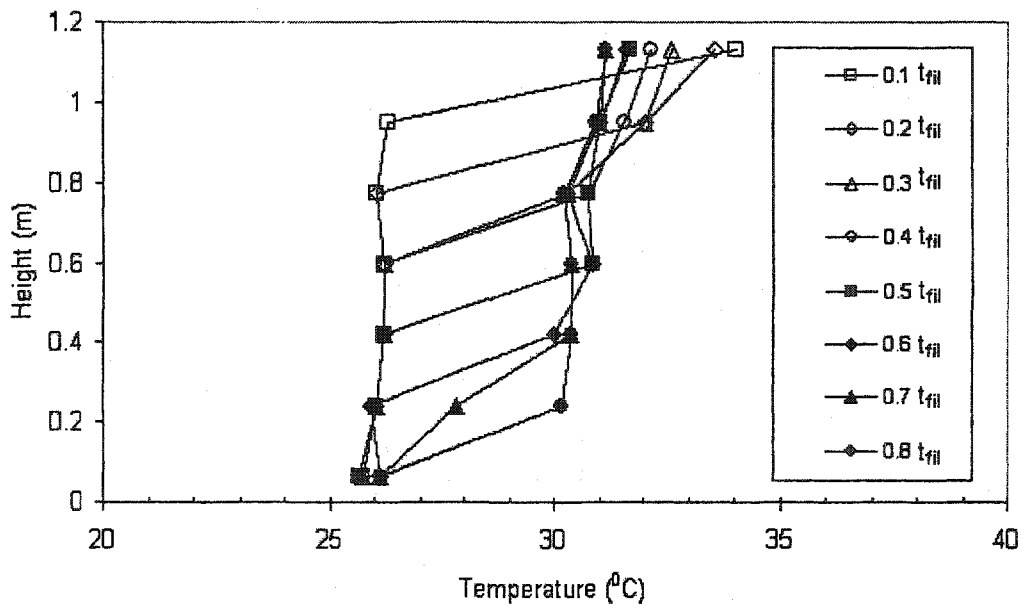


Figure B.7 Temperature profile for an inlet flow at  $T_i = 29.0 \text{ }^\circ\text{C}$  and  $u_i = 0.0137 \text{ m/s}$  ( $Re = 4782.2$ ,  $Ra = 2.25 \times 10^9$  and  $Ri = 12.84$ ).

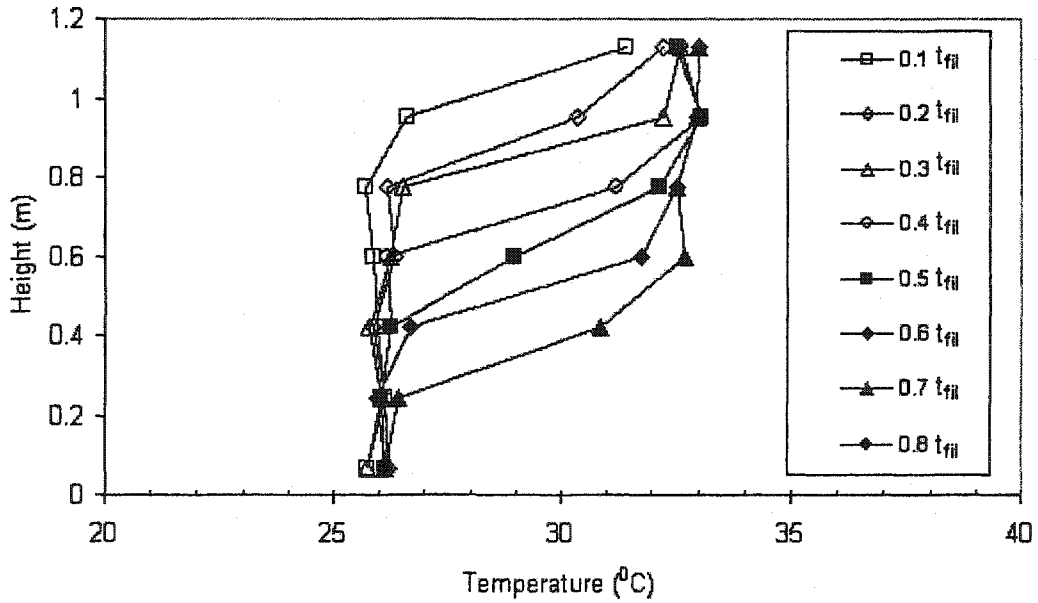


Figure B.8 Temperature profile for an inlet flow at  $T_i = 33.35.0 \text{ }^\circ\text{C}$  and  $u_i = 6.74 \times 10^{-3} \text{ m/s}$  ( $Re = 2457.14$ ,  $Ra = 4.45 \times 10^9$  and  $Ri = 135.78$ ).

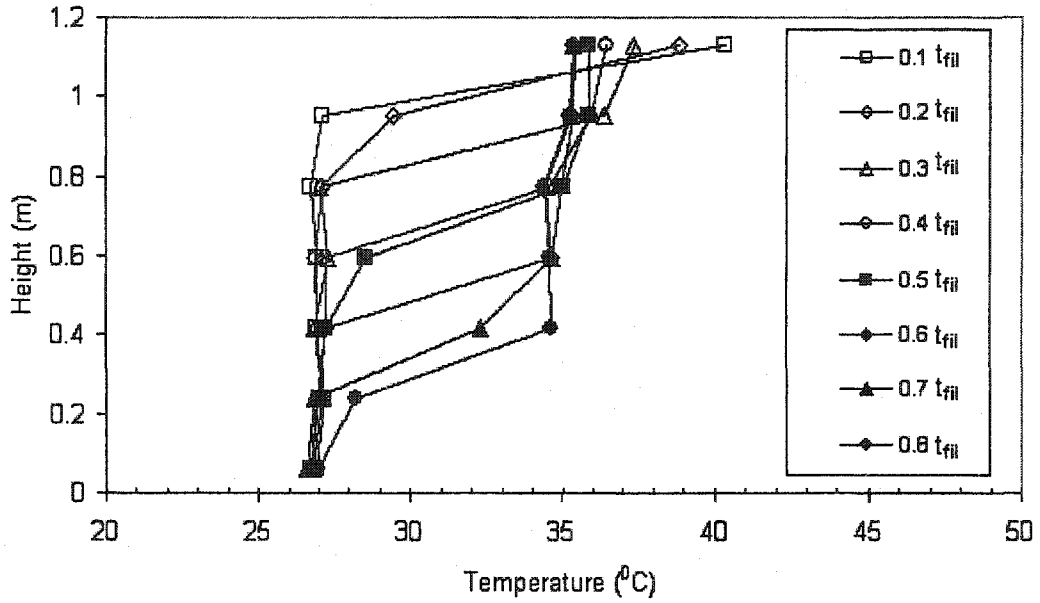


Figure B.9 Temperature profile for an inlet flow at  $T_i = 35.87 \text{ }^\circ\text{C}$  and  $u_i = 6.74 \times 10^{-3} \text{ m/s}$  ( $Re = 2501.8$ ,  $Ra = 5.66 \times 10^9$  and  $Ri = 169.98$ ).

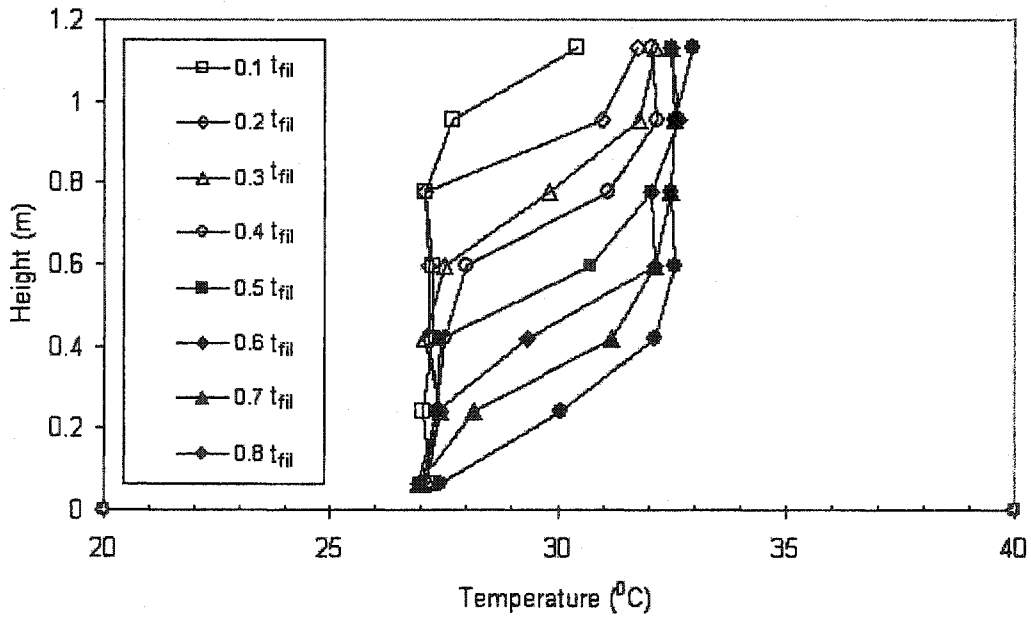


Figure B.10 Temperature profile for an inlet flow at  $T_i = 33.1 \text{ }^\circ\text{C}$  and  $u_i = 4.33 \times 10^{-3} \text{ m/s}$  ( $Re = 1581.0$ ,  $Ra = 3.7 \times 10^9$  and  $Ri = 272.63$ ).

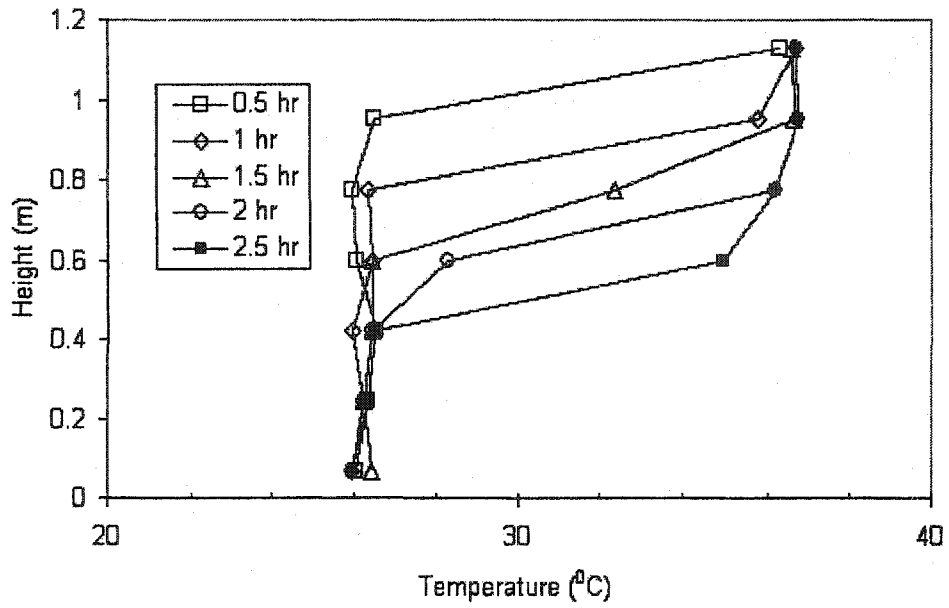


Figure B.11 Temperature profile for an inlet flow at  $T_i = 37.53 \text{ }^\circ\text{C}$  and  $u_i = 4.33 \times 10^{-3} \text{ m/s}$  ( $Re = 1650.1$ ,  $Ra = 7.43 \times 10^9$  and  $Ri = 527.24$ ).

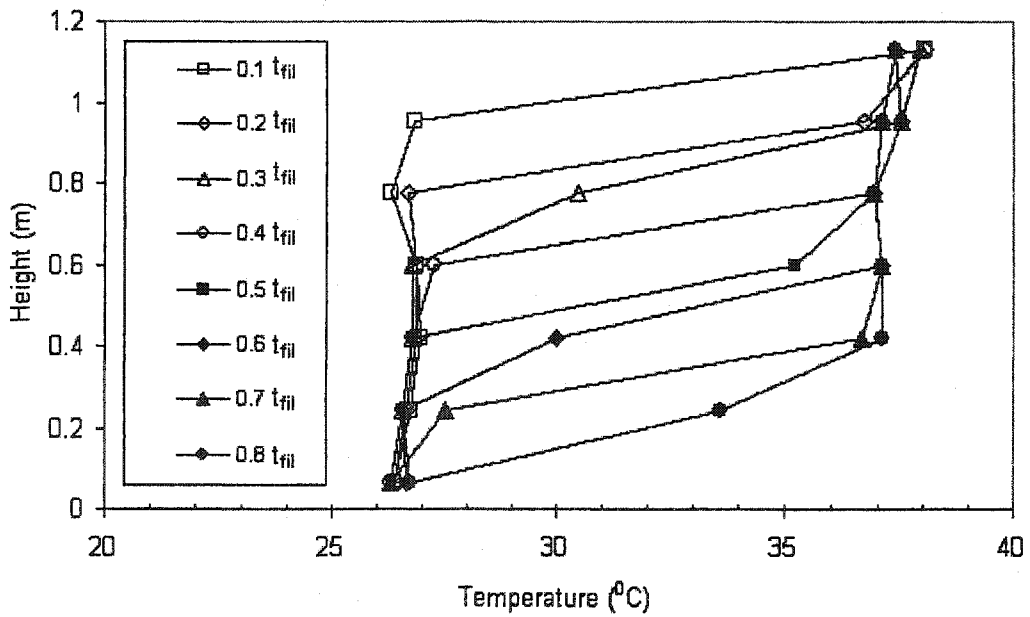


Figure B.12 Temperature profile for an inlet flow at  $T_i = 38.27 \text{ }^\circ\text{C}$  and  $u_i = 4.33 \times 10^{-3} \text{ m/s}$  ( $Re = 1650.1$ ,  $Ra = 7.98 \times 10^9$  and  $Ri = 566.4$ ).

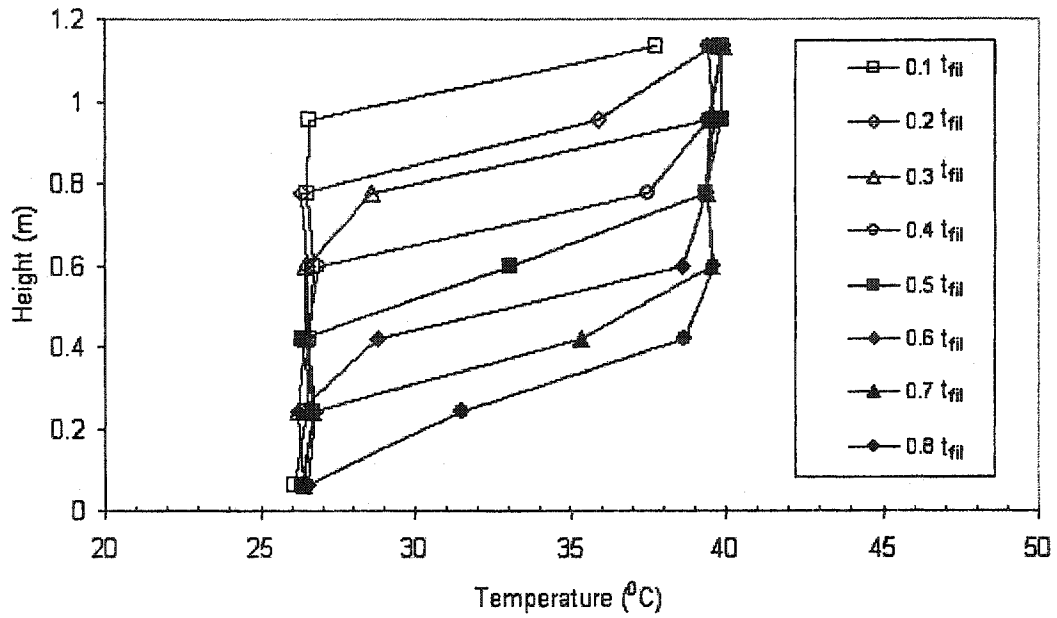


Figure B.13 Temperature profile for an inlet flow at  $T_i = 40.8 \text{ }^\circ\text{C}$  and  $u_i = 3.31 \times 10^{-3} \text{ m/s}$  ( $Re = 1292.1$ ,  $Ra = 1.04 \times 10^{10}$  and  $Ri = 1244.49$ ).

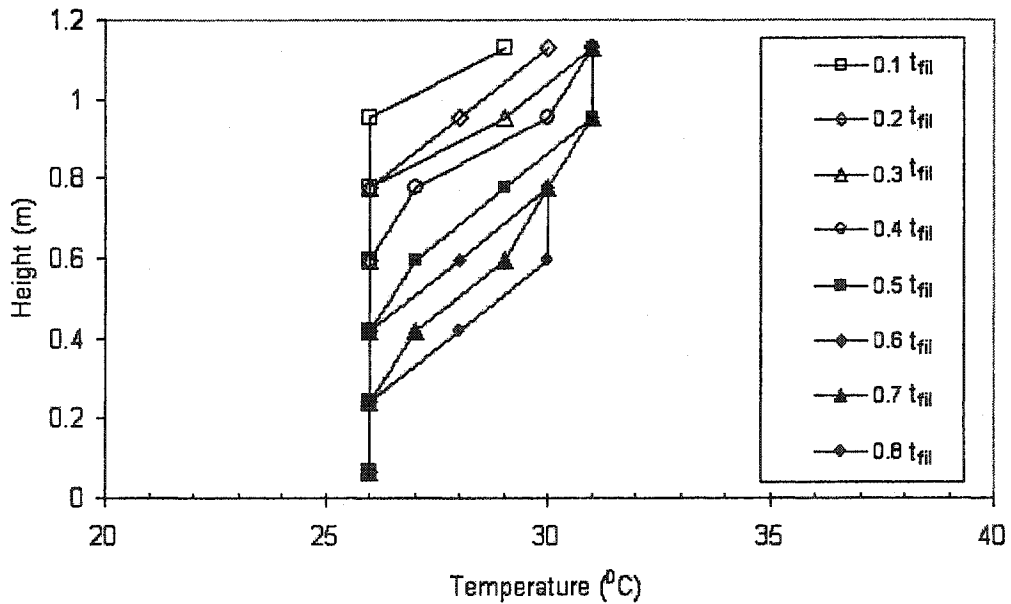


Figure B.14 Temperature profile for an inlet flow at  $T_i = 31.0 \text{ }^\circ\text{C}$  and  $u_i = 1.25 \times 10^{-3} \text{ m/s}$  ( $Re = 438.8$ ,  $Ra = 2.89 \times 10^9$  and  $Ri = 2648.8$ ).

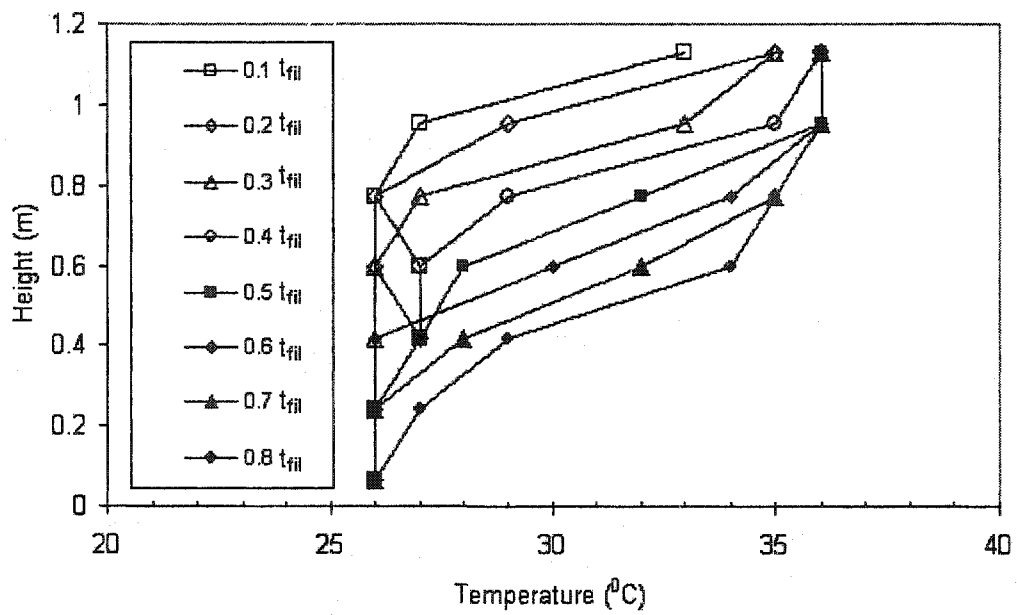


Figure B.15 Temperature profile for an inlet flow at  $T_i = 36.0 \text{ }^\circ\text{C}$  and  $u_i = 1.25 \times 10^{-3} \text{ m/s}$  ( $Re = 463.7$ ,  $Ra = 6.54 \times 10^9$  and  $Ri = 5717.56$ ).

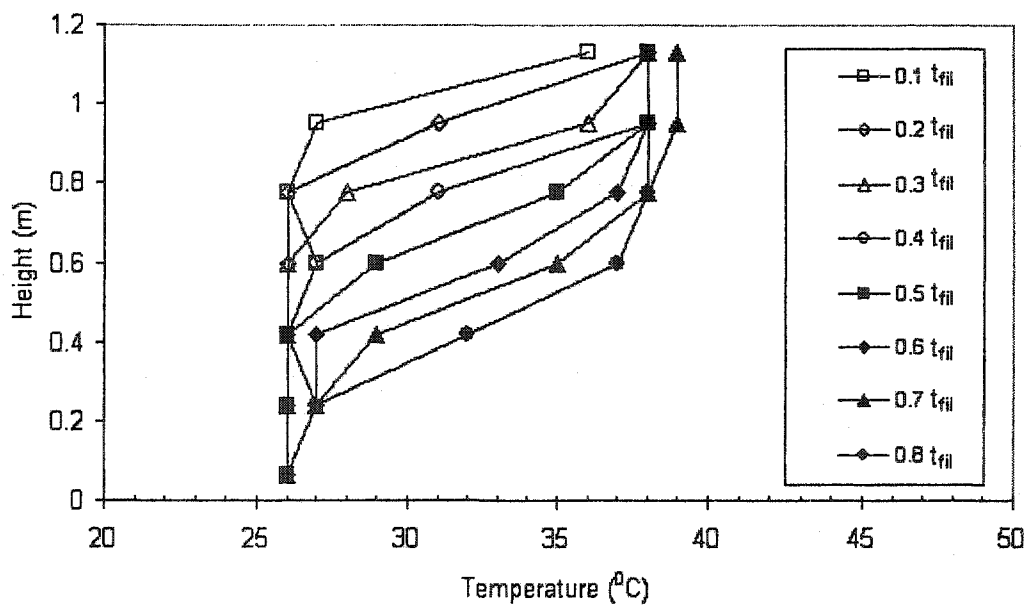


Figure B.16 Temperature profile for an inlet flow at  $T_i = 39.0 \text{ }^\circ\text{C}$  and  $u_i = 1.25 \times 10^{-3} \text{ m/s}$  ( $Re = 476.7$ ,  $Ra = 9.06 \times 10^9$  and  $Ri = 7724.9$ ).

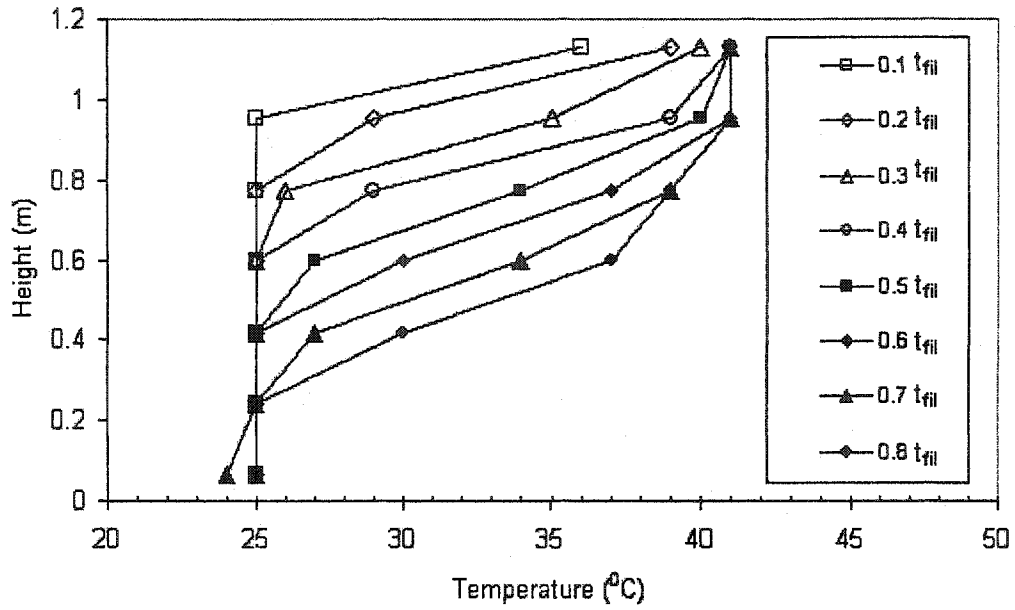


Figure B.17 Temperature profile for an inlet flow at  $T_i = 41.0 \text{ }^\circ\text{C}$  and  $u_i = 1.25 \times 10^{-3} \text{ m/s}$  ( $Re = 418.25$ ,  $Ra = 1.14 \times 10^{10}$  and  $Ri = 9627.9$ ).

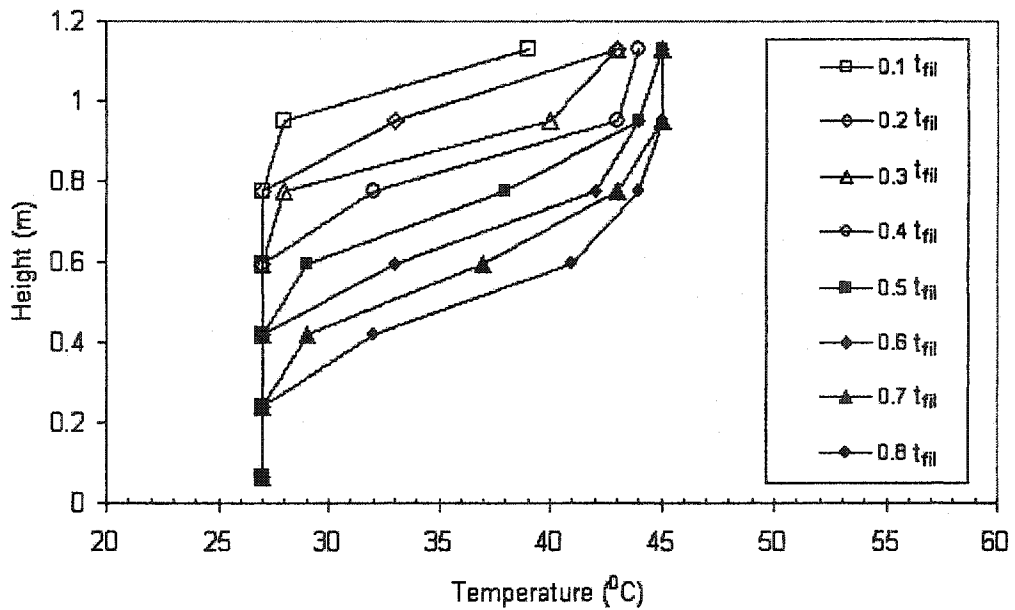


Figure B.18 Temperature profile for an inlet flow at  $T_i = 46.0 \text{ }^\circ\text{C}$  and  $u_i = 1.25 \times 10^{-3} \text{ m/s}$  ( $Re = 510.1$ ,  $Ra = 1.61 \times 10^{10}$  and  $Ri = 12939.5$ ).

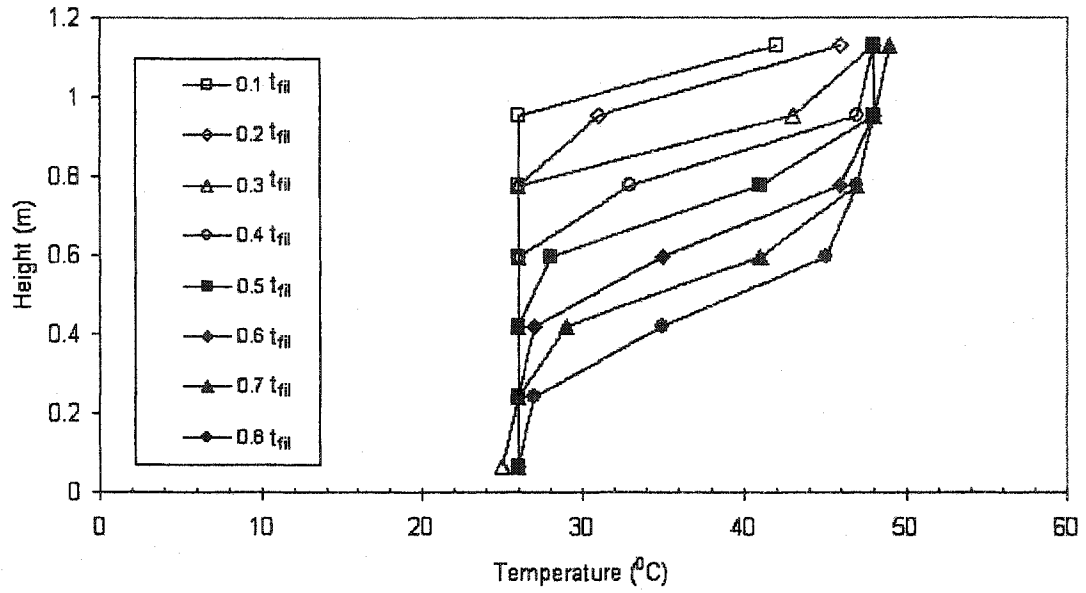


Figure B.19 Temperature profile for an inlet flow at  $T_i = 49.0\text{ }^\circ\text{C}$  and  $u_i = 1.25 \times 10^{-3}\text{ m/s}$  (Re = 525.9, Ra =  $1.96 \times 10^{10}$  and Ri = 15398.4).

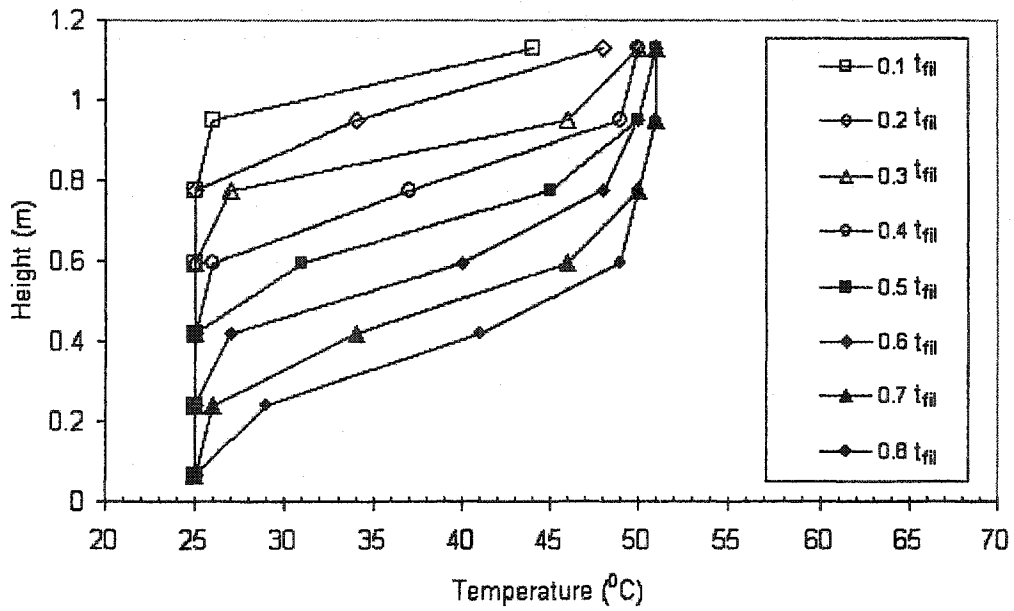


Figure B.20 Temperature profile for an inlet flow at  $T_i = 52.0\text{ }^\circ\text{C}$  and  $u_i = 1.25 \times 10^{-3}\text{ m/s}$  (Re = 537.0, Ra =  $2.4 \times 10^{10}$  and Ri = 18480.9).

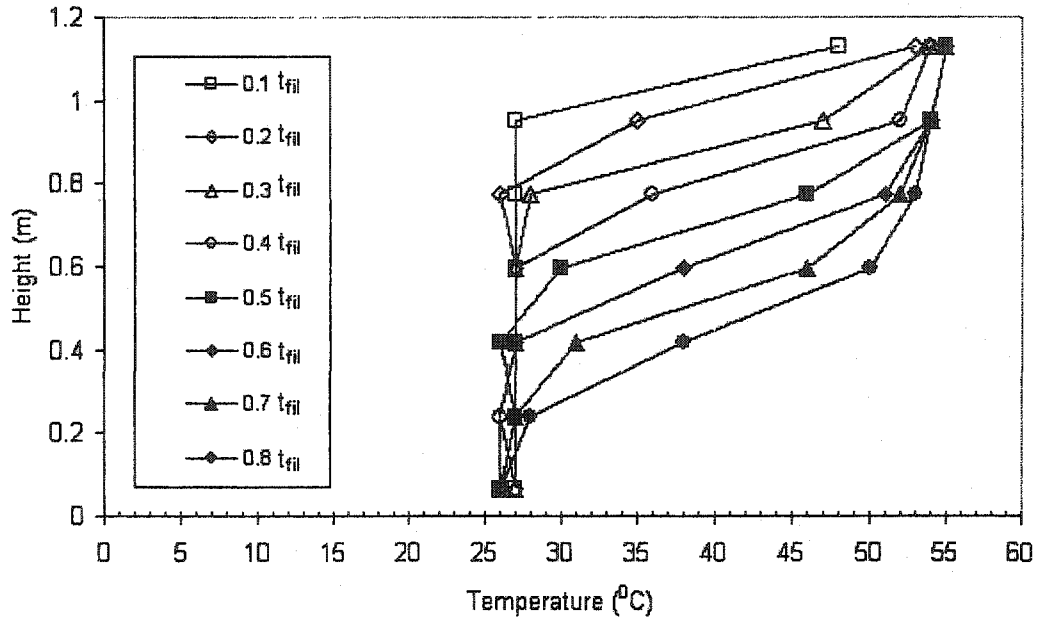


Figure B.21 Temperature profile for an inlet flow at  $T_i = 55.0^{\circ}\text{C}$  and  $u_i = 1.25 \times 10^{-3} \text{ m/s}$  ( $\text{Re} = 559.0$ ,  $\text{Ra} = 2.79 \times 10^{10}$  and  $\text{Ri} = 20691.2$ ).

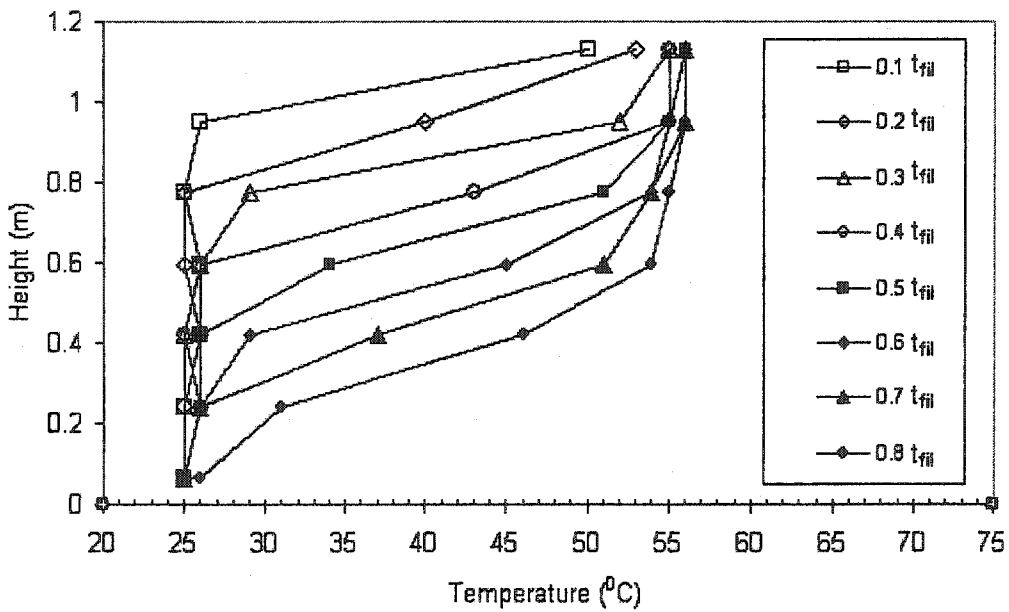


Figure B.22 Temperature profile for an inlet flow at  $T_i = 57.0^{\circ}\text{C}$  and  $u_i = 1.25 \times 10^{-3} \text{ m/s}$  ( $\text{Re} = 563.4$ ,  $\text{Ra} = 3.13 \times 10^{10}$  and  $\text{Ri} = 23093.7$ ).

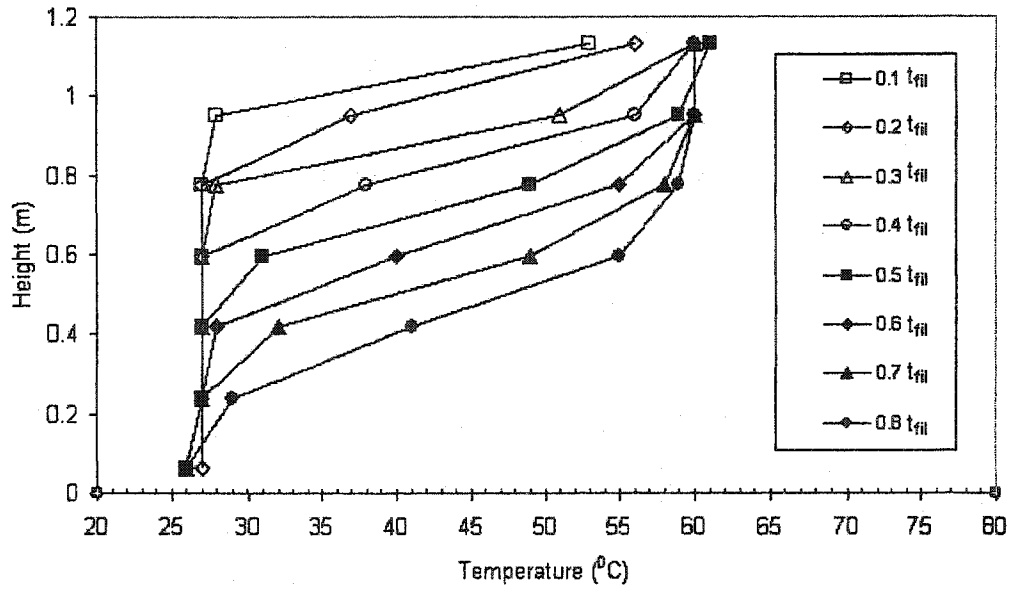


Figure B.23 Temperature profile for an inlet flow at  $T_i = 61.0 \text{ }^\circ\text{C}$  and  $u_i = 1.25 \times 10^{-3} \text{ m/s}$  ( $Re = 582.0$ ,  $Ra = 3.64 \times 10^{10}$  and  $Ri = 26145.7$ ).

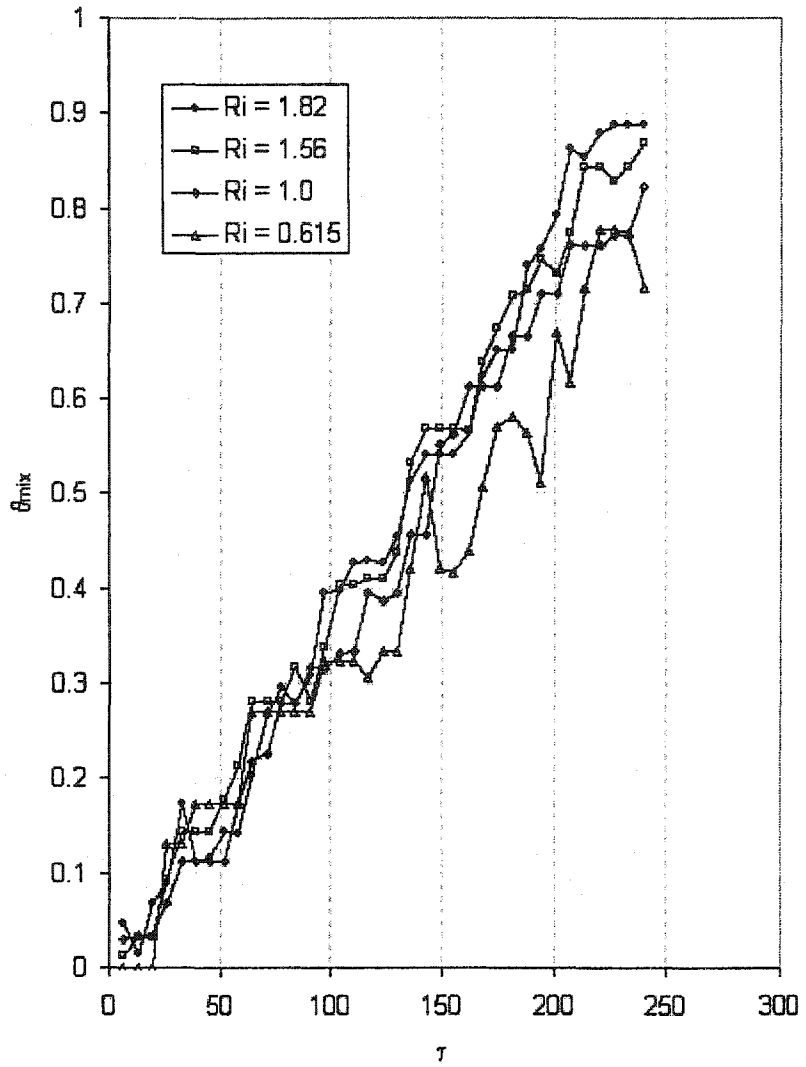


Figure B.24 Mixing tank temperature for various Richardson numbers ( $1.82 \geq Ri \geq 0.651$ ).

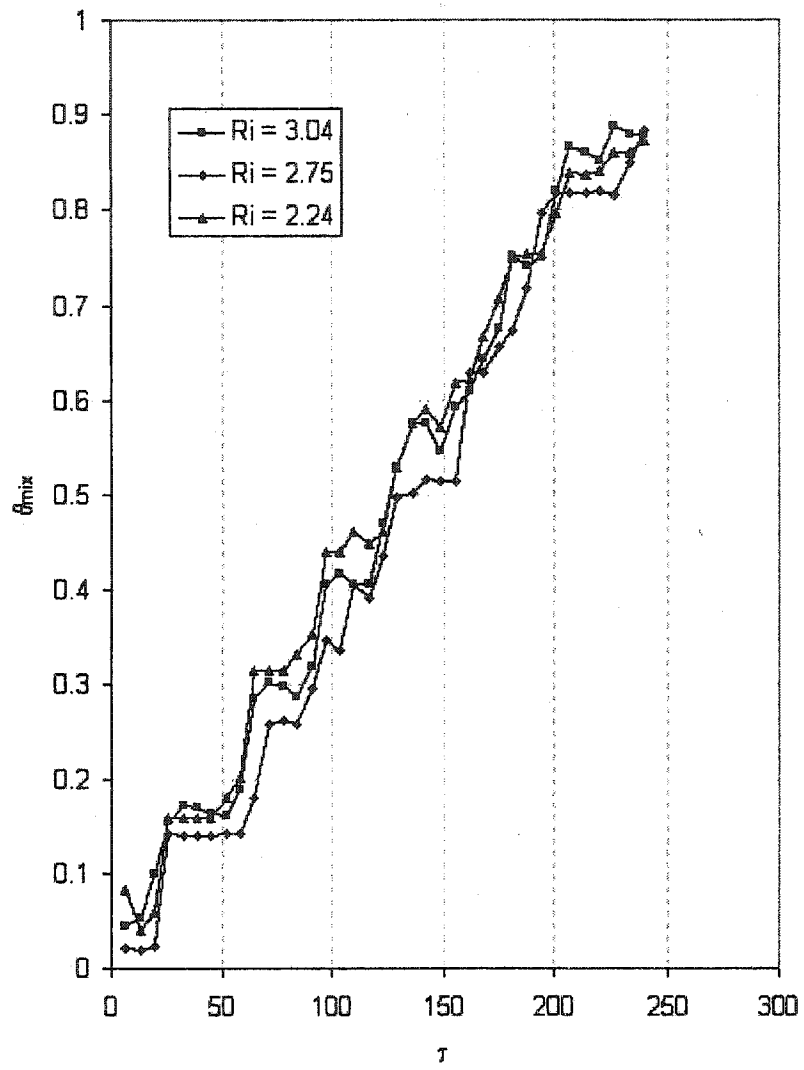


Figure B.25 Mixing tank temperature for various Richardson numbers ( $3.04 \leq Ri \leq 2.24$ ).

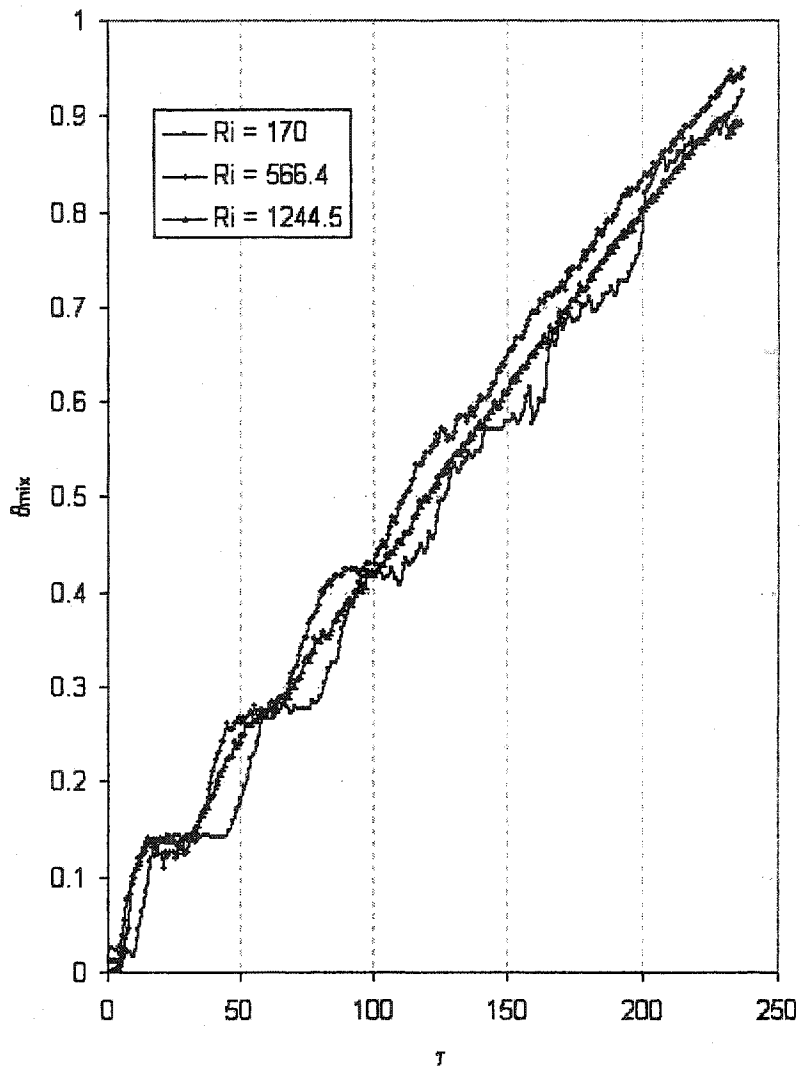


Figure B.26 Mixing tank temperature for various Richardson numbers ( $170 \leq Ri \leq 1244.5$ ).

## APPENDIX C

### Flow and Temperature Fields

Figure C.1	Flow fields in a charging process at $Re = 10^2$ and $Ra = 10^7$ ( $Ri = 185.2, \Delta\psi = 0.001$ ) .....	191
Figure C.2	Temperature fields in a charging process at $Re = 10^2$ and $Ra = 10^7$ ( $Ri = 185.2, \Delta\theta = 0.1$ ) .....	192
Figure C.3	Flow fields in a charging process at $Re = 10^3$ and $Ra = 10^7$ ( $Ri = 1.85, \Delta\psi = 0.001$ ) .....	193
Figure C.4	Temperature fields in a charging process at $Re = 10^3$ and $Ra = 10^7$ ( $Ri = 1.85, \Delta\theta = 0.1$ ) .....	194
Figure C.5	Flow fields in a charging process at $Re = 10^4$ and $Ra = 10^7$ ( $Ri = 0.0185, \Delta\psi = 0.001$ ) .....	195
Figure C.6	Temperature fields in a charging process at $Re = 10^4$ and $Ra = 10^7$ ( $Ri = 0.0185, \Delta\theta = 0.1$ ) .....	196
Figure C.7	Flow fields in a charging process at $Re = 10^3$ and $Ra = 10^8$ ( $Ri = 18.51, \Delta\psi = 0.001$ ) .....	197
Figure C.8	Temperature fields in a charging process at $Re = 10^3$ and $Ra = 10^8$ ( $Ri = 18.5, \Delta\theta = 0.1$ ) .....	198
Figure C.9	Flow fields in a charging process at $Re = 10^4$ and $Ra = 10^8$ ( $Ri = 0.185, \Delta\psi = 0.001$ ) .....	199
Figure C.10	Temperature fields in a charging process at $Re = 10^4$ and $Ra = 10^8$ ( $Ri = 0.185, \Delta\theta = 0.1$ ) .....	200
Figure C.11	Flow fields in a charging process at $Re = 10^3$ and $Ra = 10^9$ ( $Ri = 185.2, \Delta\psi = 0.001$ ) .....	201
Figure C.12	Temperature fields in a charging process at $Re = 10^3$ and $Ra = 10^9$ ( $Ri = 185.2, \Delta\theta = 0.1$ ) .....	202
Figure C.13	Flow fields in a charging process at $Re = 10^4$ and $Ra = 10^9$ ( $Ri = 1.85, \Delta\psi = 0.001$ ) .....	203
Figure C.14	Temperature fields in a charging process at $Re = 10^4$ and $Ra = 10^9$	

	( $Ri = 1.85, \Delta\theta = 0.1$ ) .....	204
Figure C.15	Mixing tank temperature for various Richardson numbers ( $Re = 10^3$ ) .....	205
Figure C.16	Mixing tank temperature for various Richardson numbers ( $Re = 10^4$ ) .....	206
Figure C.17	Dimensionless tank temperature profile at $Ri = 0.185$ ( $Re = 10^4$ and $Ra = 10^8$ ) .....	207
Figure C.18	Dimensionless tank temperature profile at $Ri = 1.85$ ( $Re = 10^3$ and $Ra = 10^7$ ) .....	208
Figure C.19	Dimensionless tank temperature profile at $Ri = 1.85$ ( $Re = 10^4$ and $Ra = 10^9$ ) .....	209
Figure C.20	Dimensionless tank temperature profile at $Ri = 18.5$ ( $Re = 10^3$ and $Ra = 10^8$ ) .....	210
Figure C.21	Dimensionless tank temperature profile at $Ri = 185.2$ ( $Re = 10^2$ and $Ra = 10^7$ ) .....	211
Figure C.22	Dimensionless tank temperature profile at $Ri = 185.2$ ( $Re = 10^3$ and $Ra = 10^9$ ) .....	212

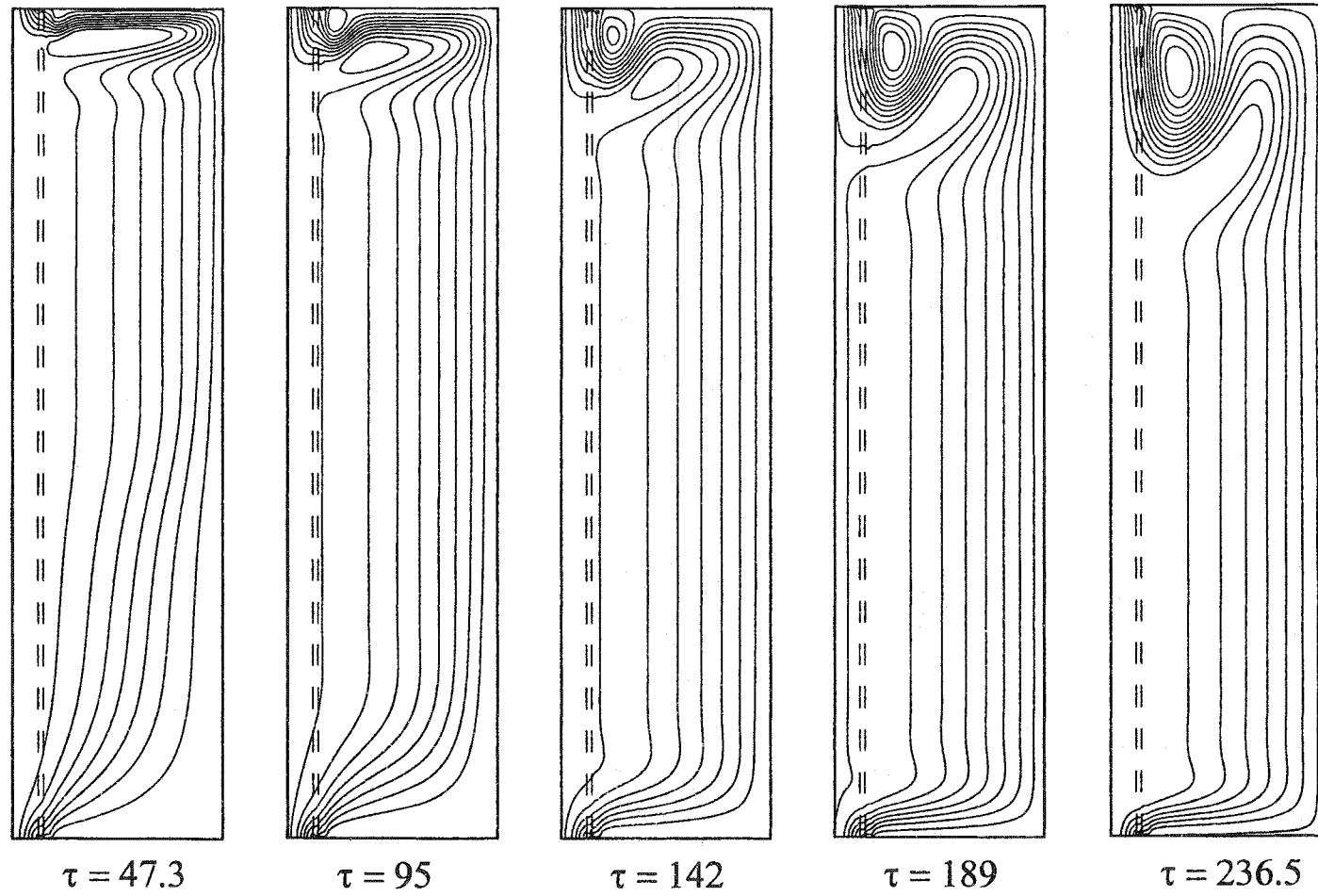


Figure C.1 Flow fields in a charging process at  $Re = 10^2$  and  $Ra = 10^7$  ( $Ri = 185.2$ ,  $\Delta\psi = 0.001$ )

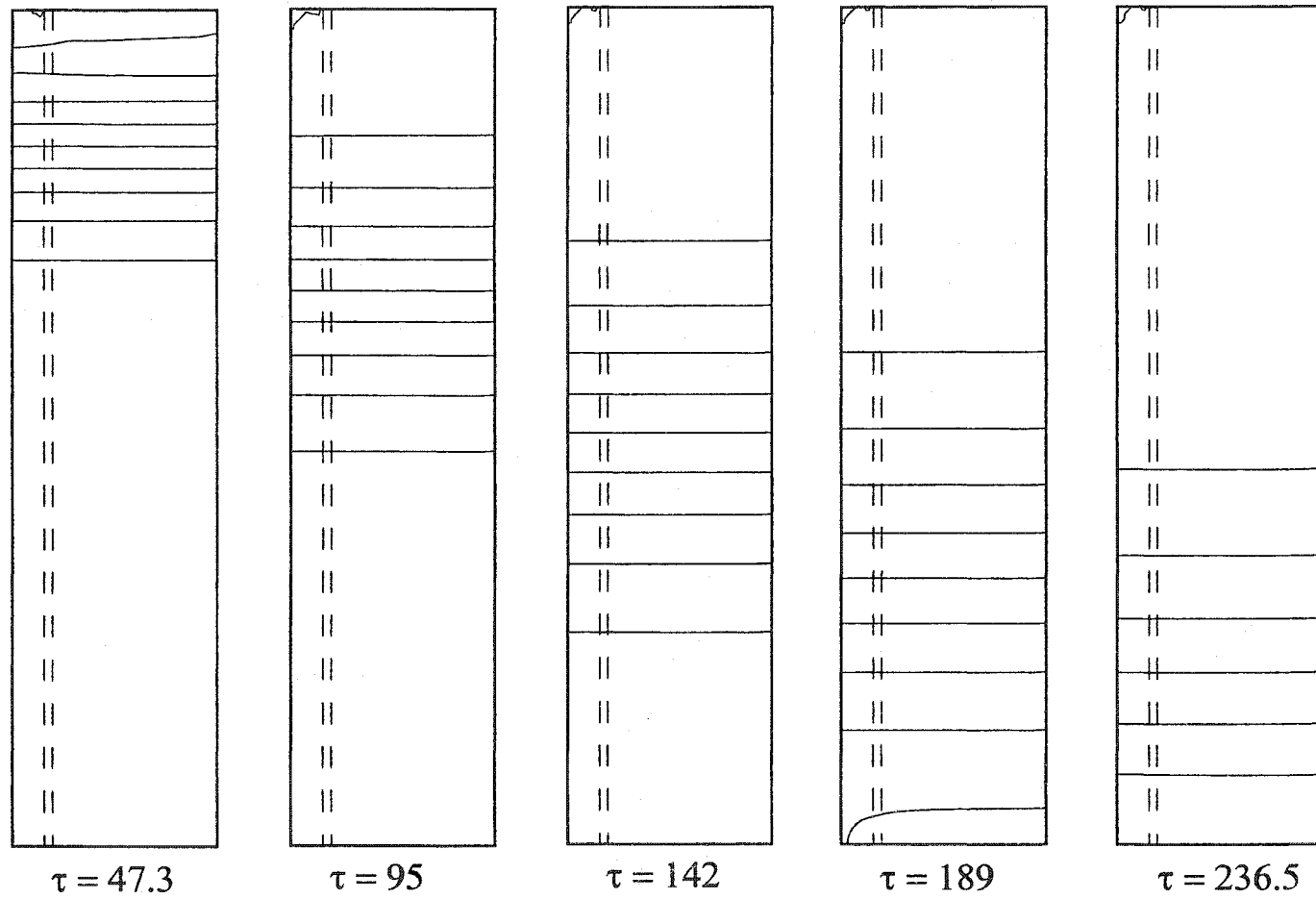


Figure C.2 Temperature fields in a charging process at  $Re = 10^2$  and  $Ra = 10^7$  ( $Ri = 185.2$ ,  $\Delta\theta = 0.1$ )

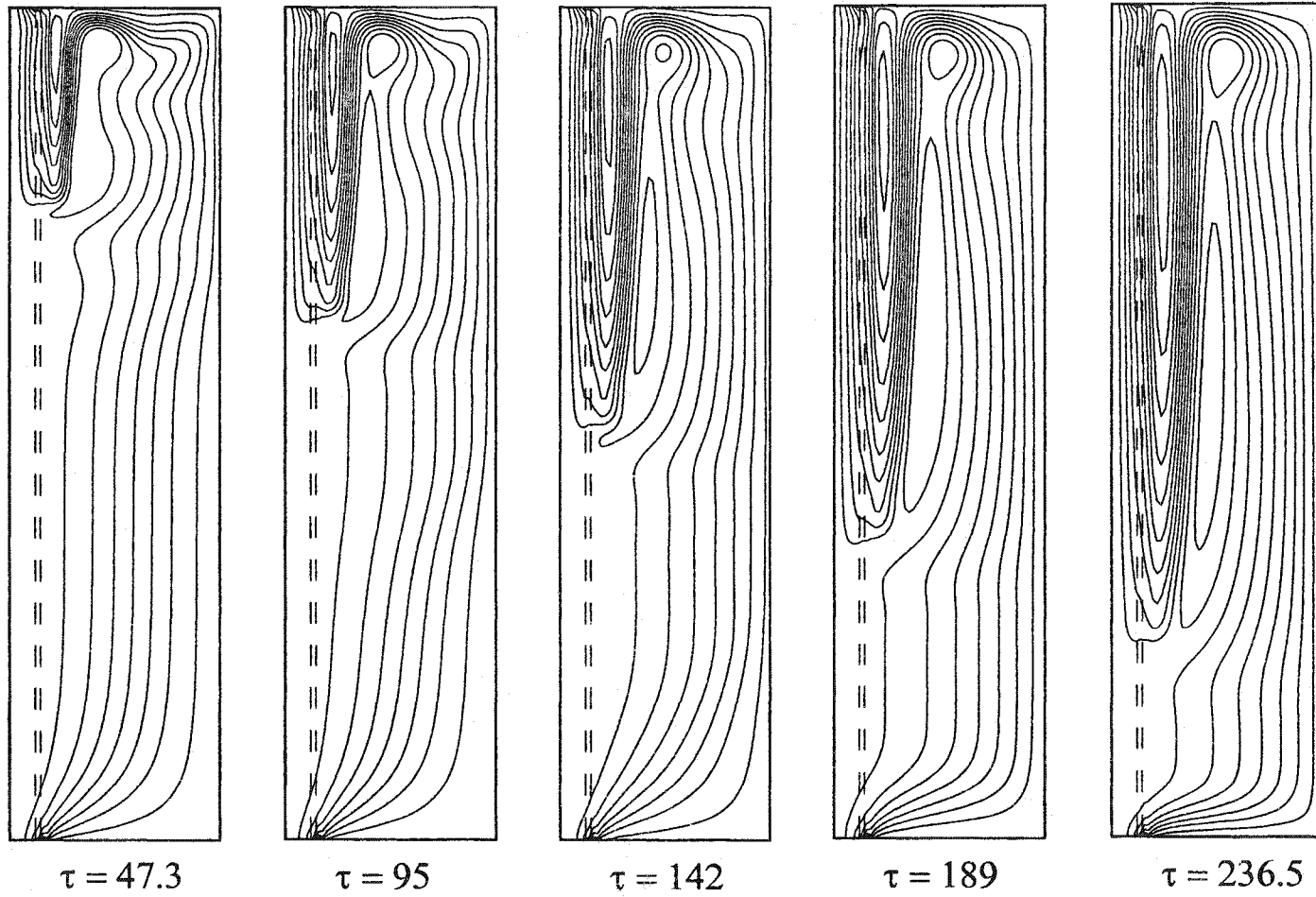


Figure C.3 Flow fields in a charging process at  $Re = 10^3$  and  $Ra = 10^7$  ( $Ri = 1.85$ ,  $\Delta\psi = 0.001$ )

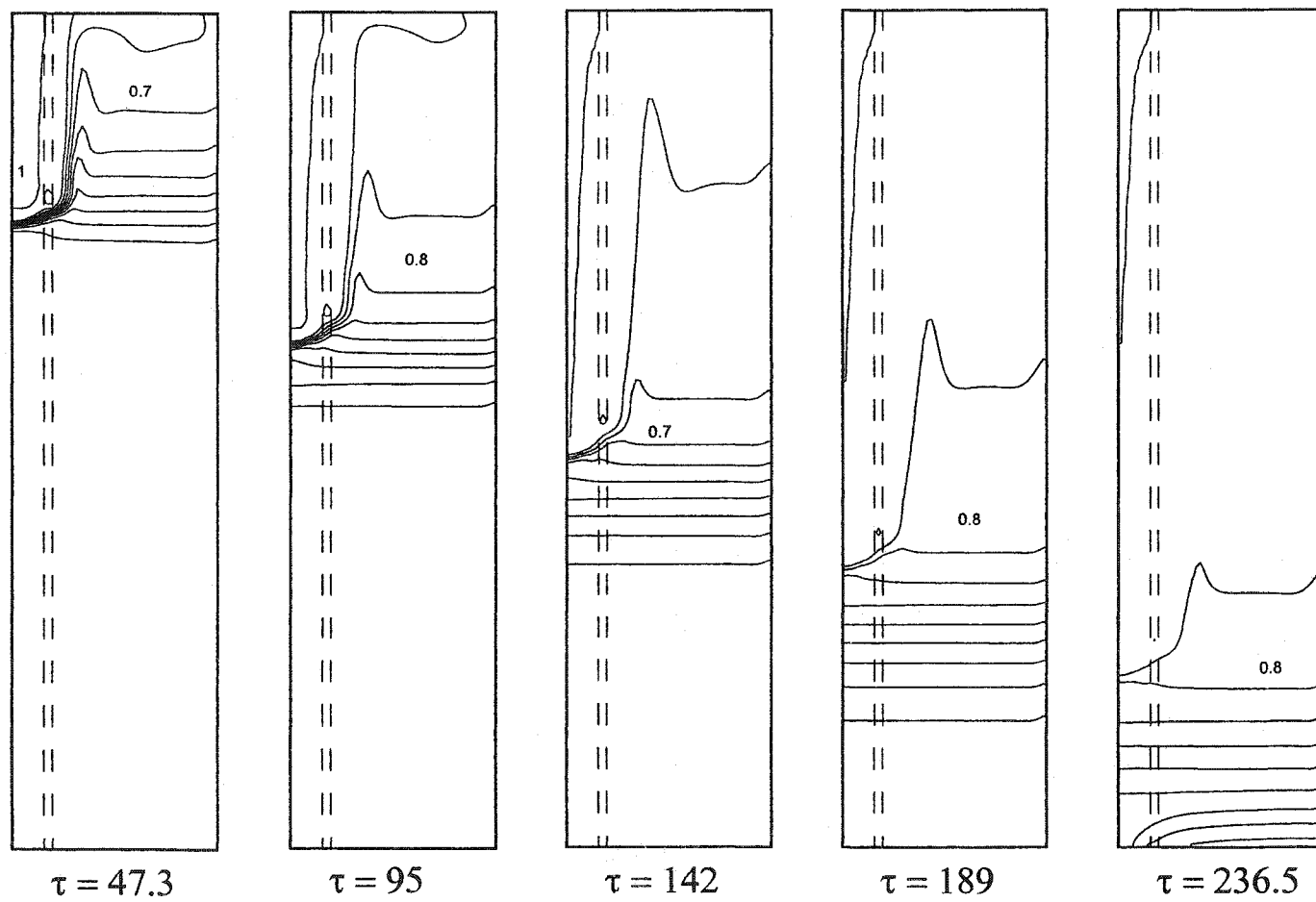


Figure C.4 Temperature fields in a charging process at  $Re = 10^3$  and  $Ra = 10^7$  ( $Ri = 1.85$ ,  $\Delta\theta = 0.1$ )

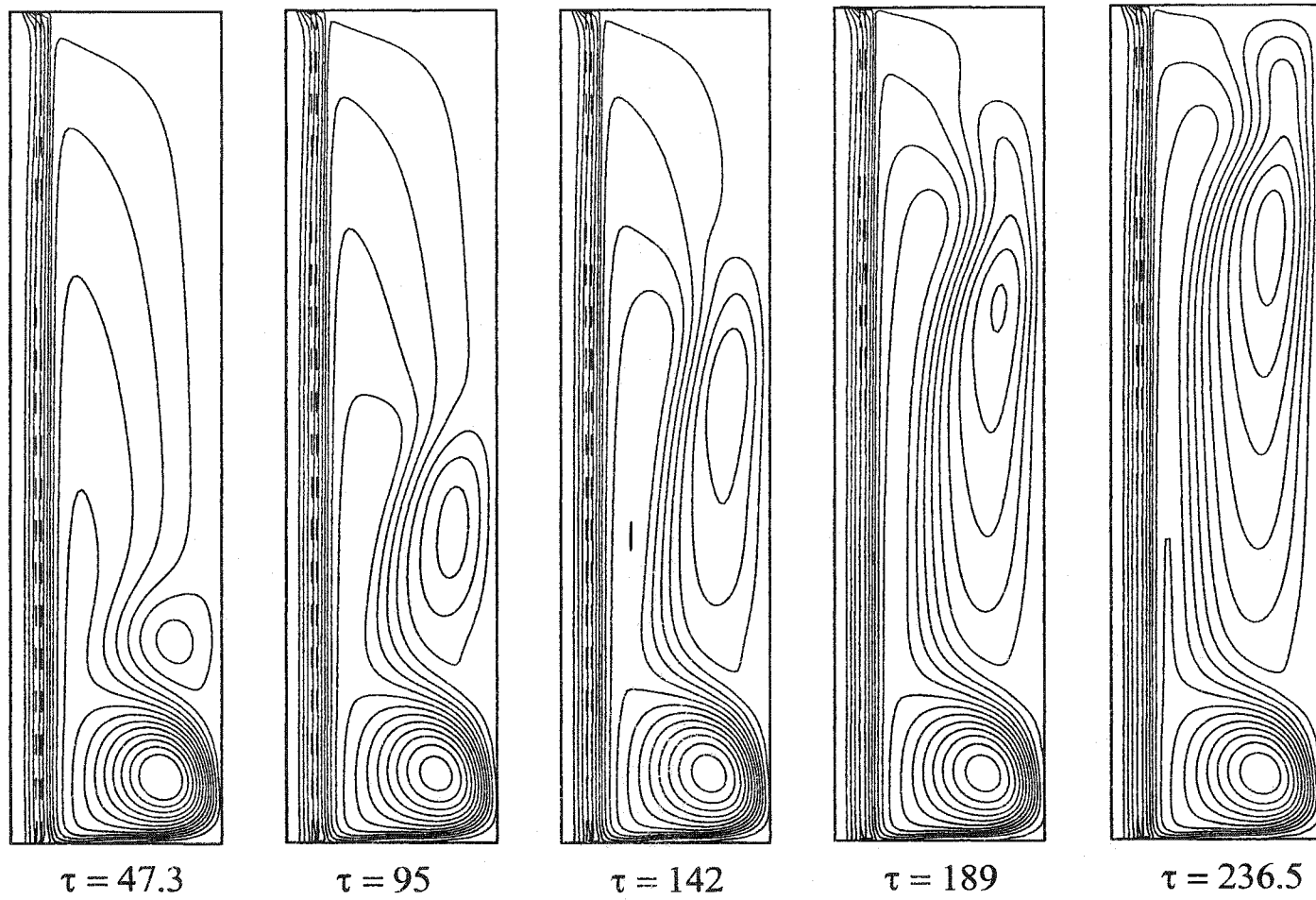


Figure C.5 Flow fields in a charging process at  $Re = 10^4$  and  $Ra = 10^7$  ( $Ri = 0.185$ ,  $\Delta\psi = 0.001$ )

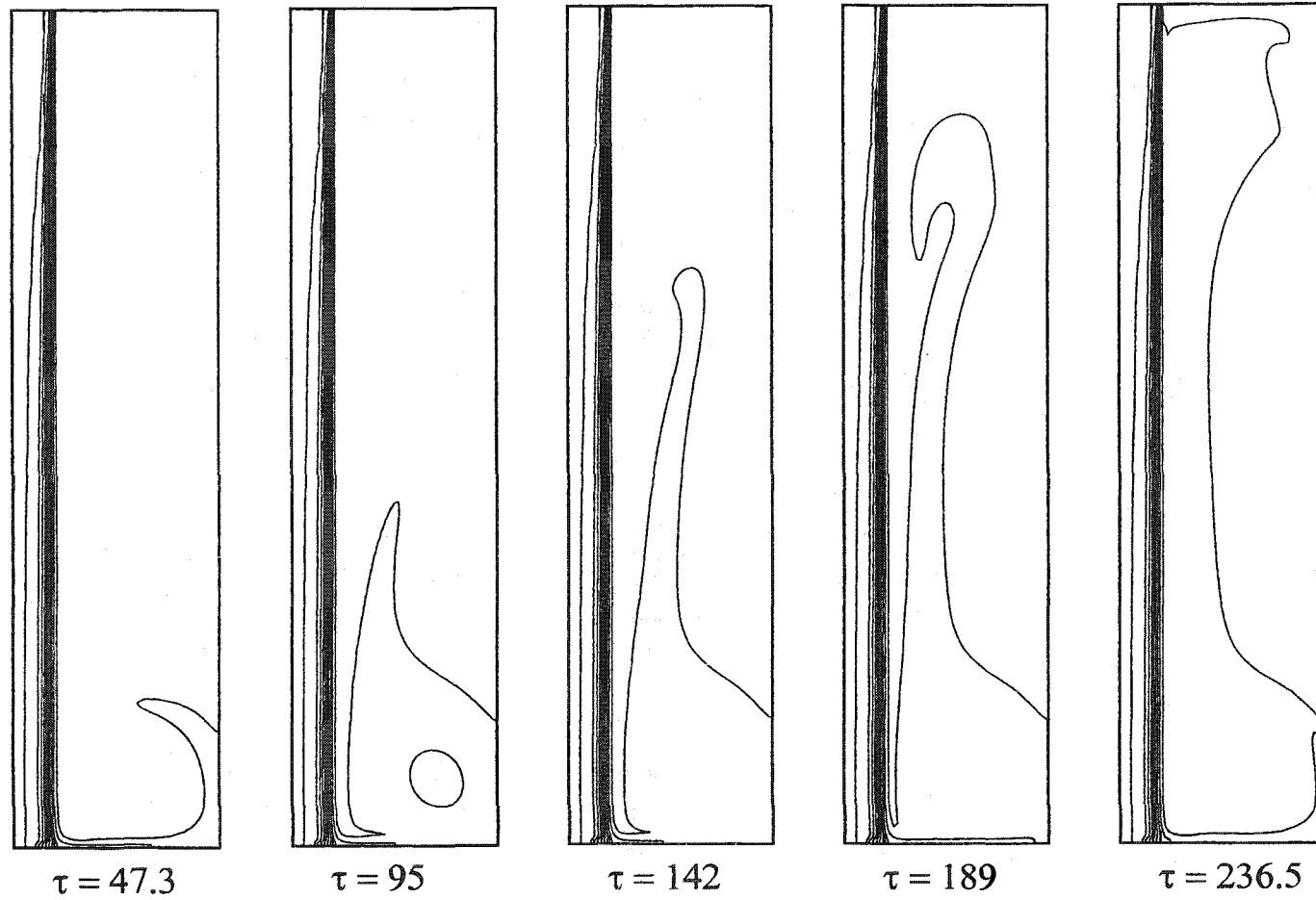


Figure C.6 Temperature fields in a charging process at  $Re = 10^4$  and  $Ra = 10^7$  ( $Ri = 0.0185$ ,  $\Delta\theta = 0.1$ )

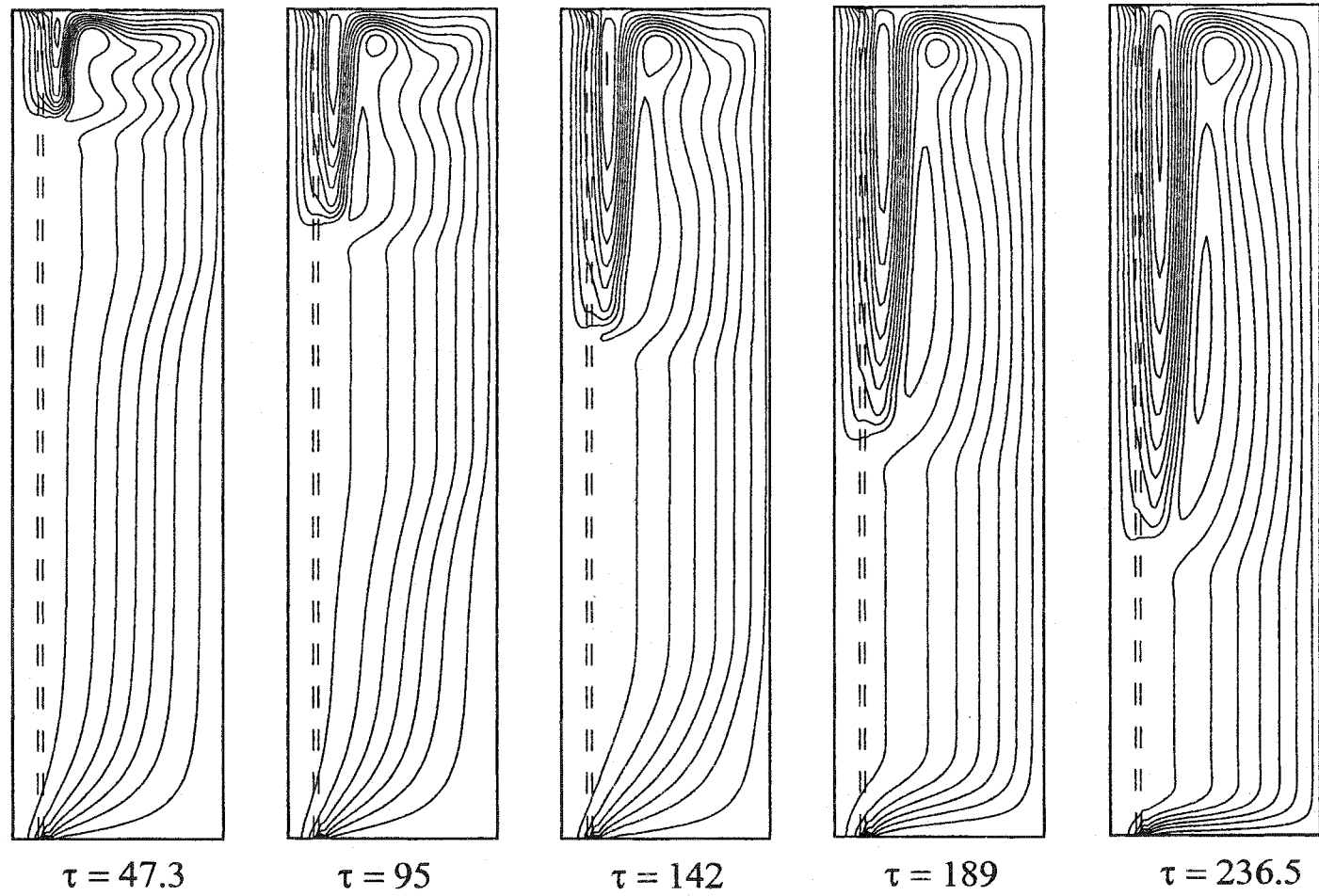


Figure C.7 Flow fields in a charging process at  $Re = 10^3$  and  $Ra = 10^8$  ( $Ri = 18.51$ ,  $\Delta\psi = 0.001$ )

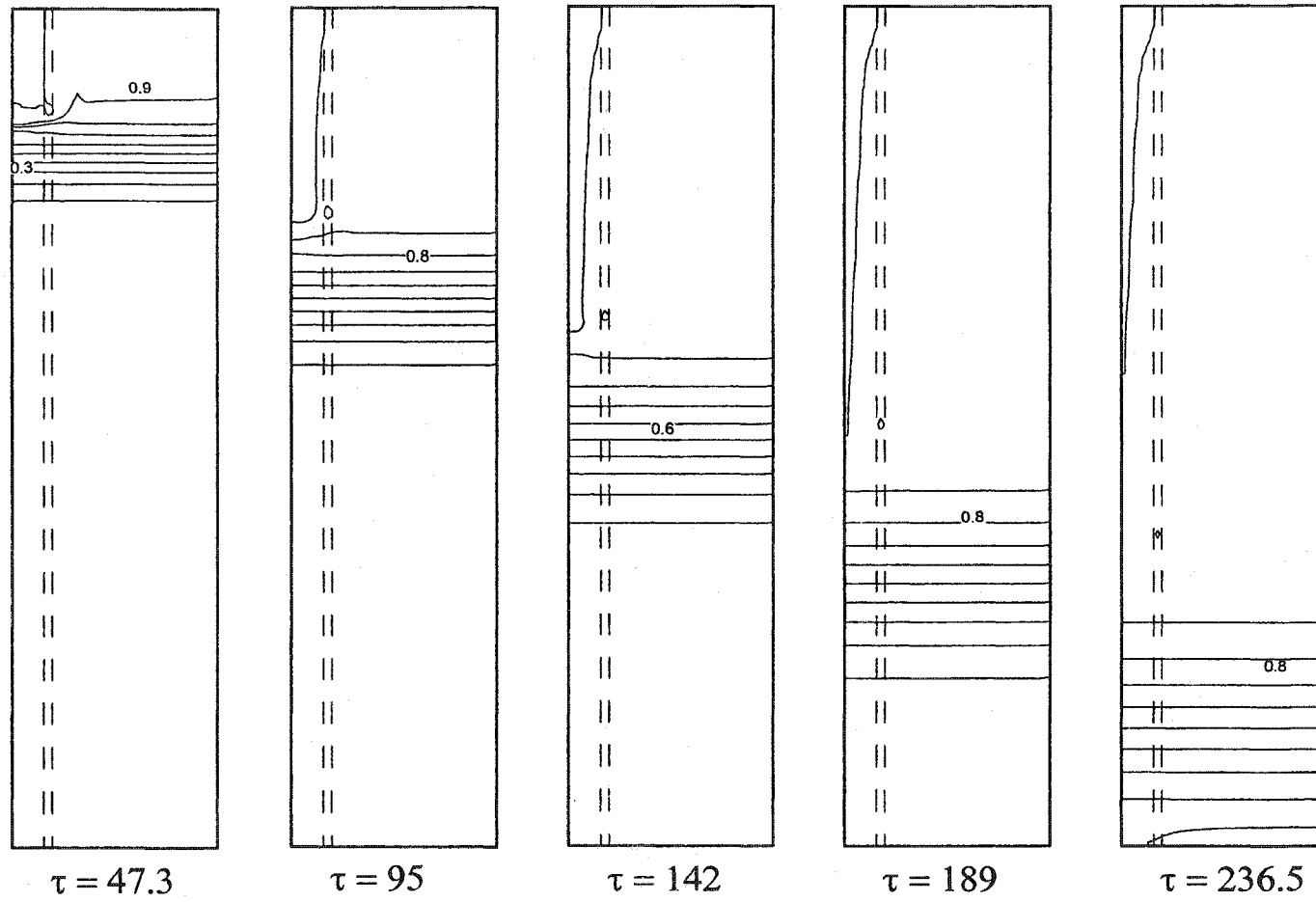


Figure C.8 Temperature fields in a charging process at  $Re = 10^3$  and  $Ra = 10^8$  ( $Ri = 18.5$ ,  $\Delta\theta = 0.1$ )

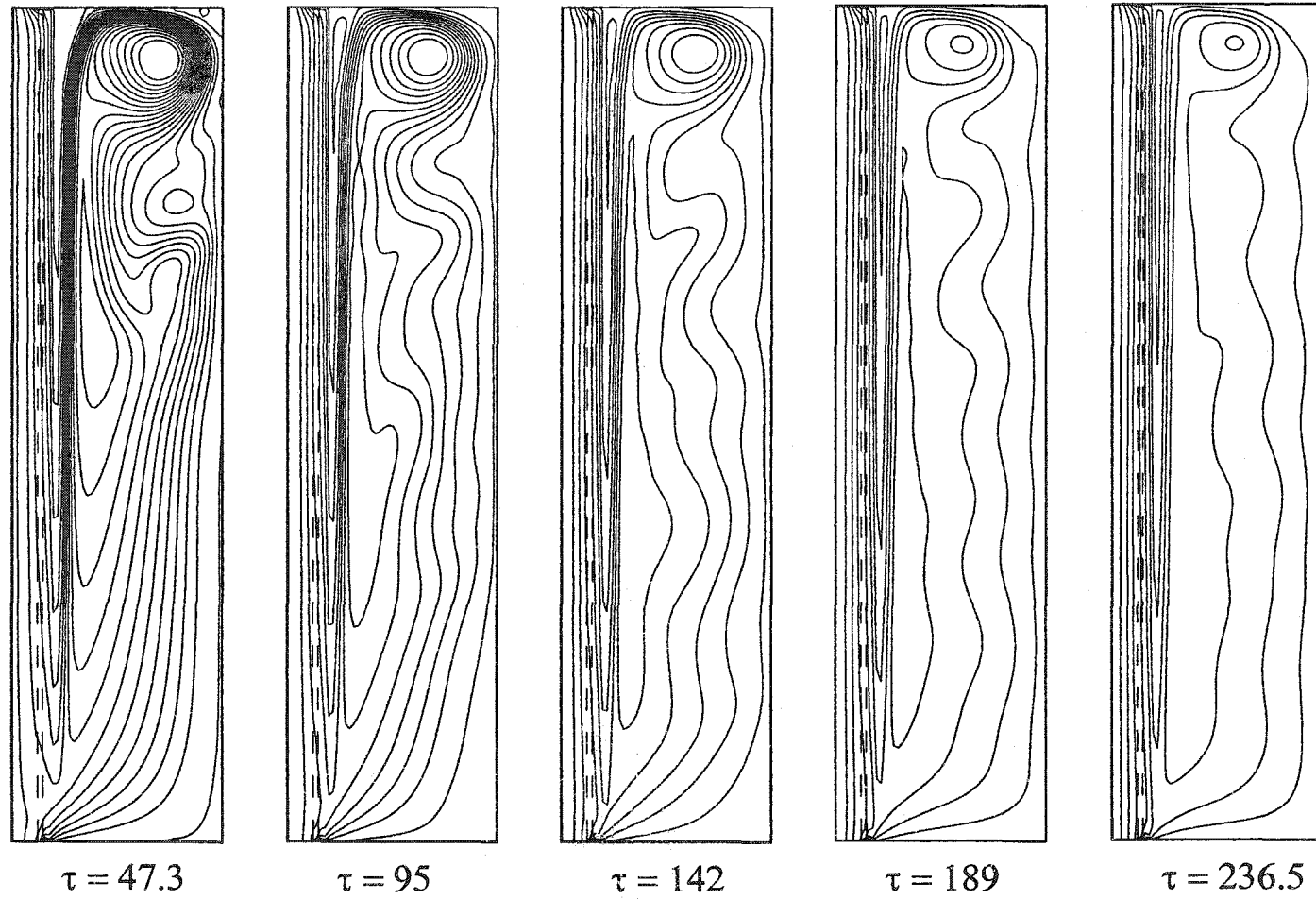


Figure C.9 Flow fields in a charging process at  $Re = 10^4$  and  $Ra = 10^8$  ( $Ri = 0.185$ ,  $\Delta\psi = 0.001$ )

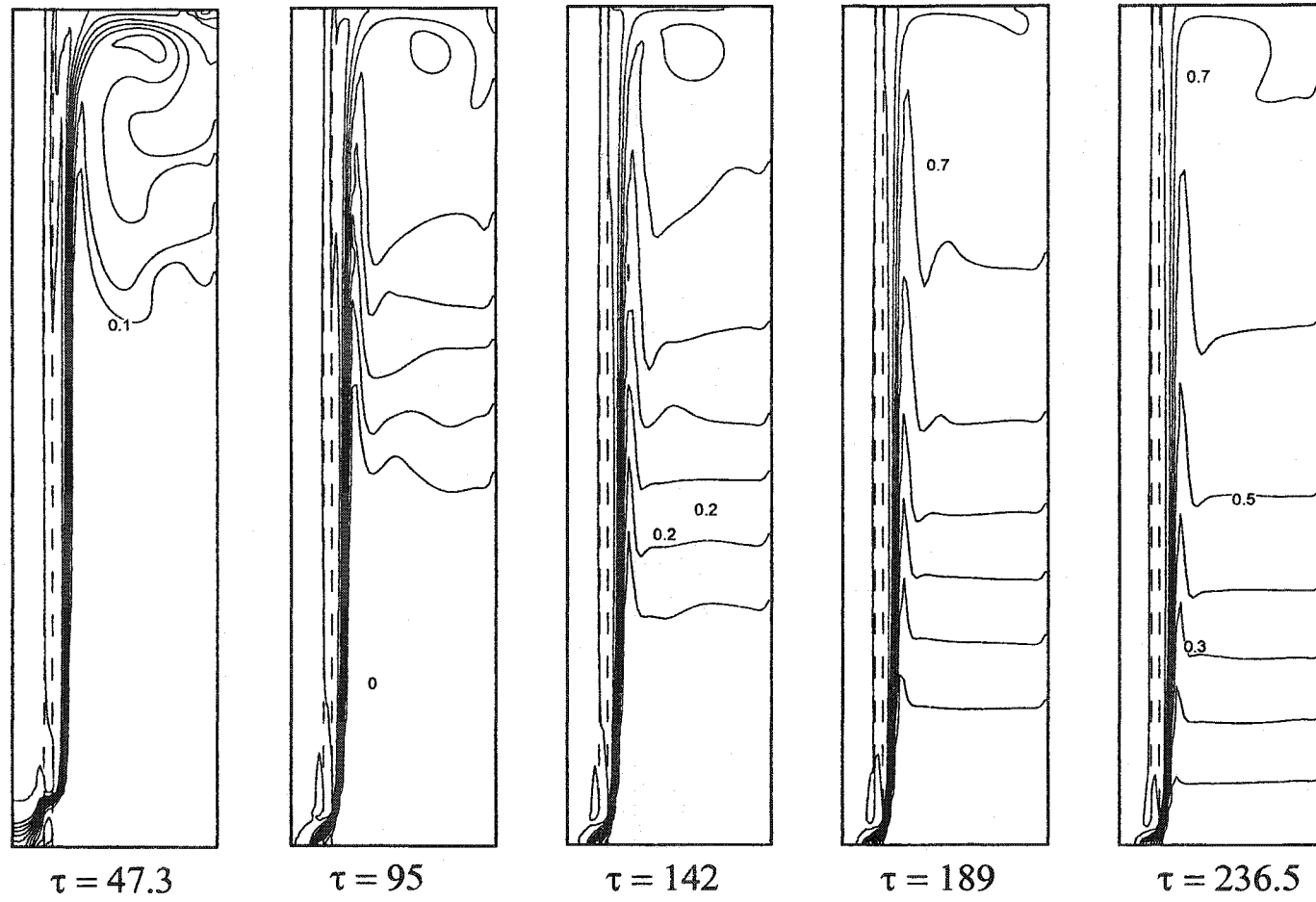


Figure C.10 Temperature fields in a charging process at  $Re = 10^4$  and  $Ra = 10^8$  ( $Ri = 0.185$ ,  $\Delta\theta = 0.1$ )

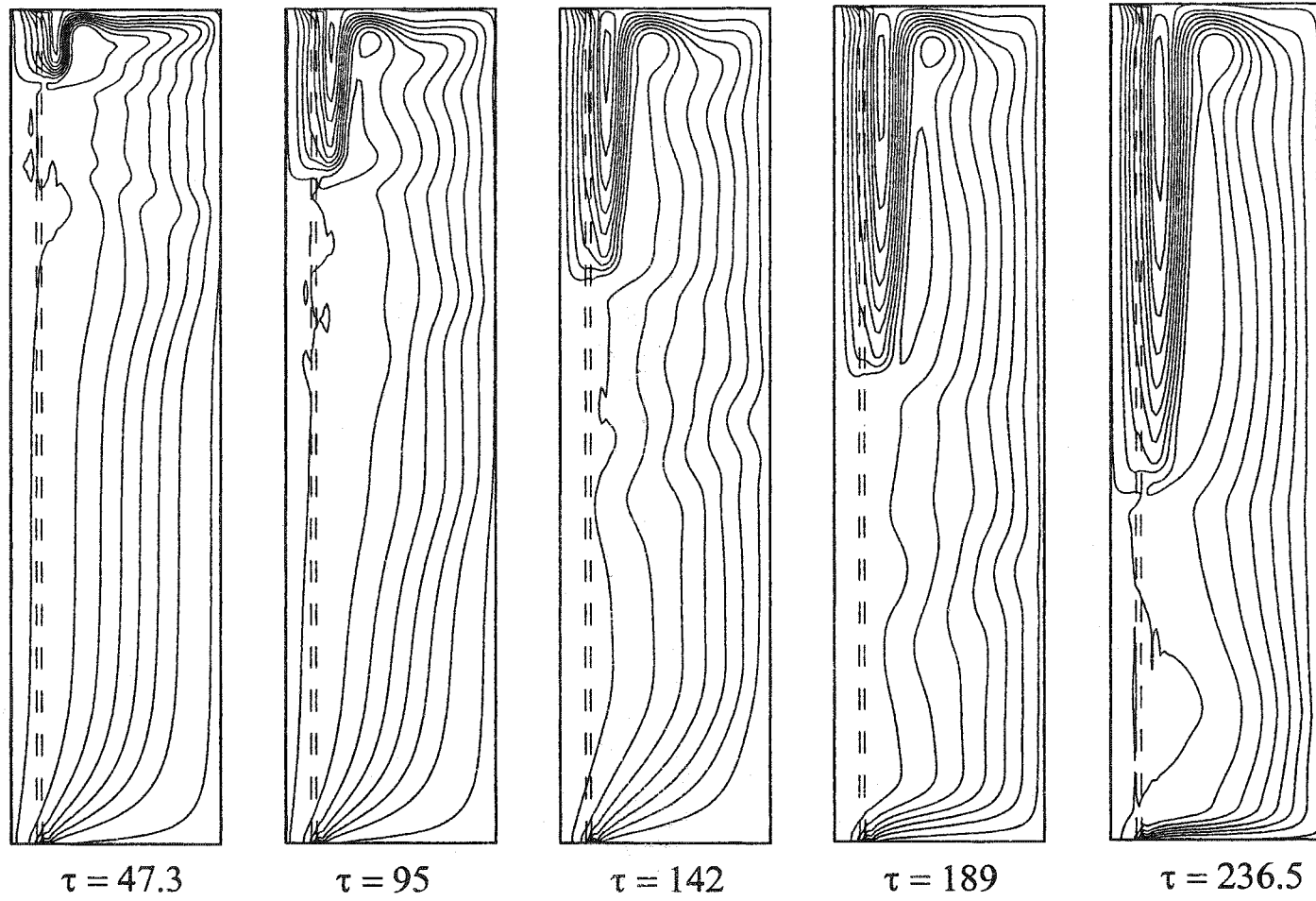


Figure C.11 Flow fields in a charging process at  $Re = 10^2$  and  $Ra = 10^9$  ( $Ri = 1.852$ ,  $\Delta\psi = 0.001$ )

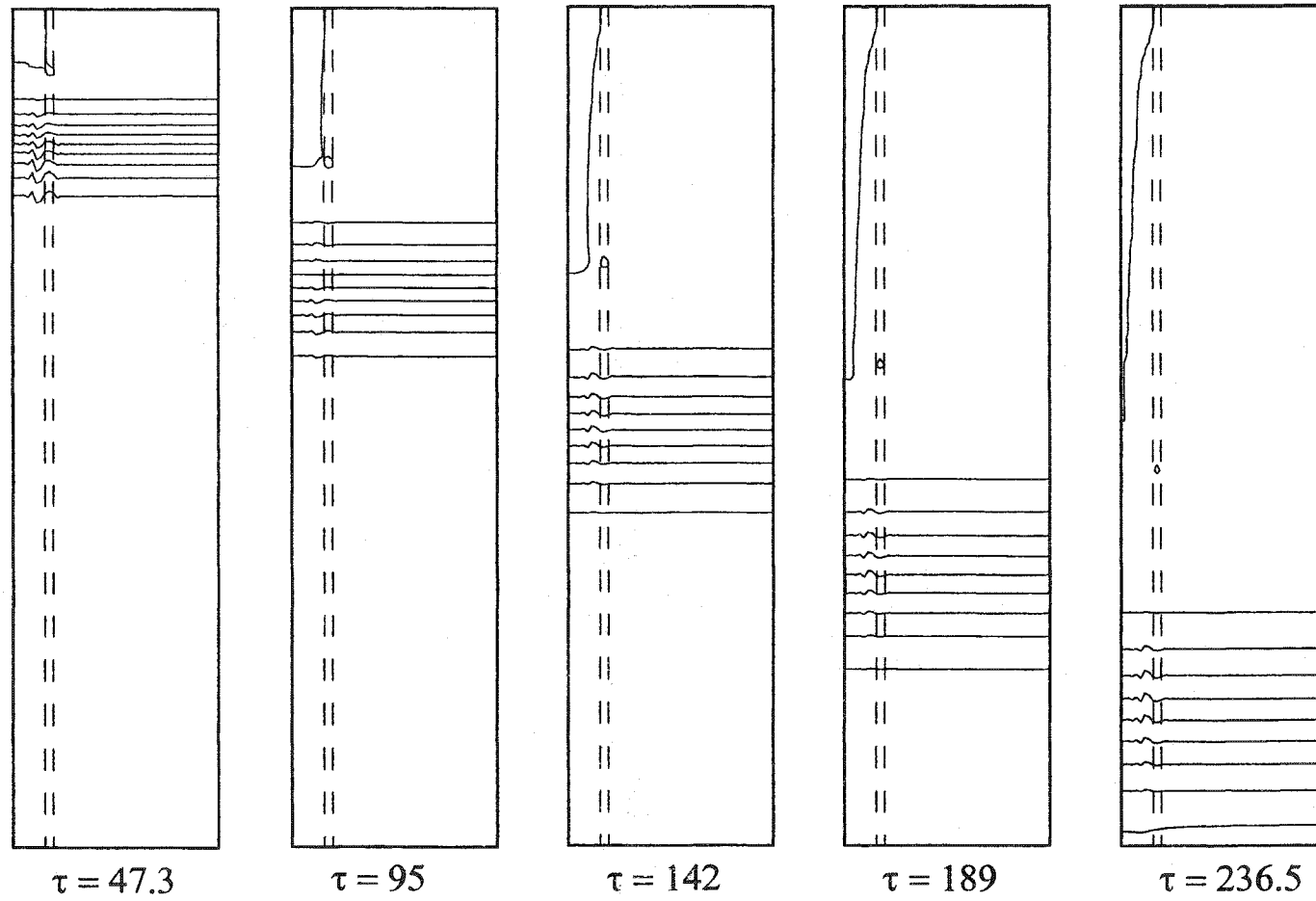


Figure C.12 Temperature fields in a charging process at  $Re = 10^3$  and  $Ra = 10^9$  ( $Ri = 185.2$ ,  $\Delta\theta = 0.1$ )

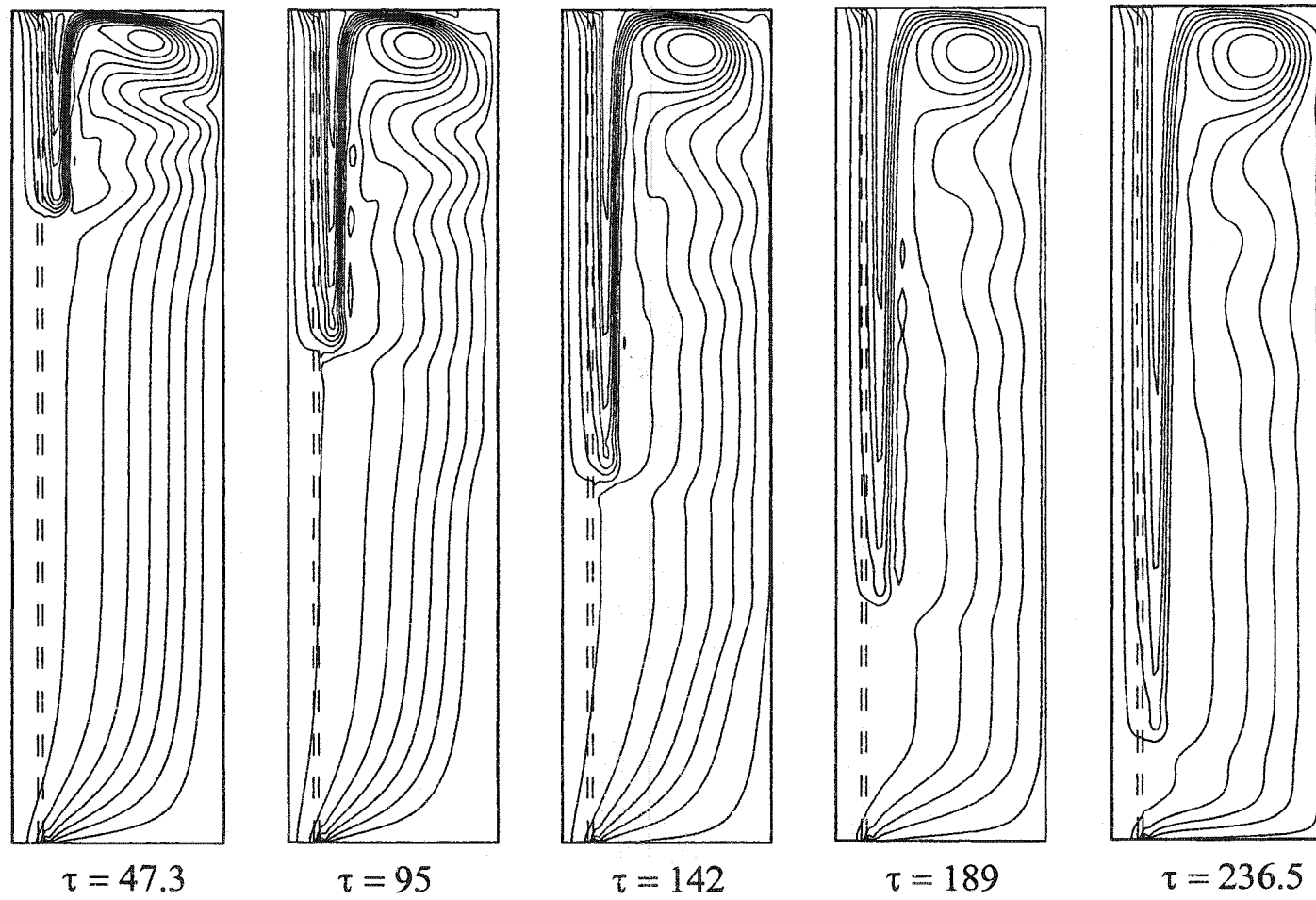


Figure C.13 Flow fields in a charging process at  $Re = 10^4$  and  $Ra = 10^9$  ( $Ri = 1.85$ ,  $\Delta\psi = 0.001$ )

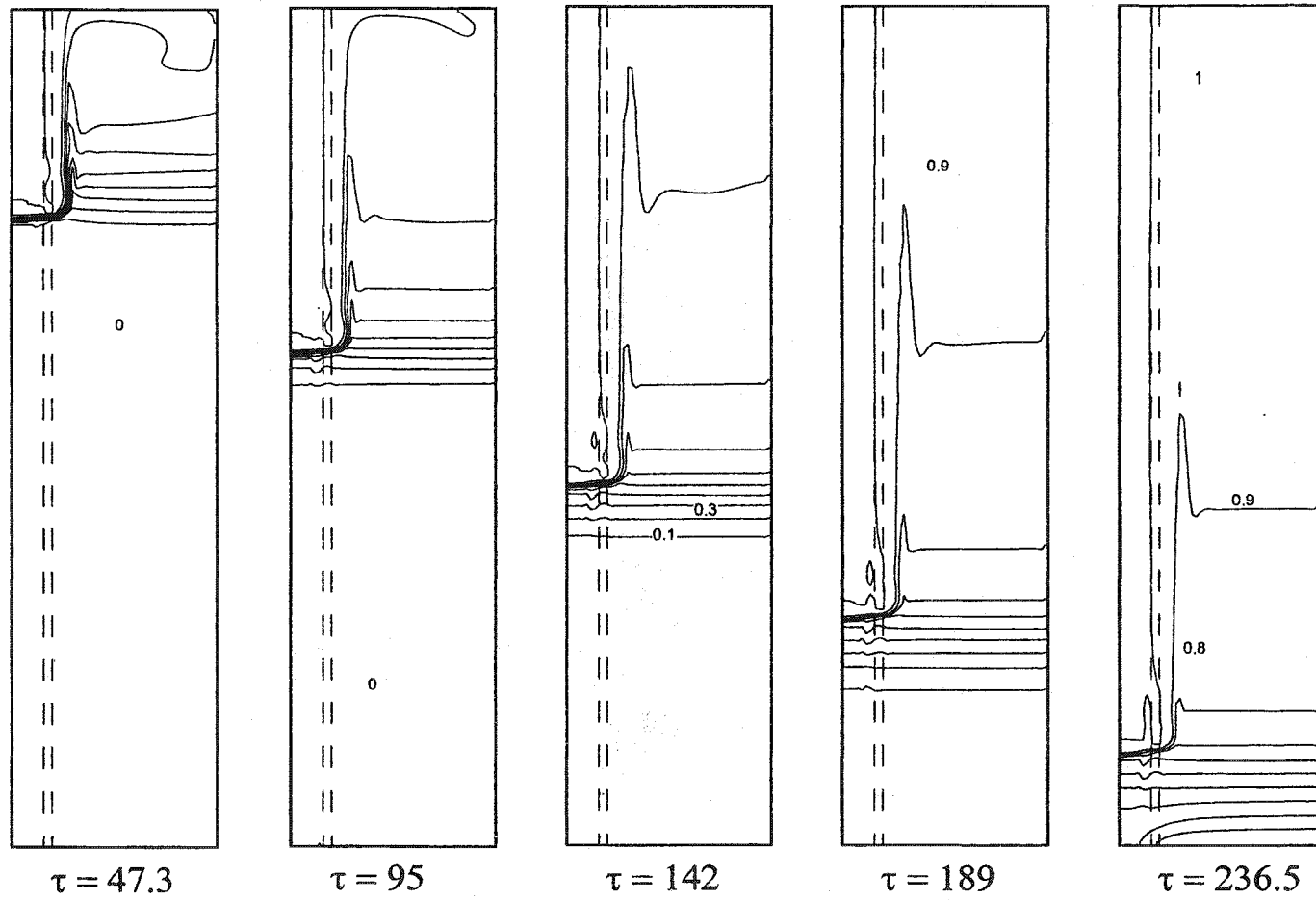


Figure C.14 Temperature fields in a charging process at  $Re = 10^4$  and  $Ra = 10^9$  ( $Ri = 1.85$ ,  $\Delta\theta = 0.1$ )

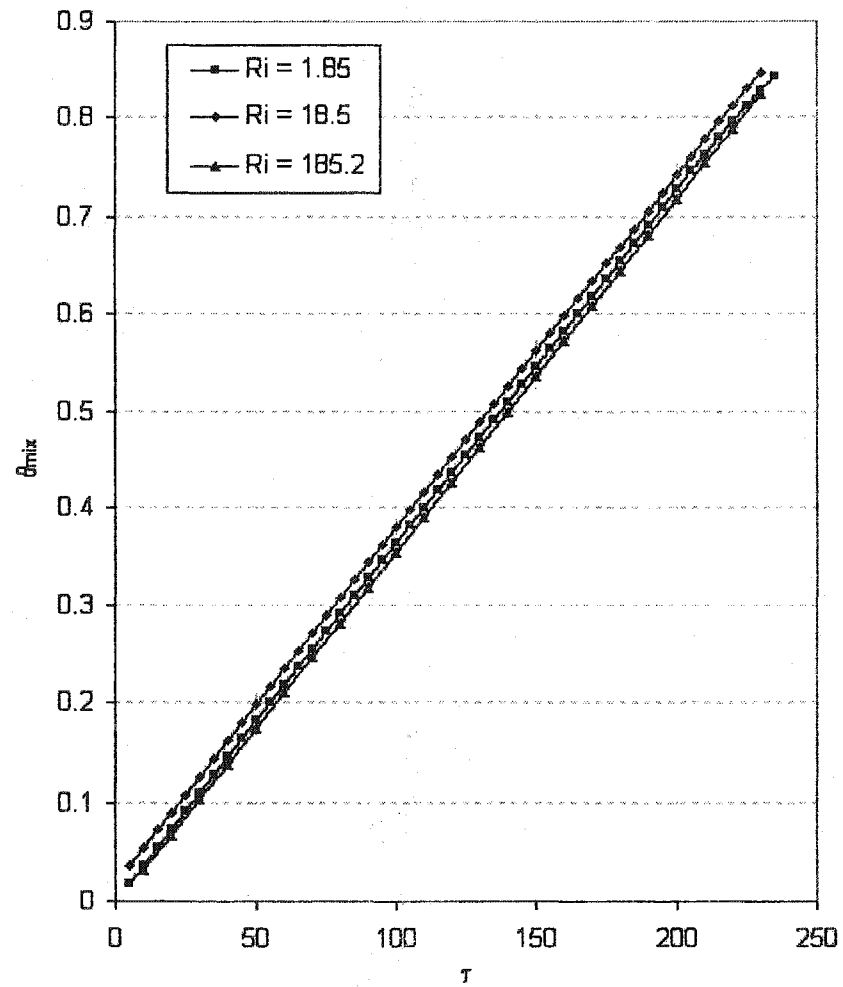


Figure C.15 Mixing tank temperature for various Richardson numbers ( $Re = 10^3$ )

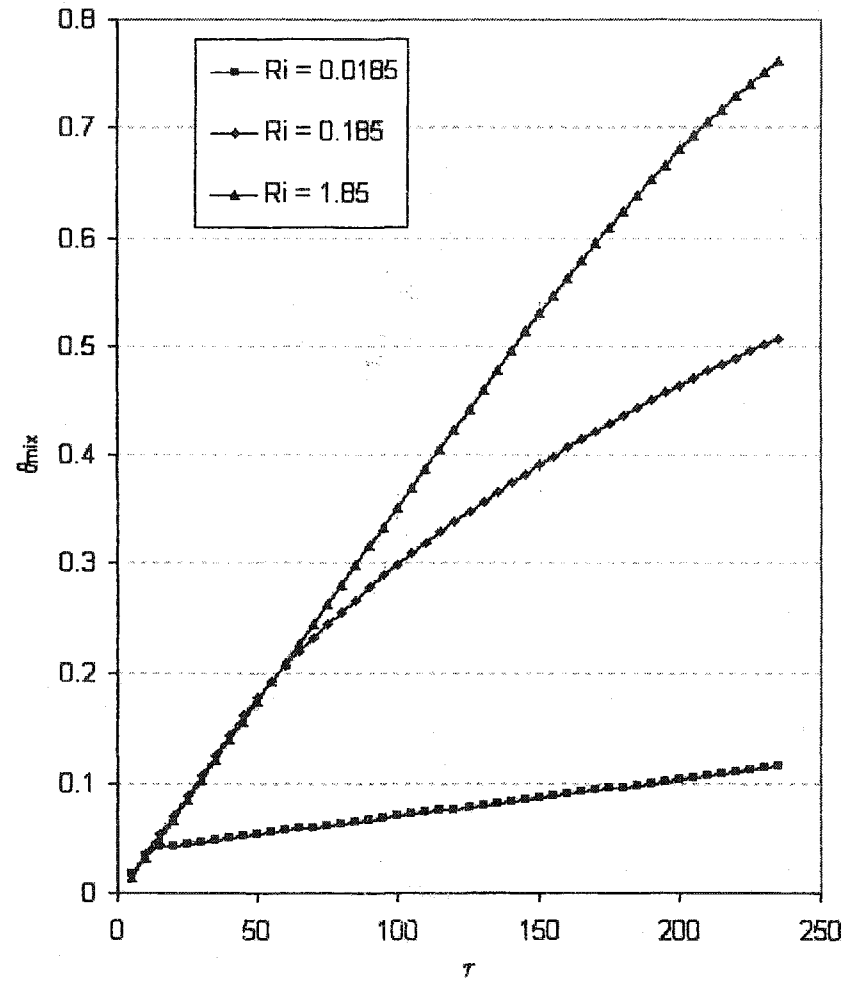


Figure C.16 Mixing tank temperature for various Richardson numbers ( $Re = 10^4$ )

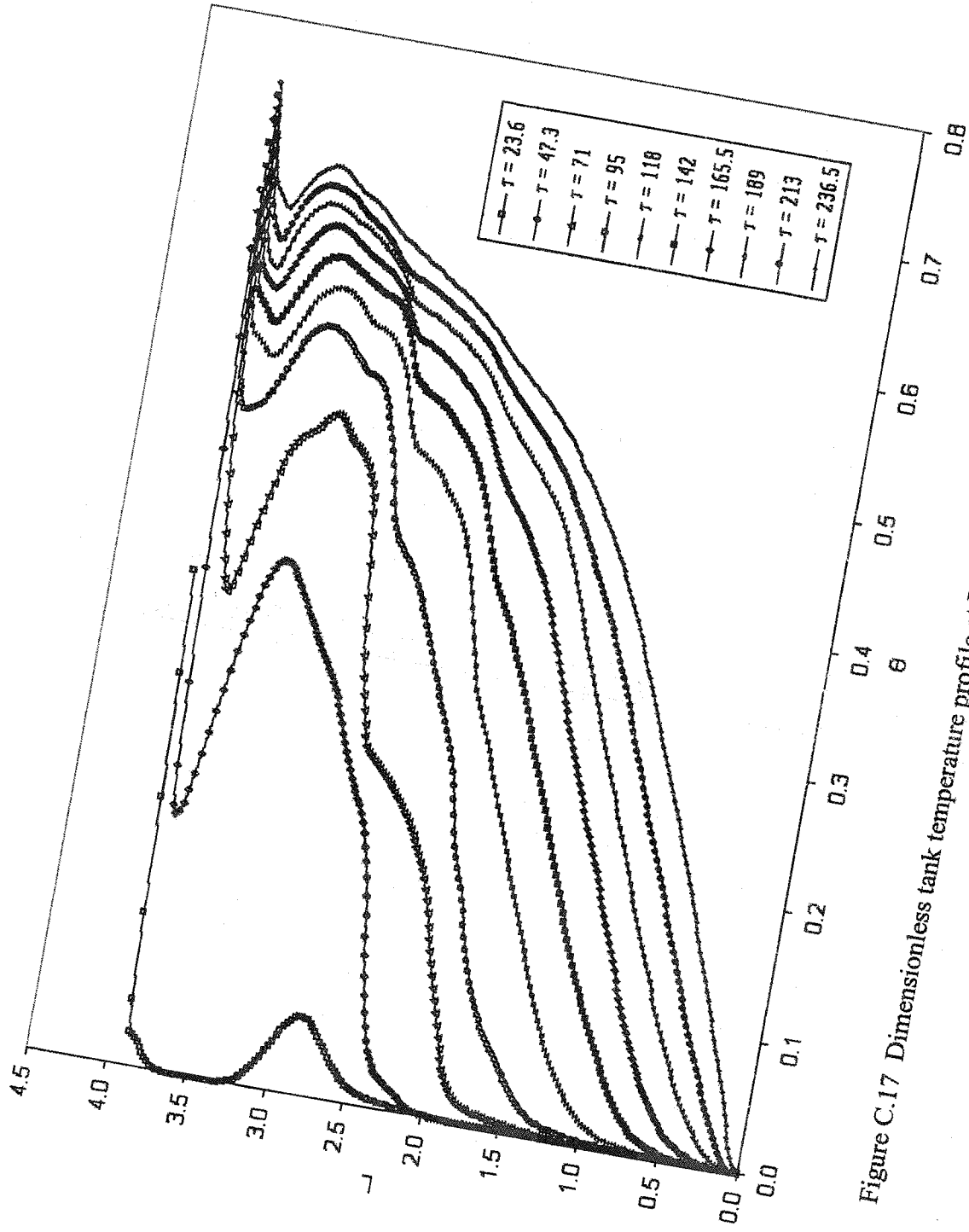


Figure C.17 Dimensionless tank temperature profile at  $Ri = 0.185$  ( $Re = 10^4$  and  $Ra = 10^8$ ).

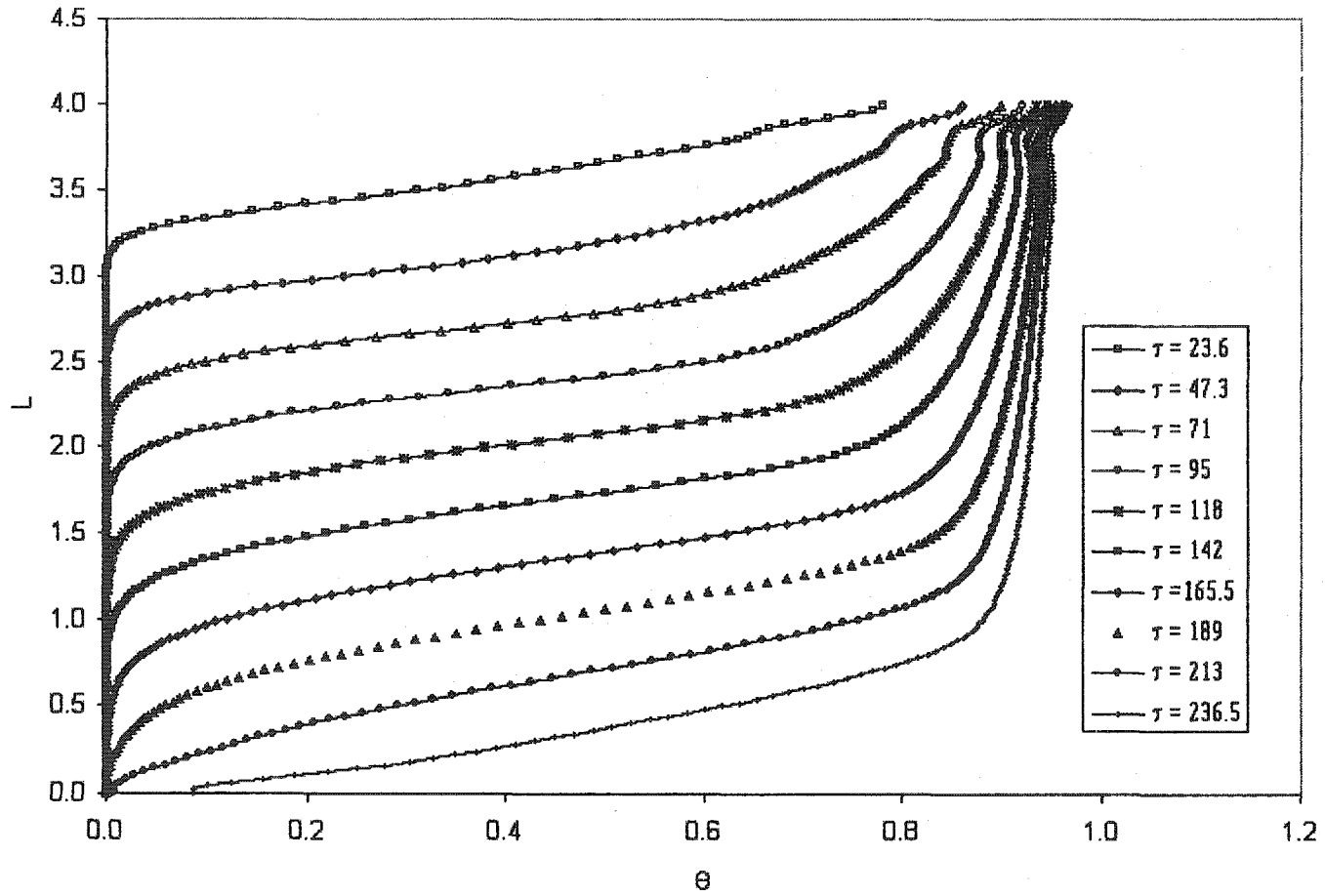


Figure C.18 Dimensionless tank temperature profile at  $Ri = 1.85$  ( $Re = 10^3$  and  $Ra = 10^7$ ).

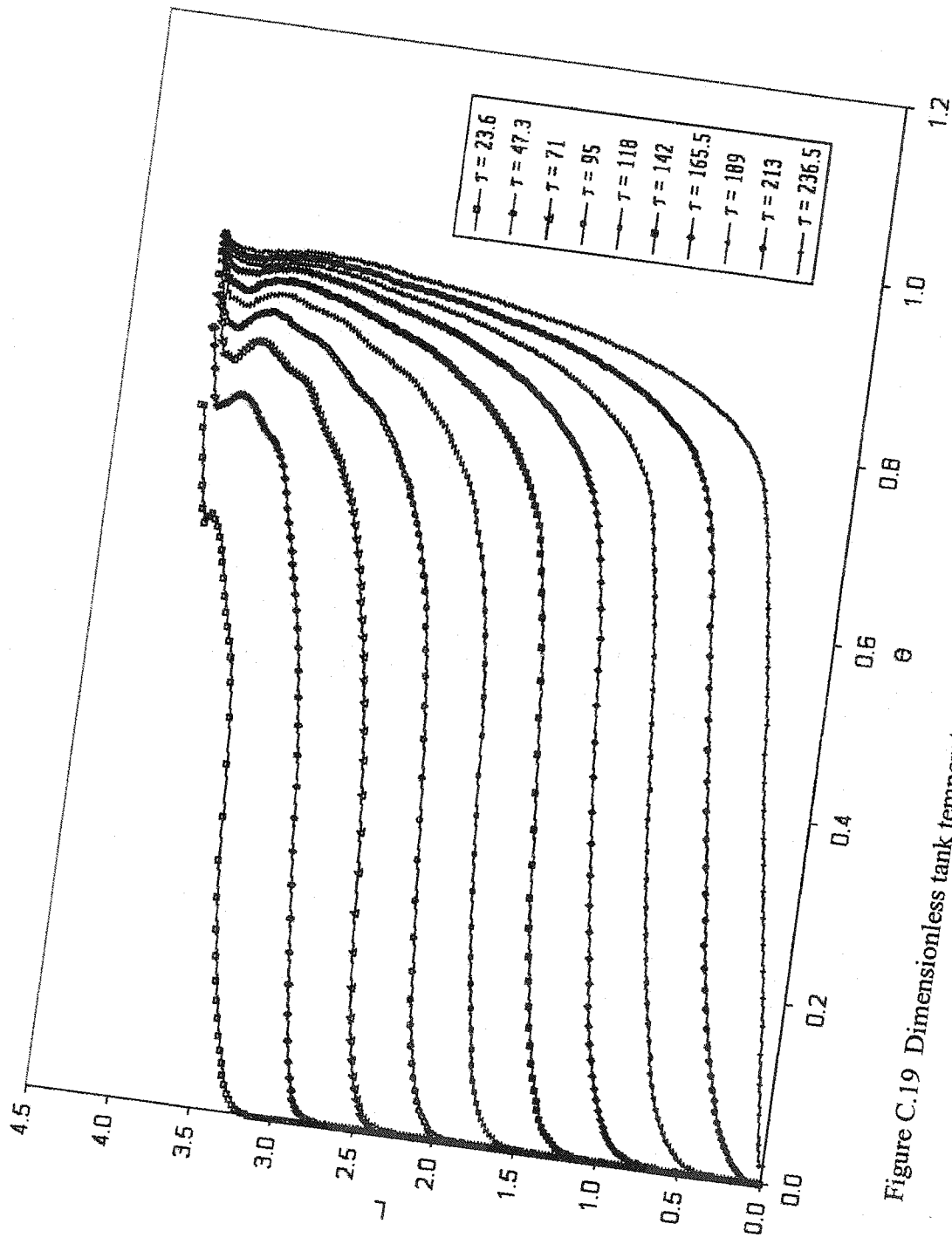


Figure C.19 Dimensionless tank temperature profile at  $Ri = 1.85$  ( $Re = 10^4$  and  $Ra = 10^9$ ).

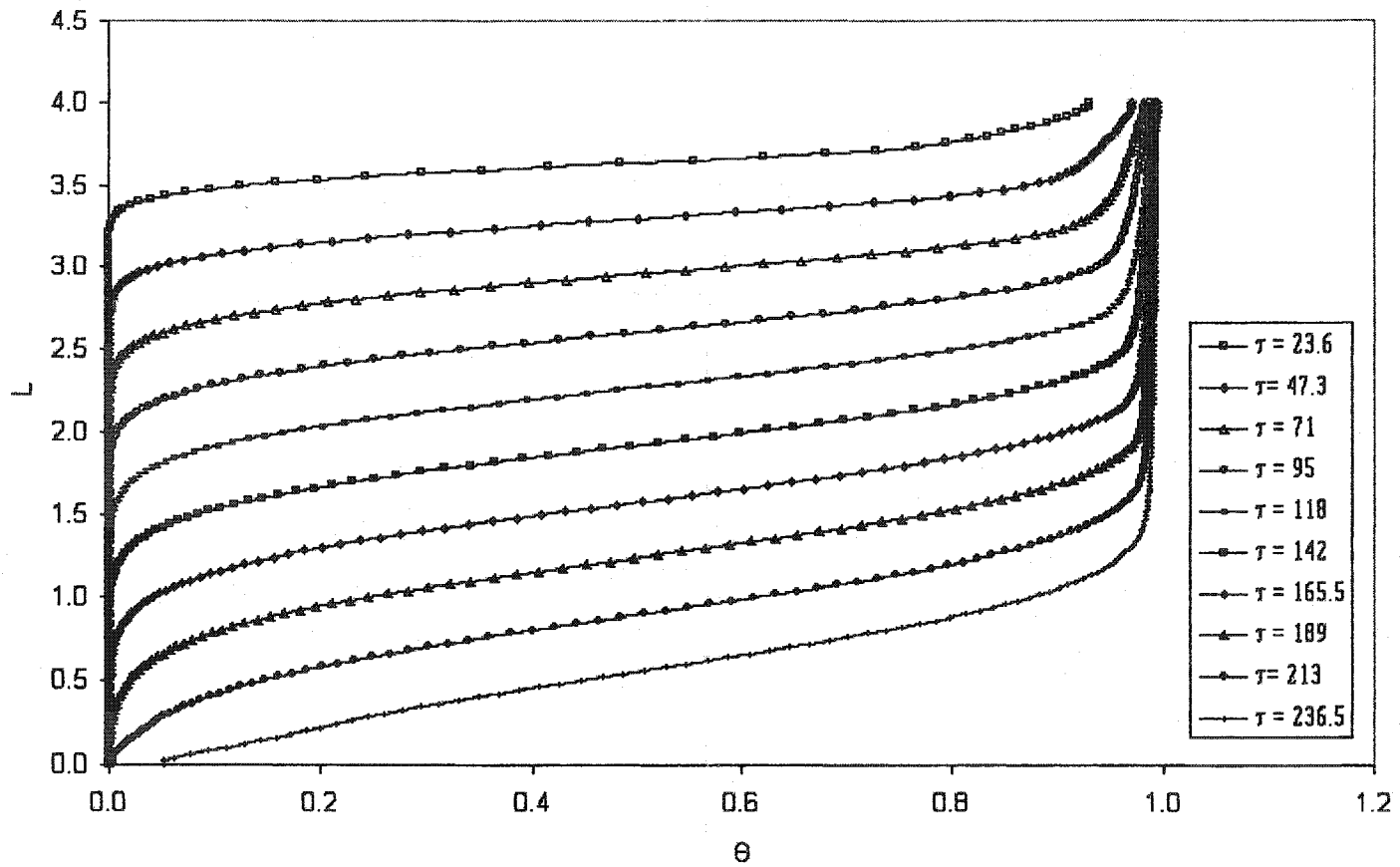


Figure C.20 Dimensionless tank temperature profile at  $Ri = 18.5$  ( $Re = 10^3$  and  $Ra = 10^8$ ).

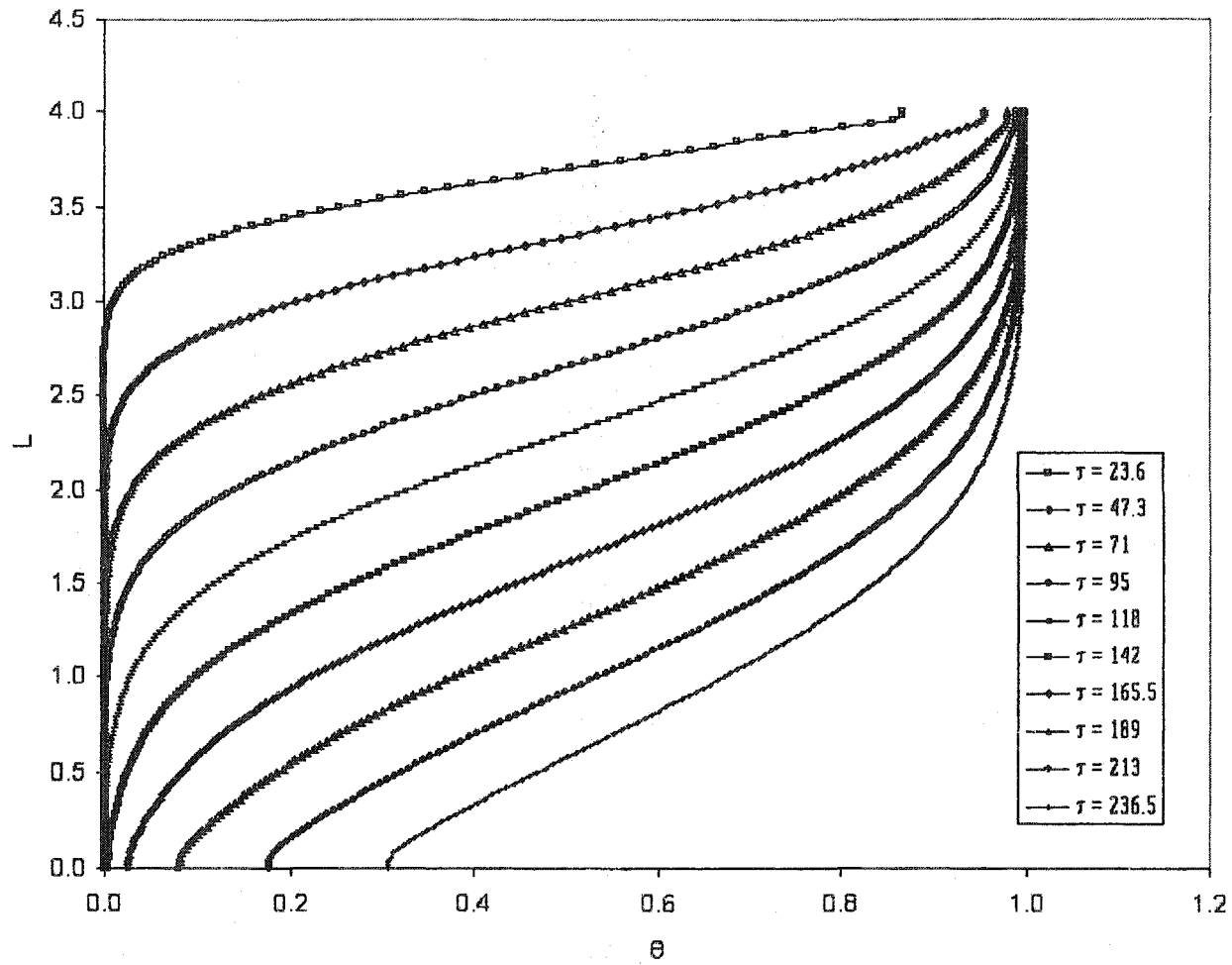


Figure C.21 Dimensionless tank temperature profile at  $Ri = 185.2$  ( $Re = 10^2$  and  $Ra = 10^7$ ).

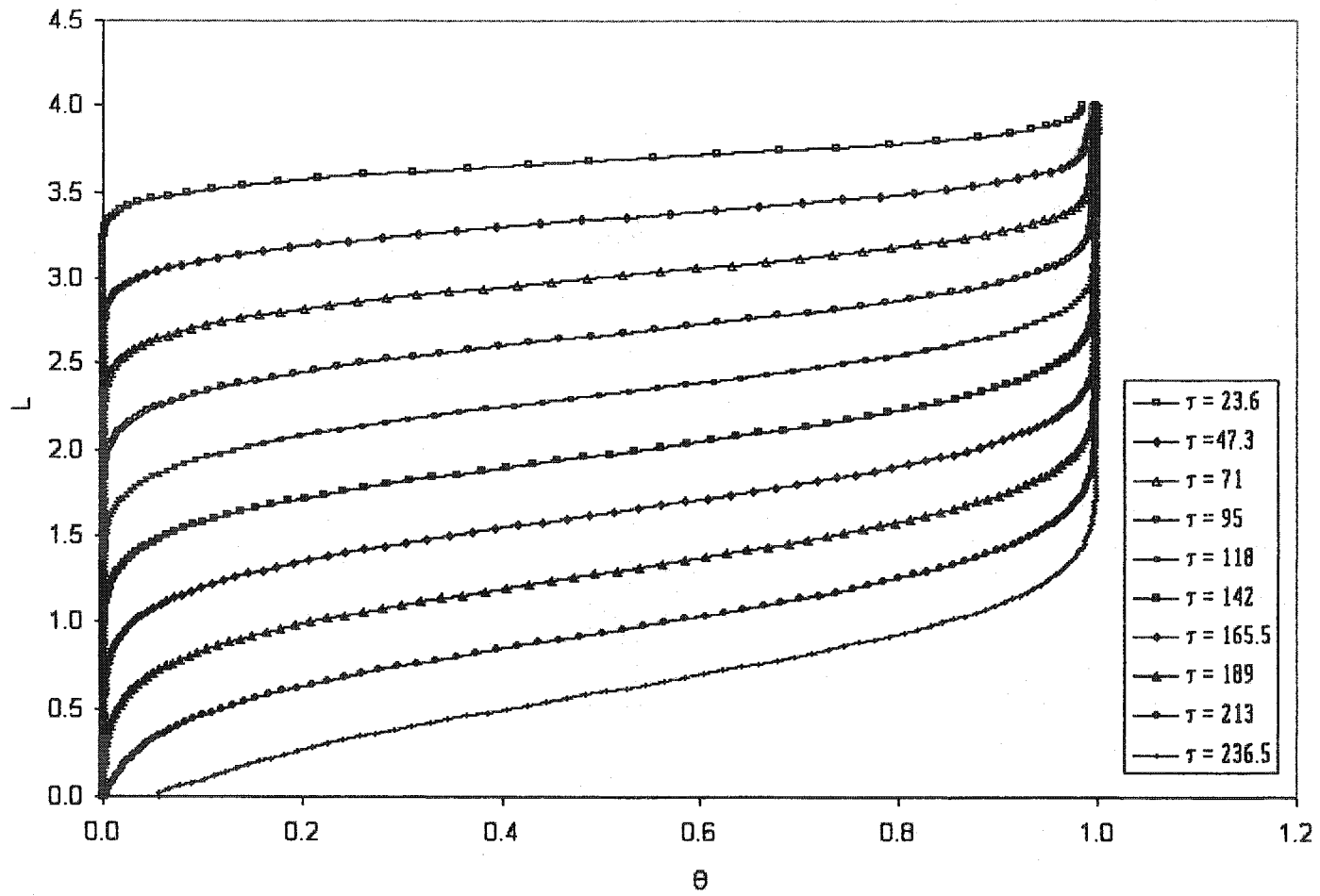


Figure C.22 Dimensionless tank temperature profile at  $Ri = 185.2$  ( $Re = 10^3$  and  $Ra = 10^9$ ).

**APPENDIX D**

**Calculation of Uncertainties**

Table D.1	Uncertainty associated with the measuring devices used in the study .....	214
-----------	---	-----

## Uncertainty Calculation

This experiment does involve some level of uncertainty that originated from the lack of accuracy in the measuring devices, and random variation in the measurands. These uncertainties include lack of precision in the measurand (precision error) and estimated fix error (bias error). Normally these uncertainties have to be treated separately, however, in this experiment manufactures-specified instrument accuracy was used which inherently combined precision and bias uncertainties. The uncertainty of the results are affected by the uncertainty of each measurands. Table D.1 is a summary of the manufacturers-specified instrument uncertainties used in this study. This section outlines the steps used to determine the uncertainties stated in the preceding chapters.

The maximum uncertainty associated with the measured flow rate defined as

$$Q_{\text{Exp}} = \frac{V}{t} = Vt^{-1}, \quad (\text{D.1})$$

can be calculated as follows

$$\frac{\omega_Q}{Q} = \left[ \left( 1 * \frac{\omega_V}{V} \right)^2 + \left( -1 \frac{\omega_t}{t} \right)^2 \right]^{\frac{1}{2}} \quad (\text{D.2})$$

Table D.1 Uncertainty associated with the measuring devices used in the study

Instrument	Manufacturers-Specified Uncertainty
Thermocouple input Module	$\pm 1 \text{ }^\circ\text{C}$
PX26 Pressure transducer	$\pm 6.895 \text{ N/m}^2$
DP25B-S Panel Meter	$\pm 0.03\%$
Sport Line stop watch	$\pm 0.01 \text{ s}$
Measuring Cylinder	$\pm 2.5 \text{ cm}^3$
Dial Caliper	$\pm 0.0025 \text{ cm}$

$$\frac{\omega_Q}{Q_{\text{Exp}}} = \left[ \left( 1 * \frac{2.5}{107.6} \right)^2 + \left( -1 * \frac{0.01}{9.8} \right)^2 \right]^{\frac{1}{2}} = 0.0232 \quad (\text{D.3})$$

which is about 2.3 %.

The theoretical Poiseuille flow rate is given by,

$$Q^* = \frac{\pi r^4}{8\mu} \left( -\frac{dP}{dx} \right) \quad (D.4)$$

To facilitate this analysis the constant terms are dropped and Equation (D.4) can be simplified to give;

$$Q^* = r^4 \Delta P \Delta L^{-1}. \quad (D.5)$$

Then the maximum uncertainty can be calculated as

$$\frac{\omega_Q}{Q^*} = \left[ \left( 4 * \frac{\omega_L}{r} \right)^2 + \left( 1 * \frac{\omega_P}{\Delta P} \right) + \left( -1 * \frac{\omega_L}{L} \right)^2 \right]^{\frac{1}{2}}, \quad (D.6)$$

$$\frac{\omega_Q}{Q^*} = \left[ \left( 4 * \frac{0.0025}{0.9525} \right)^2 + \left( 1 * \frac{6.895}{21.93} \right) + \left( -1 * \frac{0.0025}{40.64} \right)^2 \right]^{\frac{1}{2}} = 0.3145, \quad (D.7)$$

which translate into 31.4 % uncertainty.

The longitudinal permeability can be defined as

$$K_z = \frac{v\mu}{\frac{\Delta P}{L}} \quad (D.8)$$

where the velocity  $v$  is defined as,

$$v = \frac{Q_{Exp}}{\pi(r_o^2 - r_{in}^2)}. \quad (D.9)$$

First the uncertainty associated with the velocity can be calculated as

$$\frac{\omega_v}{v} = \left[ \left( \frac{\omega_Q}{Q_{Exp}} \right)^2 + \left( -2 * \frac{\omega_r}{r} \right)^2 \right]^{\frac{1}{2}} =$$

$$\left[ \left( \frac{5.474 \times 10^{-3}}{0.238} \right)^2 + \left( -2 * \frac{0.0025}{0.4762} \right)^2 \right] = 0.025 \approx 2.5\%. \quad (\text{D.10})$$

Therefore,

$$\frac{\varpi_{K_z}}{K_z} = \left[ \left( \frac{\varpi_v}{v} \right)^2 + \left( \frac{\varpi_L}{L} \right)^2 + \left( -1 * \frac{\varpi_P}{P} \right)^2 \right]^{\frac{1}{2}} =$$

$$\left[ (0.025)^2 + \left( \frac{0.000025}{0.4064} \right)^2 + \left( -1 * \frac{6.895}{64.6} \right)^2 \right] = 0.1112 \approx 11.12\%. \quad (\text{D.11})$$

For the radial permeability

$$K_r = \frac{1}{\pi} \frac{Q\mu}{2h} \frac{\ln \frac{r_e}{r_{in}}}{\Delta P}, \quad (\text{D.12})$$

the maximum uncertainty can be calculated as follows

$$\frac{\varpi_{K_r}}{K_r} = \left[ \left( \frac{\varpi_Q}{Q} \right)^2 + \left( -1 * \frac{\varpi_L}{h} \right)^2 + \left( \frac{\varpi_r}{r} \right)^2 + \left( \frac{\varpi_P}{\Delta P} \right)^2 \right]^{\frac{1}{2}} =$$

$$\left[ (0.023)^2 + \left( -1 * \frac{0.000025}{0.01905} \right)^2 + \left( \frac{0.000025}{0.0508} \right)^2 + \left( \frac{6.895}{62.2} \right)^2 \right]^{\frac{1}{2}} = 0.334 \approx 33.4\% \quad (\text{D.13})$$

The slip coefficient is defined as

$$\gamma = \frac{4\sqrt{K_z}}{r_0} \left[ 1 - \frac{Q}{Q^*} + \frac{8K_z}{r_0^2} \right]^{-1} \quad (\text{D.14})$$

Let's call the terms in the parentheses C, therefore

$$C = \left[ 1 - \frac{Q}{Q^*} + \frac{8K_z}{r_0^2} \right]^{-1}, \quad (\text{D.15})$$

which implies that

$$\gamma = \frac{4\sqrt{K_z}}{r_0} C^{-1}, \quad (\text{D.16})$$

therefore

$$\frac{\varpi_\gamma}{\gamma} = \left[ \left( \frac{1}{2} * \frac{\varpi_{K_z}}{K_z} \right)^2 + \left( -1 * \frac{\varpi_{r_0}}{r_0} \right)^2 + \left( -1 * \frac{\varpi_C}{C} \right)^2 \right]^{\frac{1}{2}}, \quad (\text{D.17})$$

where

$$\frac{\varpi_C}{C} = \left[ \left( \frac{\varpi_Q}{Q_{\text{Exp}}} \right)^2 + \left( -1 * \frac{\varpi_{Q^*}}{Q^*} \right)^2 \right]^{\frac{1}{2}} + \left[ \left( \frac{\varpi_K}{K_z} \right)^2 + \left( -2 * \frac{\varpi_{r_0}}{r_0} \right)^2 \right]^{\frac{1}{2}}. \quad (\text{D.18})$$

The maximum uncertainty associated with the slip coefficient is 16.34 %.